Tracking and Particle Identification at LHCb and Strange Hadron Production in Events with Z Boson

---

Dissertation

zur

Erlangung der naturwissenschaftlichen Doktorwürde
(Dr. sc. nat.)

vorgelegt der

Mathematisch-naturwissenschaftlichen Fakultät

der

Universität Zürich

von

Marco Tresch

von

Silenen Uri

Promotionskomitee
Prof. Dr. Ulrich Straumann (Vorsitz)
Prof. Dr. Nicola Serra
Dr. Katharina Müller
Dr. Olaf Steinkamp

Zürich, 2017

Contact
Marco Tresch
marco.tresch@cern.ch

ABSTRACT

The LHCb experiment, located at the Large Hadron Collider at CERN, is a high energy particle physics experiment dedicated to precision measurements of events containing beauty and charm quarks. The detector is built as a single-arm forward spectrometer. It uses tracking stations upstream and downstream of its dipole magnet to measure the trajectories and momenta of charged particles. This thesis describes the improvements to the track reconstruction algorithm, which were implemented for the second run of the LHC that started in spring 2015. Furthermore, the method to confirm the performance numbers on data is presented.

In addition to the tracking system, the detector uses two Ring Imaging Cherenkov detectors, upstream and downstream of the dipole magnet, together with the calorimeter and muon system, for particle identification. The detector response for the particle identification is known to be poorly modelled, since the dependence on environmental variables like temperature and pressure inside the gas moderators are difficult to simulate. This thesis presents a tool for the correction of the particle identification detector responses using calibration data.

With higher collision energy and luminosity the understanding of the soft part of a proton-proton interaction becomes more and more important for high precision measurements at LHC. The soft part includes, for example, the understanding of fragmentation and hadronisation processes, which need experimental input. This thesis presents the first measurement at LHCb of the production of K^0_S and $\mathit{\Lambda}/\overline{\mathit{\Lambda}}$, both hadrons that contain a strange quark, in an event containing a Z boson. The decay channels $Z \to \mu^+\mu^-$, $K^0_\mathrm{S} \to \pi^+\pi^-$, $\mathit{\Lambda} \to p\pi^-$ and $\overline{\mathit{\Lambda}} \to \overline{p}\pi^-$ were used. The measurements were performed as function of the opening angle between the Z boson and the strange hadron, as well as the transverse momentum p_T of the latter. The data collected by LHCb in pp collisions corresponds to an integrated luminosity of $2\,\mathrm{fb}^{-1}$ at a centre of mass energy of 8 TeV. The results are compared to Monte Carlo predictions from PYTHIA.

ZUSAMMENFASSUNG

Das LHCb Experiment, welches sich am Large Hadron Collider am CERN befindet, ist ein Hochenergiephysik Experiment spezialisiert auf die Erforschung von physikalischen Prozessen, die Beauty- und Charm-Quarks beinhalten. Der Detektor ist als einarmiges Spektrometer entlang der Strahlachse aufgebaut. Zur Messung der Flugbahn und des Impulses von geladenen Teilchen verfügt der Detektor über Spurkammern vor und nach dem Dipolmagneten. Die vorliegende Arbeit beschreibt die Verbesserungen des Algorithmus für die Spurrekonstruktion, welche für die zweite Messperiode des LHC, die im Frühling 2015 begann, implementiert wurden. Ausserdem beschreibt die Arbeit die Messmethode zur Überprüfung der Leistungsparameter in Simulation und Daten.

Zusätzlich zum Spurkammersystem besitzt der Detektor zwei Cherenkov Detektoren vor und nach dem Diplmagneten, die zusammen mit einem Kalorimeter- und einem Muon-System zur Identifikation der Teilchen benutzt werden. Das Ansprechverhalten der Detektoren zur Teilchenidentifikation ist bekanntermassen schlecht simuliert, weil die Abhängigkeit von Umgebungsvariablen wie Temperatur und Druck innerhalb der Gasmoderatoren der Cherenkov Detektoren schwierig zu simulieren ist. Die vorliegende Arbeit beschreibt ein Programm, welches das simulierte Verhalten mit Hilfe von Kalibrationsdaten korrigiert.

Die Charakterisierung der weichen Komponente einer Kollision von zwei Protonen wird mit höherer Kollisionsenergie und Luminosität immer wichtiger für Präzisionsmessungen am LHC. Unter die weiche Komponente fallen zum Beispiel Fragmentations- und Hadronisationsprozesse, für deren korrekten Beschreibung man experimentelle Daten braucht. Die vorliegende Arbeit beschreibt die erste Messung am LHCb Detektor von der Anzahl K^0_S Mesonen und $\Lambda/\overline{\Lambda}$ Bosonen, beides Hadronen, die ein Strange-Quark enthalten, in einem Kollisionsereignis mit einem Z Boson. Dafür wurden die Zerfallskanäle $Z \rightarrow \mu^+\mu^-$, $K^0_\mathrm{S} \rightarrow \pi^+\pi^-$, $\Lambda \rightarrow p\pi^-$ und $\overline{\Lambda} \rightarrow \overline{p}\pi^-$ verwendet. Die Messung wurde als Funktion des Öffnungswinkels zwischen dem Z Boson und dem Hadron, sowie des transversalen Impulses des letzteren durchgeführt. Die Menge der gesammelten LHCb pp Kollisionsdaten entspricht einer integrierten Luminosität von 2 fb^{-1} bei einer Schwerpunktsenergie von 8 TeV. Die Resultate werden mit Monte Carlo Voraussagen von PYTHIA verglichen.

Contents

Not only is the Universe stranger than we think, it is stranger than we can think.

Werner Heisenberg

1

Introduction

Throughout history, statements from well known men and women are found, claiming that everything, which is to discover, is already found and understood. The only thing left is to catalogue and order what former scientist have discovered. Today, the situation is similar in particle physics. The Standard Model (SM) of particle physics theoretically describes present measurements with an astonishing precision. However, according to cosmological observations, the SM describes only 5% of the content of the universe. This small amount is termed visible matter and consist of matter and antimatter. Roughly 27% of the universe consists of dark matter, which is only visible through the gravitational effect of it on the visible matter. There is no hint in the SM what dark matter actually is. The remaining 68% of the content of the universe is an even more exotic substance, called dark energy. It is distributed evenly throughout the universe, not only in space but also in time. An interesting observation, which is connected to the dark energy, is the rate of the expansion of the universe.

A further challenge of the SM is the observation that the visible matter in the universe mainly consists of matter and hardly of antimatter, which is called matter-antimatter asymmetry. The SM is not able to explain the difference of several orders of magnitude between the theoretically expected and the actually observed asymmetry.

The Large Hadron Collider (LHC) and its experiments are built to investigate these fundamental questions. Two distinct approaches are adopted; direct and indirect observations. A direct observation includes the measurement of an unknown particle, whereas an indirect observation is based on precision measurements of already known observables, searching for tensions with respect to the SM predictions. One experiment at the LHC that is dedicated to indirect observations is the LHCb experiment. It is presented in this thesis in section 3.2. A short review of the concepts of particle physics and the LHC is given in chapter 2 and 3. Precision measurements are only possible with excellent tracking and particle identification capabilities. Chapter 4 is devoted to the tracking of the LHCb experiment and discusses an upgrade of the tracking algorithm which is in place since 2015. Chapter 5 gives an overview of the particle identification algorithms in LHCb and introduces a method to overcome inaccuracies of the simulated detector response. Indirect observations have to be compared to predictions of the SM before an observation can potentially be classified as New Physics. Predictions for the hard scattering processes are known for many particle productions and decay modes at high precision, but there are also contributions from soft effects such as fragmentation or multi-parton interactions. The models for the soft part depend crucially on experimental input. These soft contributions become more and more important with higher collision energy and luminosity of the LHC. In line with this, chapter 6 is devoted to the measurement of particles containing strange quarks in a hard scattering event. This measurement gives an input especially in terms of the formation of particles.

Your theory is crazy, but it's not crazy enough to be true.

Niels Bohr

2

The Standard Model of Particle Physics

In the second half of the 20th century a model was developed to characterise the phenomenology of subatomic particles. It describes the elementary particles, which have no constituents nor substructure, and their interplay with the electromagnetic, the weak and the strong forces. This model is called Standard Model (SM) and is a combination of two theories: the *Glashow-Weinberg-Salam* (GWS) model [1–3] describing the combination of the weak and the electromagnetic interactions; and the *Quantum Chromodynamics* (QCD)[4–7], which describes the strong interactions. The experimental data is described precisely in many different kinematic regimes, ranging from low energies like nuclear decays up to very high energy phenomena in particle colliders. In addition, the model was able to predict new particles such as the gluon, the top quark or the Higgs boson. But the SM is not complete, as it lacks to explain several phenomena, including dark matter, the masses of the neutrinos or the fourth fundamental force, the gravity.

In this chapter a brief overview of the constitutes and dynamics of the SM is given with a focus on QCD. This overview is not meant to be complete. A more detailed description of the SM is given in [8, 9] and with focus on QCD in [4]. The aspects of the SM extensions are discussed in [10].

2.1 Particle Content of the Standard Model

In the SM particles are described as excitations of the vacuum state of the corresponding fields. The particles can be split into two groups according to their spin: full or half integer spin. Particles with half integer spin are called *fermions* and obey the Fermi-Dirac statistics [11, 12]. Those particles with full integer spin are called *bosons* and follow the Bose-Einstein statistics [13]. In the SM bosons are the force-carriers, which are exchanged between different kind of fermions and bosons to *transmit* the attracting or repelling force. In addition, each particle has a corresponding anti-particle which has the same properties except opposite charge quantum numbers. Some of the particles are their own anti-particle (*e.g.* the photon).

2.1.1 Fermions

Two groups of elementary particles, the quarks and leptons belong to the category of fermions. Quarks and leptons are themselves divided into three families or generations with two members each. The different types of quarks and leptons of one family are called flavours. Table 2.1 shows a summary of the quark and lepton families. A family forms a weak isospin doublet with components $T_3 = \pm 1/2$ and has an electrical charge difference $|\Delta Q| = 1$. The weak isospin is the charge of the weak interaction and is only carried by left-handed[1] fermions (and right-handed anti-particles). Right-handed fermions are weak isospin singlets. Furthermore, all fermions can have a weak hyper-charge Y, which is related to the electric charge Q and the weak isospin T_3 by the Gell-Mann-Nishijma formula $Q = T_3 + Y/2$ [14, 15].

Quarks carry a colour charge with three possible colours denoted as red, green and blue, which are an analogy to the spectral colours in nature: all three charges or charge and anti-charge combined are considered as colour-less. Colour charges are related to the strong interaction. In nature only colour-less objects are observable, which is called confinement of quarks. Each quark type forms a triplet of the strong interaction, whereas leptons are singlets of the strong interaction. Table 2.2 shows a summary of the charges carried by fermions.

2.1.2 Bosons

In the SM there exist five fundamental bosons. Four of them are force-carriers and have spin equal to one: the photon (γ), the $W^{\pm}$ and Z boson, and the gluon (g). The photon, responsible

---

[1] A fermion is called left-handed if its spin projection on its momentum $\vec{s} \cdot \vec{p} / (|\vec{s}| \cdot |\vec{p}|)$ is -1.

Table 2.1: Summary of the masses of elementary fermions from [16]. Since quarks are confined all quark masses except the top quark have been measured indirectly via their influence on hadronic properties. The quoted numbers have been calculated based on the minimal subtraction $\overline{MS}$ scheme [16, 17]. All upper limits correspond to the 95% confidence limit, except for the μ neutrino where it corresponds to the 90% confidence limit.

Category	**1st family**	**2nd family**	**3rd family**
Quarks	up (u) 2.3 MeV/c^2	charm (c) 1.275 GeV/c^2	top (t) 173.21 GeV/c^2
	down (d) 4.8 MeV/c^2	strange (s) 95 MeV/c^2	bottom/beauty (b) 4.18 GeV/c^2
Leptons	electron (e) 5.11 keV/c^2	muon (μ) 105.6 MeV/c^2	Tau (τ) 1.777 GeV/c^2
	e neutrino <2 eV/c^2	μ neutrino <0.19 MeV/c^2	τ neutrino <18.2 MeV/c^2

Table 2.2: The charges carried by the elementary fermions, where T_3 is the weak isospin component, Y the hyper-charge and Q the electric charge. U, D, E and N correspond to the up- and down-type quark as well as to the charged leptons and the neutrinos. The left-handed quarks and leptons form in the electroweak description of the SM a doublet, Q_L and L_L, respectively. The right-handed neutrinos, N_R carry no charge, if they exist, they will not participate in any interactions described by the SM. Table is adapted from [18].

Category		**Colour**	T_3	Y	Q
Quarks	$Q_L = \begin{pmatrix} U_L \\ D_L \end{pmatrix}$	Yes	+1/2	+1/3	+2/3
			-1/2	+1/3	-1/3
	U_R		0	+4/3	+2/3
	D_R		0	-2/3	-1/3
Leptons	$L_L = \begin{pmatrix} N_L \\ E_L \end{pmatrix}$	No	+1/2	-1	0
			-1/2	-1	-1
	E_R		0	-2	-1
	N_R		0	0	0

for the electromagnetic force, is electrically neutral and cannot interact with other photons. The mediators of the weak force are the Z and the $W^{\pm}$ bosons, where the latter carries an electric charge. The Z and the $W^{\pm}$ bosons can interact with each other, resulting in triple or quartic boson couplings. The gluon (g) mediates the strong force and carries a colour charge. There exist eight different colour charged gluons[2], each having a different combination of colour and anti-colour. The fifth boson, the Higgs boson, has spin zero and is responsible for the masses of the $W^{\pm}$ and Z bosons, the quarks and the charged leptons. Table 2.3 summarises the properties of the five bosons.

Table 2.3: Properties of the elementary bosons in the SM, where T_3 is the weak isospin component, Y the hyper-charge and Q the electric charge. The masses are from [16].

Field/Interaction	**Particle**	**Colour**	T_3	Y	Q	M
Electromagnetic	Photon (γ)	No	0	0	0	0
Weak	Z	No	0	0	0	91.19 GeV/c^2
Weak	$W^{\pm}$	No	±1	0	±1	80.38 GeV/c^2
Strong	Gluon (g)	Yes	0	0	0	0
Higgs field	Higgs (H)	No	0	0	0	125.7 GeV/c^2

2.2 DYNAMICS OF THE STANDARD MODEL

The SM is formulated using the framework of quantum field theory. It is renormalizable and based on local symmetries that extend the gauge invariance of electrodynamics to a larger set of conserved currents and charges. The structure of the SM is given by the symmetry of type $SU(3) \times SU(2) \times U(1)$. The $SU(3)$ part of the symmetry is responsible for the behaviour of the strong interaction and associated to the conservation of the colour charge (see Noether theorem [19]). The $SU(2) \times U(1)$ part describes the electroweak interactions, where the $SU(2)$ invariance is associated with the weak isospin and the $U(1)$ is associated with the weak hyper-charge.

Quarks, leptons and bosons are represented as quantum fields. The dynamics of the SM is described by a Lagrange density $\mathcal{L}_{SM}$, which can be split into separate parts:

$$\mathcal{L}_{SM} = \mathcal{L}_{EW} + \mathcal{L}_{QCD}, \tag{2.1}$$

where $\mathcal{L}_{EW}$ represents the Lagrange density of the electroweak interactions and $\mathcal{L}_{QCD}$ represents the Lagrange density of the Quantum Chromodynamics (QCD), the theory of the strong interactions.

---

[2] The strong interaction is described by the symmetry group $SU(3)$. This group has eight ($N^2 - 1$) generators, therefore there are eight gauge fields.

2.2.1 Electroweak Interactions

The electroweak Lagrangian can be split into two parts by separating the Higgs boson couplings:

$$\mathcal{L}_{EW} = \mathcal{L}_{symm} + \mathcal{L}_{Higgs} \tag{2.2}$$

The $\mathcal{L}_{symm}$ involves only gauge bosons and fermions, where a sum over all flavours of quark and leptons, generically indicated by φ, is understood:

$$\mathcal{L}_{symm} = -\frac{1}{4}\sum_{A=1}^{3} F^{A}_{\mu\nu}F^{A\mu\nu} - \frac{1}{4}B_{\mu\nu}B^{\mu\nu} + \bar{\varphi}_L i\gamma^{\mu}D_{\mu}\varphi_L + \bar{\varphi}_R i\gamma^{\mu}D_{\mu}\varphi_R. \tag{2.3}$$

Here

$$B_{\mu\nu} = \partial_{\mu}B_{\nu} - \partial_{\nu}B_{\mu} \quad \text{and} \quad F^{A}_{\mu\nu} = \partial_{\mu}W^{A}_{\nu} - \partial_{\nu}W^{A}_{\mu} - g\varepsilon_{ABC}W^{B}_{\mu}W^{C}_{\nu} \tag{2.4}$$

where B_{μ} is the gauge field associated with $U(1)$ and W^{A}_{μ} corresponds to the three gauge fields of $SU(2)$. The ε_{ABC} is the antisymmetric structure constant of the $SU(2)$ group[3]. The fermion fields are described by their left-handed and right-handed components:

$$\varphi_{L,R} = [(1 \mp \gamma_5)/2]\varphi, \quad \bar{\varphi}_{L,R} = \bar{\varphi}[(1 \pm \gamma_5)/2]. \tag{2.5}$$

The φ_L and φ_R behave differently under the gauge group. In the SM all φ_R are singlets and all φ_L are doublets. Thus mass terms for fermions of the form $\bar{\varphi}_L\varphi_R + h.c.$ are forbidden in the symmetric limit. The masses for fermions together with $W^{\pm}$ and Z masses are introduced by the mechanism of spontaneous symmetry breaking, which will be explained in the next paragraph. The covariant derivatives D_{μ} are given by

$$D_{\mu}\varphi_{L,R} = \left[\partial_{\mu} + iq\sum_{A=1}^{3} t^{A}_{L,R}W^{A}_{\mu} + ig'\frac{1}{2}Y_{L,R}B_{\mu}\right]\varphi_{L,R}, \tag{2.6}$$

where $t^{A}_{L,R}$ and $\frac{1}{2}Y_{L,R}$ are the $SU(2)$ and $U(1)$ generators, g the weak isospin coupling and g' the weak hyper-charge coupling. The physical fields of the electroweak gauge bosons photon A_{μ}, Z_{μ}, W^{+}_{μ} and W^{-}_{μ} are linear combinations of the massless W^{A}_{μ} and B_{μ} gauge fields due to the spontaneous symmetry breaking:

$$W^{\pm}_{\mu} = \frac{1}{\sqrt{2}}(W^{1}_{\mu} \mp iW^{2}_{\mu}) \tag{2.7}$$

---

[3] An antisymmetric structure constant, $\varepsilon_{\alpha\beta\gamma}$, is defined by $[t^{\alpha}t^{\beta}] = i\varepsilon_{\alpha\beta\gamma}t^{\gamma}$, where t^{i} are generators of the symmetry group and $[\ldots]$ is the anti-commutator.

$$A_\mu = \cos\theta_W B_\mu + \sin\theta_W W^3_\mu \tag{2.8}$$

$$Z_\mu = \cos\theta_W W^3_\mu - \sin\theta_W B\mu \tag{2.9}$$

where A_μ and $Z_{\ \mu}$ are orthogonal to each other and θ_W the weak mixing (or Weinberg) angle defined as $\tan\theta_W = g'/g$. The charged $W^\pm$ bosons only couple to left-handed states while the Z couples to right- and left-handed components of the fermion field.

$\mathcal{L}_{Higgs}$ contains the part responsible for the mass terms of gauge bosons and fermions. The Lagrangian has to be:

$$\mathcal{L}_{Higgs} = (D_\mu\psi)^\dagger(D_\mu\psi) - V(\psi^\dagger\psi) - \bar{\varphi}_L\Gamma\varphi_R\psi - \bar{\varphi}_R\Gamma^\dagger\varphi_L\psi^\dagger, \tag{2.10}$$

to fulfil the gauge principle and the requirement of renormalizability, where ψ includes all Higgs scalar fields as column vector. The quantities Γ include all coupling constants, called Yukawa couplings. The potential $V(\psi^\dagger\varphi)$ is symmetric under $SU(2) \times U(1)$ and contains at most quartic terms in ψ, as the theory needs to be renormalizable. The spontaneous symmetry breaking of the electroweak theory is introduced, if the minimum of the potential is obtained for non-vanishing ψ values ($\langle 0|\psi(x)|0\rangle = v \neq 0$). This results in a mass of zero mass for the photon, and $m_W = \cos\theta_W m_Z = 1/2g^2v^2$ for the Z and $W^\pm$ bosons. In case of the quarks the last two terms in eq. (2.10) change to[4]:

$$\mathcal{L}_{Yukawa} = U^i_R\,\bar{\psi}\,Y^{ij}_u\,Q^j_L + D^i_R\,\bar{\psi}\,Y^{ij}_d\,Q^j_L + h.c., \tag{2.11}$$

where $Y^{ij}_{u,d}$ are the Yukawa couplings of the up- and down-type quarks to the Higgs fields ψ. The mass of the quarks are proportional to the Yukawa coupling and v. The SM Lagrange density is degenerated across the families of quarks and leptons. However, this is not possible anymore in the case of mass terms, due to the different masses. Therefore, the Yukawa couplings are no scalars, but rather 3×3 matrices. Four independent matrices would be needed to diagonalise the Yukawa coupling matrices. But, only three of them can be chosen freely. Hence, the Yukawa matrices are not simultaneously diagonalisable. The consequence is that the mass and flavour eigenstate of one type (up or down) of quarks are not identical. By convention, the down-type quarks are chosen and a unitary 3×3 matrix is introduced to connect the flavour eigenstates D'

---

[4] The procedure is similar for leptons.

with the mass eigenstate D, the matrix is called Cabibbo-Kobayashi-Maskawa matrix V_{CKM} [20].

$$\begin{pmatrix} |d'\rangle \\ |s'\rangle \\ |b'\rangle \end{pmatrix} = V_{CKM} \begin{pmatrix} |d\rangle \\ |s\rangle \\ |b\rangle \end{pmatrix} . \tag{2.12}$$

Where the V_{CKM} matrix is defined as:

$$V_{CKM} = \begin{pmatrix} V_{ud} & V_{us} & V_{ub} \\ V_{cd} & V_{cs} & V_{cb} \\ V_{td} & V_{ts} & V_{tb} \end{pmatrix} . \tag{2.13}$$

The unitarity of the matrix and the fact that one global phase is not observable, leaves four free parameters. Three of them are quark mixing angles and one is a complex phase, which is responsible for the $\mathcal{CP}$ violation in the SM. This results in a different behaviour of particles and anti-particles in weak interactions. In experiments a strong hierarchical order of the off diagonal matrix elements is observed: $|V_{us}|$ and $|V_{cd}|$ are about 0.22, $|V_{cb}|$ and $|V_{ts}|$ of the order $4 \cdot 10^{-2}$ and $|V_{ub}|$ and $|V_{td}|$ of $3 \cdot 10^{-3}$ or $8 \cdot 10^{-3}$ respectively. Therefore, transitions between different quark families are heavily suppressed, this is called *Cabbibo suppression*. The suppression is the strongest for the transition between the first and third family. All experimental values can be found in [16].

2.2.2 Quantum Chromodynamics Interactions

The Lagrange density of the strong interactions, $\mathcal{L}_{QCD}$, has to obey the gauge symmetry associated with $SU(3)$. The QCD Lagrange density has the form:

$$\mathcal{L}_{QCD} = -\frac{1}{4} \sum_{A=1}^{8} F^{A\mu\nu} F^{A}_{\mu\nu} + \sum_{j=1}^{n_f} \bar{q}_j (i \not{D} - m_j) q_j , \tag{2.14}$$

where q_j are the quark fields of n_f different flavours with mass m_j and $\not{D} = D_\mu \gamma^\mu$, where γ^μ are the Dirac matrices and D_μ the covariant derivative:

$$D_\mu = \partial_\mu - i g_s \sum_A t^A g^A_\mu . \tag{2.15}$$

Here, g_s is the gauge coupling of QCD. The g^A_μ are the gluon fields with $A = 1 - 8$ and t^A are the $SU(3)$ group generators in the triplet representation of quarks. The gauge antisymmetric tensors are defined as:

$$F^A_{\mu\nu} = \partial_\mu g^A_\nu - \partial_\nu g^A_\mu - g_s\, C_{ABC}\, g^B_\mu\, g_\nu C \tag{2.16}$$

where C_{ABC} are the complete antisymmetric structure constants of $SU(3)$.

The most prominent properties of QCD are asymptotic freedom and confinement. The effective coupling of an interaction vertex in field theory is modified by the interaction. The intensity of the transmitted force depends on the transferred momentum squared, Q^2. In case of QCD the relevant coupling parameter for physical processes is $\alpha_s = \frac{g_s^2}{4\pi}$. The coupling $\alpha_s(Q^2)$ decreases for increasing Q^2 and vanishes asymptotically. In other words, the coupling increases with increasing distance, R, as $Q^2 \simeq \frac{1}{R^2}$. This behaviour is called asymptotic freedom. It is in contrast to the behaviour of the electrical force in QED, where the coupling gets smaller with increasing radius, an effect also called screening. In QED, the screening can occur near a charged particle by virtual charged pair production, which causes the vacuum to become polarised in the region surrounding the particle. The polarisation makes the vacuum a dielectric medium in which the apparent charge is less than the true charge. This leads to a decreasing coupling parameter in QED with larger radius. In QCD, the anti-screening is a result of the self coupling of the gluon (due to the quadratic term of the gauge field in $F^A_{\mu\nu}$). Similar as in QED, virtual quark-antiquark pair production induces a colour charge polarisation in the vacuum. But the virtual gluons, which carry a colour and anti-colour charge augment the colour charge. Due to the large number of different gluon types the screening from the virtual quark-antiquark gets suppressed. The anti-screening has two important consequences. First, despite the large coupling constant at low energies, the asymptotic freedom allows calculations of cross-sections involving strong interactions by the perturbation theory as long as the processes occur at high energies. Second, if two quarks are separated, the coupling α_s will increase until the field energy is sufficient to create a new $q\bar{q}$ pair. This effect is called quark confinement, and states that no finite amount of energy can liberate a quark.

2.2.3 PERTURBATIVE QCD

In perturbative QCD, scattering amplitudes are written as a perturbation series expansion in powers of the coupling constant α_s. Terms with the lowest power of α_s are called leading order (LO) terms, the next higher order next-to-leading order (NLO) and so on. These terms can be represented by graphs, so called Feynman diagrams, which consist of external lines, representing initial and final states, vertices representing the interactions, and internal lines and loops representing intermediate particles. Figure 2.1 shows an example of a LO Feynman diagram for an electron and positron annihilation, which produces a quark anti-quark pair with a photon as intermediate particle. The perturbation series expansion for the cross-section calculation does converge only for coupling constants, which are less than one.

The coupling constant in QCD α_s can be written at leading order as:

$$\alpha_s(Q^2) = \frac{4\pi}{b_0 \ln(Q^2/\Lambda^2_{QCD})} \tag{2.17}$$

where Λ^2_{QCD} is a constant called QCD scale ($\approx$ 200 MeV), Q^2 the transferred momentum squared and b_0 is a constant called the 1-loop beta-function coefficient. Here, b_0 equals $(33-2n_f)/(12\pi)$[16] and is dependent on the number of quark flavours (n_f). The perturbative approach is limited in QCD to high and medium Q^2, as for low momentum transfer the expansion does not converge anymore. The perturbative QCD (pQCD) is therefore replaced at the Λ_{QCD} limit by phenomenological models.

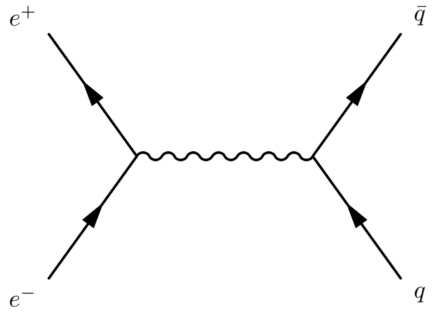

Figure 2.1: The figure shows the leading order Feynman diagram for electron and positron annihilation, which produces a quark anti-quark pair with a photon as intermediate particle.

2.3 QCD in Proton-Proton Collisions

The description of proton-proton scattering is further complicated by the internal structure of the protons. The hadronic final state of proton-proton interactions can be described as the superposition of several contributions: products of the partonic hard scattering with the highest transverse momentum p_T, including initial and final state radiation; hadrons produced in additional parton interactions, multi-parton interaction (MPI); and beam-beam remnants (BBR) resulting from the hadronisation of the partonic constituents that did not participate in the other scatters [21]. Those contributions are classified as either hard or soft depending on the Q^2 at which the process occurs. The resulting products of MPI and BBR form together the underlying event (UE).

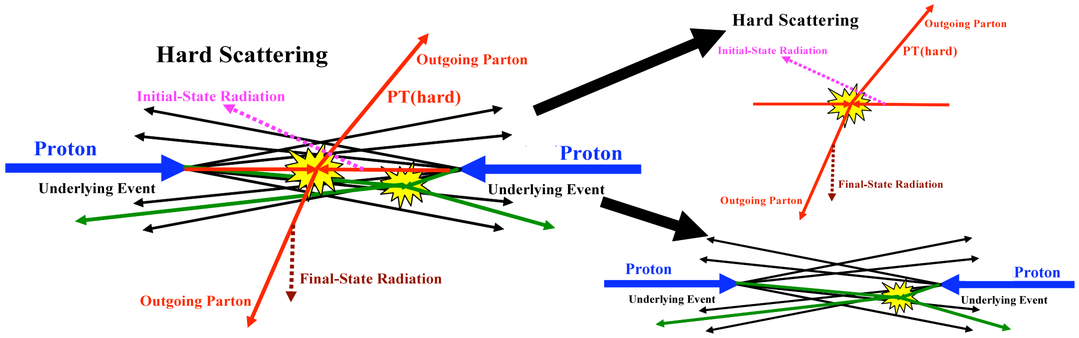

Figure 2.2: The components of a proton-proton collision: the products of the partonic hard scattering process with the highest transverse momentum p_{T} is indicated in red, hadrons produced by additional interactions in green and beam-beam remnants in black. Figure adapted from [22].

2.3.1 HARD SCATTERING

Hadrons contain two types of quarks, valence quarks (q_v) and sea-quarks (q_s). The valence quarks define the quantum numbers of the hadron and determine its behaviour, *e.g.* if it is a proton (uud) or a neutron (udd). The sea-quarks are virtual quark-antiquark pairs originating from the gluon splitting within the hadron. The annihilation of sea-quarks forms again a gluon, which results in a constant flux of gluons and sea quarks inside hadrons. The distribution of gluon and quarks inside a hadron is described by the parton density functions (PDFs), $f_{a|p}(x, Q^2)$. These PDFs parametrise the probability to find a parton a, with the momentum fraction x at the momentum scale Q^2 inside the hadron with momentum p.

The hard scattering process between two protons can be described using the factorisation theorem formulated by Drell and Yan [23]. They postulated that the cross-section for a hard process σ_{AB} can be formulated as a convolution of the partonic cross-section σ_{ab} with the PDFs of the proton $f_{a|A}(x, \mu_F)$. Here μ_F is an arbitrary scale, called the factorisation scale. Its value is usually set to the same value as the renormalisation scale μ_R, which is set to the scale of the process, *e.g.* in the case of Z production to the mass of the Z. The factorisation scale divides the divergent and convergent parts of the calculation, σ_{ab} and $f_{a|A}(x, \mu_F)$, respectively. The PDFs can be scaled from one scale Q to another using the Dokshitzer-Gribov-Lipatov-Altarelli-Parisi (DGLAP) equations [24–27], resulting in a Q^2-evolution of the PDFs. The factorisation and renormalisation scales are not physical. If all terms are included in the perturbative expansion, the cross-section would be independent of the choice of the scale.

As the PDFs parametrise the non-perturbative part of the hadronic interaction, it is not possible

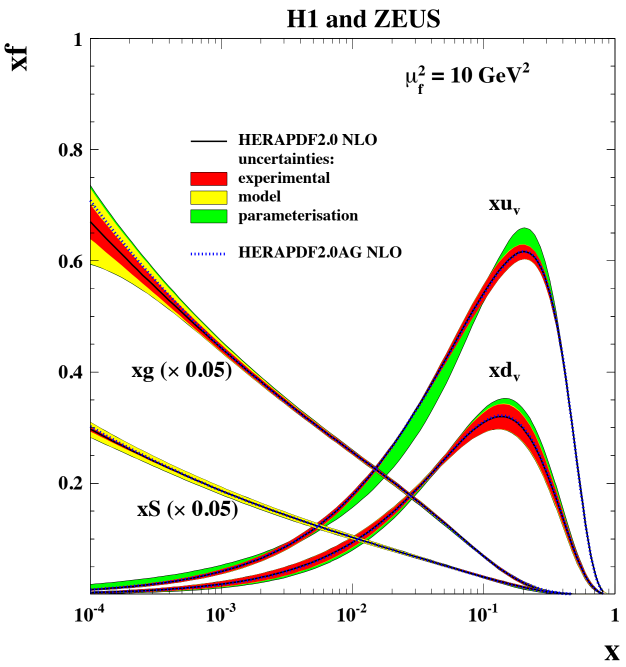

Figure 2.3: The parton distribution functions for the two valence quarks are shown, the sea quarks $xS = 2x(\bar{U} + \bar{D})$ and gluons at $\mu_F^2 = 10\,\mathrm{GeV}^2$ with the HERAPDF2.0 parton distribution model at next-to-leading order (NLO). The experimental, model and parameterisation uncertainties are shown. The dotted lines represent HERAPDF2.0AG NLO with an alternative gluon parametrisation. Detailed information of the different HERAPDF models are given in [28].

to calculate them. Instead, they have to be extracted from data through global fits to various data sets, such as structure function measurements from deep inelastic (DIS) at HERA, jet production at TEVATRON, measurements with electroweak bosons at LHC or fixed target data. There are different global analyses available (*e.g.* CTEQ [29], MSTW [30] and NNPDF [31]), which differ on the parametrisation of the PDFs and the choice of input data. This results in small difference between the results of the global analyses. Figure 2.3 shows an example of PDFs of the proton for the valence and the sea quarks as extracted by HERAPDF[28]. The gluon and sea quark contribution is scaled down by a factor of 20. The valence quarks are dominant at high-x values, whereas the gluon and the sea quark distributions are strongly rising for low-x.

2.3.2 Soft Processes in Hard Collisions

One of the dominant sources of the underlying event are multi-parton interactions (MPI). In a collision of two hadrons more than one pair of partons can interact, because hadrons are composite particles. In addition, the measurements of the PDFs of the proton show that the parton density inside the proton rises for low-x. Therefore, the probability for secondary collisions increases leading to additional soft-QCD interactions. Other sources of UE include multiple scattering of primary particles, interactions of the remnants with other protons and interactions between particles from the beam remnants.

As discussed in section 2.2.3, the perturbative approach is limited to high momentum transfer, high-Q^2. In the low-Q^2 regime, phenomenological models are used to describe the processes. These models can be split in two categories according to their occurrence in the event; parton showering and hadronisation. Figure 2.4 shows a schematic overview of an example of a hard scattering process in a proton-proton collision for decreasing Q^2. The perturbative and non-perturbative parts of the production are indicated by dashed lines.

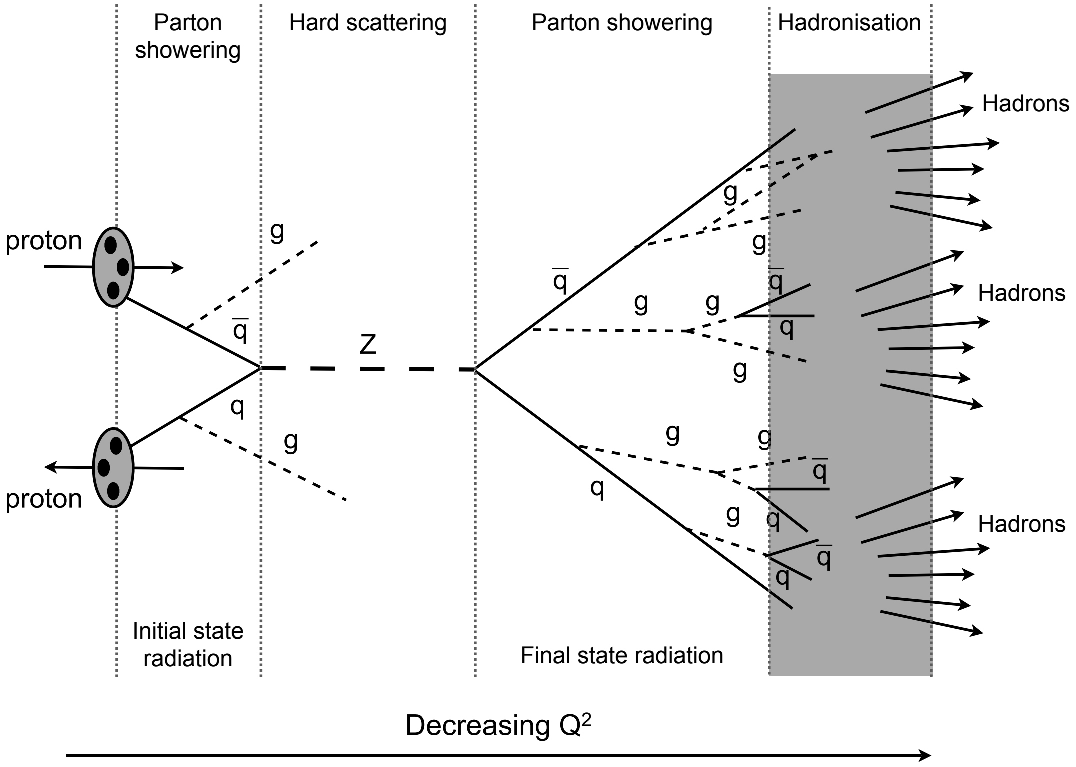

Figure 2.4: This schematic shows a hard scattering process in a proton-proton collision, the leading order production of a Z boson, which decays to a quark anti-quark pair. Areas, where soft interactions are dominant, are highlighted in grey. The figure is adapted from [32].

Initial and final state parton showers are used for dealing with higher order terms, which are not included in a given perturbative calculation. As partons carry electromagnetic and/or colour charge, the higher order contributions will take the form of emissions of gluons or photons. This is usually achieved by adding additional radiative processes, where a parton is allowed to branch into a parton with lower energy plus for example an emitted gluon. This process is repeated until the branching particles reach a predefined energy above the confinement.

In the hadronisation process all coloured objects are converted into colourless final state hadrons. Usually either the string fragmentation model or the cluster model is used for this. The string model is based on the starting assumption that the energy of the colour dipole field between a $q\bar{q}$ pair, increases linearly with the separation between both charges. If the energy is large enough a second $q'\bar{q}'$ or even a third $q''\bar{q}''$ pair can be produced. Those new quarks and anti-quarks are then combined with the original $q\bar{q}$ pair to colour-less meson or baryon states. The splitting stops as soon as only on-mass-shell hadrons remain.

The cluster model starts by splitting all of the coloured gluons from the parton shower into quark anti-quark pairs or diquark anti-diquark pairs. Then, the resulting quarks are combined with their nearest neighbours to form colourless clusters. The type of the hadrons is determined by the constituents of the cluster.

These models are implemented in various event generators like PYTHIA [33], HERWIG++ [34, 35] and SHERPA [36]. PYTHIA uses the string model for the hadronisation, while HERWIG++ and SHERPA use the cluster model.

In addition to different models for the soft physics, the event generators use different tuning of the models to described previous measurements. Historically, hadronisation models were tuned on LEP results and MPI parameters were tuned on TEVATRON and LHC results. Today, those tunings are performed simultaneously on LHC data, as the LHC probes QCD in regions were the LEP and TEVATRON data offer little constraints [37]. Reference [38] gives further information on the tuning of Monte Carlo event generators for the LHC.

The proper tuning of the event generator models for the LHC is important, as the SM processes need to be measured and understood in the LHC regime before any new physics discovery can be made. Furthermore, a key point in today's physics discoveries is the simulation of both; background and signal events, especially with the rise of multivariate methods, where the discrimination between signal and background is tuned to predictions from Monte Carlo event generators.

In chapter 6 recent measurements of LHCb on the forward energy flow and strange meson productions are discussed. The strange meson production is a powerful probe of hadronisation models at pp colliders, as protons have no net strangeness and the production via double parton scattering of two strange sea quarks is rather unlikely[39]. The observed discrepancies between models and measurements of strange meson production and the forward energy flow motivates a measurement of the strange meson production in a hard scattering event of a Z boson.

2.4 Z Boson Production

At leading order (LO), the Z boson is produced in a hadron collision through the Drell-Yan [23] annihilation of an incoming quark-antiquark pair, see fig. 2.5. In addition to the on-shell Z boson production, there are contributions from off-shell photons γ^* and $\gamma^* Z$ interference. In the following, these processes are not distinguished. Higher order processes of Z boson production involve gluons or initial state partons, which are reconstructed as hadronic jets in the detector. Two examples of next-to-leading order (NLO) Feynman diagrams for the Z boson production are shown in fig. 2.6.

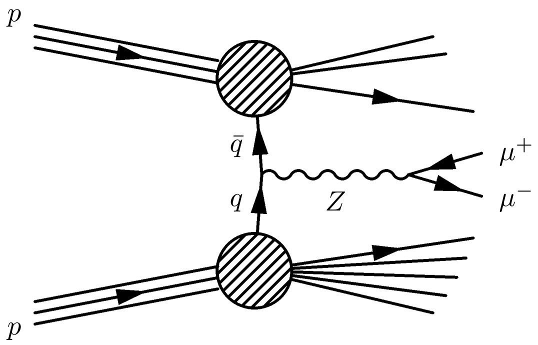

Figure 2.5: The figure shows the leading order Feynman diagram for Z production through the Drell-Yan process in a proton proton collision.

Figure 2.7 shows the contribution of different flavours of quark-antiquark annihilation to the Z boson production at the LHC as function of the rapidity. All flavours contribute to the production of the Z boson in the central region, while at large absolute rapidity values up-antiup quark annihilation is dominating.

Figure 2.8 shows the cross-sections for relevant processes in pp ($p\bar{p}$) colliders as function of the centre-of-mass energy ($\sqrt{s}$). The production cross-section of a Z boson is linearly rising with $\sqrt{s}$, while the total cross-section is almost flat in $\sqrt{s}$.

The momentum transfer of the process, Q^2, the centre-of-mass energy, $\sqrt{s}$ and the fractional

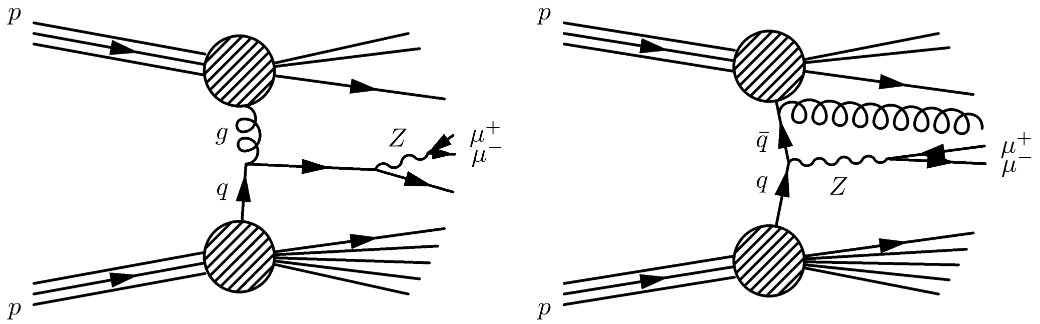

Figure 2.6: The figures show the NLO Feynman diagrams for Z production through the Drell-Yan process in a proton proton collision, (left) the quark gluon scattering with a resulting quark jet in the final state, (right) the Drell-Yan process with a gluon radiation producing a gluon jet.

momenta, x_1 and x_2 of the two partons in the hard scatter are connected by the relation:

$$Q^2 = x_1 x_2 s. \tag{2.18}$$

In addition, the rapidity y of the rest frame of the hard scatter in the laboratory frame is connected to the fractional momenta x_1 and x_2 by

$$x_{1,2} = \frac{Q}{\sqrt{s}} e^{\pm y} \tag{2.19}$$

with the boundary conditions $x_{1,2} \leq 1$. Therefore, large absolute values of the rapidity are equivalent to high x_1 and low x_2 or vice versa. Figure 2.9 shows the $x - Q^2$ space that can be probed by various experiments. The acceptance of fixed target and HERA experiments are represented in green. The HERA results cover a large range in x down to 10^{-6} at Q^2 values below those probed by ATLAS and CMS. LHCb probes two distinct regions indicated in orange: one at high x interleaving with the regions of the fixed target, HERA and TEVATRON experiments, and the second one is unique to LHCb probing at low x at Q^2 values above those probed by the HERA experiments. It should be noted that the HERA measurements at low x are preformed at very low Q^2 where the perturbative approach is not expected to hold. Both regions are complementary to ATLAS and CMS. For the Z production, $Q^2 = M_Z^2$, x values down to about 1×10^{-4} can be probed in LHCb.

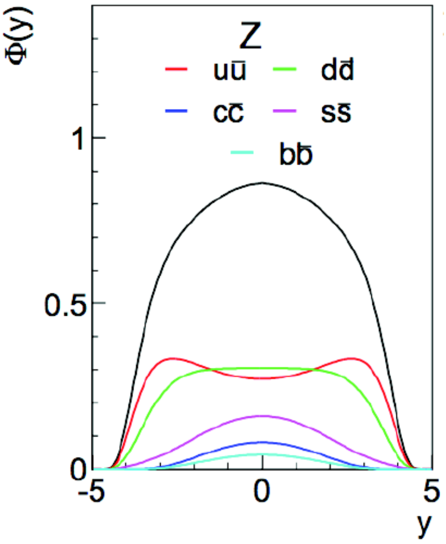

Figure 2.7: The figure shows the contribution of different quark flavours to the Z boson production at LHC for a centre-of-mass energy of 14 TeV as a function of the rapidity. Figure adapted from [40].

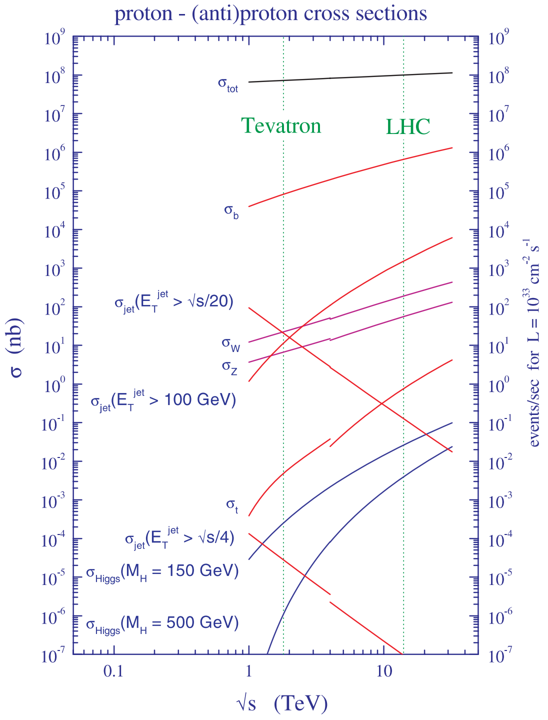

Figure 2.8: Standard model cross sections at the Tevatron and LHC colliders, taken from [41].

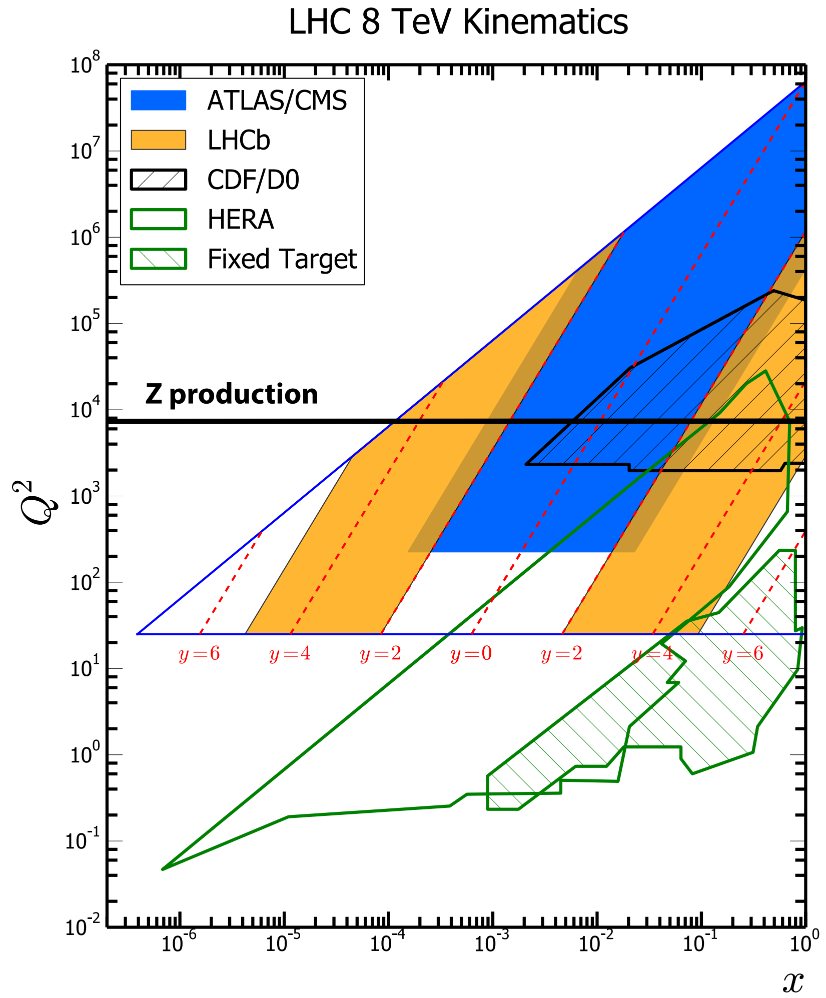

Figure 2.9: The region of the (x, Q^2) space probed by previous experiments as well as ATLAS, CMS and LHCb at a centre-of-mass energy of 8 TeV. Figure adapted from [42].

2.5 *b* QUARK PRODUCTION AT HADRON COLLIDERS

The main analysis topics of the LHCb experiment are based on composite particles of b quarks. The characteristics of their production and their behaviour was the main motivation for the design of the detector. Three production mechanisms for b quarks are relevant in proton-proton collisions, their Feynman diagrams are shown in fig. 2.10 and 2.11. They can be divided according to their order of the strong interaction coupling strength.

At leading-order (LO), there are processes of quark anti-quark annihilation $q\overline{q} \to b\overline{b}$ and gluon gluon fusion $gg \to b\overline{b}$. These processes are at second order of the strong interaction coupling strength $\mathcal{O}(\alpha_s^2)$ and are commonly called *pair production*. At next-to-leading order (NLO), processes with $\mathcal{O}\,(\alpha_s^3)$ take place. These are new contributions include *gluon-splitting* and *flavour-excitation*, and corrections to the pair production. A NLO process including a $g \to b\overline{b}$ transition is called gluon splitting. A processes, where a sea-quark from one of the beam particles is scattered on a parton from the other beam, is called flavour-excitation.

Figure 2.8 shows the cross-sections for relevant processes in pp ($p\bar{p}$) colliders as function of the centre-of-mass energy ($\sqrt{s}$). The $b\bar{b}$ cross-section has approximately a linear dependence on $\sqrt{s}$ in the region of the LHC with a similar slope as Z or W production, the $t\bar{t}$ cross-section has a linear dependence with a larger slope than $b\bar{b}$, while the total cross-section is almost flat in $\sqrt{s}$. The relative contributions to the total production cross-section of $b\bar{b}$ and $c\bar{c}$ are shown in fig. 2.12 as function of $\sqrt{s}$. For higher centre-of-mass energy the relative contribution of higher order processes is increasing. In case of the LHC, the dominant production mechanism is flavour excitation.

In pp collision, $b\bar{b}$ quark pairs are often produced with a large boost in the direction of one of the incoming protons. In addition, both of them end up either in forward or backward direction, due to a strong correlation between b and $\bar{b}$ quark. Figure 2.13 shows the θ and η dependencies of the b quark production at LHC, where η is defined as $\eta = -\ln[\tan(\theta/2)]$. This dependence played an important role for the design of the LHCb experiment, see section 3.2.

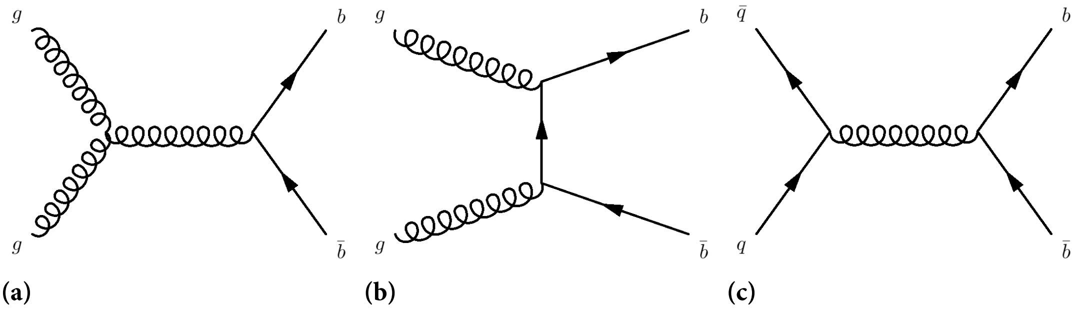

Figure 2.10: Feynman diagrams for leading order $b\bar{b}$ production in proton-proton collisions. Figure (a) and (b) show gluon-gluon fusion processes and figure (c) shows the quark-antiquark annihilation process.

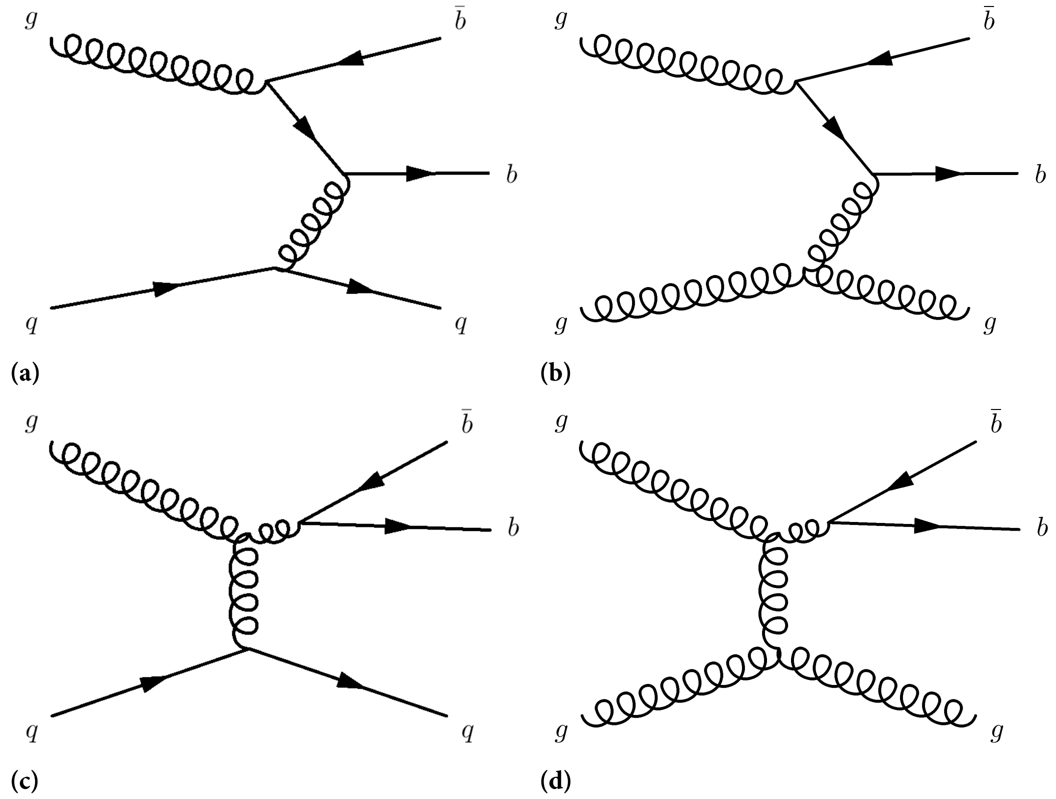

Figure 2.11: Feynman diagrams for next-to-leading order $b\bar{b}$ production in proton-proton collisions. Figures (a) and (b) show flavour-excitation processes, and figures (c) and (d) show gluon-splitting processes.

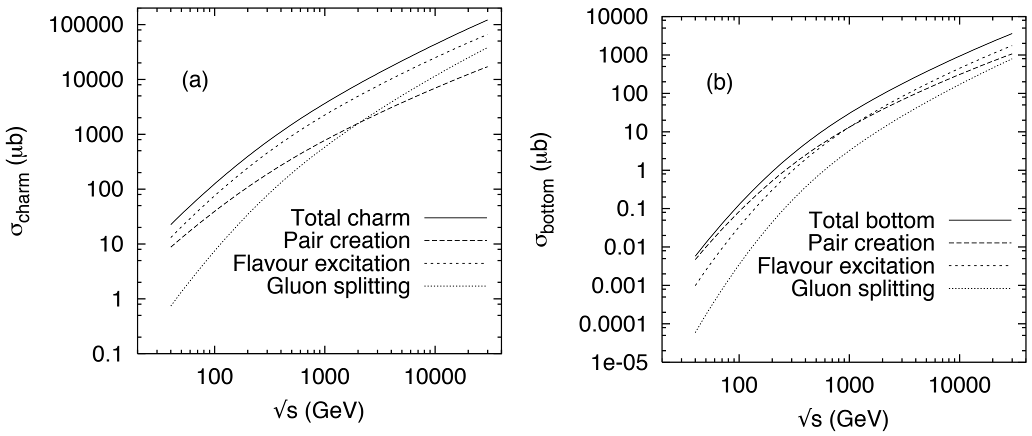

Figure 2.12: The total charm (left) and bottom (right) cross sections for pp collisions as function of $\sqrt{s}$. Figure taken from [43]

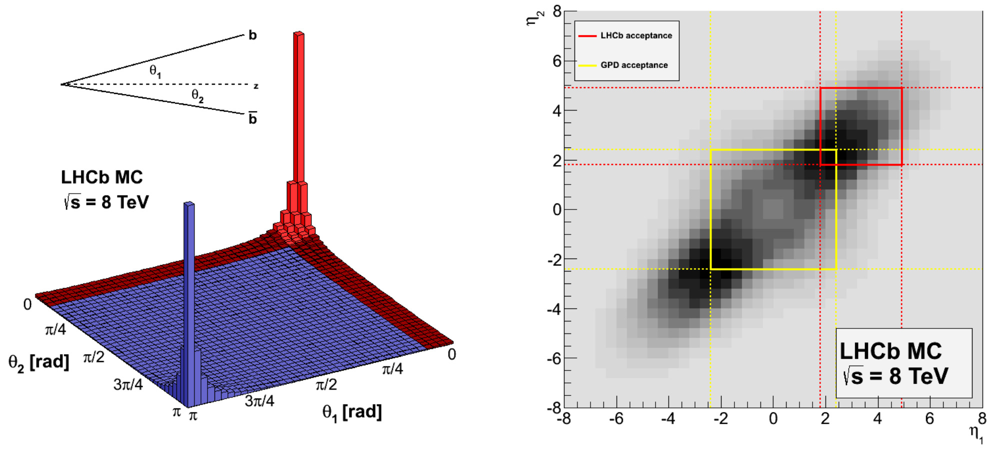

Figure 2.13: (left) The distribution of the azimuthal angles θ and (right) the pseudo-rapidity, η, for the b and $\overline{b}$ quarks produced in pp collisions at centre-of-mass energy of 8 TeV. The red region and the red lines show the acceptance of LHCb, the yellow lines show the acceptance of ATLAS and CMS [44].

People are saying I don't need science, I have everything,
but everything is based on science.

Rolf-Dieter Heuer

3

Large Machines for Tiny Particles

Mankind has always been curious about his environment and this curiosity led to deeper understanding of the nature. In 400-370 B.C. Democritus and Leucippus, two ancient greek philosophers, postulated that everything was made of *atoms*. They described them as indestructibles, with empty space between them and their mass concentrated in the centre and always being in motion. Furthermore, they proposed that many kinds of these atoms would exist only different in shape and size [45]. These theories were considered highly philosophical, it was only in the 13th century on that the idea of experimental evidence as a proof of a theory was accepted.

In 1898, Joseph John Thomson experimentally proofed the existence of the electron [46] which was postulated by George Johnstone Stoney in 1874. The discovery was made during studies of the properties of cathode rays. This event can be seen as the beginning of elementary particle physics. Later, in 1911, Ernest Rutherford together with John Cockcroft and Ernest Walton made the discovery that an atom consists of a *central attracting mass surrounded by rings of rotating electrons*[47]. They used an α-particle emitter as source for scattering the emitted particles on gold atoms. Since then, experiments using particles to scatter or collide on other particles got bigger and bigger. Today, the largest accelerator is the Large Hadron Collider (LHC) at CERN. Four large experiments are located at the accelerator, where two of them, CMS and ATLAS, are general purpose detectors hunting for the Higgs and new particles and the other two, ALICE and LHCb are specialised detectors. The main purpose of the ALICE experiment is to study phenomenons like the quark gluon plasma, whereas the LHCb experiment is mainly focusing on b-physics, specially on $\mathcal{CP}$-violation and rare decays.

This chapter gives a short description of the LHC and its location CERN. Further, it will give an overview over the LHCb detector at LHC with summaries of each sub-detector.

3.1 Large Hadron Collider

The large hadron collider, short LHC, is surely an impressive machine. The immense size, the cryogenic systems and the complex combination of different pre-accelerators and detectors fascinate scientists over the whole world.

The collider is located at CERN[1] at the franco-swiss border in Geneva. CERN was founded in 1952 with the intention to establish a fundamental physics research organisation in Europe with world-class ambitions. Initially, the research program was concentrated on understanding the inside of an atom, but today our knowledge goes beyond, thus the main focus has changed to study the constituents of matter and the forces acting between them.

The idea of a hadron collider in the tunnel of the Large Electron-Positron Collider (LEP) at CERN has first been mentioned in 1977 by the former CERN director general Sir John Adams. He suggested that the potential LEP tunnel should be wide enough for a superconducting proton collider of above 3 TeV beam energy [48, 49]. In 1981, after the approval of the LEP by the CERN Council and during ongoing discussions on the geological situation in the area, CERN director general Herwig Schopper argued that the suggested circumference of 22 km is too small for a future successful pp collider in the LEP tunnel [50].

Electron-positron colliders or lepton colliders in general have a well defined centre of mass energy $\sqrt{s}$ at the collision point, which is exactly equal to the sum of the energy of both colliding beams. The initial production state is tuneable and therefore, allows accurate measurements of thresholds of various particle productions, followed by precision measurements of different particles due to the known production threshold.

Hadron colliders are more complex. Due to the composite structure of hadrons, which contain gluons, sea- and valence-quarks, strong and electroweak interactions take place and collisions do not have well defined centre-of-mass energy. Furthermore, proton remnants produce additional particles, which are not from hard collisions. Hence collision events are less clean than in lepton

---

[1] Initially CERN was the abbreviation for Conseil Européen pour la Recherche Nucléaire or European Council for Nuclear Research. Today only the abbreviation is left.

colliders. However, equally sized hadron colliders can reach higher energies than lepton colliders, because they have much smaller energy loss due to synchrotron radiation, which is emitted when a charged particle is accelerated radially.

In general, any accelerated charged particle emits electromagnetic radiation. In case of a collider, bending magnets keep the particles on the trajectory by applying a magnetic field perpendicular to their velocity. The acceleration of a charged particle is given by the Lorentz equation:

$$\frac{d\mathbf{p}}{dt} = e\left(\mathbf{E} + \frac{\mathbf{v} \times \mathbf{B}}{c}\right), \tag{3.1}$$

where **p**, e and **v** are the particle momentum, charge and velocity and **E** and **B** are the electric and magnetic fields. For a circular acceleration, the power radiated by a relativistic particle is given by

$$P = \frac{2}{3}\frac{e^2 c}{R^2}\left[\frac{E}{mc^2}\right]^4 . \tag{3.2}$$

A detailed derivation of the radiated power is given in [51, 52]. The energy loss per turn is given by multiplication with the revolution time $2\pi R/c$,

$$\Delta E = \frac{4\pi}{3}\frac{e^2}{R}\left[\frac{E}{mc^2}\right]^4 . \tag{3.3}$$

This equation shows, that a large bending radius and a high particle mass are needed to reach high particle energies with moderate energy loss per turn.

In 1990, Carlo Rubbia summarised the relation between hadron and lepton machines as following: *In the past high energy machines like hadron colliders were used for exploration and high precision e^+ e^- instruments were used for consolidating* [54]. Figure 3.1 shows the different accelerators and their equivalent beam energy as dependence of time. The equivalent energy assumes the beam is hitting stationary proton targets. Both, proton and electron accelerators have an exponential dependence of their beam energy as function of time. Since the last forty years storage ring colliders, like the LHC are the dominating technology for accelerators to get to the highest possible beam energies. Today, the planning of the international linear collider (ILC) [55] has started, which is an electron linear collider for precision measurements on LHC level.

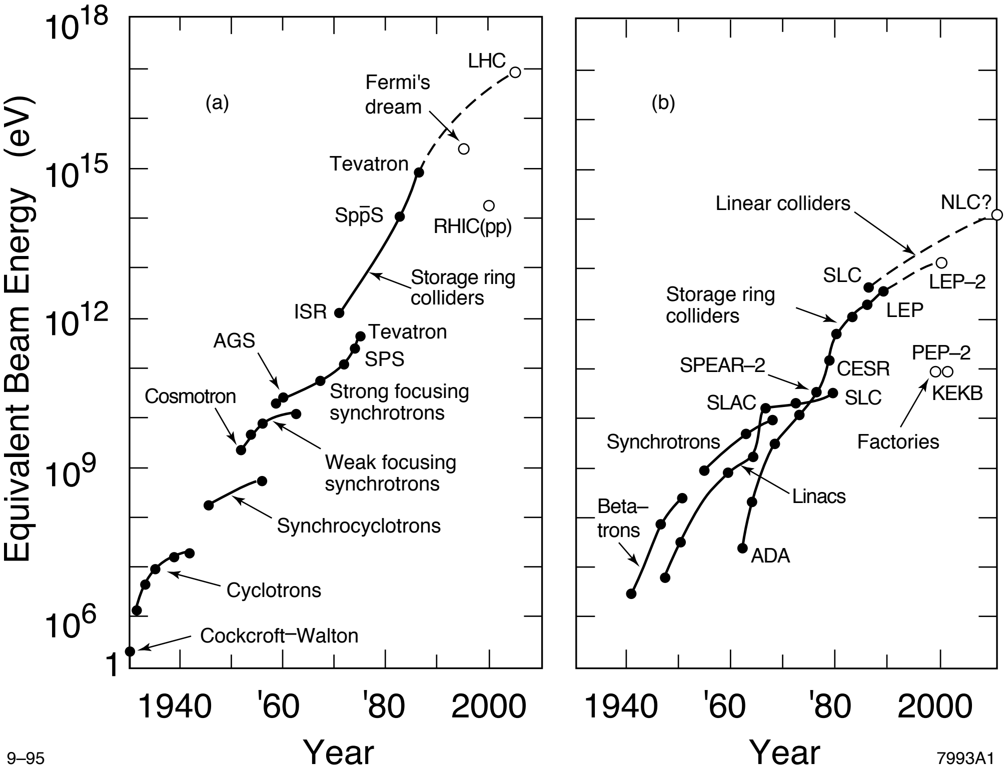

Figure 3.1: The equivalent energy of high energy particles is plotted versus time when the accelerator was built. (a) is for proton accelerators and (b) for electron accelerators. The equivalent energy assumes the beam is hitting stationary proton targets. Each solid dot represents an accelerator which has been built, an open circle is an accelerator not yet existing. Each solid curve connects accelerators built or designed with a common technology. The date of the figure is 1995, taken from [53].

3.1.1 LAYOUT

The 26.7 km long LEP tunnel, built between 1984 and 1989, sets the boundaries for the LHC machine. The tunnel consist of eight straight sections and eight arcs, and the depth below surface varies between 45 to 170 m with an inclination of the collider plane of 1.4% towards the Lac Léman. Each straight section is approximately 528 m and each arc is around 2.45 km long. The configuration of particle-antiparticle with a common vacuum and magnet system for both circulating beams, as at the Tevatron, was no option for a luminosity of $L = 10^{34}\,\mathrm{cm}^{-2}\mathrm{s}^{-1}$, as antiprotons are harder to produce in large numbers than protons (see for example ref. [56]). To install two separated storage rings in the tunnel was technically impossible, due to the limited geometrical size of only 3.74 m in diameter. This led to the adoption of the twin-bore magnet design that was proposed by John Blewett at Brookhaven laboratory in 1971 [57]. It was known as the two in one super-conducting magnet design, and consists out of a common mechanical structure and cryostat but with separate coils and beam channels [58]. Figure 3.2 shows the cross-section of the cryodipole of the LHC.

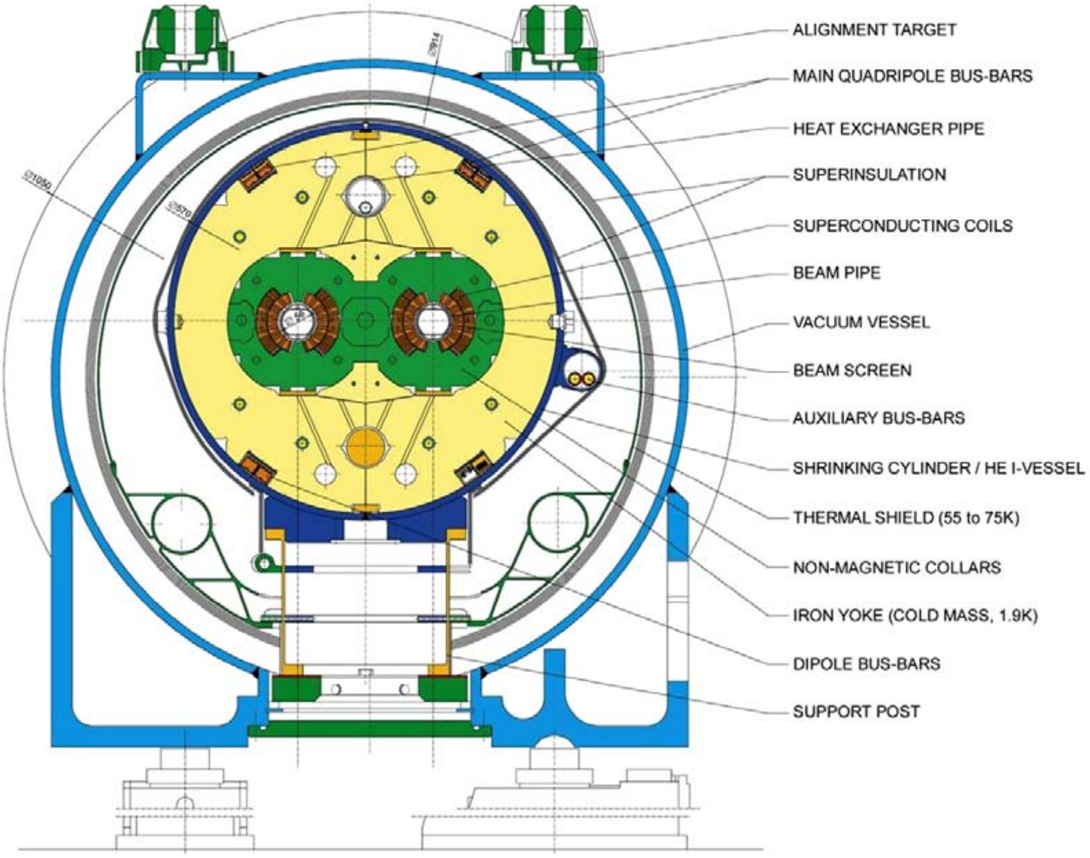

Figure 3.2: Cross-section of cryodipole of the LHC. Figure adapted from ref. [57].

For the maximum design beam energy of 7 TeV a nominal magnetic field strength of 8.3 T is needed, as the maximum beam momentum (or energy) is determined by the field of the dipoles in the LHC arcs, which bend the beams. This magnetic field strength is only achievable with superconducting magnets cooled down with superfluid helium at 1.9K.

Figure 3.3 shows a schematic layout of the LHC. At intersection point (IP) one and five the two high luminosity experiments, CMS and ATLAS are located opposite to each other. Both of them are general-purpose detectors with a broad physics programme ranging from studying the Stan-

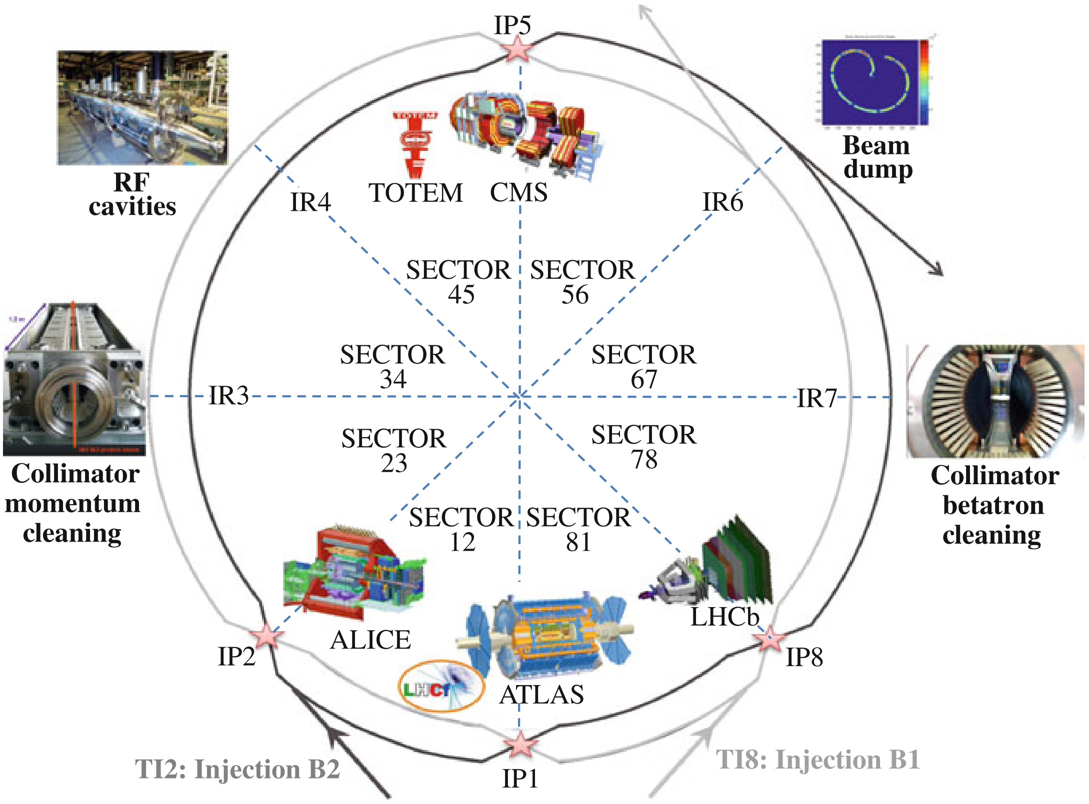

Figure 3.3: Geometry of the LHC with eight arcs and eight straight sections. The two beams cross at the interaction points IP1, IP2, IP5 and IP8.[59]

dard Model (SM) to searching for new physics (such as extra dimensions) [60, 61]. Two additional experiments are located at IP two and eight, ALICE and LHCb. The former is a heavy-ion detector, designed for studying the physics of strongly interacting matter at extreme energy densities[62]. The second is specialised on studying the differences between matter and antimatter by using particles containing beauty or charm quarks. More information on LHCb is given in section 3.2 or [63]. Besides the four large experiments there exist three smaller experiments at the LHC: TOTEM[64], which is dedicated to the measurement of proton-proton interactions cross-section and in-depth studies of the proton structure. TOTEM is located at the IP5 on either side of the CMS detector; LHCf[65], which aims to study the neutral particle production cross-section in the forward region of proton-proton and nucleus-nucleus interaction. It is located at the ATLAS experiment; and MoEDAL[66] searches for magnetic monopoles and is located in front of the LHCb experiment.

The beam-injections for the two beams are also located at IP2 and IP8. In the intersection region (IR) three and seven, two collimation systems are installed, the first for cleaning high momentum offsets and the second for cleaning high betatron amplitudes respectively. At IR4 the radio-frequency (RF) system is located for each beam separately, serving as main acceleration system for the beams. The frequency of each RF system has to be tuned precisely to the revolution frequency of the particles in the beam. The beam dump system for each beam is located at IP5. This system consist of a series of kicker and septum magnets to deflect the particles from the nominal beam direction, and a dilution magnet for sweeping the particle beam in a "e" shape over a graphite target, in a way that the beam does not hit one single spot. The graphite target is located 750 m from the extraction point in a shielded cavern. A more detailed description is given in [67].

3.1.2 System of Accelerators

The proton source for the LHC is a bottle of hydrogen gas at the starting point of the linear accelerator 2 (Linac 2). The hydrogen atoms pass through an electric field to strip off their electrons. At the end of Linac 2, remaining protons have reached the energy of 50 MeV/c^2. Afterwards the protons are accelerated from 50 MeV/c^2 to 1.4 GeV/c^2 in the proton synchrotron booster (Booster). It consist of four superimposed synchrotron rings. The next part in the acceleration chain is the proton synchrotron (PS), the key component of CERN's accelerator complex. The PS, built in 1959, does not only accelerate the protons further up to 25 GeV/c^2, it also creates 25 ns bunches of protons. Before the protons finally enter the LHC, they are injected into the super proton synchrotron (SPS), built in 1976, which accelerates the protons further up to 450 GeV/c^2. Then the protons are transferred to the LHC, where they are further accelerated to the final design energy of 7 TeV. Figure 3.4 shows the complex in a schematic way, including all transverse lines.

In addition to protons, ions are used in the LHC as well. The ion source is enriched lead, which is evaporated in an oven. The lead gas loses some electrons by passing trough a plasma. Afterwards the ions are accelerated in the Linear accelerator 3 (Linac 3). They are then injected into the low energy ion ring (LEIR) which accelerates them from 4.2 MeV/c^2 to 72 MeV/c^2. Afterwards the ions are injected into the PS and then take the same path to the LHC as protons. The maximum energy of ions per beam in the LHC depends on their content of protons (N_p) and neutrons (N_n). It is reduced by a factor, $\frac{N_p}{N_p+N_n}$, with respect to the maximal proton beam energy.

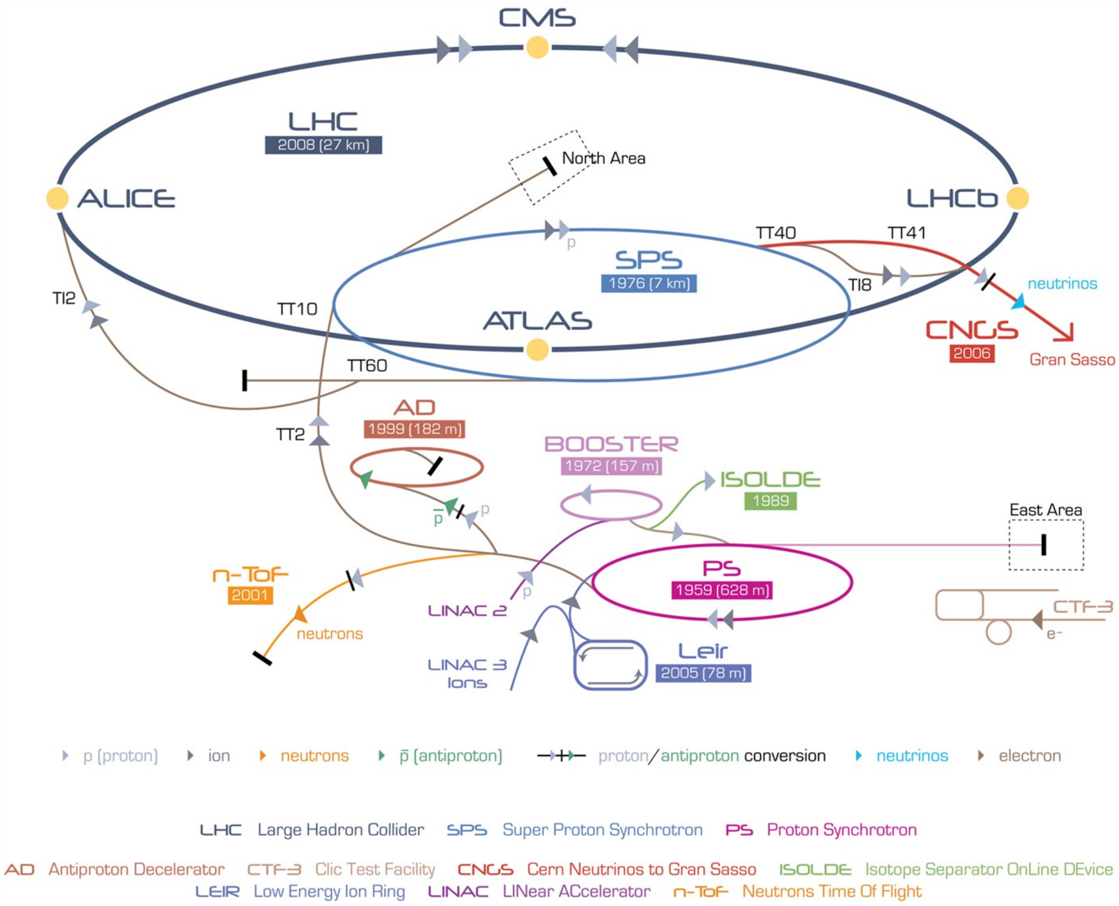

Figure 3.4: Accelerator complex at CERN. Only the large LHC experiments are shown. Figure taken from ref. [68].

3.1.3 PERFORMANCE

Two parameters are interesting for the comparison of accelerators in terms of performance: the beam energy and the luminosity. The second is a measure for the number of collisions in one interaction between two bunches. The number of collision events per second is given by:

$$\frac{dN}{dt} = \sigma \cdot \mathcal{L} \tag{3.4}$$

where σ is the cross-section of the event under investigation and $\mathcal{L}$ the (instantaneous) luminosity. In addition, experiments are quoting the integrated luminosity, $\int \mathcal{L} dt$, as a measure of their acquired data size. It has the unit of an inverse area. The instantaneous luminosity depends only on the beam parameters. For a Gaussian beam distribution it can be written as:

$$\mathcal{L} = \frac{N_b^2 \cdot n_b \cdot f_{rev} \cdot \gamma_r}{4\pi \cdot \varepsilon_n \cdot \beta^*} \cdot F \tag{3.5}$$

where N_b is the number of particles per bunch, n_b the number of bunches per beam, f_{ref} the revolution frequency, γ_r the relativistic gamma factor, ε_n the normalised transverse beam emittance, β^* the beta function at the collision point, and F the geometric luminosity reduction factor due to the crossing angle at the interaction point.

The first beams started in fall 2008, but due to an accident, which damaged several magnets, the LHC was shut down for almost two years for repair work and check of all the electrical connections in the accelerator. In 2010, the LHC was ready for delivering first physics data at half of the design centre of mass energy $\sqrt{s} = 7$ TeV with few bunches and lower luminosity than originally designed. Both were steadily increased in 2010 and 2011, still at $\sqrt{s} = 7$ TeV. The centre of mass energy was kept at this level, as massive superconducting magnets need training to handle high currents without loosing their superconductivity. These high currents are needed for reaching the designed magnetic field energy. A training of a superconducting magnet involves steadily increasing the current until the magnet quenches[2], then the current is increased again. At first this happens at low currents, but over time it is able to reach the designed current, as the components of the magnet settle in. In 2012, the LHC accelerator group enhanced the centre of mass energy to 8 TeV with steadily increasing luminosity. These enhancements lead to a higher Higgs production cross-section, which was a crucial part of the Higgs discovery by the CMS and ATLAS collaborations in the same year[69, 70]. The design values of the LHC for the performance quantities and the operation parameters in 2011 and 2012 are listed in table 3.1. The data acquisition from 2009 until 2013 is called Run I. During the long shutdown one (LS1) from 2013 until beginning of 2015 further consolidations of the superconducting splices in the magnets were performed, weak magnets were exchanged and minor maintenance work were made to prepare the machine for the full design luminosity with collisions at a centre of mass energy of 14 TeV. The data acquisition period, Run II, has started in 2015 and will last until 2018, a detailed plan is kept up to date in [71].

---

[2] A superconducting magnet has to be operated at very low temperature, as superconductivity is a low temperature phenomenon. A tiny amount of energy in the magnet can warm it up, stopping the magnet to be superconducting. This is called a quench. In this moment the current has to be safely extracted in a short time.

Table 3.1: Key LHC design values and their values in 2011 and 2012[72, 73].

Quantaty	**Design**	**2011 (peak)**	**2012 (peak)**
Beam energy [TeV]	7	3.5	4
Bunch population collision (10^{11})	1.15	1.45	1.6
Number of bunches	2808	1380	1380
Bunch spacing [ns]	25	50	50
Stored energy [MJ]	362	112	143
Luminosity at CMS/ATLAS [$\mathrm{cm}^{-2}\mathrm{s}^{-1}$]	1×10^{34}	3.5×10^{33}	7.7×10^{33}
Luminosity at LHCb [$\mathrm{cm}^{-2}\mathrm{s}^{-1}$]	0.2×10^{33}	0.4×10^{33}	0.4×10^{33}

3.2 LHCb Experiment

LHCb is a dedicated experiment for measuring decays of particles containing heavy quarks with the main goal to search for indirect evidence of new physics via CP violation. In addition, rare decays of beauty and charm hadrons are investigated by searching differences between precisely predicted processes of the Standard Model (SM) and the measurements or by studying the distinct flavour structure of the SM with non tree-level flavour-changing-neutral currents.

In either way, large data samples and precisely measured particle properties are needed. Due to the large beauty and charm production cross-section at the LHC [74, 75], LHCb has been able to collect about 10^{12} events with decays of particles containing heavy quarks during 2011 and 2012. The charm and beauty cross-sections are approximately 10 and 200 times smaller than the total cross-section. Hence, the separation of backgrounds from decays of interest is crucial. Displaced vertices and high transverse momentum signatures are exploited for background suppression. Furthermore, particle identification (see chapter 5), excellent impact parameter (see fig. 3.12), decay time, invariant mass and momentum resolution are needed for oscillation studies of hadrons, for the reduction of combinatorial background and the separation of kinematical similar decays. In addition, a high bandwidth data acquisition system and a robust trigger are necessary for managing the high event rate of the LHC.

LHCb has considerably enlarged its physics program over time. For example, measurements of the production of electroweak gauge bosons in the forward region have been performed, which probe a unique kinematic region. Further, measurements of newly discovered exotic particle properties, searches for lepton number and lepton flavour violation, measurements in proton-lead collision and measurements of the Higgs boson in the forward direction are either under investigation or successfully performed. In the following an overview of the LHCb detector is given. This is followed by a more detailed description of the subsystems.

3.2.1 Detector Layout

The LHCb [63, 76, 77] is a single-arm forward spectrometer, covering angles from about 10 to 250 (300) mrad in the vertical (horizontal) direction. The detector geometry originates from the fact that b and $\overline{b}$ are produced in pairs and preferably in the forward or backward direction, see section 2.5. The geometry of LHCb allows to reconstruct a large fraction of b and $\overline{b}$ by only covering a small solid angle. A right handed coordinate system is used with the z-axis in beam direction and the y-axis along the vertical direction. The geometrical coverage of the detector is often given in terms of the pseudo-rapidity, as defined in section 2.5. Figure 2.13 shows the pseudo-rapidity coverage of LHCb in comparison to the general purpose detectors (GPD) ATLAS and CMS.

The dimensions of the LHCb detector are approximately 20 m in length, and 10 m in height and width. It is allocated at IP8 of the LHC, previously used by the DELPHI experiment during the LEP time. The cavern was optimised for a 4π detector. Therefore, the collision point had to be displaced to maximise the available space in the existing cavern for the installation of a forward spectrometer. Figure 3.5 shows the schematic overview of the LHCb detector.

In pp collisions, the forward region is dominated by high particle multiplicities resulting in high occupancies of the detector elements. The separation of primary and secondary vertices, and the ability to reconstruct all tracks of importance are crucial for many analyses in LHCb. For events with high occupancy these tasks are extremely difficult and lead to large uncertainties. Hence, the LHCb detector is optimised for operating with an average design luminosity of $2 \times 10^{32}\ \mathrm{cm}^2\mathrm{s}^{-1}$ at centre-of-mass energy of 14 TeV, which keeps the occupancy at a manageable level. The luminosity is roughly 100 times smaller than for ATLAS and CMS. The low luminosity is achieved by adjusting the transverse overlap of the two colliding beams. To keep the luminosity stable over a run, the separation of the two beams is adjusted accordingly. This procedure is called luminosity levelling. In fig. 3.7 the luminosity levelling is visible for the data acquisition in 2012.

The design for LHCb foresaw to run at an average number of visible proton-proton interactions per bunch crossing of $\mu_{vis} = 0.4$ and a maximum peak luminosity of $5 \times 10^{32}\ \mathrm{cm}^2\mathrm{s}^{-1}$ at centre of mass energy $\sqrt{s} = 14$ TeV to collect an integrated luminosity of $2\ \mathrm{fb}^{-1}$ per year. Figure 3.6 shows the peak luminosity and the average μ_{vis} as function of time. While the highest luminosity in 2010 was already 75% of the design luminosity, indicated as dashed line, the μ_{vis} was much larger than the design value, due to the low number of bunches in the machine. This demonstrated that the

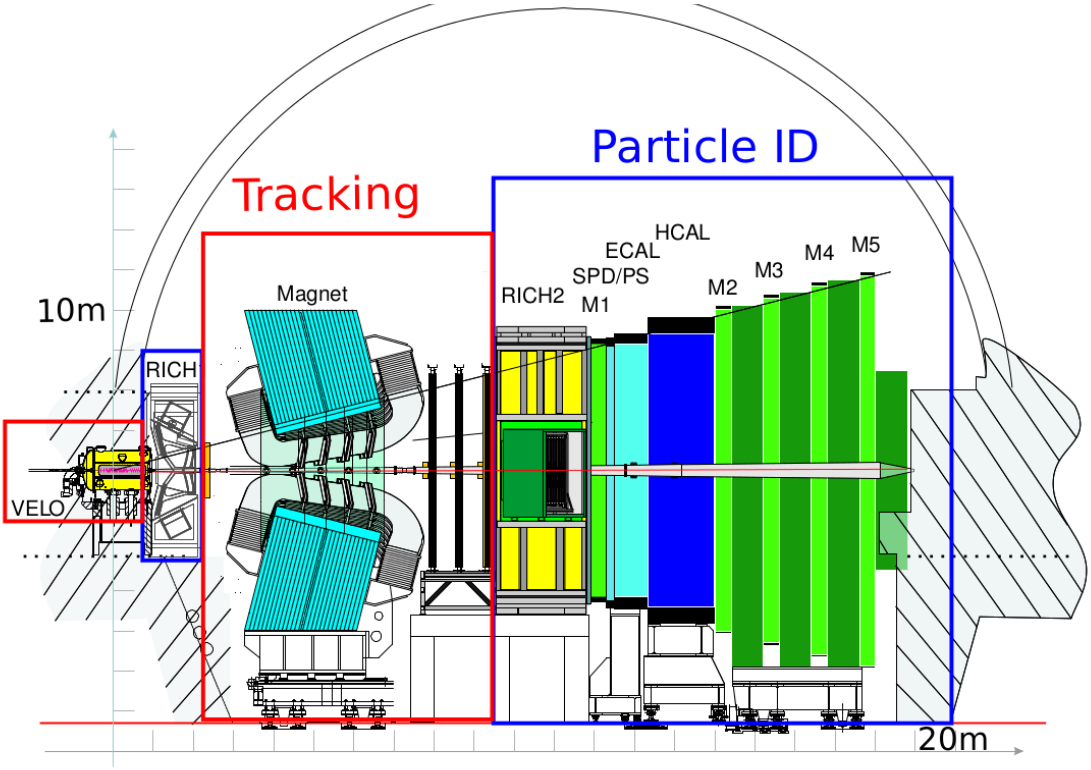

Figure 3.5: Systematic overview of the LHCb detector [44].

data acquisition system, trigger and reconstruction, work efficiently even on harsh conditions. In 2011, LHCb was acquiring data at a luminosity of 3.5×10^{32} cm^{2}s^{-1} with $\mu_{vis} = 1.5$ at $\sqrt{s}$ =7 TeV and in 2012, at 4×10^{32} cm^{2}s^{-1} with $\mu_{vis} = 1.7$ at $\sqrt{s}$ =8 TeV. The later is double the design luminosity for LHCb. Figure 3.7 shows the evolution of the recorded luminosity for the years 2010 to 2012 [78].

The subsystems of the LHCb detector can be split into three categories: The tracking system is designed to measure the three components of the particle momenta and the particle identification system to determine the particle type. The trigger system selects the events, which are of interest for physics analysis. In the following each category is described in detail.

3.2.2 TRACKING SYSTEM

The LHCb tracking system consists of the vertex locator (VELO), the dipole magnet and four planar tracking stations; the Tracker Turicensis (TT) upstream of the dipole magnet and the tracking stations T1-T3 downstream of the magnet. All three T stations are split into inner tracker (IT)

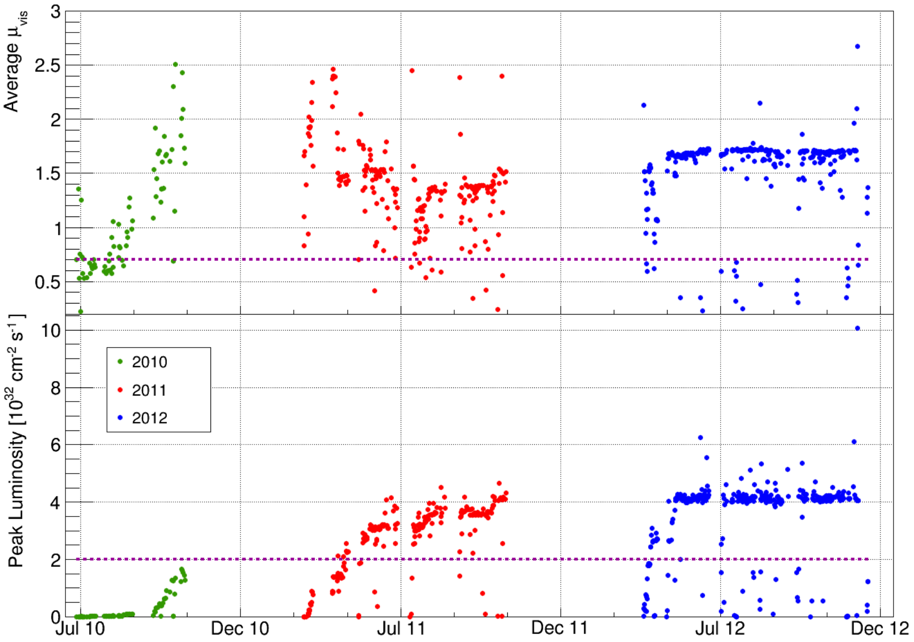

Figure 3.6: Average number of visible interactions per bunch crossing (top) and instantaneous peak luminosity (bottom) at the LHCb interaction point in the period 2010-2012. The dotted lines show the design values. Taken from reference [78].

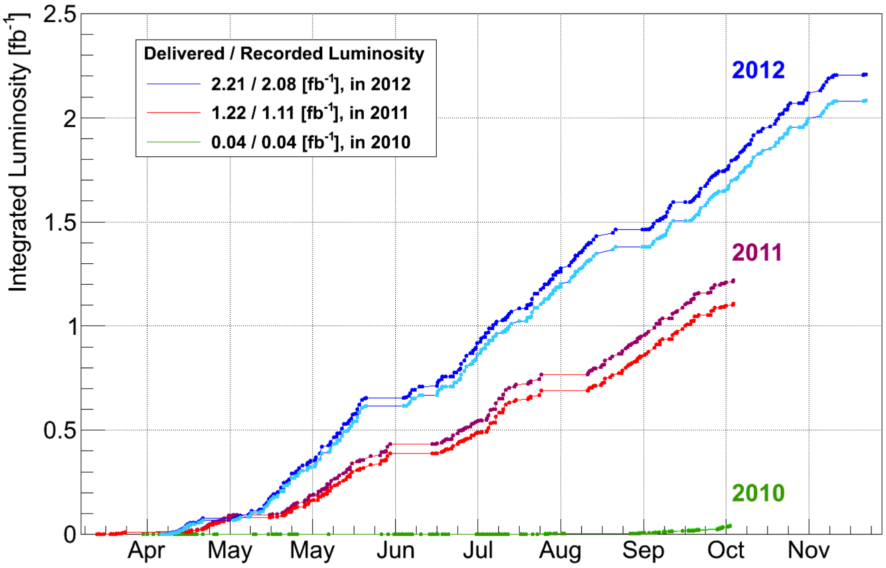

Figure 3.7: The figure shows the delivered (dark coloured lines) and recorded (light coloured lines) integrated luminosities at LHCb during the three years of LHC Run I. Taken from reference [78].

and outer tracker (OT). While the VELO measures the position of primary and secondary vertices with high precision, the tracking stations measure the direction and the momenta of charged particles. The latter are determined from the curvature of the flight path through the magnet.

3.2.2.1 Vertex Locater

The VELO [79, 80] is the sub-detector closest to the *pp* interaction point. It provides precise measurements of primary and secondary vertices as well as first track segments. For the precise determination of vertices, it is crucial, that the active material of the detector is as close as possible to the interaction region.

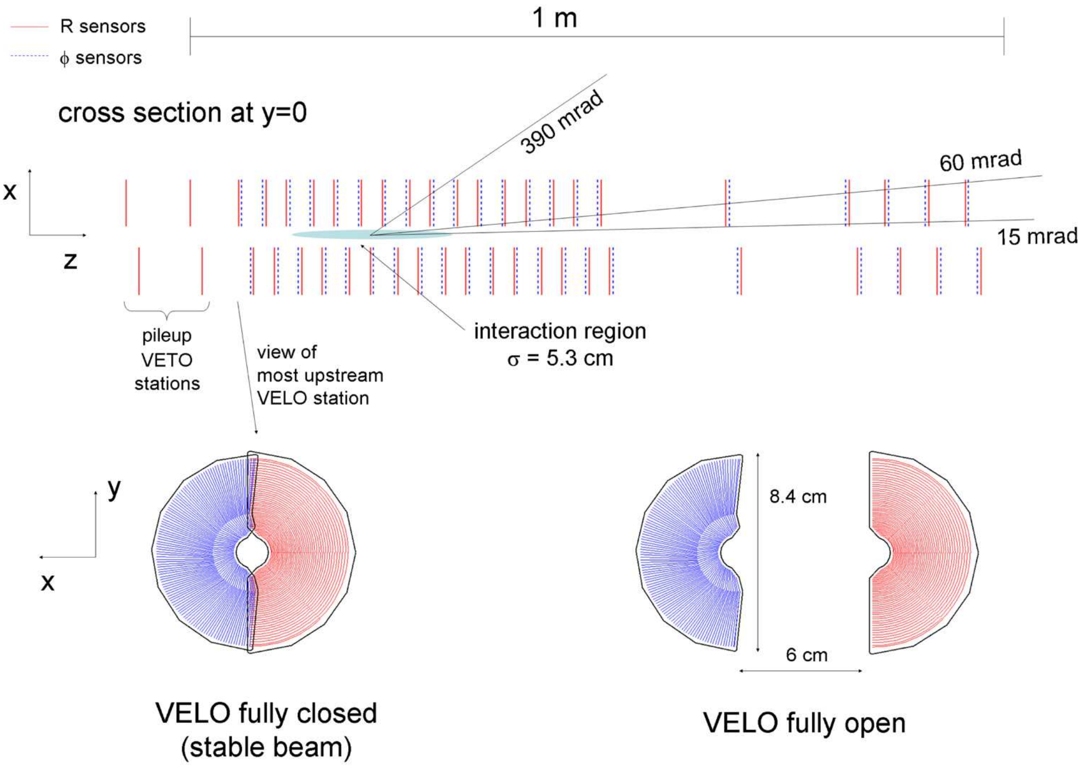

Figure 3.8: Cross-section in the (x,z) plane of the VELO silicon sensors, at $y = 0$, with the detector in the fully closed position. The front face of the first modules is also illustrated in both the closed and open positions. The two pile-up veto stations are located upstream of the VELO sensors [80].

Figure 3.8 shows the cross section of the VELO in the (x,z) and in the (x,y) plane. The detector consists of 21 stations of silicon micro-strip sensors in a $r - \varphi$ geometry. The r-sensor provides information on the radial distance, while the φ-sensor provides information on the azimuthal angle of a charged particle's track. One station consists of two modules, one on each side of the beam axis. One r-sensor and one φ-sensor together form a module with a half circular active area. The (r, φ) geometry was chosen in contrast to a rectilinear scheme, due to a lower reconstruction time of tracks and vertices. Two additional stations upstream are designed to veto pile-up events and estimate the number of collisions per bunch crossings. They consist of $r-$sensors only.

The geometry of the VELO is given by the requirements to detect particles with a pseudo-rapidity in the range of $1.6 < \eta < 4.9$ and emerging from primary vertices in the range of $|z| < 10.6$ cm. Due to the condition that a track should cross at least three VELO stations, the size of the sensors with respect to the beam axis (8 mm at closest and 42 mm at most) and the position in z of the stations is constraint (the three most downstream stations have to be at approximately $z = 65$ cm). The VELO has a full length of 1 m. To minimise alignment issues and covering the full azimuthal acceptance, the two modules in one station are overlapping. The backward acceptance of the VELO is $-3.5 < \eta < -1.5$, due to the upstream stations.

The minimal distance of the modules to the beam is smaller than the beam aperture required by the LHC during injection. Hence, the VELO can retract both half sides during injection. The design requires to keep the modules for each detector half in an aluminium box under vacuum. The side facing the beam is formed by corrugated foils, termed Radio Frequency foils (RF-foils). They protect the beam vacuum from outgassing of VELO sensors and shield the VELO against RF pickup from the LHC beams.

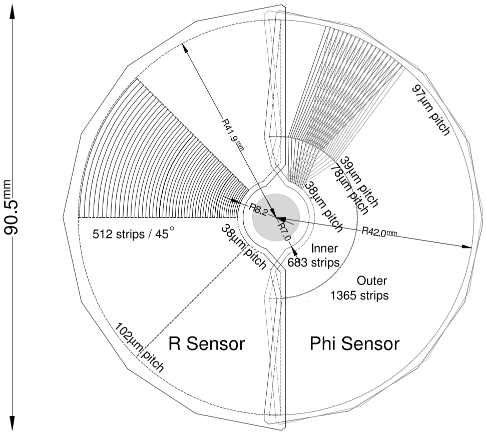

Figure 3.9: Sketch illustrating the (r, φ) geometry of the VELO sensors. For clarity, only a portion of the strips are illustrated. In the φ-sensor, the strips on two adjacent modules are indicated, to highlight the stereo angle. The different arrangement of the bonding pads leads to slightly larger radius of the $r-$sensor; the sensitive area is identical [80].

The sensors are built out of a silicon n-bulk with n^+ implants forming the strips with strip isolation achieved by the use of a p-spray. Figure 3.9 shows the conceptual layout of the sensor. For the r-sensor the implants are concentric semi-circles, with a pitch of 38 µm closest to the beam and linearly increasing to 101.6 µm for the outermost sensor. All strips of the r-sensor are subdivided in four regions of 45°, to minimise the occupancy and strip capacitance. For the φ-sensors a subdivision into two regions is used, inner and outer, with strips running radially from the centre to the outer edge. The same reasons for the design hold as for the r-sensors. The inner region starts with a pitch of 38 µm, which increases linearly up to 78 µm at a radius of 17.25 mm. The outer region starts at this radius with a pitch of 39 µm and linearly increases up to a pitch of 97 µm. Both regions have a skew of 20° at 8 mm to the radial for the inner region and of 10° at 17 mm to the radial for the outer region. The inner and outer skew is reversed to each other. Adjacent φ-sensors are reversed to each other to distinguish fake hits from true hits. The different pitch width ensures that the contributions of the measurements given by the VELO stations have roughly equal weight. The read out electronics of the sensors are placed outside of the VELO acceptance and are used to fix the geometrical position. This design keeps the amount of dead material in the acceptance to a minimum.

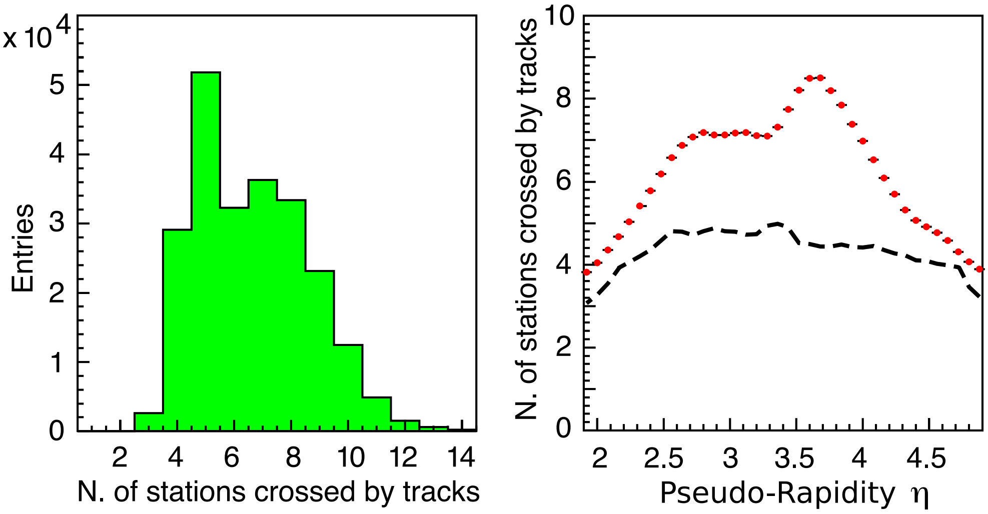

Figure 3.10: The left plot shows the number of stations hit per track in the VELO and the right plot shows the number of hits of a track in the VELO modules as a function of the pseudorapidity of the track. The dashed line indicates the limit above which 95% of the tracks lie. Both figures are taken from [80].

Figure 3.10 shows that all tracks inside the LHCb acceptance pass through at least three modules. Figure 3.11 shows the individual hit resolution of the sensors with a minimum raw resolution of

7 µm. The impact parameter (IP) resolution of the VELO is $(15 \pm \frac{29}{p_T})$ µm. Figure 3.12 shows the definition of the IP. These results were obtained in a test beam. The detector occupancy is a key parameter in the performance of the track algorithms and pattern recognition. It was measured to be around 1% for data with $\mu_{vis} = 1.7$. The contribution from noise to the occupancy is negligible.[78]

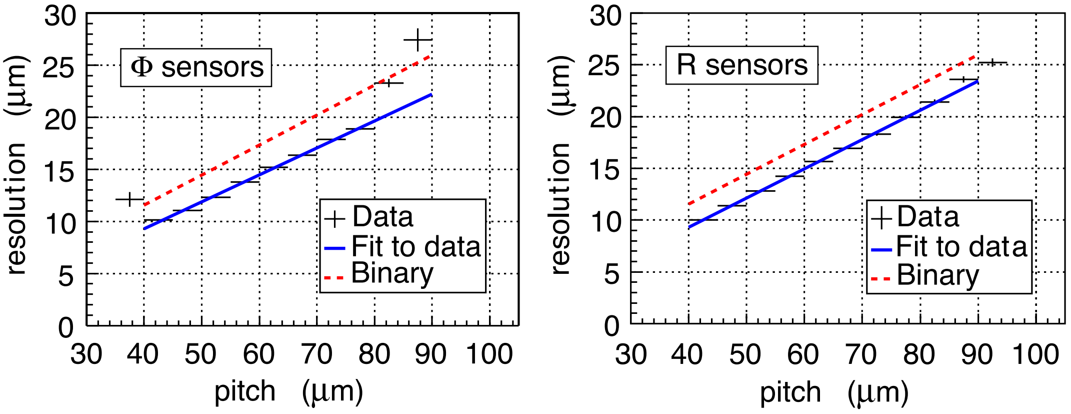

Figure 3.11: Raw hit resolution as a function of strip pitch as measured in the test beam for particles of normal incidence. The dashed line indicates the resolution expected for digital readout. The data points show the resolution as measured from the weighted centre of the charges on the strips. Both figures are taken from [80].

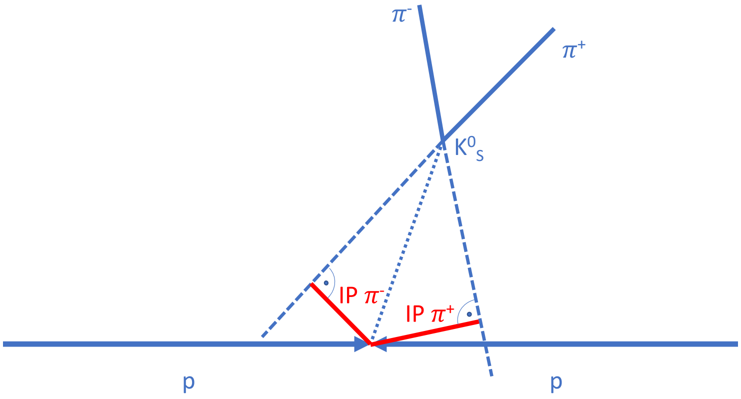

Figure 3.12: Impact parameter (IP) definition in case of a K^0_s decaying to two pions. The IP is indicated in red.

3.2.2.2 TRACKER TURICENSIS

The Tracker Turicensis (TT) [77, 80, 81] is found upstream of the magnet between the magnet and the RICH1. It is a planar tracking station consisting of silicon micro-strip sensors arranged in four layers. All four are housed in one large light tight and thermally and electrically insulated detector volume. The temperature is kept below 5°C to reduce ageing effects and the detector volume is flushed with nitrogen continuously to avoid condensation on the cold surface. The layers are set up in an (*x*-*u*-*v*-*x*) configuration, where the first and last layer are arranged with vertical strips in the LHCb coordinate system and the second and third layer are rotated by a stereo angle of -5° and +5°, respectively. The rotation of the *u* and *v* layers allows the y-coordinate of the track to be measured, but with a lower resolution than the x-coordinate. In total, the TT has an active area of 8.4 m^2 with 143360 individual strips.

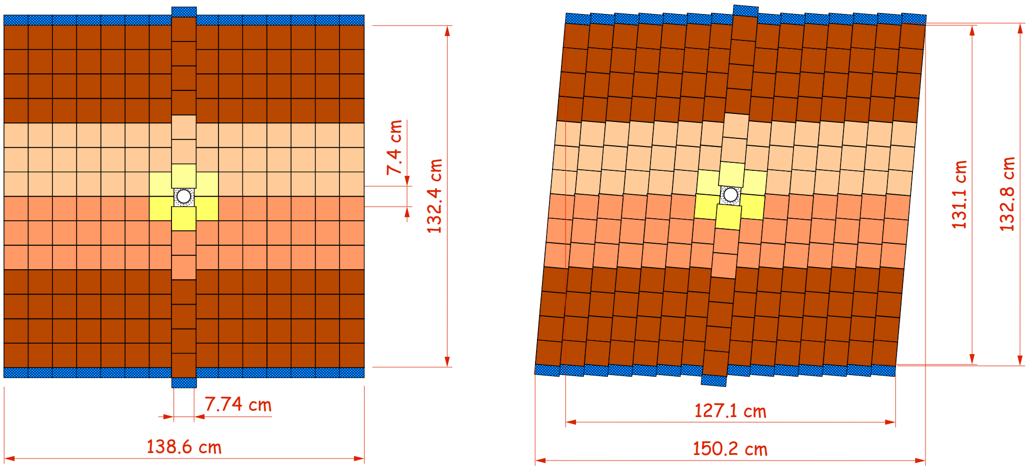

Figure 3.13: Layout of the first layer (left) and second layer (right) in TT, the second has a tilt of 5°.Different readout sectors are indicated by different shadings. The blue shaded region indicates the readout electronics [82].

Figure 3.13 shows the layout of the first and the second layer. Each one is build of half modules, which are joined to cover the full LHCb acceptance. Adjacent modules within a detection layer are staggered by about 1cm in z and overlap by a few millimetres in x to avoid acceptance gaps and simplify the relative alignment of the individual modules. The four detection layers are grouped into pairs of two (*x*,*u*) and (*v*,*x*). The two groups are separated by approximately 27 cm along the LHC beam axis. The first group has 30 half-modules while the second group has 34 half-modules, due to the larger acceptance at higher z.

Each half module consists of a row of seven silicon sensors with a stack of two or three readout hybrids at one end. To keep the occupancy at a manageable level, the half modules close to the beam-pipe are split into three readout sectors. The sectors are connected with Kapton cables to the hybrids at one end of the half module. For the other modules, the sensors are grouped into two readout sectors. This results in a maximum strip length of 38 cm. Figure 3.14 illustrates the layout of a half-module.

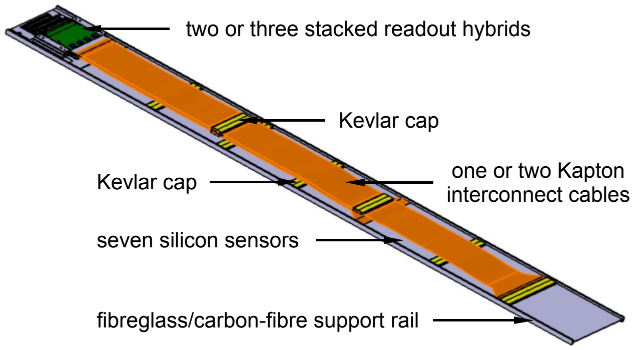

Figure 3.14: View of a TT detector module with three readout sectors [82].

The silicon sensors have a thickness of 500 µm with single-sided p^+-on-n sensor structure. They are 9.64 cm wide and 9.44 cm long and carry 512 readout strips with a strip pitch of 183 µm.

Multiple scattering of particles in the dead material inside the acceptance of a tracking station is the major issue for a good hit resolution. Therefore, the TT was designed such that all the hybrids and electronics are outside of the acceptance of LHCb, keeping as much dead material out of the active area as possible. This results in a hit resolution of roughly 50 µm and a hit efficiency of almost 100%. Table 3.2 shows the hit efficiency and resolution in 2011 and 2012 for data and simulation. The small discrepancy between simulation and data can be partially explained by the remaining misalignment of the modules. The average occupancy with $\mu_{vis} = 1.7$ in the TT varies between 1.9% for the sectors closest to the beam pipe and 0.2% for the outermost modules. The occupancy from noise is negligible [78].

Table 3.2: Summary of the hit efficiency and resolution measurements of the TT made using 2011 and 2012 data. Results are shown as well for simulated events. Table taken from [78].

Measurement	2011 Data	2012 Data	2011 MC	2012 MC
Hit efficiency	99.7%	99.8%	99.9%	99.9%
Hit resolution	52.6 µm	53.4 µm	47.8 µm	48.0 µm

3.2.2.3 The Magnet

A warm dipole magnet is used in the LHCb experiment to bend the trajectory of charged particles and hence allow to measure their momenta [80, 83]. The magnet consists of a window-frame yoke made of laminated low carbon steel and saddle-shaped coils, mirrored symmetrical above and below the beam pipe. The design of the magnet was constrained by the needs of the RICH to have less than 2 mT at their location behind shielding and a field as high as possible in the region between the VELO and TT. In addition, the experimental hall inherited from DELPHI gave some further technical constraints.

The coil consists of fifteen layers of pure hollow aluminium conductors with a channel for water cooling inside. These layers can slide freely upon their supports.

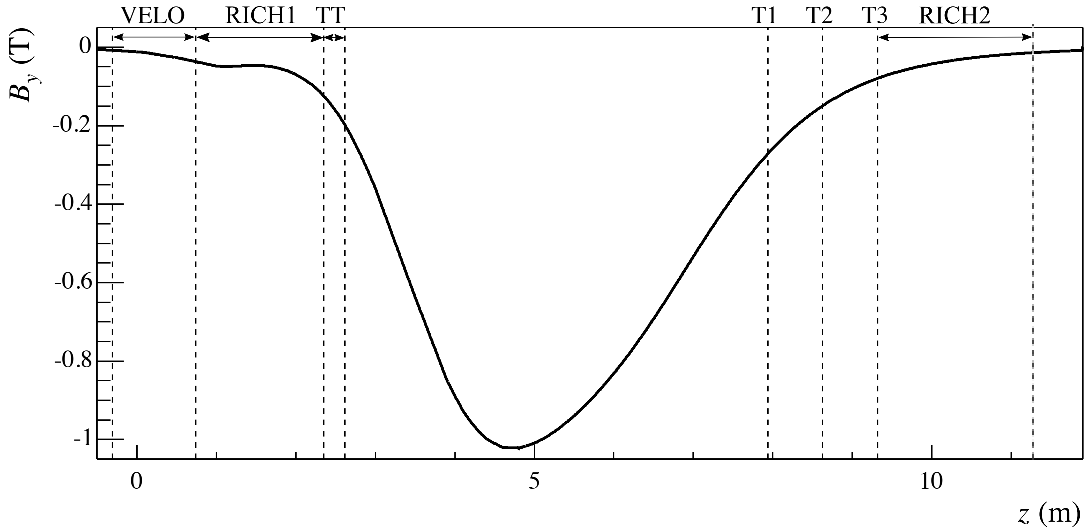

Figure 3.15: The figure shows the main component of the magnetic field strength along the z axis for magnet polarity down [84].

The magnet produces a vertical magnetic field with $\int \vec{B}d\vec{l} = 4\,\mathrm{Tm}$. The magnet polarity is regularly reversed during data acquisition to minimise systematic effects of the measurements. Since the magnet field is perpendicular to the beam axis, additional beam optics are required to take into account the bending of the magnet on the proton beam. Figure 3.15 shows the magnetic field in the y direction as function of z. The measurement was performed with an array of Hall-probes with a precision of $4 \cdot 10^{-4}$. The absolute field value is reproducible for both polarities.

3.2.2.4 INNER TRACKER

The Inner Tracker (IT)[80, 81] is the centre part of the T stations. Due to the high flux in the region around the beam pipe, the IT is built with silicon strip sensors. The IT consists of three stations and each station of four detector boxes as illustrated in Figure 3.16 (left). As for TT the boxes are light tight and electrically and thermally insulated. The temperature is kept below 5°C and the box is continuously flushed with nitrogen to avoid condensation on the cold surfaces.

Each detector box consists of four layers in the same configuration as in TT. In the first and last layer the silicon strips are oriented vertically, while the inner two layers have a stereo angle of -5° and 5°, respectively. Each of these layers consists of seven modules. The modules inside the top and bottom boxes have only one silicon micro-strip sensor while the side boxes have two silicon micro-strip sensors. Figure 3.16 (right) shows the layout of an x detection layer inside one of the IT station.

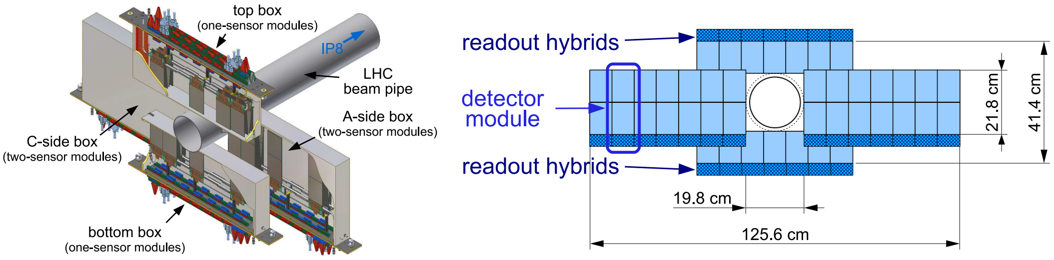

Figure 3.16: (left) View of the four IT detector boxes arranged around the LHC beam-pipe. (right) Layout of an x detection layer in the second IT station. Both figures are taken from [84].

There are two slightly different types of sensors used in IT. Both types are p^+-on-n sensors, 7.6 cm wide and 11 cm long, and have 384 readout strips with a strip pitch of 198 μm. However, the sensors for one-sensor modules are 320 μm thick, and those for two-sensor modules are 410 μm thick. The corresponding thickness was chosen to ensure sufficiently high signal-to-noise ratios for each module type while minimising the material budget of the detector. In IT the readout electronics is inside the acceptance in contrast to the VELO and TT.

In total, the IT has an active area of 4 m^2 with 129024 readout strips, where the strip length is between 11 and 20 cm. The hit resolution and efficiency are similar to the ones from TT, approximately 50 μm and 100% respectively. Table 3.3 shows the hit efficiency and resolution of the IT in 2011 and 2012. As for TT, the small discrepancy between simulation and data can be partially explained by the remaining misalignment of the modules. The average occupancy is found to vary between 1.9% and 0.2% with $\mu_{vis} = 1.7$, where the boxes above and below the beam pipe have the lowest occupancy. The contribution from noise is negligible [78].

Table 3.3: Summary of the hit efficiency and resolution measurements of the IT made using 2011 and 2012 data. Results are shown as well for simulated events. Table taken from [78].

Measurement	**2011 Data**	**2012 Data**	**2011 MC**	**2012 MC**
Hit efficiency	99.8%	99.9%	99.9%	99.9%
Hit resolution	50.3 µm	54.9 µm	53.8 µm	53.9 µm

3.2.2.5 Outer Tracker

The Outer Tracker (OT)[80, 85] is a drift-time detector located at the outer part of T1-T3. Each T station consists of four layers, arranged the same way as the IT. One layer is built by an array of individual gas-tight straw-tube modules. Each module consists of two staggered layers (monolayers) of 64 drift-tubes each with an inner diameter of 4.9 mm. Figure 3.17 shows the layout of the modules. The counting gas is a mixture of Argon (70%) and carbon dioxide (30%). The system offers the possibility of using up to three gas components.

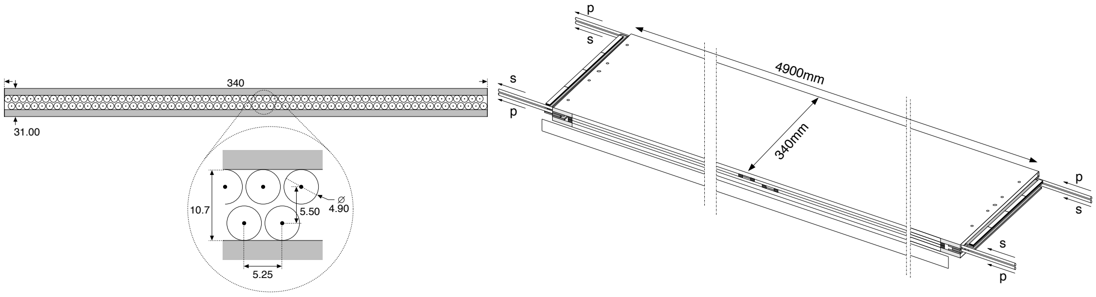

Figure 3.17: Cross-section of a straw-tube module (left) and overview of a straw-tube module design (right). Figure taken from [80].

There are two kind of modules, the short modules (type S) located above and below the beam pipe, and the long modules (type F) located on each side of the beam pipe. For the latter the monolayers are split longitudinally in the middle into two parts with individual straw tubes. Each section has a separate readout. To avoid an inefficient region in the middle, the splitting is done at different positions of both monolayers in one module. The full F-module has an active length of 4850 mm and contains in total 256 straw-tubes. The modules of type S are just half the length of type F and have one readout hybrid at the outer module end and a total of 128 single drift tubes. One layer consists of 14 long and 8 short modules. This results in a total of 168 long and 96 short modules for the complete OT detector with about 55000 single straw-tube channels.

The total active area is around 29 m^2. The OT has an efficiency of almost 100% for tracks close to the central half of the straw (closer than 1.25 mm to the wire). The single hit resolution is 205 µm, close to the design value of 200 µm. The average occupancy is at maximum around 20% with a negligible contribution from noise[78].

3.2.3 PARTICLE IDENTIFICATION

Particle identification (PID) plays a crucial role for LHCb. Several detector systems have been developed to separate different particle types. The Ring Imagine Cherenkov detectors (RICH) are used for separating mainly pions, kaons and protons using Cherenkov light. The calorimeter system measures the energy of the particles and identifies electrons, photons and hadrons. The most downstream detector finally identifies muons. In the following a short overview of each system is given.

3.2.3.1 RING IMAGINE CHERENKOV DETECTOR

In 1934, Pavel A. Cherenkov discovered a *Visible emission of clean liquids by action of γ radiation*[86]. In his nobel lecture in 1958 he first mentioned the possibility of using this radiation for particle identification.

Cherenkov radiation is emitted if a particle pass through a medium faster than the speed of light in that medium. Radiation photons are emitted at a characteristic angle θ_C with respect to the particle trajectory. This angle depends on the velocity of the particle $\beta = v/c$ and on the refraction index of the medium n,

$$\cos\theta_C = \frac{1}{n\beta}. \tag{3.6}$$

If the particle momentum is known, the measurement of the θ_C can be used to determine the mass of the particle and hence its type.

LHCb has two RICH detectors [80, 87]. While RICH1 is located between the VELO and TT covering the full LHCb acceptance, RICH2 is positioned between the last tracking station and the first muon station.

Figure 3.18a shows a schematic layout of the RICH1 detector. Aerogel (n=1.03 [88]) and C_4F_{10} (n=1.0014, at 0°C, 101.325 kPa and 400 nm [88]) are used as radiators to identify particles within

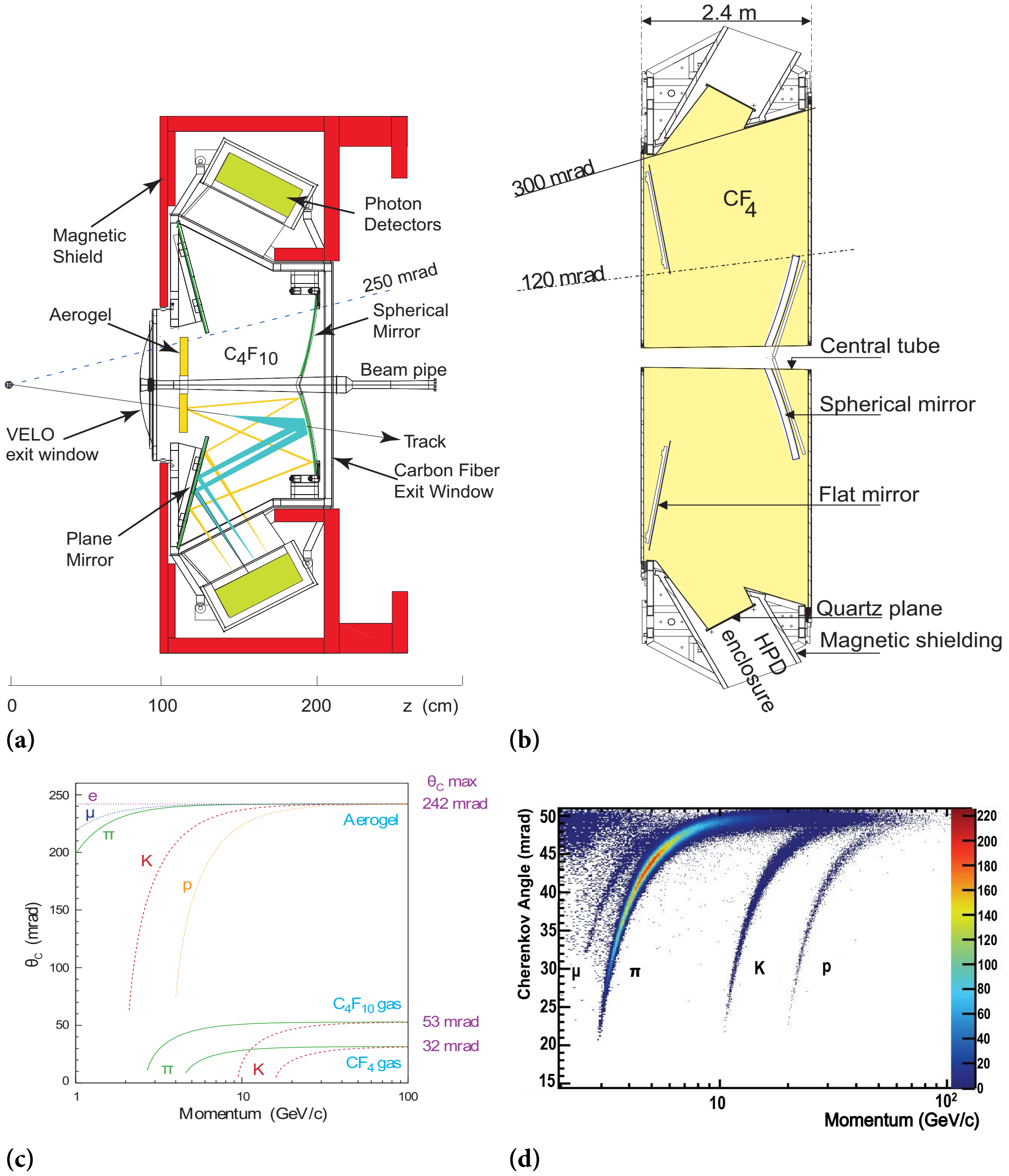

Figure 3.18: (a) and (b) show a side view of the schematic layout of the RICH1, respectively the top view of the RICH2 detector. (c) shows the expected Cherenkov angle versus particle momentum for the RICH radiators. (d) shows the measured Cherenkov angle as a function of track momentum in the C_4F_{10} radiator. Figure (a) and (b) are taken from [80]. Figure (c) and (d) are taken from [78, 80].

a momentum range of 2 to 40 GeV/c in the LHCb acceptance. The emitted Cherenkov light is reflected by a spherical and a plane mirror to an array of Pixel Hybrid Photon Detectors (HPDs) at the top and bottom of RICH1, outside the acceptance. In the HPDs the photoelectrons are accelerated onto a pixel sensor, which provides a position measurement. This allows to reconstruct the circles produced by the Cherenkov light, where the circular radius is proportional to the Cherenkov angle and hence to the velocity.

Figure 3.18b shows a schematic layout of the RICH2 detector. There are three main differences between RICH1 and RICH2. First, RICH2 uses only one radiator, CF_4 (n=1.0005, at 0°C, 101.325 kPa and 400 nm [88]), which allows the identification of particles with a momentum range from 15 GeV/c up to 100 GeV/c. Second, it covers only a reduced angular acceptance of 15 mrad to 120(100) mrad in the bending (non-bending) plane. And third, the mirrors are situated to the left and right of the beam pipe. For both RICH detectors a magnetic shielding of the HPDs is installed, to minimise the distortions of the photoelectrons induced by the fringe field of the dipole magnet of LHCb.

Figure 3.18c shows the expected Cherenkov angles θ_C for the different radiators used in RICH1 and RICH2. Figure 3.18d shows the measured Cherenkov angles as a function of the track momentum in C_4F_{10}.

3.2.3.2 Calorimeter System

The calorimeter system [80, 89] serves several purposes. Among others one purpose is to provide the transverse energy information of hadron, electron and photon candidates for the hardware trigger in LHCb (*cf.* section 3.2.4). Furthermore, it is needed for the identification of electrons, photons and hadrons and for measuring their energies and positions.

The calorimeter system consists of four parts; the scintillating pad detector (SPD), the pre-shower detector (PS), the electromagnetic calorimeter (ECAL) and the hadronic calorimeter (HCAL). All of them have an active region, which is divided into two subregions in case of the HCAL and three subregions in case of the others. Each subregion has a segmentation of different granularity. Figure 3.19 shows the segmentations for one quarter of the relative detector face.

The pad/pre-shower (SPD/PS) detector consists of two scintillating pad layers separated by a 15 mm thick lead absorber. Both pad layers are read out by wave length shifting fibres guiding the light to one multi-anode photomultiplier tube (MAPMT) per pad. One pad has the size of one cell in the corresponding subregion. The first pad layer, the SPD is used for identifying charged particles, mainly for the differentiation of electrons from photons. The lead absorber and the second pad layer form the PS detector, which provides a longitudinal segmentation to the ECAL and is used to improve the discrimination between pions and electrons. All together, SPD/PS have a combined radiation length of 2.5 X_0.

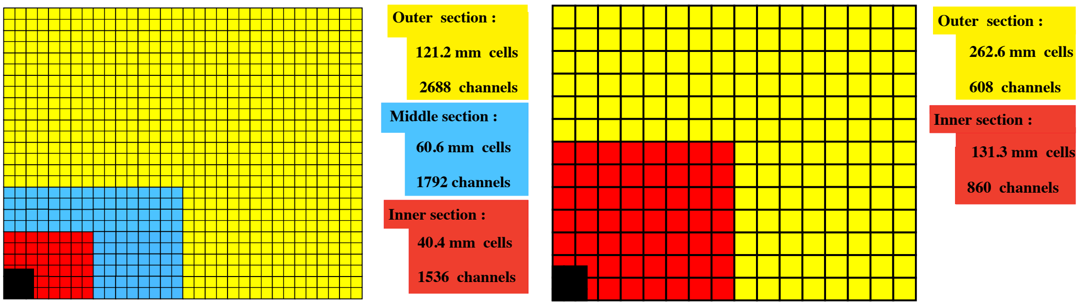

Figure 3.19: Lateral segmentation of the SPD/PS and ECAL (left) and the HCAL (right). One quarter of the detector front face is shown. Figure taken from [80].

Directly after the SPD/PS follows the ECAL, which is built as shashlik calorimeter, *i.e.* a sampling scintillator/lead structure. The lead layers are 2 mm and the scintillating layers are 120 μm thick. Each cell of a subregion consists of 66 scintillating/lead layers, which results in a radiation length of 25 X_0 (42cm). As in SPD/PS, the light of the scintillators in the ECAL is collected by plastic wave-length shifting fibres, with the difference that the read out is done by one photomultiplier per scintillator stack in one cell. The measured relative energy resolution for an energy range of 10 to 100 GeV/c^2 is:

$$\frac{\sigma_E}{E} = \frac{10\%}{\sqrt{E}} + 1\% \quad \text{with } E \text{ in } \text{GeV}/c^2, \tag{3.7}$$

where the first term is due to statistical fluctuations and the second is due to the instrumental resolution.

The HCAL is a sampling calorimeter as the ECAL, but made of 1 cm thick iron absorber and scintillating tiles of 3 mm thickness as active material oriented in parallel to the beam axis. Along the beam axis the tiles have a length corresponding to the hadronic interaction length in iron (197 mm). Wave-length shifting readout fibres are running parallel to the beam axis to the downstream rear edge of HCAL into one photomultiplier per subregion cell. The grouping of the different parallel running layers into cells is done such that the absorber structure is identical over the whole HCAL. The measured relative energy resolution in the energy range of 10 to 100 GeV/c^2 is

$$\frac{\sigma_E}{E} = \frac{69\%}{\sqrt{E}} + 9\% \quad \text{with } E \text{ in } \text{GeV}/c^2, \tag{3.8}$$

where the terms are the same as for the ECAL.

3.2.3.3 Muon Detector

Triggering on muon and offline muon identification is crucial for the physics program of LHCb. The muon system [80, 90] consists of five stations (M1-M5) of rectangular shape. The inner and outer angular acceptance is 20 (16) mrad and 306 (258) mrad in the bending (non-bending) plane respectively. The total active area of the muon system is 435 m^2.

The stations M2-M5 are interlaced with 80 cm thick iron absorbers and located downstream, after the calorimeter system. To penetrate the whole muon system, a muon with a minimum momentum of 6 GeV/c is needed, as the total interaction length is roughly 20 X_0, including the muon system absorber and the calorimeter system. Station M1 is placed in front of the calorimeter system, to improve the p_T measurement in the trigger. Figure 3.20 shows the side view of the muon system.

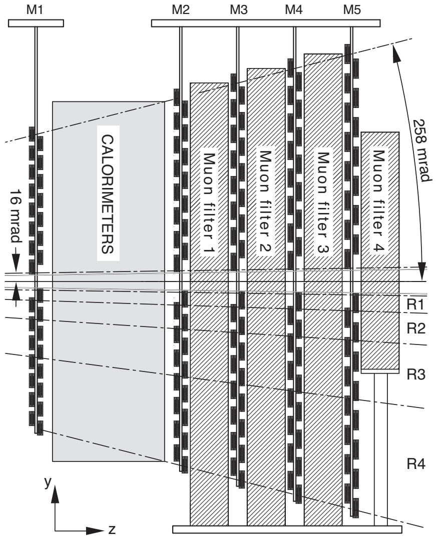

Figure 3.20: Side view of the muon system. Figure taken from [80].

To keep the particle flux and the channel occupancy in the detector constant, the detector has four regions with different segmentation (R1-R4). The layout of the muon stations is shown in fig. 3.21. The dimensions and their segmentations scale in the ratio 1:2:4:8 (R1, R2, R3, R4). The right part of fig. 3.21 shows the partition into logical pads for station M1, which defines the (x,y) granularity. While the number of pad columns per chamber is double (half) for M2-M3 (M4-M5) compared to the corresponding region of station M1, the number of pad rows per chamber is the same for any region and any station.

Multi-wire proportional chambers (MWPC) are used to detect the signal from the muons in all regions except the inner region of M1. In this region, triple-GEM detectors are used, because the expected particle rate exceeds safety limits for ageing of the MWPC. Both, the MWPCs and triple-GEM detectors are using a gas mixture of $Ar/CO_2/CF_4$ but with different relative percentage.

In total, the muon system includes 1368 MWPC chambers. Each is built in case of M2-M5 (M1) out of four (two) gas gaps with 5 mm thickness, 2 mm wire spacing and an anode-cathode spacing of 2.5 mm. Figure 3.22 shows a schematic overview of one MWPC chamber and a cross section. The vertical wire is logically connected with an *AND* to the horizontal cathode pad. The two gas gaps are logically combined with an *OR*, forming the logical pads shown in Figure 3.21. This operation provides redundancy and increases the detector efficiency.

The inner part of station M1 is built of 12 chambers consisting of two triple-GEM detectors, which are logically *OR*-ed. One chamber has an active area of $20 \times 24\,\mathrm{cm}^2$.

3.2.4 TRIGGER

The LHCb trigger system [80, 91] has a two stage structure; the level 0 trigger (L0) implemented in custom made hardware, followed by the high level trigger (HLT) implemented in software running on a dedicated computing farm. Figure 3.23 shows a scheme of the LHCb trigger chain. The bunch crossing frequency at the interaction point of LHCb is 40 MHz. The visible[3] interaction crossing frequency is 10 MHz due to the lower luminosity and the bunch structure.

The L0 trigger reduces the rate down to 1 MHz. It uses information of the pile-up detector in the VELO, the calorimeter system and the muon system. The pile-up detector aims at distinguishing between crossings with single and multiple visible interactions. In 2011 and 2012 it was only used for luminosity measurements[78]. The calorimeter and muon system informations are used to trigger on high transverse energy (E_T) electrons, photons, π^0 and hadrons, or high p_T-muons. In total the L0 trigger has a latency of 4 µs, where half of it is due to cable delays, the time-of-flight of particles and delays of the front-end electronics.

In order to reduce the event rate from 1 MHz down to 2 kHz, which is the maximum rate LHCb can write data to tape, the HLT makes use of the full event data. The HLT runs on the Event Filter Farm (EFF) with around 29000 computing cores and is divided into two stages HLT1 and HLT2, because the rate of 1 MHz is still to high for a full event reconstruction. HLT1 reconstructs parti-

---

[3] An interaction is defined to be visible if it produces at least two charged particles with sufficient hits in the VELO and T1-T3 to allow them to be reconstructible[80].

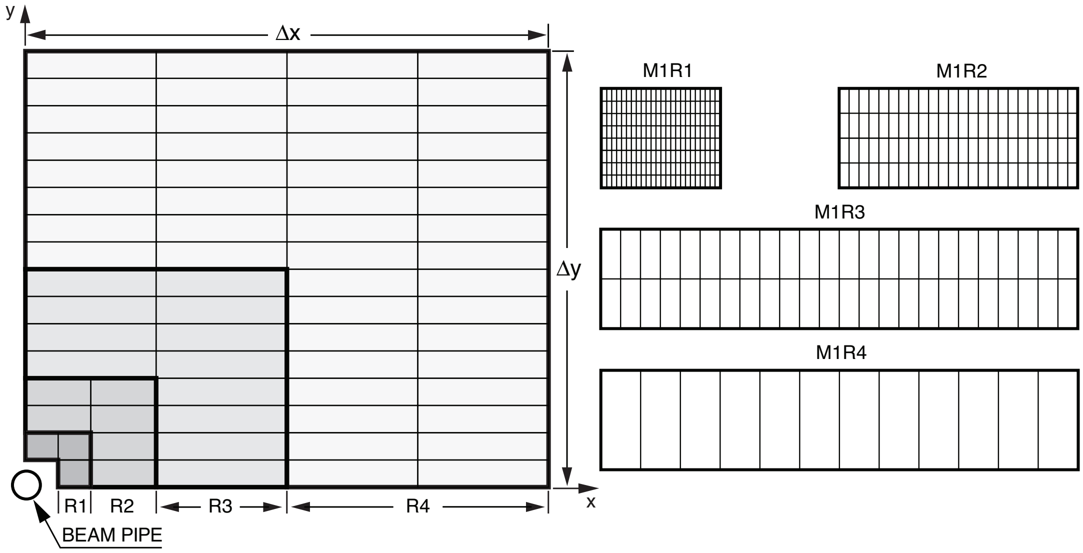

Figure 3.21: Left: Front view of a quadrant of a muon station. Each rectangle represents one chamber. Each station contains 276 chambers. Right: division into logical pads of four chambers belonging to the four regions of station M1. Figure taken from [80].

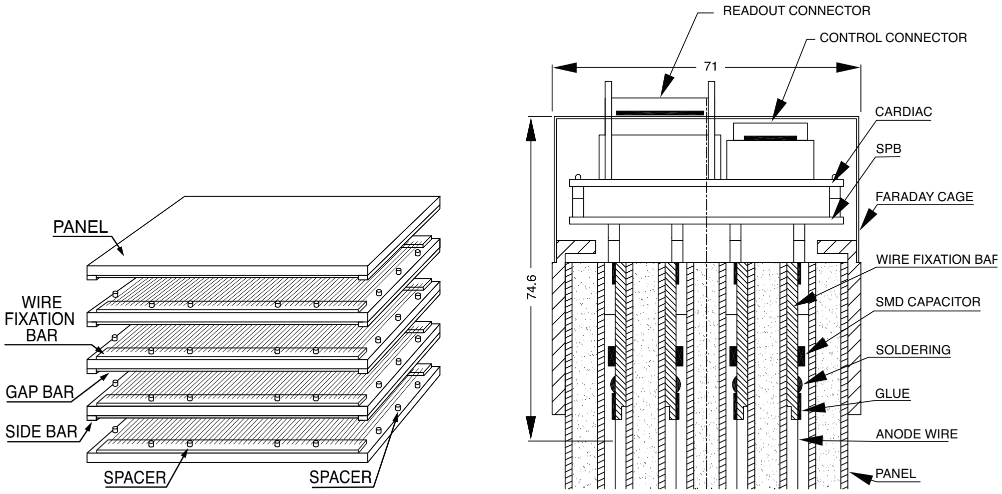

Figure 3.22: (left) Exploded schematic view of a MWPC chamber of the muon system showing the various elements. (right) Cross section of a wire chamber showing the four gas gaps and the connection to the readout electronics. Figure taken from [80].

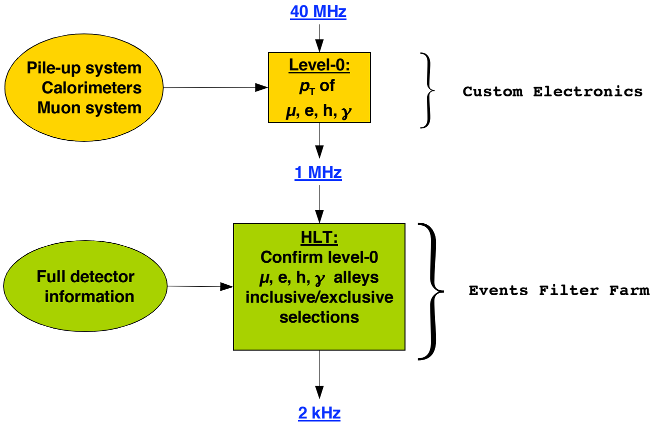

Figure 3.23: Scheme of the LHCb trigger chain. Figure taken from [80].

cles in the VELO and T-stations corresponding to the L0 objects, or confirming the absence of a charged particle in case of L0 photon and π^0 candidates. After the HLT1 the rate is around 30 kHz, which is low enough to run full or partial event reconstruction algorithms to select specific event candidates. The reconstruction algorithms are as close as possible to the offline reconstruction algorithms.

Before the data is saved to disk a full offline reconstruction is applied. Afterwards in a reprocessing of the fully reconstructed data a so called stripping is applied, which is in principle applying common used pre-selections algorithms on the data. There are two categories of stripped events; the particle containers for final state particles or some most used intermediate particles and the stripping lines, which are sophisticated pre-selections for specific analysis types. The idea behind this stripping is saving time for the individual analyses and providing consistent selections for basic particles/decays.

There is a computer disease that anybody who works with computers knows about. It's a very serious disease and it interferes completely with the work. The trouble with computers is that you 'play' with them!

Richard P. Feynman

4

Track Reconstruction in LHCb

This chapter provides an introduction to track reconstruction in LHCb. First an overview of the passage of particles through matter is given, followed by the description of the tracking algorithms in LHCb. Finally the improvements applied on the most important tracking algorithm in LHCb for the detector upgrade are shown together with the validation on measured data. The improvements on the tracking algorithm were developed, tested and implemented by Espen Bowen and myself, whereas the validation on measured data was fully done by myself.

4.1 Passage of Charged Particles Through Matter

Particles flying through matter, interact with the electrons and nuclei in the material through different processes. Three important types of interactions, which are important for the measurement of the traces of particles are explained in detail: the electromagnetic interaction, the hadronic interaction and multiple scattering.

4.1.1 Electromagnetic Interactions

Several types of electromagnetic interactions of charged particles are distinguished. An overview is given in the following.[1]

4.1.1.1 Ionisation for Heavy Charged Particles

Ionisation takes places, if charged particles passing through matter either excite an atom to a higher state or ionise it directly by interacting with the outer electrons. The mean energy loss by moderately relativistic charged heavy particles is well-described by the Bethe-Bloch equation[16]:

$$\left\langle -\frac{dE}{dx} \right\rangle = Kz^2 \frac{Z}{A} \frac{1}{\beta^2} \left[\frac{1}{2} \ln \frac{2m_e c^2 \beta^2 \gamma^2 T_{max}}{I^2} - \beta^2 - \frac{\delta(\beta\gamma)}{2} \right], \tag{4.1}$$

where $K = \frac{4\pi e^4}{c^2 m_e} N_A$ with e the electron charge, c the speed of light, m_e the mass of the electron and N_A the Avogadro constant, z the charge number of the incident particle, Z the atomic number of the absorber, A the atomic mass of the absorber, $\beta = \frac{v}{c}$ the velocity, I the mean excitation energy, T_{max} the maximal energy transfer to an electron in a single collision and $\delta(\beta\gamma)$ a correction due to the polarisation of the absorber, the so-called density effect. Figure 4.1 shows the mean rate of energy loss or stopping power as function of the particle momentum or $\beta\gamma$ for muons in copper.

Equation (4.1) is valid in the range of $0.1 < \beta\gamma < 1000$ and has an accuracy of a few percent. At the lower limit, corrections due to the atomic binding are needed. Above the upper limit, the energy loss due to radiative processes starts to be dominant (see section 4.1.1.2 about Bremsstrahlung).

Equation (4.1) needs to be modified for electrons and positrons, since the masses of the scattering partners are of the same size and in case of electrons, the two particles are indistinguishable. Figure 4.2 shows the fractional energy loss per radiation length (see section 4.1.1.2) in lead as function of the electron/positron energy. At low energies (in lead below $E_c = 7.3\,\text{MeV}$, see section 4.1.1.2), electrons and positrons mainly lose energy by ionisation. Because the electrons are indistinguishable from the atomic electrons, the energy loss is smaller than for positrons. In case of large energy transverse (in lead above 0.255 MeV per collision) additional processes contribute to the energy loss below low energies: Møller scattering in case of electrons[92], and Bhabha scattering[93] and annihilation in case of positrons[94].

---

[1] There are as well Cherenkov and transition radiation. These are not affecting the track reconstruction in LHCb. The Coulomb scattering plays a role in terms of multiple scattering (see section 4.1.2).

4.1.1.2 BREMSSTRAHLUNG

If a charged particle is accelerated, it emits electromagnetic radiation. Whereas the acceleration can be due to a magnetic field, as in case of synchrotron radiation described in section 3.1 or due to another charged particle as the atomic nucleus in matter. This process is called Bremsstrahlung. Bremsstrahlung can be quantified by the mean radiation length X_0, which is defined as the average distance an electron has to fly to lose all but $1/e$ of its energy by Bremsstrahlung. The mean energy loss due to Bremsstrahlung is defined as [95]:

$$\frac{dE}{dX} = -\frac{E}{X_0}. \tag{4.2}$$

Bremsstrahlung is dominant for electrons above the critical energy $E_c = \frac{610\,\text{MeV}}{Z+1.24}$ for solids and liquids, *e.g.* in silicon the critical energy is $E_c = 40$ MeV. Hence it is the dominating process at the LHC energy for electrons. For other particles with mass M the energy loss due to Bremsstrahlung is suppressed by the factor $(\frac{m_e}{M})^2$, where m_e is the electron mass. [16, 95]

4.1.2 MULTIPLE SCATTERING

A charged particle, which is flying trough material, is deflected by many small-angle scatters (multiple scattering). For charged particles the deflections are due to Coulomb scattering (also called Rutherford scattering), whereas in case of hadrons the strong interaction contributes as well. For small angles of deviation, a Gaussian approximation can be used to describe the distribution of the projected angle with the width θ_0[16] given by:

$$\theta_0 = \frac{13.6\,\text{MeV}}{\beta c p} z \sqrt{x/X_0}\left[1 + 0.038\ln(x/X_0)\right], \tag{4.3}$$

where p, βc and z are the momentum, velocity and charge number of the incident particle, and x/X_0 the thickness of the scattering medium in radiation lengths. From eq. (4.3) it follows that multiple scattering gets important for small momenta. Especially, it dominates the position resolution of a detector for small momenta. Therefore, the amount of material inside the flight path of particles has to be reduced to a minimum for a good position resolution over a wide range of momenta's.

In reality the total material in a detector is a mixture of different types. The correct procedure is to get first X_0 and x for the mixture and then use eq. (4.3) to calculate θ_0 (detailed information are in [16]).

4.1.3 HADRONIC INTERACTIONS

Charged and neutral hadrons can interact strongly. They either break up the nuclei which release protons and neutrons (so-called spallation) or scatter inelastically at the nuclei, producing new hadrons. Similar to the radiation length, a nuclear interaction length can be defined as $\lambda_{int} = \frac{M}{N_A \rho \sigma_{inel}}$, where ρ is the density of the material, M the molar mass and σ_{inel} the inelastic scattering cross-section. In lead for example, the nuclear interaction length is $\lambda_{int} = 17.59\,\mathrm{cm}$ and in dry air at 1 atm it is $\lambda_{int} = 74.77\,\mathrm{m}$[16]. The nuclear interaction length describes the mean free path between two hadronic interactions. The cross-section depends on the charge, the momentum and type of the particle.

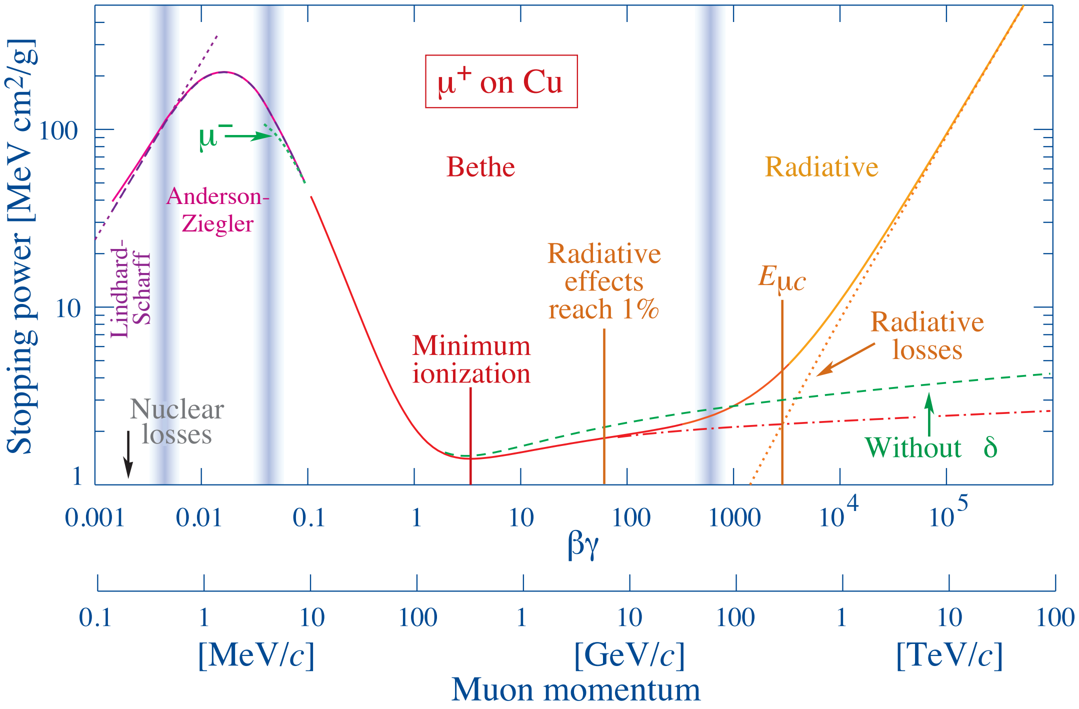

Figure 4.1: Stopping power ($=\langle -\frac{dE}{dx} \rangle$) for positive muons in copper as a function of $\beta\gamma = p/Mc$ over nine orders of magnitude in momentum (12 orders of magnitude in kinetic energy). Figure taken from [16].

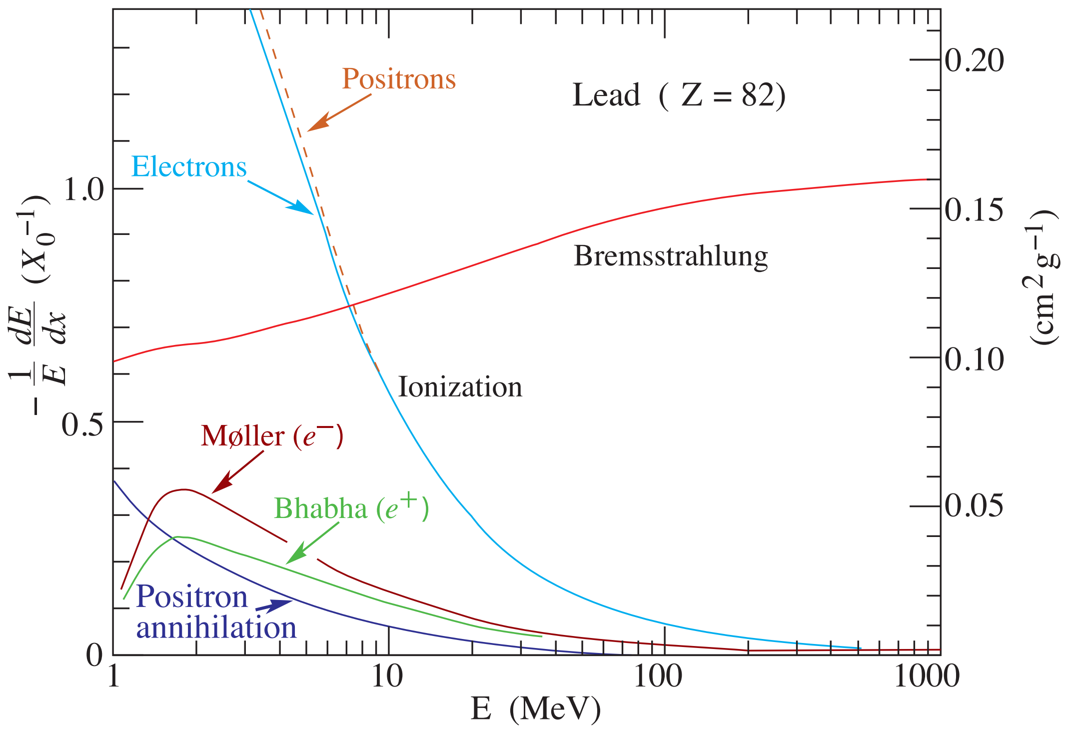

Figure 4.2: Fractional energy loss per radiation length in lead as a function of electron or positron energy. Electron (positron) scattering is considered as ionisation when the energy loss per collision is below 0.255 MeV, and as Møller (Bhabba) scattering when above. Below an electron/positron energy of 10 MeV, the energy loss in lead is smaller for electrons than positrons as the electrons are indistinguishable from the atomic electrons. Figure taken from [16].

4.2 FLIGHT PATH RECONSTRUCTION

The flight path of a charged particle incloses several informations. First it contains the position in time of the particle and the direction of flight. Furthermore if the charged particle flies through a magnetic field, the curvature of the flight path leads to the momentum of the particle and its charge. Tracking is nothing else then reconstructing the flight path of a charged particle as accurately as possible to extract these observables.

The modern particle detectors are usually sampling detectors [96], where the detector volume is filled with several devices measuring pieces of information of the flight path of the particles. The challenging task is to find all particle tracks by combining all informations and accurately determining their track parameters. A typical collision event at LHCb has a large number of tracks in the order of several hundreds. Tracking can be separated into two parts: Pattern recognition and fitting. Both are explained in the following or in more detail in [84, 97].

4.2.1 TRACK STATE

A track state is described by line segments tangential to the particle's trajectory. In LHCb tracks are pointing either in forward or backward direction. Therefore track states are parametrised as function of the z coordinate. These states are described by five parameters and a five dimensional covariance matrix for the uncertainty at a given z position:

$$\begin{bmatrix} x \\ y \\ t_x \\ t_y \\ \frac{q}{p} \end{bmatrix} \text{ with } t_x = \frac{\partial x}{\partial z}, t_y = \frac{\partial y}{\partial z} \tag{4.4}$$

where q is the charge and p the momentum of the particle. The z position of the track state can be anywhere along the flight path, but in general it is chosen to be at the measurement planes of the tracking detectors. In the track model, two operations on the track state are of particular interest: propagation and projection.

The relation between a measurement, m_z, and a state is described by the projection:

$$m_z = h_z(\vec{x}_z) \tag{4.5}$$

where h_z is the projection function. If for example the detector directly measures only one coordinate, then h_z is a linear function and can be represented with a matrix.

The propagation provides a relation between a track state at z_2 and at z_1:

$$\vec{x}_{z_2} = f_{z_1 \rightarrow z_2}(\vec{x}_{z_1}) \tag{4.6}$$

where f stands for the propagation function. In this step effects from multiple scattering can be taken into account by $\vec{w}_z$ when the particle travels through material. The function f depends on the chosen propagation and can be highly non-linear in magnetic fields [98]. In absence of a magnet field, f simplifies for a straight line extrapolation to:

$$f_{z_1 \to z_2}(\vec{x}_{z_1}) = F_{z_1 \to z_2}\vec{x}_{z_1} = \begin{bmatrix} 1 & 0 & \Delta z & 0 & 0 \\ 0 & 1 & 0 & \Delta z & 0 \\ 0 & 0 & 1 & 0 & 0 \\ 0 & 0 & 0 & 1 & 0 \\ 0 & 0 & 0 & 0 & 1 \end{bmatrix} \vec{x}_{z_1} \tag{4.7}$$

where $\Delta z = z_2 - z_1$. A detailed discussion of track states is given in references [84, 97].

4.2.2 TRACK DEFINITIONS

In LHCb tracks are classified in several types, according to the sub-detectors involved in the reconstruction of the tracks. Figure 4.3 shows schematically the main track types. There are several other types for special purposes, which are not mentioned here. Below the main track types are described shortly and ordered according to their importance for LHCb.

LONG TRACKS Long tracks cross the whole tracking system, from VELO up to the T-stations. They have the most accurate momentum measurement of all track types, and are therefore the most important ones in the LHCb experiment.

DOWNSTREAM TRACKS Downstream tracks only leave hits in the TT and the T stations. They are produced mostly by charged long lived particles with considerable displaced origin from the interaction point. The momentum resolution is worse than for long tracks, due to the missing part of the path from the VELO.

UPSTREAM TRACKS Upstream tracks only leave hits in the VELO and TT. They originate from low momentum particles, which are bent out of the acceptance by the magnetic field. Hence, the momentum resolution is worse than for downstream and long tracks. Upstream tracks are mainly used for the RICH1 reconstruction.

VELO TRACKS They only traverse the VELO and are not detected elsewhere in the LHCb detector. The momentum cannot be determined but as they have mostly large polar angles, they an be used to accurately determine the primary vertex. Reconstruction of VELO tracks in the backward direction is possible as well, by using the pile-up veto system. These tracks are used in central exclusive production analyses at LHCb [99].

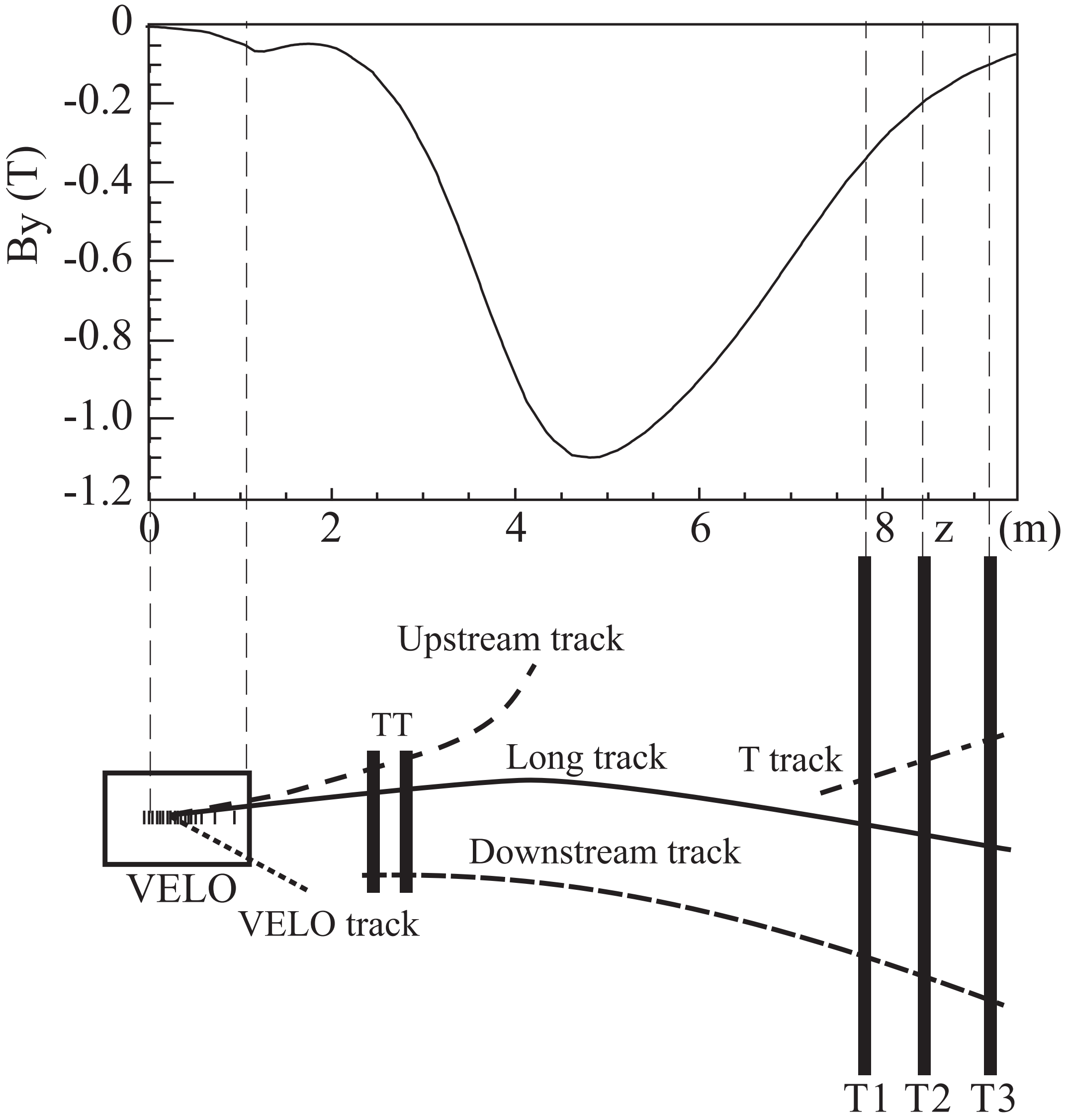

Figure 4.3: A schematic illustration of the various track types. For reference the main B-field component (B_y) is plotted above as function of the z coordinate. Figure is taken from [80].

T TRACKS They are reconstructed in the T stations only. Either they originate from material interactions or from decays of very long living particles. The T tracks are used in the RICH2 reconstruction and the internal alignment of the T-stations. The momentum of a T track can be estimated only by using the p-kick method under the assumption, that the particle originated from the interaction point. The p-kick method uses the instance, that the influence of the magnetic field can be described by an instant kick of the momentum vector in the centre of the magnet. Details can be found in [84].

4.2.3 Pattern Recognition

Several hundred of flight paths through the detector are recorded for one collision. Every charged particle leaves a signal through ionisation or bremsstrahlung and undergoes scattering processes in the detectors or the beampipe. Pattern recognition aims for combining informations from the tracking sub-detectors to disjoint track candidates. The different algorithms used in LHCb for pattern recognition are described in the following.

4.2.3.1 Velo Seed

The magnetic field inside the VELO is negligible, therefore tracks inside VELO can be considered as straight lines. The pattern recognition first searches in the $r - z$ projection using the r-sensors and adding the φ-sensor measurements afterwards. More information about the algorithm can be found in references [100, 101].

4.2.3.2 T Seed

Inside the T-stations a small fringe field of the magnet is present (see fig. 4.3). Hence the pattern recognition looks for a parabolic track in the (x, z) plane. The track candidate is at first built by a reasonable three-hit-combination for the hits of the x-layers in all three stations. Afterwards additional hits are added to the candidate, if they originate from a defined search region around the parabola. At last the hits from the stereo plane are added. Tracks passing through IT and OT are treated specially. More information on the T-seed pattern recognition algorithm is given in ref. [102, 103].

4.2.3.3 Forward Tracking

This algorithm searches for long tracks. The idea of the forward tracking algorithm is that by knowing the direction at one point before and one point after the magnet, the trajectory in the field can be determined by the equations of motion and the known magnetic field. In the forward tracking algorithm, VELO seeds are used as input. Those have a defined position and slope. This information is used to open a search window on every x-plane in the T-stations. Hits in this region are propagated with a *Hough transformation* to a reference plane, called Hough plane (see fig. 4.4). Resulting clusters are fitted and outliers are removed using a χ^2 criterium. Track candidates fulfilling multiple track quality requirements are then used to search for hits in the stereo planes, u and v, of IT. The x position can be derived from the u,v measurements using the y information from the VELO seed. The resulting hits are again propagated to the Hough plane and searched for clusters, which are fitted and outliers removed based on a χ^2 criterium. The best track candidate is selected according to multiple track quality requirements. Finally TT hits are added using selection criteria and clustering/projection procedures. More information is given in [104, 105].

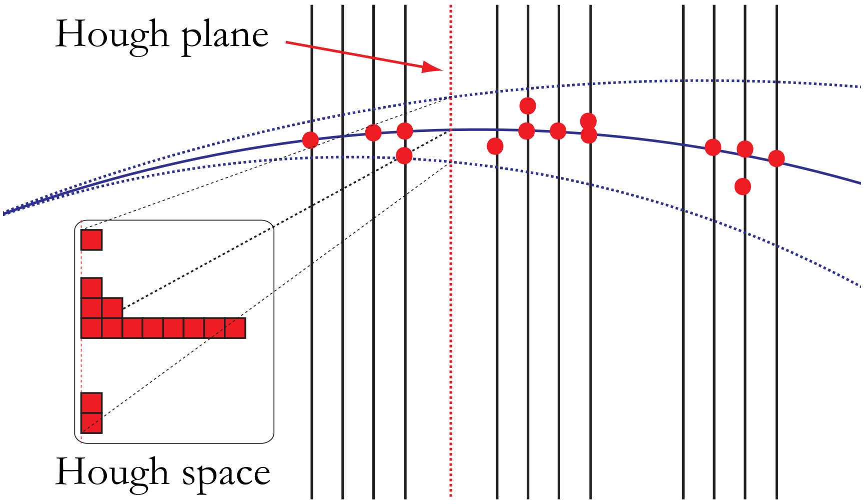

Figure 4.4: The Hough transform is shown as sketch. The extrapolated track is shown in solid blue and the search window in dashed blue. Hits, which are inside the search window, are projected along the extrapolated track onto the Hough space. The hits from the same track will cluster around the extrapolated track position, whereas other hits are randomly distributed. The figure is adapted from ref. [97].

4.2.3.4 TRACK MATCHING

An additional method for long track reconstruction uses track matching. This algorithm uses all standalone T tracks and VELO seeds as input. Both are propagated to the bending plane of the magnet. It uses the fact that the magnetic field is homogeneous enough that the correct track combinations intersect in the focal plane at a fixed z position. The difference in position and slope are used to form a compatibility requirement on the VELO-T station track candidate. As in the forward tracking algorithm the TT hits are added only at the end. More details on the algorithm can be found in [106, 107].

4.2.3.5 Downstream Tracking

The downstream tracking algorithm is similar to the forward tracking algorithm. It starts from tracks in T-stations and adds then information from TT. This fact makes it harder to reconstruct tracks, as the four layers in TT leave not much room for redundancy. No seeds and hits are used, which are already reconstructed as long tracks. More details on the algorithm are in [108].

4.2.3.6 Upstream Tracking

The upstream tracking algorithm is similar to the downstream tracking. Instead of T-station seeds, VELO seeds are used, if they have not been used previously. More details on the algorithm are in [109].

4.2.3.7 Final Track Selection

The track reconstruction starts by building first VELO and T seeds. The reconstruction of long tracks has priority. The forward tracking algorithm and the track matching are reconstructing independently long tracks. Therefore a mechanism has to be in place to avoid saving the same track twice (clones). For this purpose LHCb has an algorithm called *Clone Killer* [110]. If two tracks are detected to be clones of each other, only the track with the most hits assigned is kept. Afterwards the downstream and upstream tracking is performed. As downstream tracks and upstream tracks are shortened long tracks, only hits and seeds are used which are not part of a long track. The output are downstream and upstream tracks, respectively. VELO and T seeds which are not part of either a long, upstream or downstream track, are categorised as type VELO or T track.

4.2.4 Parameter Estimation

In LHCb a Kalman filter [111] is used for fitting the output of the pattern recognition, providing the best estimate of the trajectory and corresponding parameters, like momentum and vertex position. The Kalman filter adds measurements one-by-one to the final fit, and updates each local track state at the current z-position of the corresponding measurement. The method is mathematically equivalent to a least-squares fit, but the iterative approach of the Kalman filter avoids the computationally disadvantageous matrix inversion. In addition, the Kalman filter has the advantage that the full trajectory is known after the fit and not just one point. This is helpful for adding calorimeter clusters, RICH and muon detector information to the track candidate.

Further the Kalman filter provides a natural way to include multiple scattering and other process disturbances. These advantages let the filter to become a common procedure in high energy physics. The Kalman fit procedure has three distinct steps.

- **Prediction:** A prediction of the track state is given by propagating the former state according to eq. (4.6). This step takes multiple scattering into account.
- **Filtering:** This step updates the prediction of the track state with the measurement taken at this position. The updated track state after the filtering is the best estimate of the trajectory using the incorporated measurements.
- **Smoothing:** In the smoothing step, all track states are updated in reverse order using a smoother equation [84, 111]. Afterwards the information of all measurements is taken into account at every track position.

Prediction and filtering are repeated until all measurements from the pattern recognition are taken into account. The Kalman filter is independent of the order in which the measurements are added. In LHCb the results are added in the upstream direction.

4.3 VELOTT-FORWARD PATTERN RECOGNITION

The current trigger system has to reduce the collision rate down to the readout rate of 1 MHz. This reduction step, performed by the level-0 trigger (see section 3.2.4), causes the largest inefficiency of the trigger system and limits the sensitivity to low-momentum signatures. One of the main goals of the LHCb upgrade project is to remove this bottleneck with a trigger-less readout and a full software trigger [112–114]. The upgrade is planned to take place at the end of Run II (see section 3.1.3 for the definition of run periods). A full software trigger offers flexibility in designing selections and allows efficient triggering on low-momentum signatures. Both are necessary to maximise the possibility for discovering New Physics and let LHCb become a multi-purpose detector in the forward direction. The software trigger should be as close as possible to the full reconstruction, as an implication, the run time of the track reconstruction needs to be improved.

For this purpose a new reconstruction chain for long tracks [115] was developed including upstream reconstruction as an intermediate step. The upstream reconstruction is a further development of the upstream tracking algorithm of the reconstruction chain in Run I. The new reconstruction chain for long tracks of the upgrade [116] is adapted for Run II. The algorithm for Run

II, hereinafter VeloTT-Forward chain, is explained in more details in [117]. In the following a short summary is given.

4.3.1 VeloTT-Forward Algorithm

Similar as the forward algorithm described in section 4.2.3.3, VELO seeds are used as input. These seeds are extrapolated linearly to the z position in the centre of TT. Seeds outside of the TT acceptance are not considered. For extrapolated seeds inside the TT hole, with a radius of 40 mm, no VELO-TT combination is done.

A search window in x is defined based on a minimum momentum requirement. The value of the requirement comes from either a minimum p or p_{T} requirement, depending which one gives the largest value for the track in question. The minimum p is defined as zero, whereas $p_{\mathrm{T}} = 0.1\,\mathrm{GeV}/c$ is convert into a p value by using the polar angle of the VELO seed ($\theta = \sqrt{t_x^2 + t_y^2}$). The resulting requirement is used to calculated the expected deviation in x at the TT, which becomes the search window.

In every layer of TT the hits are sorted by their x position at $y = 0$. A binary search on each layer is used to find the first hit inside the search window. The hits are then looped over until the next hit lies outside the search window in x. The x position in the stereo layers is calculated using the y position of the extrapolated VELO seed. Hits inside the search windows in x and in y, are stored.

Clusters of TT hits inside the search window are built with an iterative procedure. Figure 4.5 shows a schematic overview of the clustering. In a first step a doublet is formed by taking one hit in the first and one in the second layer of the first station of TT. If the difference between the x-slope of the doublet and the x-slope of the VELO seed is below a threshold (typically 0.02), it is linearly extrapolated to the third layer where a tolerance window is opened. Triplets are formed, if there are hits within the window. Furthermore for each triplet the doublet is extrapolated to the fourth layer where a reduced search window is opened. Quadruplets are formed from the compatible hits, together with the corresponding triplet. Compatible hits are formed together with the corresponding triplet to quadruplets. If no quadruplets are found from any of the triplets, the doublets are extrapolated directly to the fourth layer to find triplets. This is repeated for all doublet combinations. To account for missing hits in TT, the clustering sequence is run in reverse order if no quadruplets were found. In this case the doublets are built by one hit in the third and fourth layer, respectively. The hits from each TT cluster are combined with the corresponding VELO seed to VeloTT track candidate. This results in several candidates with the same VELO seed. Track candidates with triplets are rejected if a track candidate with a quadruplet with the same VELO seed existed.

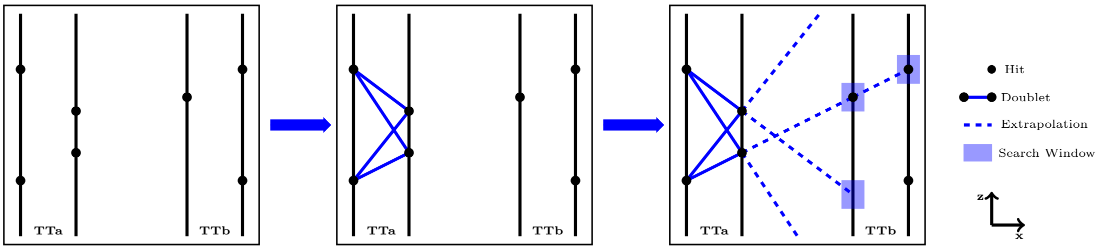

Figure 4.5: A schematic view of the clustering of TT hit candidates. Doublets in the first two layers are formed and then extrapolated linearly to the third and fourth layers to form triplets and quadruplets. Figure is adapted from [117].

For each VeloTT candidate a straight line is fitted with a simple χ^2 fit to the TT hits, as the deflection by the small magnetic fringe field inside TT can be neglected. The track candidate for one VELO seed with the lowest χ^2 is considered as the best track candidate and written out to the VeloTT output for further processing. Each final candidate consists of an additional track state at TT with a p estimated by the p-Kick method[84].

The VeloTT track candidate is then used as input for the Forward algorithm, which was introduced earlier (section 4.2.3.3). VELO seeds are only used as input to the forward algorithm to prevent inefficiency, if their extrapolation falls into the acceptance of the TT hole. The acceptance has the shape of an annulus with inner radius of 33 mm and outer radius of 40 mm. The inner radius is a backward projection of the inner hole of the T-stations and the outer radius is the radius of the TT hole. The information of the momentum and charge of the VeloTT track results in a smaller search window in the T stations than with just the information of VELO and thus leads to a significantly reduced execution time and ghost-rate of the forward algorithm. The ghost-rate is defined as

$$\text{Ghost rate} = \frac{N_{\text{ghost tracks}}}{N_{\text{tracks}}}, \tag{4.8}$$

where ghost tracks are tracks with no matching real particle.

4.3.2 PERFORMANCE

The performance of the new upstream algorithm (VeloTT) and the new long track algorithm (VeloTT-Forward) was studied with a sample of 60k simulated $B^0 \to K^{*0}\mu^+\mu^-$ events at a centre of mass energy of 13 TeV, 25 ns bunch spacing and the visible interaction in pp collisions per bunch crossing, $\mu_{vis} = 1.9$. In the following the performance is studied in terms of track reconstruction efficiencies, ghost-rates and execution times of the algorithms. The track reconstruction efficiency is defined as:

$$\varepsilon_{rec} = \frac{N_{\text{reconstructible and reconstructed}}}{N_{\text{reconstructible}}}. \tag{4.9}$$

Where the following definitions of reconstructible and reconstructed are used (adapted from [117]):

- A particle is reconstructible as VELO track if there are hits associated to it in at least three r and three φ VELO sensors.
- A particle is reconstructible as an upstream track if it is reconstructible as a VELO track and has at least one hit in each of the TT stations.
- A particle is reconstructible as a T track if it has at least one x and one stereo hit associated to it in each of the three T stations.
- A particle is reconstructible as a long track if it fulfils the requirements to be reconstructible in both the VELO sub-detector and the T stations.
- A particle is considered reconstructed as a long track if at least 70% of both the VELO and T station hits on a track are associated to it and the track has no more than one wrongly associated TT hit.
- A particle is considered reconstructed as a upstream track, if it is reconstructible as a long track, has been correctly reconstructed in the VELO and has a matched TT hit in at least three TT layers.

This categorisation is only possible using generator level information available in simulated samples. Furthermore, additional requirements are made to the numerator and the denominator in eq. (4.9) (adapted from [117]) to ensure that the tracks are inside the LHCb acceptance and belonging to the correct decay.

- The particle is required not to be an electron.
- The particle is required to be a daughter from a b-hadron.
- The pseudo-rapidity of the particle must lie between 2 and 5.
- The particle must have $p_{\mathrm{T}} > 0.5\,\mathrm{GeV}/c$.

In case of the ghost-rate, the last two requirements are applied to the numerator and denominator in eq. (4.8) as well.

4.3.2.1 UPSTREAM ALGORITHM

Table 4.1 shows the reconstruction efficiency, ghost-rate and execution time of the upstream algorithms for Run I (upstream-one) and for Run II (upstream-two). The track reconstruction efficiency is shown in fig. 4.6 as function of p, p_{T} and η. The ghost-rate is shown in fig. 4.7 as function of p, p_{T} and η. The upstream-two algorithm shows large improvements in execution time and efficiency, where the latter is most prominent at high p and high η. The new efficiency of upstream-two has a small drop at low p and is constant for $p > 5\,\mathrm{GeV}/c$, while upstream-one has as well the drop off at low p but an additional fall off to higher p, since tracks do not leave a signal in TT due to the beam-pipe hole. The dip in efficiency at $\eta = 3.4$ or 67 mrad is a result of a support structure in the RICH1. The second dip in efficiency starting at $\eta = 4$ is induced by the beam-pipe hole in TT. There is a slightly higher ghost-rate for the new implementation, but it is not problematic as ghost tracks can be further reduced during offline analysis. The structure above $\eta = 4$ in the ghost-rate is induced by the treatment of the beam-pipe hole of TT in the algorithm.

Table 4.1: The performances of upstream-one and upstream-two in terms of track reconstruction efficiency, ghost-rate and execution time [117]. The uncertainties on the efficiency numbers are purely statistical.

	Efficiency (%)	**Ghost rate (%)**	**Timing (ms)**
upstream-one	92.74 ± 0.06	7.21 ± 0.02	32.5
upstream-two	97.77 ± 0.03	11.60 ± 0.03	0.50

4.3.2.2 FORWARD ALGORITHM

Table 4.2 shows the reconstruction efficiency, ghost-rate and execution time of the Forward algorithm taking VELO or VeloTT tracks as input (Velo-Forward and VeloTT-Forward). Figure 4.8 and fig. 4.9 show the reconstruction efficiency and the ghost-rate as function of p, p_{T} and η. The ghost-rate and execution time is drastically reduced by using VeloTT tracks as input of the Forward algorithm with the small cost of a reduced track reconstruction efficiency by about 4%. However, this loss in efficiency can be retrieved in a later stage of the software trigger [118]. The structure in the η distribution of the efficiency is mirroring the performance of the upstream-two algorithm, as discussed in section 4.3.2.1. The ghost-rate is rising at $\eta = 4.4$, which is an effect of the treatment of the beam-pipe hole in the TT and IT. In addition, the ghost-rate gets similar above $\eta = 4.8$ for Velo-Forward and VeloTT-Forward, which is an effect of the pass through of VELO tracks inside the TT beam-pipe hole.

Table 4.2: The performances of the Forward algorithm using VELO or VeloTT tracks as input in terms of track reconstruction efficiency, ghost-rate and execution time is shown [117]. The uncertainties on the efficiency numbers are purely statistical.

	Efficiency (%)	**Ghost rate (%)**	**Upstream-two (ms)**	**Forward (ms)**
VELO-Forward	93.15 ± 0.05	46.86 ± 0.04	-	13.71
VeloTT-Forward	89.23 ± 0.07	17.13 ± 0.03	0.50	4.08

4.3.3 IMPLICATION

The new reconstruction chain for long tracks, VeloTT-Forward, fulfils the requirements in execution time and performance in efficiency and ghost-rate to be included in the first stage of the software trigger. The execution time and ghost-rate of the Forward algorithm are significantly reduced due to the smaller search windows opened on the p_T estimation of the VeloTT track. The usage of the VeloTT tracks in the first stage of the software trigger in Run II gives the possibility to loosen cuts that have been imposed in Run I to control the trigger rate. The impact parameter (IP, see fig. 3.12 for the definition) cut requirements on VELO tracks can be removed and the p_T threshold of the Forward tracking can be loosen from 1.2 GeV/c to 0.5 GeV/c. As a result, the signal efficiency for charm physics increased dramatically by a factor four and for the first time lifetime unbiased triggers for hadronic final states could be implemented in the LHCb trigger [117].

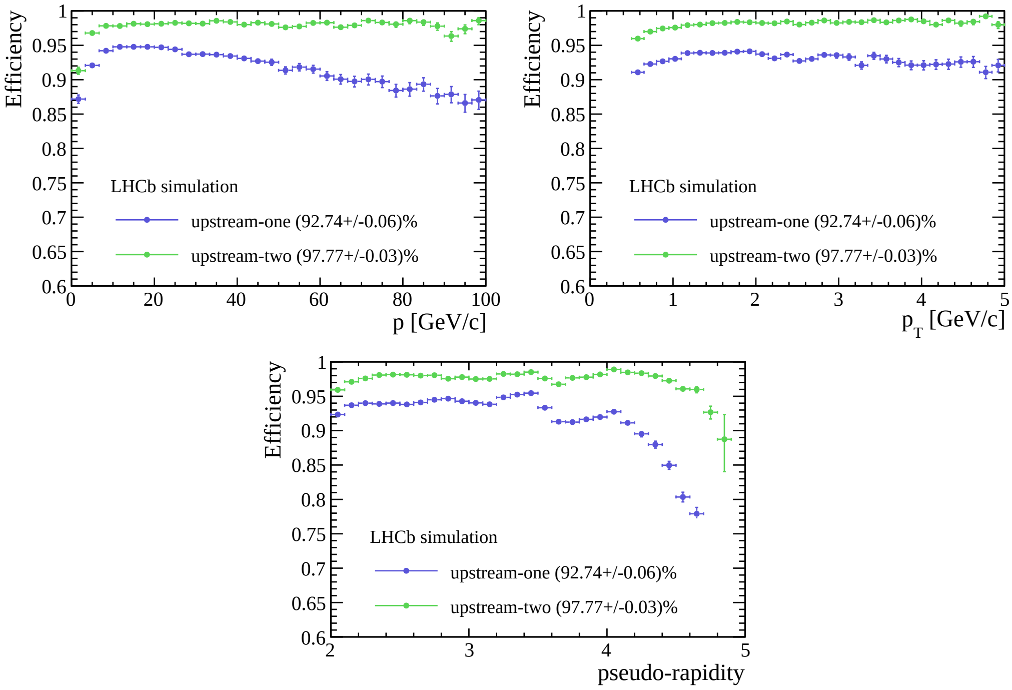

Figure 4.6: The track reconstruction efficiency of the VeloTT algorithms for Run I and Run II as a function of p, p_{T} and η.

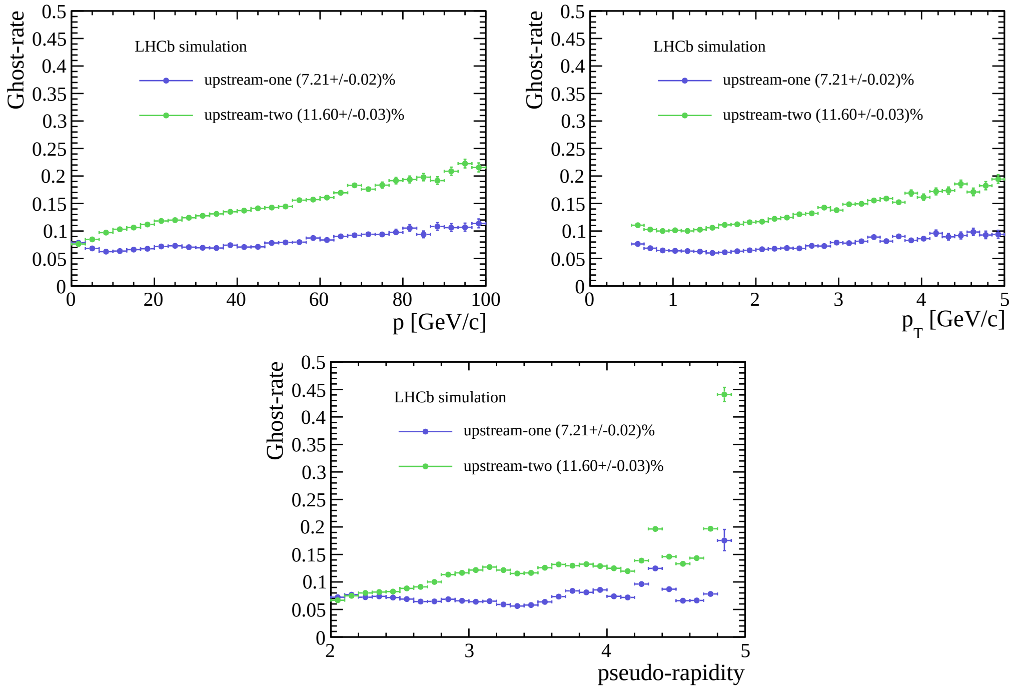

Figure 4.7: The ghost-rate of the VeloTT algorithms for Run I and Run II as a function of p, p_{T} and η.

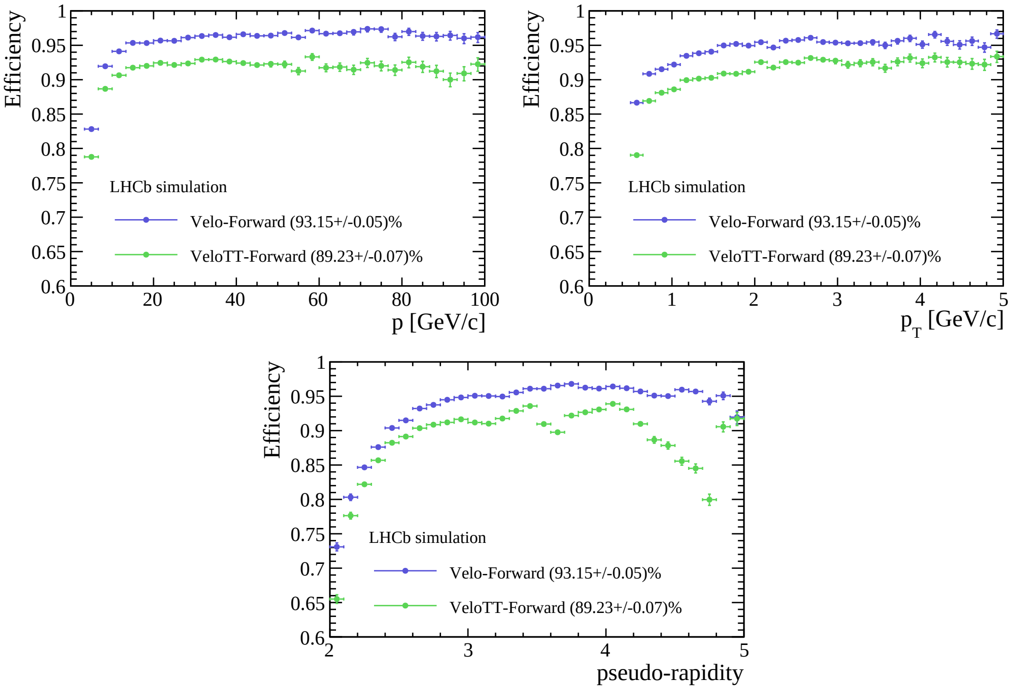

Figure 4.8: The track reconstruction efficiency of the Forward algorithm using VELO or VeloTT tracks as a function of p,p_{T} and η.

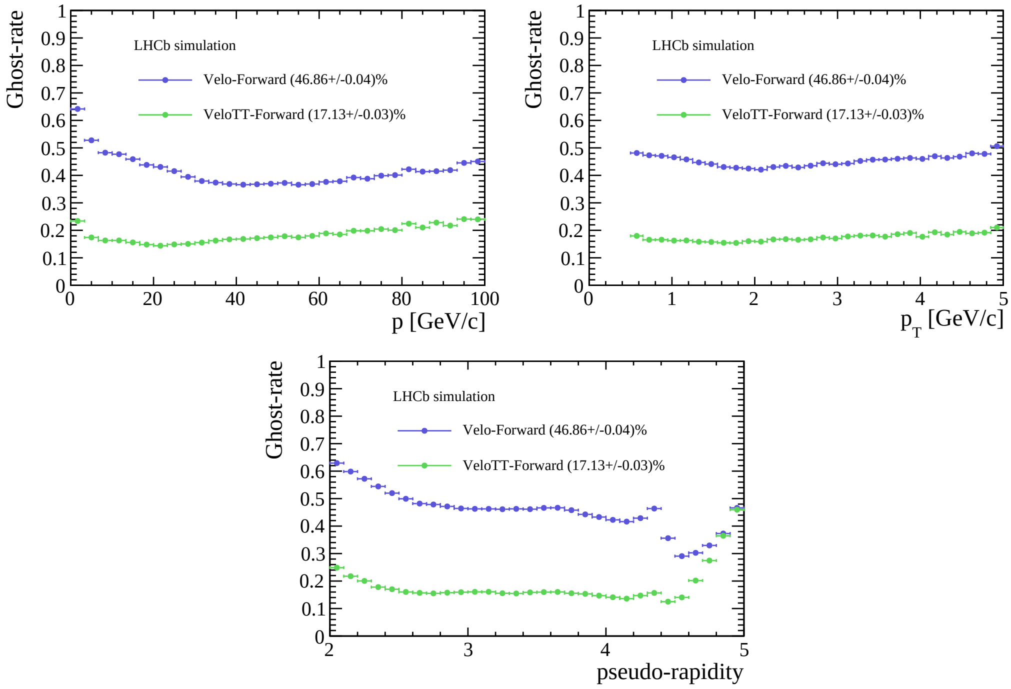

Figure 4.9: The ghost-rate of the Forward algorithms using VELO or VeloTT tracks as a function of p, p_{T} and η.

4.4 Validation on Data

The reconstruction efficiency shown in table 4.2 is based on simulated events. Before the algorithm can be used in the official reconstruction chain, the performance of the algorithm has to be verified on data. For this purpose a tag-and-probe technique similar as in Ref.[119] is used. This section briefly describes the method, the data sample obtained in 2011 at centre of mass energy of 7 TeV and the result of the verification.

4.4.1 Tag-and-Probe Method

There are several ways to measure the tracking efficiency on data. One method is to check for the presence of a track using a sub-detector, which was not used in the normal track reconstruction procedure. The efficiency can then be calculated by the ratio of those tracks with the tracking sequence of interest applied versus all of the tracks.

A possible way in practice (tag-and-probe method) is, to use resonances with a large branching fraction to two-prong decays. One track is required to be fully reconstructed and called *tag-track*, the other track is partially reconstructed without using the detector parts of interest and called *probe-track*. The second track needs to carry enough information to allow to reconstruct the invariant mass of the combination of tag- and probe-track with sufficiently high resolution. The invariant mass distribution is used to reject background events. Afterwards, the tracking efficiency is derived from the ratio of probe tracks containing the relevant detector information and all probe tracks.

In case of the VeloTT-Forward algorithm, it is not possible to measure the efficiency directly, as not enough independent sub-detectors are left to have a sufficiently high resolution in the invariant mass. Instead the efficiency loss between both chains of interest, Velo-Forward and VeloTT-Forward, is derived using the formula:

$$\text{efficiency loss} = \left(1 - \frac{N_{\text{VeloTT-Forward}}}{N_{\text{Velo-Forward}}}\right) \tag{4.10}$$

where $N_{\text{VeloTT-Forward}}$ ($N_{\text{Velo-Forward}}$) corresponds to the number of candidates found using the VeloTT-Forward (Velo-Forward) chain.

4.4.2 DATA SAMPLES

The two-prong decay $J/\psi \to \mu^+\mu^-$ is used for the validation on data. In a first step, the efficiency loss as determined was verified using generator information on simulation using a sample of 600k simulated $J/\psi \to X\mu^+\mu^-$ events with a centre of mass energy of 7 TeV, $\mu_{vis} = 2.5$ and 50 ns bunch spacing. In a second step the efficiency loss was determined from data using a sample of 130k events from 2011 at 7 TeV and compared to simulation.

The track of the tag muon candidate has to be a fully reconstructed track identified as muon and must have a transverse momentum p_{T} above 500 MeV/c. The track of the probe muon candidate is only partially reconstructed as VELO-Forward or as VeloTT-Forward track. In both cases, the reconstruction does not include the assignment of particle identification information from the RICH, calorimeter and muon system, to avoid inefficiencies from other detector parts than those of interest. Instead the track of the probe muon candidate has to fulfil similar requirements as for the performance measurement in section 4.3.2. The probe track must have a p_{T} above 500 MeV/c and a p above 3 GeV/c and the pseudo-rapidity η must lie between 2 and 5. The selection conditions for the track of the tag and probe muon candidate are summarised in table 4.3. Further, it is required that the two tracks from the J/ψ come from a common vertex by requiring a χ^2 minimum distance (DOCA χ^2) between the two daughter tracks below 20. The invariant mass of the combination of tag and probe muon has to lie within 80 MeV/c^2 of the known mass of J/ψ [16], and the χ^2 of the vertex fit of the J/ψ candidate has to be smaller than 16.

Table 4.3: Selection conditions on the muon track for tag and probe. Where η is the pseudo-rapidity of the track.

Tag	**Probe**
$p_{\mathrm{T}} > 500\,\mathrm{MeV}/c$	$p_{\mathrm{T}} > 500\,\mathrm{MeV}/c$
PIDmu>0	$p > 3\,\mathrm{GeV}/c$
-	$2 < \eta < 5$
DOCA $\chi^2 < 20$	DOCA $\chi^2 < 20$
Combination	
vertex fit χ^2 < 16	
$\lvert M_{\mu\mu} - PDG_{J/\psi}\rvert < 80\,\mathrm{MeV}/c^2$	

4.4.3 RESULTS

An unbinned extended maximum likelihood fit is applied for extracting the number of signal candidates. The fit model uses a sum of two Crystal Ball [120] functions with same mean and tail parameters for the signal. The background is parametrised as a straight line. The tail parameters for the Crystal Ball were fixed to the values extracted from the fit to the J/ψ signal distribution in simulation, where both muons were fully reconstructed.

Figure 4.10 shows the fit of the simulation for both chains, Velo-Forward and VeloTT-Forward and fig. 4.11 the fit of the measured data for both chains. The extracted numbers of signal candidates together with their resulting efficiency loss are summarised in table 4.4. Furthermore, the two values for the efficiency loss are compared to the efficiency loss obtained on the $J/\psi \to \mu^+\mu^-$ simulation dataset by using the same method as for the performance measurement in section 4.3.2. The uncertainties from the tag-and-probe method are obtained from the fit and are only statistical.

Table 4.4: Results obtained using generator information available in simulation and using the tag-and-probe method in simulation and data. The uncertainties are only statistical.

	Simulation		**Data**
	$J/\psi \to \mu^+\mu^-$ **(%)**	**tag-and-probe**	**tag-and-probe**
Velo-Forward	98.20 ± 0.02	594509 ± 1395	121533 ± 809
VeloTT-Forward	95.00 ± 0.03	573459 ± 1352	116915 ± 773
Efficiency Loss	3.26 ± 0.03	$(3.5 \pm 0.3)\%$	$(3.8 \pm 0.9)\%$

The efficiency loss for the tag-and-probe method is compatible on data and simulation, as expected. Furthermore, the efficiency loss with the tag-and-probe method is consistent with the efficiency loss determined from the true efficiencies measured in simulation. Therefore, it can be concluded, that the performance numbers in section 4.3.2 extracted in simulation are a reliable estimate of the performance on data.

However, the efficiency numbers in table 4.4 can not be directly compared to the numbers in section 4.3.2. One issue is the larger centre of mass energy in Run II which leads to higher multiplicity events than in Run I. The lower average visible interactions of 1.1 in Run II compared to 1.7 in Run I compensates part of the former effect. As fig. 4.12 shows, a higher multiplicity in an event leads to a lower tracking efficiency. In addition, the decay properties of the two decays are different. Figure 4.13 shows the comparison of the multiplicity variables for $J/\psi \to \mu^+\mu^-$

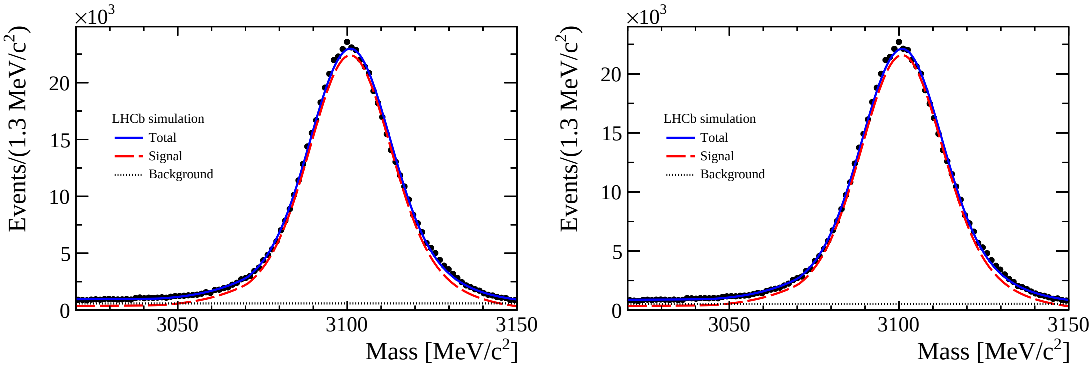

Figure 4.10: Invariant mass of the reconstructed $J/\psi \to \mu^+\mu^-$ with the tag-and-probe method on simulation. On the left (right) the distribution for Velo-Forward (VeloTT-Forward) is shown. The long dashed line in red shows the signal, the short dashed line in black shows the background and the straight line shows the combination in blue.

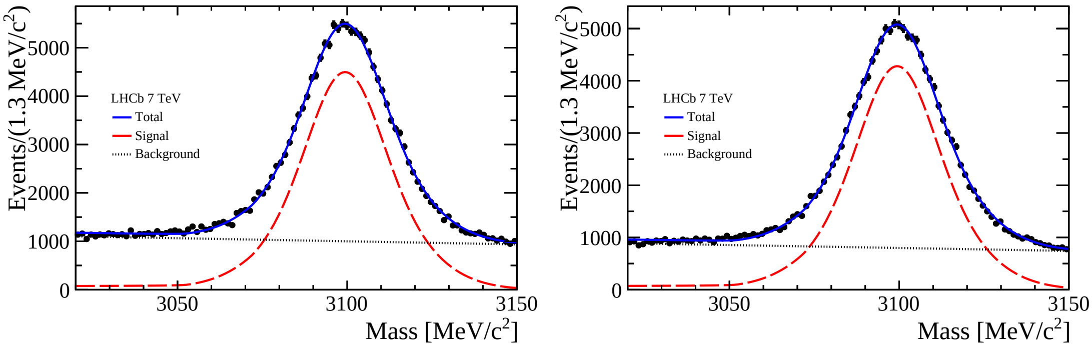

Figure 4.11: Invariant mass of the reconstructed $J/\psi \to \mu^+\mu^-$ with the tag-and-probe method on measured data. On the left (right) the distribution for Velo-Forward (VeloTT-Forward) is shown. The long dashed line in red shows the signal, the short dashed line in black shows the background and the straight line shows the combination in blue.

and $B^0 \to K^{*0}J/\psi$ with $J/\psi \to \mu^+\mu^-$. The latter is a resonant background of $B^0 \to K^{*0}\mu^+\mu^-$ with the same event properties but with larger statistics. Candidates of $B^0 \to K^{*0}J/\psi$ tend to have larger multiplicity than $J/\psi \to \mu^+\mu^-$ candidates and are therefore expected to have a slight reduced efficiency. Furthermore, $B^0 \to K^{*0}\mu^+\mu^-$ decays probe a different kinematic region than $J/\psi \to \mu^+\mu^-$ decays. Figure 4.14 shows the comparison of the true p and p_{T} between particles originating from $J/\psi \to \mu^+\mu^-$ and $B^0 \to K^{*0}\mu^+\mu^-$ decays. Particles in $J/\psi \to \mu^+\mu^-$ tend to have a momentum higher than 12 GeV/c and transverse momentum higher than 1 GeV/c where the efficiency is high (see fig. 4.8), whereas the opposite is the case for particles from $B^0 \to K^{*0}\mu^+\mu^-$. It is therefore understood that the performance for $J/\psi \to \mu^+\mu^-$ is larger then for $B^0 \to K^{*0}\mu^+\mu^-$ in the order of a few percent.

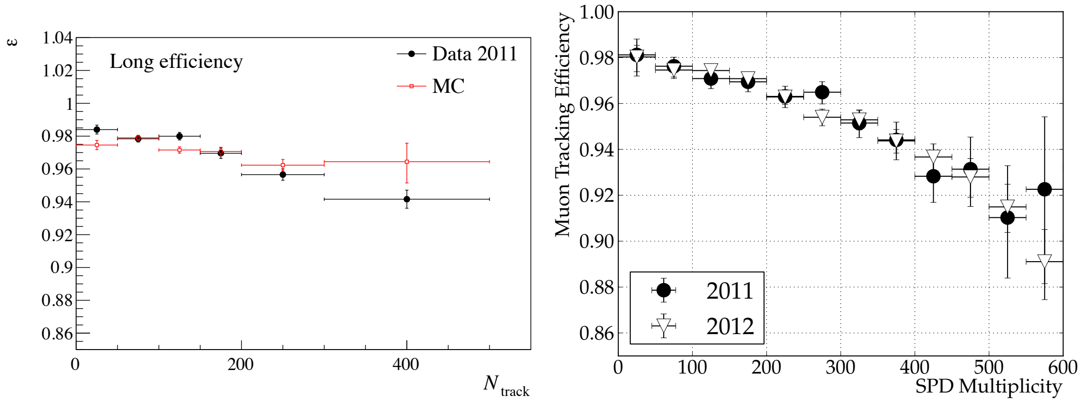

Figure 4.12: The track reconstruction efficiency for 2011 data and simulation as function of the track multiplicity N_{track} is shown left [97]. The track reconstruction efficiency as function of the SPD multiplicity for 2011 and 2012 data for high p_{T} tracks is shown right [42].

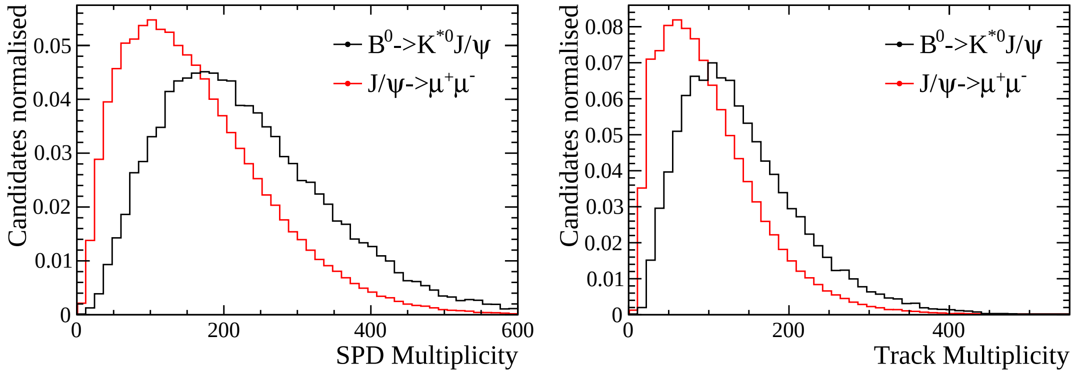

Figure 4.13: The track multiplicity (left) and the SPD multiplicity (right) of the decay $B^0 \to K^{*0}J/\psi$ and $J/\psi \to \mu^+\mu^-$ are shown. Both sample are simulated, but the first one with 2012 and the second one with 2011 run conditions.

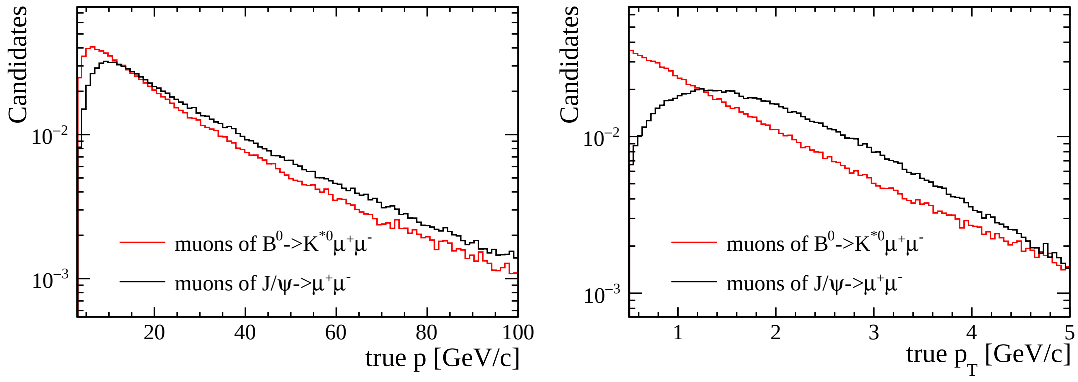

Figure 4.14: The comparison of the true momentum p, true transverse momentum p_{T} and true pseudorapidity for $B^0 \to K^{*0}\mu^+\mu^-$ and $J/\psi \to \mu^+\mu^-$.

If I could remember the names of all these particles, I'd be a botanist.

Enrico Fermi

5

Particle Identification

The physics program of LHCb involves precision measurements of *CP* violation and rare decays. These measurements include the study of baryons, beauty and charm mesons, reconstructed in many final states like hadronic, (semi-)leptonic or radiative. Achieving the goal of LHCb is not possible without an extensive particle identification (PID) system.

In the following, the methods to extract the PID information of the individual detectors is discussed first, followed by the description of the methods to combine the individual PID information. Finally, a method to correct the poorly modelled PID response in simulation is presented. The method was implemented and tested by myself with the help of Andrea Contu and Prof. Nicola Serra in terms of coding and developing the idea, respectively.

5.1 PARTICLE IDENTIFICATION IN LHCB

Four detector elements in LHCb provide PID. These are two RICH detectors, the calorimeter system and the muon detector. Charged hadrons are primarily identified using information from the RICH detectors. Electrons and positrons are mainly identified by the calorimeter system and muons by the muon detectors. Neutral particles like photons or π^0, are identified using the Calorimeter system. In the following, the performance of each PID sub-system is described in detail.

5.1.1 Particle Identification Based on the Calorimeter System

5.1.1.1 Electron Identification

Electrons and positrons are identified using information derived from the ECAL, the PS and the HCAL. The combination of the different sources of information is based on signal and background likelihood distributions constructed for each sub-detector. Whereas the likelihood distributions are based on the energy deposit in the corresponding sub-detector and the matching estimator between a cluster and any track defined for a charged particle. The matching estimator is defined as a χ^2 metric:

$$\chi^2_{\text{2D}} = (\vec{r_{\text{tr}}} - \vec{r_{\text{cl}}})^T \left(\mathcal{C}_{\text{tr}} - \mathcal{S}_{\text{cl}}\right) (\vec{r_{\text{tr}}} - \vec{r_{\text{cl}}}) \tag{5.1}$$

where $\vec{r_{\text{tr}}}$ and $\vec{r_{\text{cl}}}$ represent the local coordinates of tracks and clusters, respectively, at the average energy-weighted position of clusters in z, which is corrected assuming logarithmic energy dependence. The $\mathcal{C}_{\text{tr}}$ is the covariance matrix of $\vec{r_{\text{tr}}}$ and $\mathcal{S}_{\text{cl}}$ is the cluster energy spread matrix. A cluster of a neutral particle is considered to be isolated for larger χ^2. For each sub-detector, the log-likelihood difference for the electron and hadron hypothesis is computed $\Delta \log \mathcal{L}(e-h)$, where

$$\Delta \log \mathcal{L}(e-h) = \log \mathcal{L}(e) - \log \mathcal{L}(h) = \log \left(\frac{\mathcal{L}(e)}{\mathcal{L}(h)} \right). \tag{5.2}$$

The combination of all three estimators is done by taking the sum of the individual estimators [78]:

$$\Delta \log \mathcal{L}^{CALO}(e-h) = \Delta \log \mathcal{L}^{ECAL}(e-h) + \Delta \log \mathcal{L}^{HCAL}(e-h) + \Delta \log \mathcal{L}^{PS}(e-h). \tag{5.3}$$

The combined electron identification efficiency versus the misidentification rate is shown in fig. 5.1.

5.1.1.2 Photon Identification

At LHCb, converted and non-converted photons are treated separately. Photons converted before the magnet are reconstructed from electron-positron tracks. Both, the electron and positron, are selected according to the electron PID variables, a minimum p_{T} value and an E/p value within the appropriate range. The algorithm only combines electron-positron pairs which are close in the vertical direction (3-200 mm). The pairs are selected according to their p_{T}, their di-electron mass

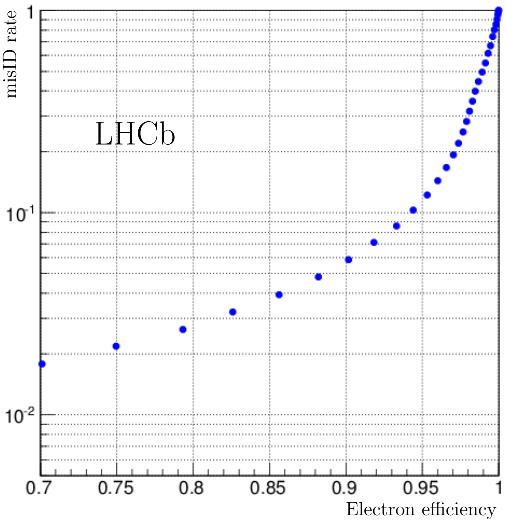

Figure 5.1: Electron identification efficiency versus misidentification rate evaluated using data recorded in 2011 [78].

and their reconstructed vertex position. In addition, a Bremsstrahlung algorithm is used to recalculated the electron energy including the Bremsstrahlung photons measured by the calorimeters.

For non-converted photons, the identification is done by computing a photon hypothesis likelihood based on signal and background probability density functions. These are based on several variables, the PS energy deposit in front of the ECAL cluster cells, the matching estimator between the cluster and any track defined for a charged particle, and the ratio between the energy of the central cell of the ECAL cluster and the total ECAL energy. For the identification of the non-converted photons, the difference in log-likelihood between the photon and the background hypotheses $\Delta \log \mathcal{L}(\gamma - Background)$ is calculated. Figure 5.2 (left) shows the performance of the photon estimator for converted and non-converted photons, as well as the combination of both in terms of purity and efficiency obtained for candidates with $p_{\mathrm{T}} > 200\,\mathrm{MeV}/c$. The best performance is achieved for non-converted photons.

Neutral pions decaying into two photons with low transverse energy, E_{T} are reconstructed as two well separated photons. At higher E_{T} (typically E_{T} >2 GeV), a π^0 candidate can be misidentified as a photon, if both final state photons cannot be separated as a pair of clusters inside the calorimeter granularity. To avoid misidentification of π^0 and photons, the difference in the distribution of the expected energy deposit of a photon with respect to a π^0 is used. This difference is evaluated with a neural network classifier trained with photons from a simulated $B^0 \to K^{*0}\gamma$ sample as signal

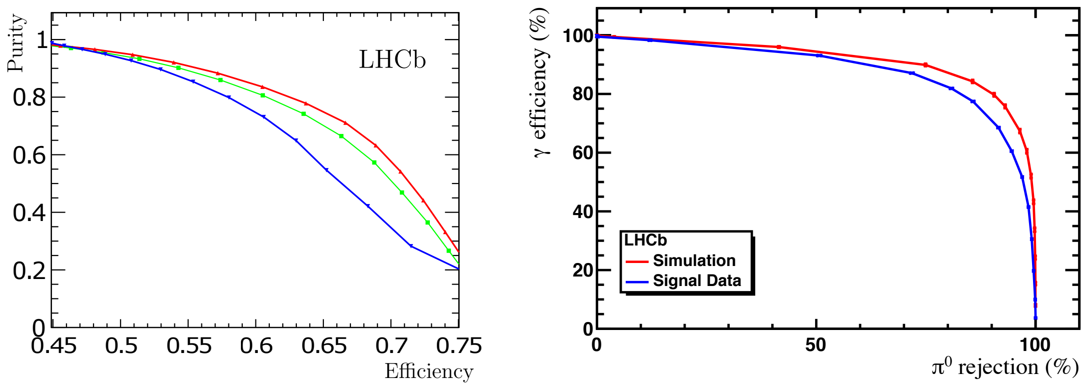

Figure 5.2: Left: Performance of the photon identification for candidates with $p_{\mathrm{T}} > 200\,\mathrm{MeV}/c$. Purity as function of efficiency for the full photon calibration sample (green), the converted candidates (blue) and the non-converted candidates (red). Right: Photon identification efficiency as a function of π^0 rejection efficiency for the $\gamma - \pi^0$ separation tool for simulation, the red curve, and data, the blue curve[78].

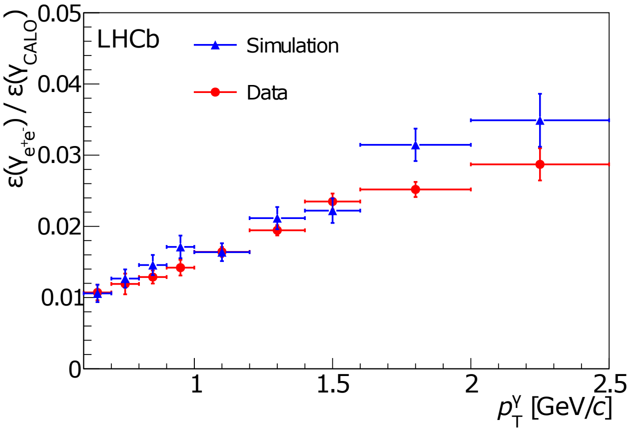

Figure 5.3: Ratio of photon detection efficiencies, converted ($\gamma \rightarrow e^+e^-$) divided by non-converted (γ_{CALO}), from the decay of π^0 mesons in data (red) and simulation (blue) [78].

and π^0 mesons from a mixture of B decays as background. The π^0 are reconstructed and selected as photons with the same preselection as it was used for the signal sample. The identification reaches a photon identification efficiency of 95% while rejecting 45% of the merged π^0 mesons background that are reconstructed as photons. Figure 5.2 (right) shows the photon identification efficiency as function of the π^0 rejection efficiency for simulation and data.

The ratio of photon detection efficiency between converted and non-converted photons from the decay of π^0 mesons is shown for simulation and data in fig. 5.3. The photon detection efficiency is well reproduced in simulation, implying a good description of the the detector material and also good performances of the reconstruction algorithms for photons, electrons and π^0. Additional information are given in ref. [78, 89, 121].

5.1.2 Particle Identification Based on the RICH

The primary role of the RICH is to identify charged hadrons, π, K, p, in addition it can be used also for the identification of charged leptons (see section 5.2). For the determination of the particle species, the Cherenkov angle is combined with the track momentum, measured by the tracking system (as described in chapter 4), for each track.

The RICH detectors operate in a high occupancy environment, which leads to overlapping Cherenkov cones. For the efficient reconstruction of such events, an overall event log-likelihood algorithm has to be used for the combination of track information and Cherenkov angle. This algorithm includes all tracks in the event and considers both RICH detectors simultaneously for an optimal treatment of tracks where Cherenkov cones overlap.

As most particles produced in pp collisions are pions, the log-likelihood algorithm starts with the pion hypothesis for all tracks. The overall likelihood is calculated for this set of hypotheses using the distribution of photon hits, the associated tracks and their errors. Afterwards, the likelihood is recomputed changing the mass hypothesis to e, μ, K and p for each track in turn, whereas the other hypotheses are unchanged. The change with the largest increase in the likelihood is used to set a new mass hypothesis for that track. This is repeated until all tracks have been set to their optimal hypothesis. As this procedure is quite CPU intensive, modifications, explained in detail in [88], were made to counter this.

The final results are $\Delta \log \mathcal{L}$'s for each track, where the value corresponds to the change in the log-likelihood when the hypothesis of the track is changed from the pion hypothesis to the electron, muon, kaon or proton hypothesis.

Figure 5.4 shows the identification efficiency and the corresponding misidentification rate as function of the track momentum for the K/π, p/π and p/K separation. They are shown for two different cuts on the $\Delta \log \mathcal{L}$, where the harsher cut is able to reduce the misidentification rate to a minimum by keeping a reasonable high identification efficiency.

Figure 5.5 shows the pion misidentification fraction versus the kaon identification efficiency as function of the track multiplicity and the number of reconstructed primary vertices, where the cut on the $\Delta \log \mathcal{L}$(K-π) is varied. A dependency on the track multiplicity is visible, where higher multiplicity leads to less efficient identification. The same is visible for the number of primary vertices in the event.

5.1.3 Particle Identification Based on the Muon System

The muon identification using the muon system only can be divided in two steps: at first loose binary selection and then a likelihood method. The loose binary selection (IsMuon) of muon candidates is based on the signal in the muon chambers of a particle passing the calorimeters and iron filters. Based on the extrapolated trajectory, hits in the muon stations are associated to a track, if they are within a field of interest. This region is parametrised as a function of track momentum (p) at each station and separately for each muon system region. The parametrisation is determined from simulation. IsMuon is defined according to the number of stations with hits. The number of stations, which are needed to have a muon signal, is a function of p, as shown in table 5.1.

Table 5.1: Muon stations required to trigger the IsMuon decision as a function of momentum range [122].

Momentum range	**Muon stations**
$3\,\mathrm{GeV}/c < p < 6\,\mathrm{GeV}/c$	M2 and M3
$6\,\mathrm{GeV}/c < p < 10\,\mathrm{GeV}/c$	M2 and M3 and (M4 or M5)
$p > 10\,\mathrm{GeV}/c$	M2 and M3 and M4 and M5

The second step is based on the logarithm of the ratio between the likelihoods for the muon and non-muon hypotheses (muDLL). The likelihoods are based on the cumulative probability distributions of the average squared distance significance D^2 of the hits in the muon chamber with respect to the linear extrapolation of the tracks from the tracking system. The D^2 distribution is much narrower, close to zero, for true muons than the other particles that are falsely selected by the IsMuon requirement.

Figure 5.6 shows the muon efficiency and misidentification probabilities to protons, pions and kaons as a function of the particle momentum for IsMuon alone and with additional cuts on muDLL. It is visible in the figures, that the selection cut on muDLL reduces the muon efficiency at low momentum, but significantly reduces the misidentification probability for π, p and K. Additional informations are given in [122].

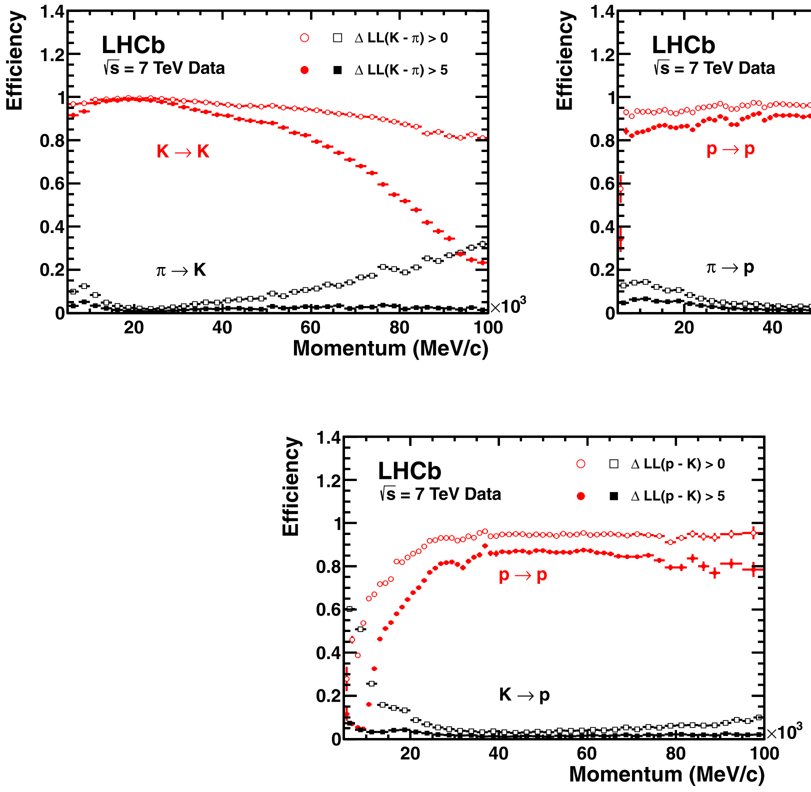

Figure 5.4: RICH identification efficiency and misidentification rate for K/π, p/π and p/K separation measured on data as a function of track momentum. Two different $\Delta\log\mathcal{L}$ requirements are imposed on the samples, resulting in the open and filled marker distributions [88].

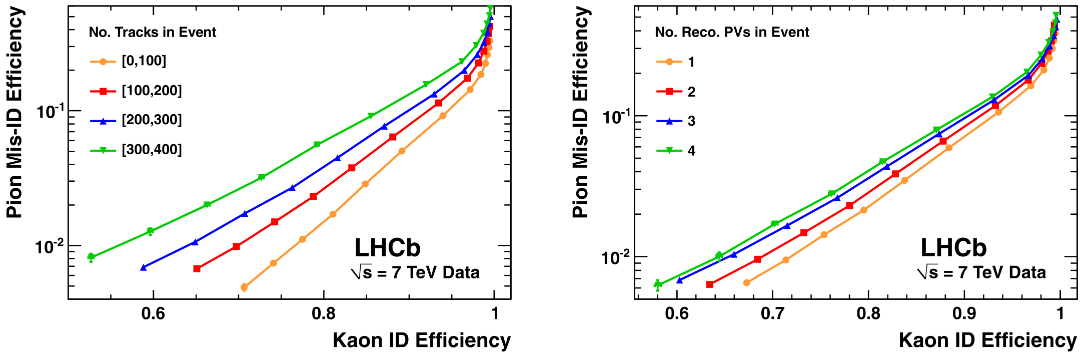

Figure 5.5: Pion misidentification fraction versus kaon identification efficiency as measured in 7 TeV LHCb collisions: (left) as a function of track multiplicity, and (right) as a function of the number of reconstructed primary vertices. The efficiencies are averaged over all particle momenta [88].

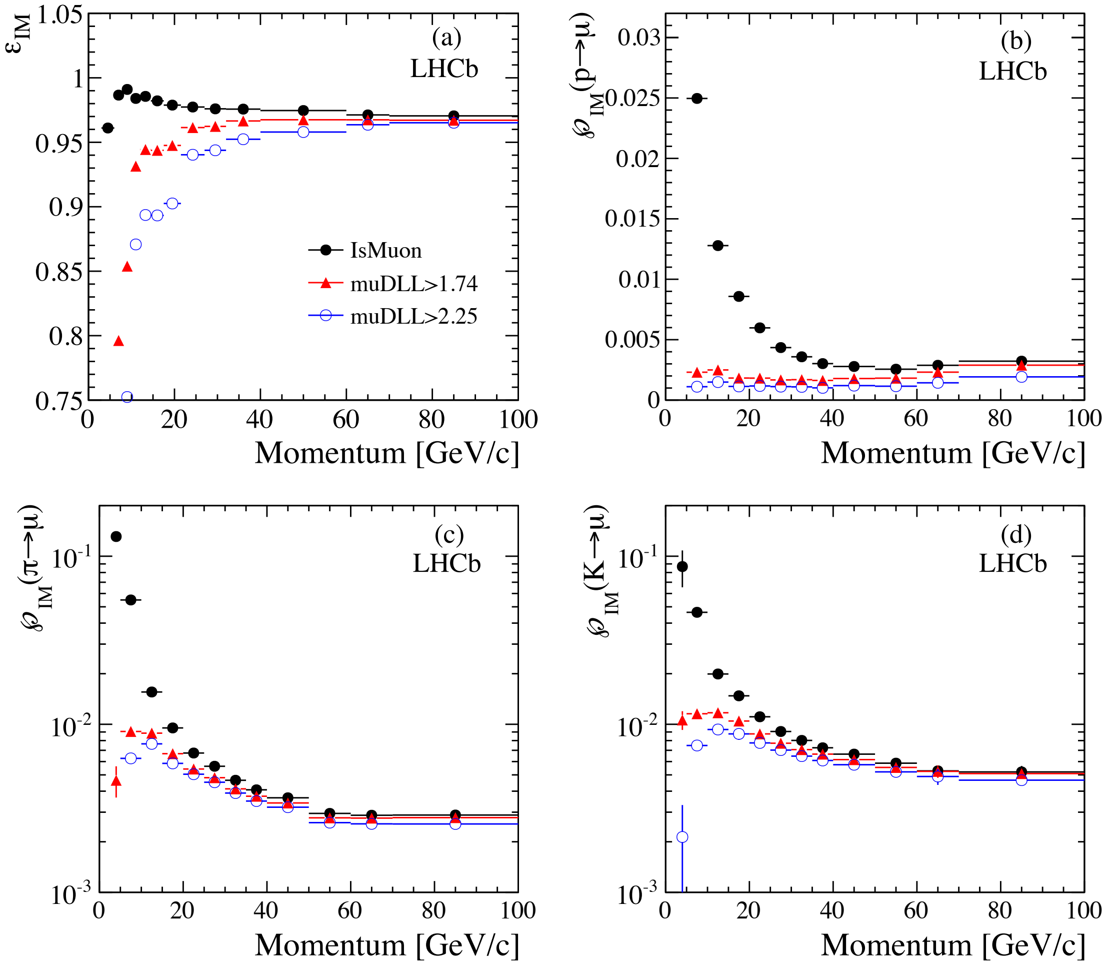

Figure 5.6: Muon efficiency (a) and misidentification probabilities for protons (b), pions (c) and kaons (d) as a function of the particle momentum for the IsMuon requirement alone (black solid circles) and with the additional cuts muDLL$\geq$ 1.74 (red triangles) and muDLL$\geq$ 2.25 (blue circles) [122].

5.2 COMBINATION OF PARTICLE IDENTIFICATION IN LHCB

Each PID system provides information, which is useful for the other PID systems for discriminating background contributions. For example, the RICH system provides some separation between leptons and hadrons, which can be used for the PID in the calorimeter system. Hence, a combined PID information provides a much more powerful set of PID variables. Two different ways of combining these informations exist in LHCb, the likelihood method and a multivariate method [77].

5.2.1 Likelihood Method

The combination of all PID information is in case of the likelihood method straightforward. The various likelihoods from the detectors are simply combined by multiplication:

$$\mathcal{L}_{comb}(e) = \mathcal{L}^{RICH}(e) \cdot \mathcal{L}^{\mathrm{CALO}}(e) \cdot \mathcal{L}^{\mathrm{MUON}}(\mathrm{non}\,\mu) \tag{5.4}$$
$$\mathcal{L}_{comb}(\mu) = \mathcal{L}^{RICH}(\mu) \cdot \mathcal{L}^{\mathrm{CALO}}(\mathrm{non}\,e) \cdot \mathcal{L}^{\mathrm{MUON}}(\mu) \tag{5.5}$$
$$\mathcal{L}_{comb}(h) = \mathcal{L}^{RICH}(h) \cdot \mathcal{L}^{\mathrm{CALO}}(\mathrm{non}\,e) \cdot \mathcal{L}^{\mathrm{MUON}}(\mathrm{non}\,\mu), \tag{5.6}$$

where h stands for hadron. As in the PID algorithm of the RICH, all resulting $\Delta \log \mathcal{L}_{comb}$'s are related to the pion hypothesis. Figure 5.7 shows the electron identification efficiency versus the misidentification rate, where the combined information of all PID elements in LHCb is used. The comparison to fig. 5.1 shows a clear improvement, *e.g.* at $\sim 90\%$ electron efficiency the pion misidentification rate drops from $\sim 6\%$ to $\sim 0.6\%$.[78].

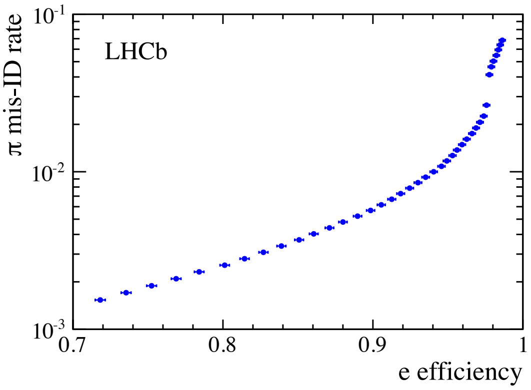

Figure 5.7: The pion misidentification rate versus the electron identification probability is shown when the cut is varied on the combined likelihood difference. It is measured on 8 TeV collision data [78].

5.2.2 Multivariate Method

The likelihood approach has several drawbacks. First of all the approach assumes that all PID information can be represented by a likelihood, and excludes with this assumption information like: sub-detector acceptance flags, number of shared muon hits etc. Second, the sub-detectors have different ranges for their $\Delta \ln \mathcal{L}$ (DLL). As a result the DLLs from the RICH have to be rescaled to match the muon and calorimeter DLL for the combination. In addition the various combined DLLs have different ranges for their values. And as a last point, the DLLs from the RICH can have a spike at DLL$(X - \pi) = 0$, if both, X and π, are below the Cherenkov threshold of the RICH.

A more powerful way of combining the different PID informations is achieved by using a multivariate method with TMVA[123] as framework. In this approach tracking information like fit quality, momentum estimates, track degrees of freedom, charge estimate from the VELO and ghost probability of a track are combined together with the DLLs from the individual systems and as well their acceptance flags and shared hits into a single probability value for each particle type (ProbNNX, where X indicates the particle type). A complete list is given in section A.1. The training of the multivariate classifier is done on inclusive events with a B decay. Figure 5.8 shows the comparison of the performance for the likelihood and multivariate method. The multivariate method performs clearly better as there is a larger area beneath the curve.

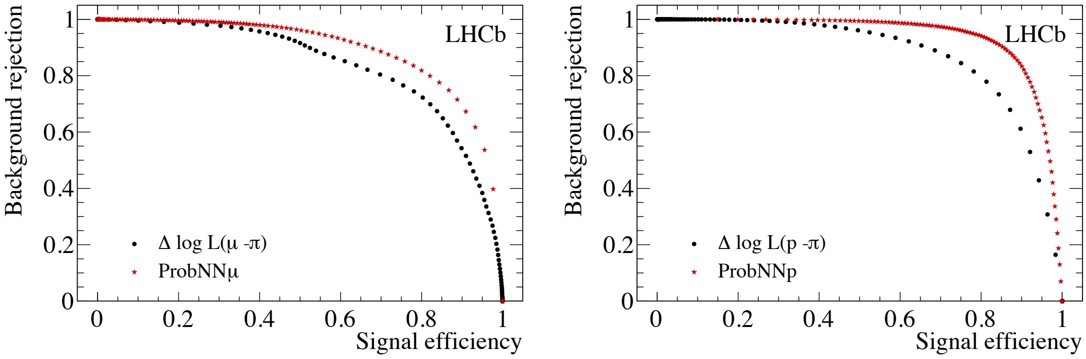

Figure 5.8: Background rejection versus muon (left) and proton (right) identification efficiency is shown, measured in the $\Sigma \to p\mu^+\mu^-$. The variables $\Delta \ln \mathcal{L}(X-\pi)$ indicated in black and the ProbNNX indicated in red, are compared for $5 - 10$ GeV/c muons and $5 - 50$ GeV/c protons, using data sidebands for backgrounds and simulation for the signal. Figures are taken from [78].

5.3 RESAMPLING METHOD

The particle identification variables provided by the two methods are used in many selections to enhance the purity. High energy physics analyses are usually developed on simulation, especially analyses using a multivariate method in the selection are strongly depending on it. The LHCb PID estimator response is known to be poorly modelled in simulation. There are two main reasons, a lower detector occupancy in simulation than in data, which affects the PID efficiency (fig. 5.5), and changing operation conditions. For example, the temperature and pressure in the gas-moderator of the RICH influences the refraction index and therefore the PID response.

As an example fig. 5.9 shows the comparison in simulation and real data of the DLLK response for a kaon in the decay $B^0 \to J/\psi K^{*0}$ with $J/\psi \to \mu^+\mu^-$ and $K^{*0} \to K^+\pi^-$. The exact selection requirements are explained later (section 5.4). In the following a technique is explained, to correct for the differences between simulation and measurement.

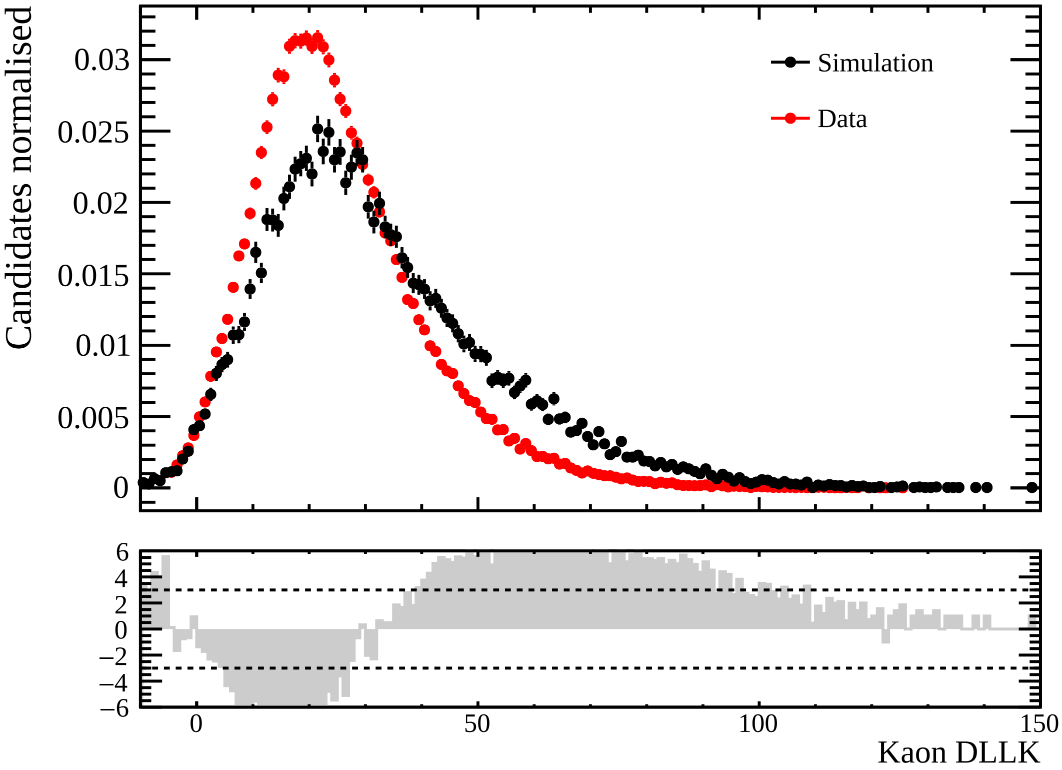

Figure 5.9: The upper figure shows the response of the DLL for a kaon under the mass hypothesis of a kaon. The response for measured data is shown in red, for simulation in black. The lower figure shows the pull between simulation and measurement.

5.3.1 TECHNIQUE

The PID response of the LHCb detector can be characterised by: the particle momentum, the pseudo-rapidity of the particle and the track multiplicity of the event ($p, \eta, ntracks$). The individual DLL of the calorimeter, muon and RICH systems have a strong dependence on the particle momentum. The different granularity of the calorimeter and muon system introduce a dependence on the pseudo-rapidity. And finally the track multiplicity of the event is a measure for the occupancy. A higher occupancy leads to a higher ambiguity in the individual particle identification. Figure 5.5 shows the dependence on the event multiplicity in case of the RICH system.

The basic idea of the resampling technique is to generate a new correct PID response for each particle in a simulated data set, according to the distribution in measured data. This is achieved by using the dependence of the PID response on the particle type and $(p, \eta, ntracks)$.

The implementation is done in two steps using the already available PID calibration datasets and functions of the PIDcalib package of LHCb [124], the available datasets are discussed in section 5.3.2. In a first step the PID distributions are extracted from the calibration data for each particle type in bins of $(p, \eta, ntracks)$. In the second step the actual resampling of the PID variables is performed. In the following both steps and their input configurations are described in detail.

5.3.1.1 Extraction of PID Distribution

For the resampling of the PID response, the distributions of the PID variables are needed in bins of $(p,\eta,ntracks)$ for each particle type. The extraction step is the most time consuming part, but since several analyses have similar kinematic distributions in p, η and $ntracks$, it is not needed to repeat this step several times. Therefore, the extraction of these distributions is split from the actual resampling.

The script performing the extraction step requires as input the version of the stripping configuration, the magnet polarity, the particle types required for the resampling and the PID variables which are needed. The stripping configuration is needed, as the reconstruction of the particles can slightly change between versions and certain PID responses, like the RICH or the multivariate approach, are depending on the reconstruction. The magnet polarity is necessary, as the PID response depends on the detector region and therefore has not to be equal between different magnet polarities.

Listing 5.1: Example running command

```
python MakePIDdistributionsRunRange.py ”20” ”MagUp” ”[Pi,Mu,K,P]” ”[DLLp,DLLK,DLLmu]”
```

The default configuration uses the standard binning scheme of the PIDcalib package for p, η and $ntracks$, see table 5.2. The binning scheme can be configured by optional input variables to match the analysis. Furthermore, additional selection cuts and a selection of run ranges can be applied by optional input requirements. Listing 5.1 shows an example of a command. Additional information on each input parameter is given in section A.2.

Table 5.2: Default binning scheme of the PIDcalib package, additional information can be found in the binning file of the package [124].

Particle type	Variable	Binning scheme
K, π, p, e	p [GeV/c]	3 : 9.3 : 15.6 : 19 : 24.4 : 29.8 : 35.2 : 40.6 : 46 : 51.4 : 56.8 : 62.2 : 67.6 : 73 : 78.4 : 83.8 : 89.2 : 94.6 : 100
	η	1.5 : 2.375 : 3.25 : 4.125 : 5
	ntracks	0 : 50 : 200 : 300 : 500
μ	p [GeV/c]	3 : 6 : 8 : 10 : 12 : 14.5 : 17.5 : 21.5 : 27 : 32 : 40 : 60 : 70 : 100
	η	1.5 : 2.375 : 3.25 : 4.125 : 5
	ntracks	0 : 50 : 200 : 300 : 500

The final output is a ROOT file. By default, it contains one folder named DEFAULT. The name changes if additional selection cuts are given as input, in this case the folders are named according to the input selection. Each of these folders contains a subfolder for each selected particle type. This particle type subfolder contains:

- One multidimensional histogram of the particle candidates of the calibration datasets. The histogram has p, η, *ntracks* and all the extracted PID variables as dimensions.
- One histogram for each projection of the total multidimensional histogram onto one of its dimensions.
- One multidimensional histogram for each bin in $(p, \eta, ntracks)$.

An example of the folder structure of such a ROOT file is given in fig. A.1. Figure 5.10 shows the histograms of the projections of the total multidimensional histogram from the command in listing 5.1. The first three histograms on p, η and *ntracks* (fig. 5.10a-5.10c) are showing the used binning scheme. The other three histograms (fig. 5.10d-5.10f) show the three extracted PID variables, DLLp, DLLK and DLLmu for the pion. As expected, all of them are on the negative side. As those distributions are extracted for the total available phase space, the structure seen in this distributions can be different for selected decays.

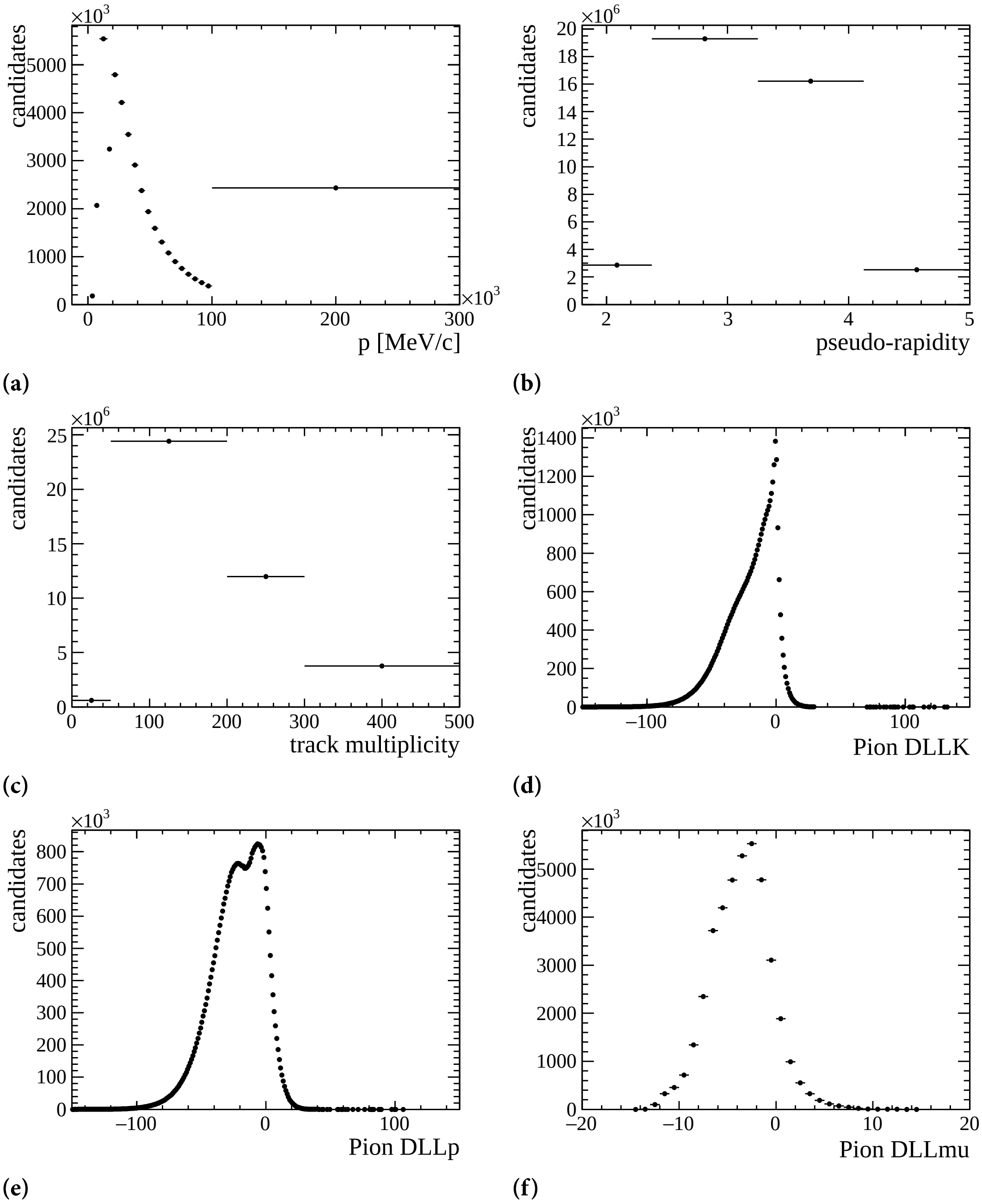

(a) **(b)** **(c)** **(d)** **(e)** **(f)**

Figure 5.10: The one dimensional projections of the total multidimensional histogram, which are saved in the ROOT file from the command in listening 5.1.

5.3.1.2 Resampling of the PID Variables

The resampling is performed iteratively over the events, using the actual file to resample and the output of the former step as input. The iterative process consist of three steps:

- The particle type, p, η and *ntracks* are extracted for each particle in the event.
- The corresponding projection is loaded for each (type, p, η and *ntracks*) combination.
- At last the PID variables are resampled according to the loaded distributions in the last step. Then it starts again from the beginning for the next event.

The script produces a new ROOT file, which contains a copy of the original input file and the resampled variables with *corr* appended at their former name. The required input conditions are more complex than for the extraction of the PID distribution, due to the interaction with an arbitrary simulated data set. Table 5.3 summarised the required input variables. There exist different naming schemes for the PID variables, especially the scheme used in the PIDcalib package is not the same as the default in the reconstruction software of LHCb. Therefore a python dictionary exists in the script, which matches both naming scheme. By default correlations between the PID variables are not taken into account, as the resampling uses one dimensional projections of the distributions. Only correlations resulting from the kinematic variables are mapped. An additional input flag *–correlation* can be activated to ensure, that additional correlations between the PID variables are taken into account using a multidimensional approach. Possible issues related to this approach are discussed in section 5.4.1.4. Additional input options are explained in more detail in section A.3.

Table 5.3: required input parameter of the resampling of the PID variables `MakePIDCorrection.py`. The input variables partName and particles use the naming scheme for the particles of the simulated file.

required input	**description**
mcFile (”MC_file.root”)	Defines the path to the simulated file to correct
mcFilePathToTree (”tuple/DecayTree”)	Sets the internal path to the TTree of the MC_file
partName (”[K:lab1/K,Pi:lab2/Pi]”)	Connects the particle type (K) to correct and the folder (lab1/K) in the library file
particles (”[K,Pi]”)	Defines the particle to correct
pidVars (”[PIDp,PIDK]”)	Defines the PID variables to correct
pidLibrary (”output.root”)	Defines the path to the library file with the extracted PID distributions

Listing 5.2 shows an example command for the resampling of the PID variables, where lab1 and lab2 are the different name of the cut conditions used in the extraction.

Listing 5.2: Example code

```
python -i MakePIDCorrection.py ”MC_file.root” ”tuple/DecayTree” ”[K:lab1/K,Pi:lab2/Pi]”
          ”[K,Pi]” ”[PIDK,PIDp]” output.root
```

5.3.2 Calibration Datasets

The number of PID calibration datasets was growing over the years, today 26 stripping lines are used to produce them. The involved decay modes have to be as pure as possible without the use of PID information from the RICH, calorimeter and muon systems. Ideally the decay modes are chosen such, that the total physics phase space in LHCb is covered. In LHCb calibration datasets exist for the five most common charged, long-lived particle species: kaons, pions, protons, electrons and muons.

Table 5.4: Overview of the decay modes, which are used to select calibration samples. Hard (soft) refers to calibration tracks with high (low) p and p_{T} [125].

Species	Soft		Hard	
$e^{\pm}$	-		$J/\psi \to e^+e^-$	a
$\mu^{\pm}$	$D_s^+ \to (\Phi \to \mu^+\mu^-)\pi^+$	b	$J/\psi \to \mu^+\mu^-$	a
$\pi^{\pm}$	$K_S^0 \to \pi^+\pi^-$	c	$D^* \to D^0\pi^+, D^0 \to K^-\pi^+$	c
$K^{\pm}$	$D_s^+ \to (\Phi \to K^+K^-)\pi^+$	b	$D^* \to D^0\pi^+, D^0 \to K^-\pi^+$	c
$p^{\pm}$	$\Lambda \to p\pi^-$	c	$\Lambda \to p\pi^-$	c
			$\Lambda_c^+ \to pK^-\pi^+$	d

---

[a] A tag-and-probe method was used to extract a PID free dataset.

[b] No PID requirements are needed, after 2015 the selection is performed with tag-and-probe[125]

[c] No PID requirements are needed.

[d] PID requirements are applied only on kaon and pion.

Table 5.4 gives an overview of the used decay modes. Certain decays are selected without PID requirements at all, and others like $J/\psi \to \mu^+\mu^-$ decays use a tag-and-probe method (see section 4.4.1) with PID requirements on the tag particle but not on the probe particle. The ${}_s\mathcal{P}lot$[126] technique is used to remove remaining combinatorial background contribution in each decay mode.

The final calibration datasets are available for both magnet polarities, MagUp and MagDown, and for several versions of stripping configurations. The magnet polarity is important, because

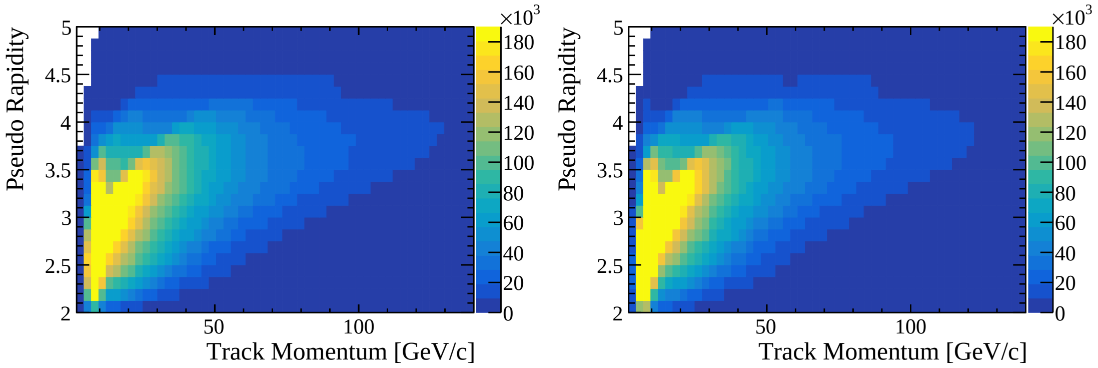

(a) Kaon sample

(b) Pion sample

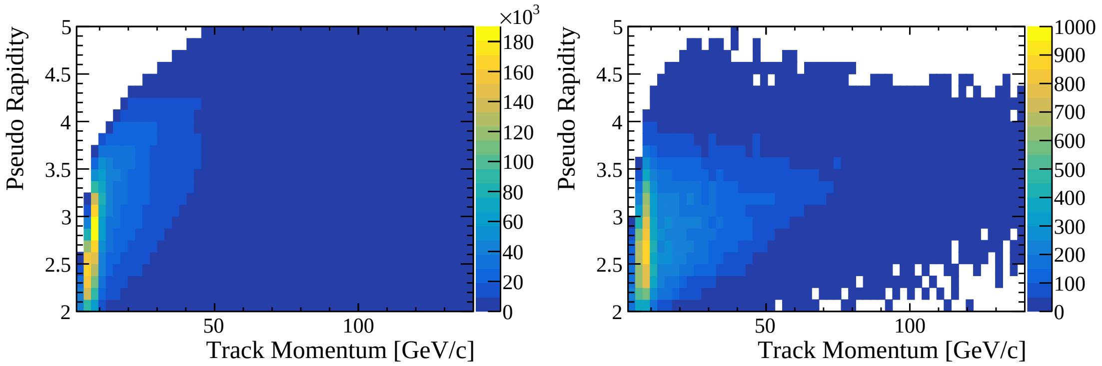

(c) Muon sample

(d) Electron sample

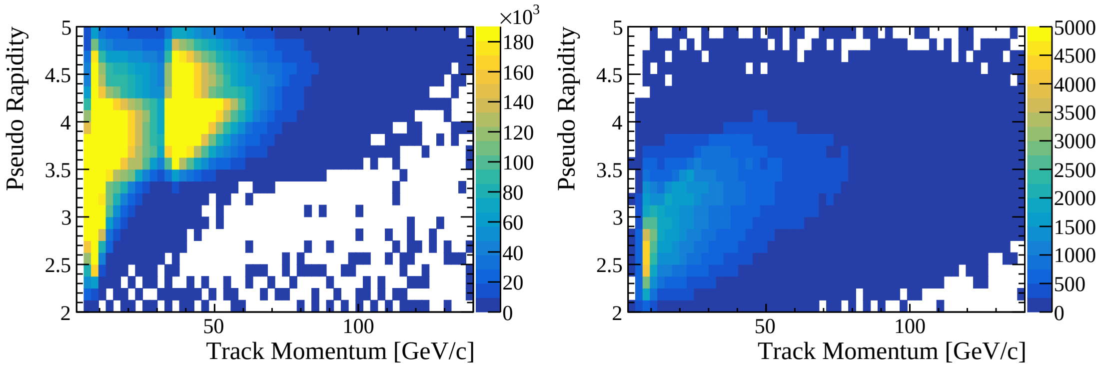

(e) Proton sample (only $\Lambda \to p\pi^-$)

(f) Proton sample (only $\Lambda_c^+ \to pK^-\pi^+$)

Figure 5.11: The figures show the distribution of the calibration data in track η and p for the stripping version 20 and magnet polarity up, only the electron sample is of stripping version 21 as the samples in version 20 is rather small.

the different detector regions must not give the same PID response for the same particle species, p, η and multiplicity.

Figure 5.11 shows the distribution of the calibration data in track η and p for all five species in Run I. The region at low momentum and large pseudo-rapidity in the kaon, pion, muon and electron sample is originated in the acceptance of the LHCb detector. This affects the most the muon and then the electron samples, as they are mostly identified in the muon stations and calorimeter system, respectively. The white regions at high momentum for the electron and proton samples are due to the kinematic and selection of the corresponding decay channel. The two proton decay channels are separated out of an historical reason. The decay channel $\Lambda \rightarrow p\pi^-$ was first included as calibration dataset. But as it can be seen in fig. 5.11e, the sample does not cover the region with low pseudo-rapidity and high momentum. Hence, another proton calibration sample had to be chosen and the choice was $\Lambda_c^+ \rightarrow pK^-\pi^+$, which does cover the before missed region.

5.4 VALIDATION OF THE RESAMPLING TECHNIQUE

The resampling technique was developed and tested on $B^0 \rightarrow J/\psi K^{*0}$ ($J/\psi \rightarrow \mu^+\mu^-$ and $K^{*0} \rightarrow K^+\mu^-$) decay sample with an integrated luminosity of 0.37 fb^{-1} at centre of mass energy of 7 TeV. The selection follows the $B^0 \rightarrow K^{*0}\mu^+\mu^-$ ($K^{*0} \rightarrow K^+\mu^-$) analysis in [127]. An event candidate has first to pass a hardware trigger, which selects muons with a transverse momentum, $p_{\mathrm{T}} > 1.48\,\mathrm{GeV}/c$. In the software trigger at least one of the final state particles is required to have both $p_{\mathrm{T}} > 0.8\,\mathrm{GeV}/c$ and impact parameter (IP) $> 100\ \mu\mathrm{m}$ with respect to all of the primary proton-proton interaction vertices in the event. The definition of the IP is explained in fig. 3.12.

Afterwards the following selection requirements are applied to further reduce the combinatorial background. Both muons need to have sufficient hits in the muon system to be consistent with a muon, *IsMuon* and a $\mathrm{DLL}_{\mu\pi} > -3$. All the final state particles have to lie in the LHCb acceptance, $2 < \eta < 5$, have p between 2 and 100 GeV/c and an IP χ^2 distance greater than 4. The invariant mass of both muons combined has to be located in the mass range of $3060 < m_{\mu\mu} < 3140\,\mathrm{MeV}/c^2$. Furthermore, the vertex fit χ^2 of the J/ψ candidate has to be smaller than 15. Candidate needs to have an K^+ μ^- invariant mass in the range $792 < m_{K^+\mu^-} < 992\,\mathrm{MeV}/c^2$. And the invariant mass of the reconstructed B^0 candidate out of K^+ μ^- μ^+ μ^- has to be in the range $5150 < m_{B^0} < 5600\,\mathrm{MeV}/c^2$. In addition, the vertex of the B^0 candidate has to be significantly displaced form the proton-proton interaction vertex, requiring the flight distance (FD) χ^2 to be bigger than 16. Finally, the angle between the flight direction of the B^0 candidate and its momentum vector has to be small, requiring the cosine of the angle, $DIRA > 0.99995$. Requirements on the PID are made to reduce the part of the mis-identification of kaon and pion, the kaon has $\mathrm{DLL}_{K\pi} > -5$, the pion has $\mathrm{DLL}_{K\pi} < 25$ and (Kaon $\mathrm{DLL}_{K\pi}$ - pion $\mathrm{DLL}_{K\pi}$)> 10. The selection requirements are summarised in table 5.5. The remaining combinatorial background in the data sample is estimated by applying the ${}_s\mathcal{P}lot$[126] technique, whereas, in the simulation sample the B^0 candidate has to be a true B^0.

Table 5.5: Selection requirements for the $B^0 \to J/\psi K^{*0}$ sample.

Particle	**Selection**
B^0	$5150 < m_{B^0} < 5400\,\mathrm{MeV}/c^2$
B^0	FD $\chi^2 > 16$
B^0	$DIRA > 0.99995$
K^{*0}	$792 < m_{K^{*0}} < 992\,\mathrm{MeV}/c^2$
J/ψ	$3060 < m_{\mu\mu} < 3140\,\mathrm{MeV}/c^2$
J/ψ	Vertex $\chi^2 < 15$
track	IP $\chi^2 > 4$
track	$2 < \eta < 5$
track	$2 < p < 100\,\mathrm{GeV}/c$
$\mu^\pm$	isMuon True
$\mu^\pm$	$\mathrm{DLL}_{\mu\pi} > -3$
K^+	$\mathrm{DLL}_{K\pi} > -5$
π^+	$\mathrm{DLL}_{K\pi} < 25$
K^+ and π^+	(K^+ $\mathrm{DLL}_{K\pi}$ - π^+ $\mathrm{DLL}_{K\pi}$)> 10

5.4.1 DISCUSSION

Figures (5.12-5.17) show the comparison of the simulated and measured data samples with and without resampling for the PID variables of kaon, pion and muon of the $B^0 \to J/\psi K^{*0}$ decay. For the resampling the true identity of the particle is used and the track multiplicity was resampled according to the distribution in data before it was used in the PID resampling[1]. The special correlation flag for the multidimensional approach was enabled. In general, the difference of the PID variables in data and simulation is significantly smaller after the resampling, especially for the DLL variables. In the following the PID variables are discussed in detail.

---

[1] The re-weighting of the simulation to match the distribution in data was no option, as the track multiplicity was needed as value for each event.

5.4.1.1 KAONS

The distributions of the PID variables of kaons are shown in fig. 5.12 and fig. 5.13. The left column shows the comparison of simulation and data without resampling, whereas the right column shows the comparison with resampling. The kaon DLLK is positive as expected (see fig. 5.12b). But it has a small discrepancy around zero between data and resampled simulation, which will be discussed later in section 5.4.1.4. The DLLmu is mostly negative as expected (see fig. 5.12d). The kaon DLLp distribution is peaking at positive values but the larger tail is as expected on the left hand side. The kaon ProbNNk in fig. 5.13b is kaon-like peaking at one. There is as in the DLLK a small discrepancy between data and resampled simulation at zero. The other two, ProbNNmu and ProbNNp are as expected peaking at zero (see fig. 5.13d and fig. 5.13f).

5.4.1.2 MUONS

The distributions of the PID variables of muons are shown in fig. 5.14 and fig. 5.15. The resampled simulation sample compared to the data is shown on the right column, whereas the not resampled simulation is shown on the left column. All the distributions look as expected, the DLLK and the DLLp are mainly negative and the DLLmu positive. The ProbNNmu is peaking at one as expected, whereas the ProbNNk and ProbNNp distribution are peaking at zero.

5.4.1.3 PIONS

The distributions of the PID variables of pions are shown in fig. 5.16 and fig. 5.17. The DLLk distribution of the pion is negative as expected. There are some small differences between resampled simulation and data at positive values (see fig. 5.16b). The DLLmu distribution is mainly negative as expected (see fig. 5.16d), the slight shift between resampled simulation and data has the same origin as the difference in DLLK. The distribution of the DLLp for pions is as expected around zero. The larger discrepancy between resampled simulation and data at positive values has the same origin as the differences in the other two distributions and it is discussed in section 5.4.1.4. All of the ProbNNs are peaking at zero as expected. The differences between simulation and data seen in the DLL distributions are visible as well in the ProbNN distributions.

5.4.1.4 DISCREPANCIES

There are two main issues, which result in remaining discrepancies. At first, the cut, $(K\mathrm{DLL}_{K\pi} - \pi\mathrm{DLL}_{K\pi}) > 10$, in the selection is used to reduce the kaon-pion mis-identification. Still there is some remaining kaon-pion swap visible. In the ProbNNk (fig. 5.13b) and DLLK (fig. 5.12b) variable of the kaon, it is visible that in the simulation there are more pions identified as kaons than in data. In case of the pion it is visible that more kaon like particles are reconstructed as pions in data than in simulation. This can be seen in the ProbNNk (fig. 5.17b) and DLLK (fig. 5.16b) variable of the pion. In both distributions, the amount of candidates at higher values is larger for data than simulation. Furthermore, the distribution of the DLLmu (fig. 5.16d) variable of the pion is shifted to the right, as can be expected for kaons which have a slightly larger DLLmu. A similar shift is visible in the DLLp (fig. 5.16f) and ProbNNp (fig. 5.17f) of the pion, the discrepancies at higher values in both PID variables are introduced by the misidentified kaon like particles, as they have a larger probability to higher PIDp and ProbNNp values than pions. These observations lead to the conclusion, that the kaon-pion swap is not modelled in simulation accurately enough. Secondly, in the ProbNNmu (fig. 5.15d) variable of the muon a small discrepancy is visible at zero. This is introduced by statistical effects coming from the finite number of events in the calibration data, as it is not visible if the resampling is performed without the correlation flag applied (see fig. A.5d).

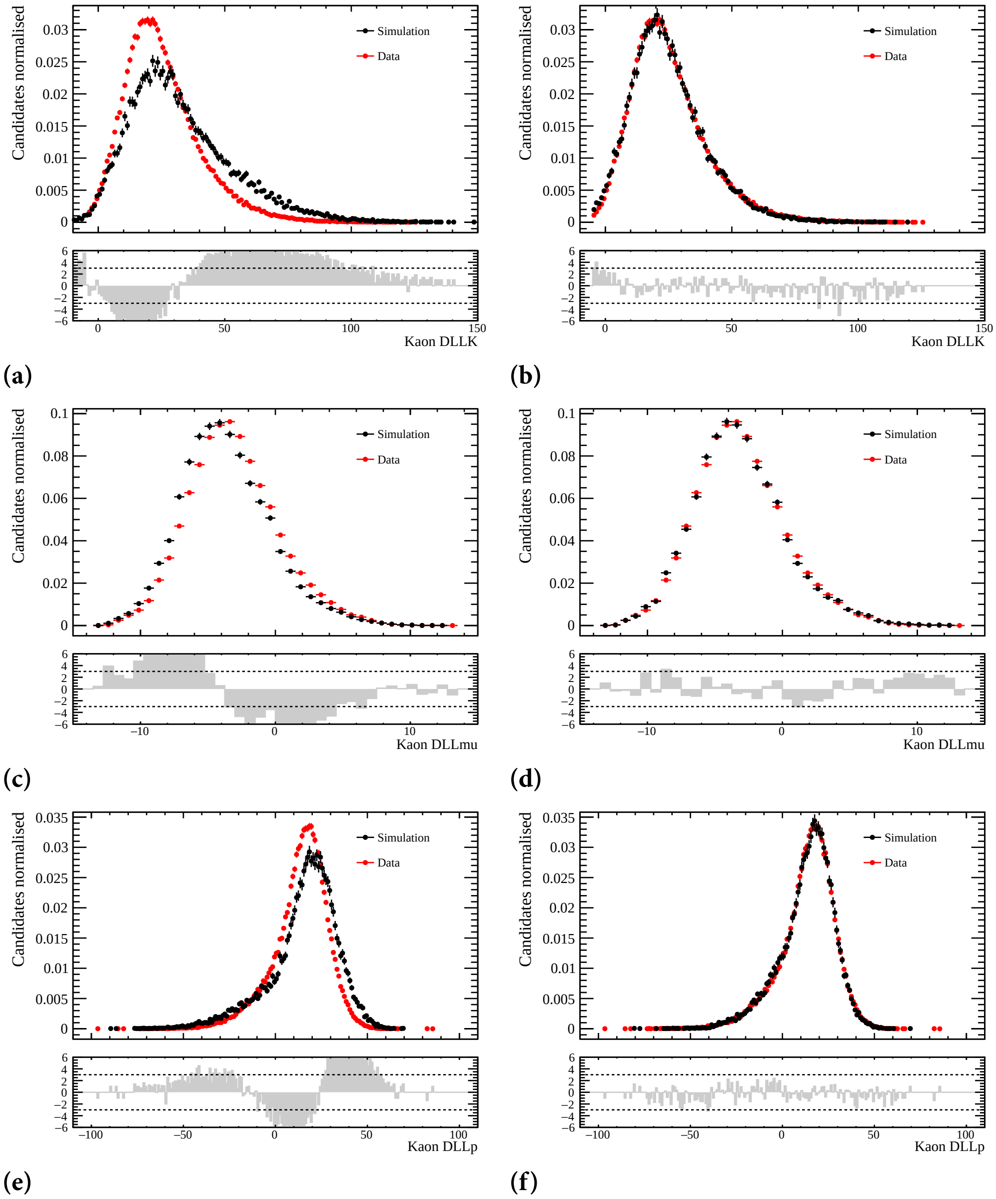

(a) (b)

(c) (d)

(e) (f)

Figure 5.12: Comparison of the DLL distribution for kaons of the $B^0 \to J/\psi K^{*0}$ decay. The left (right) column shows the simulation without (with) resampling in comparison to data.

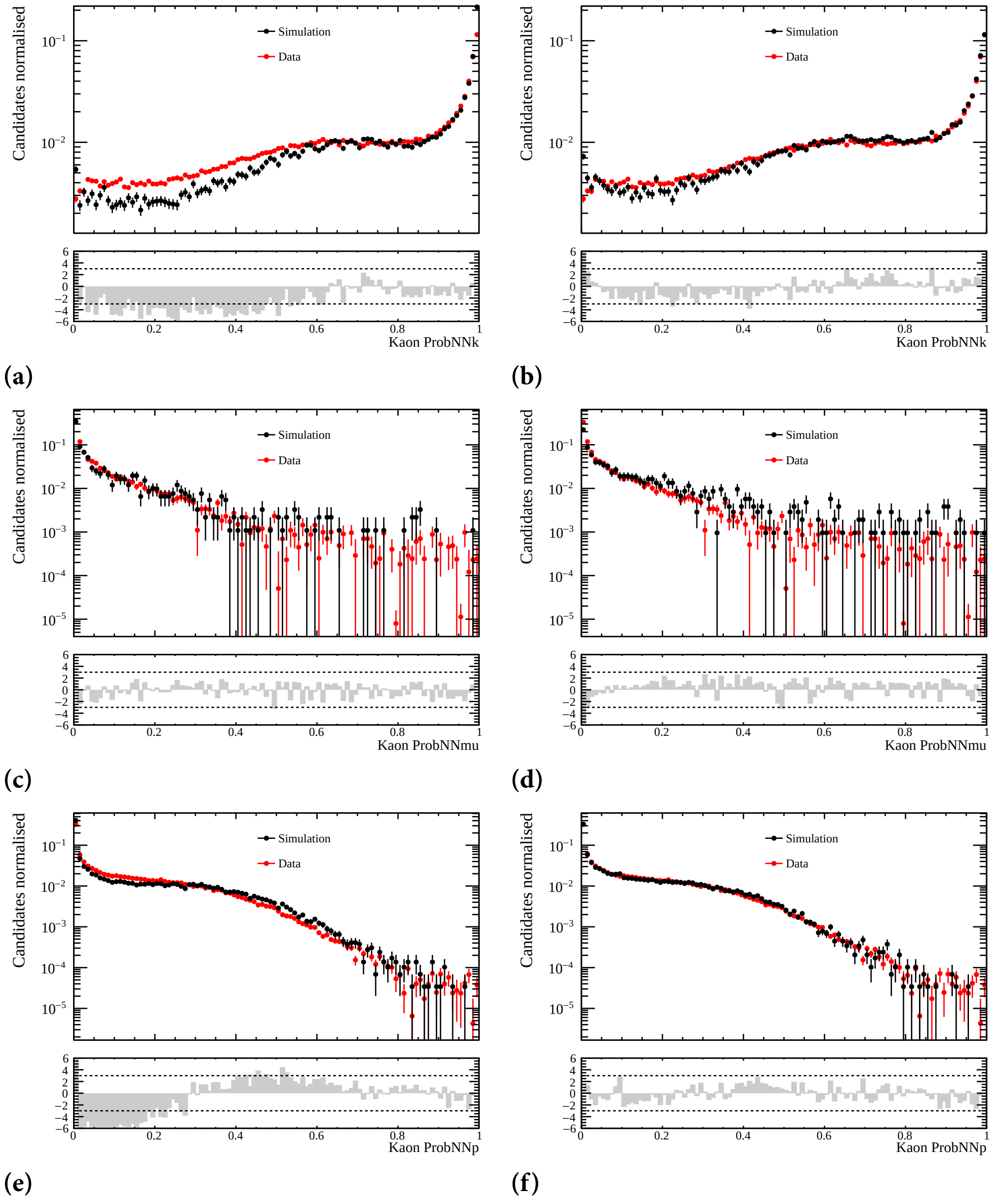

(a) **(b)**

(c) **(d)**

(e) **(f)**

Figure 5.13: Comparison of the ProbNN distribution for kaons of the $B^0 \to J/\psi K^{*0}$ decay. The left (right) column shows the simulation without (with) resampling in comparison to data.

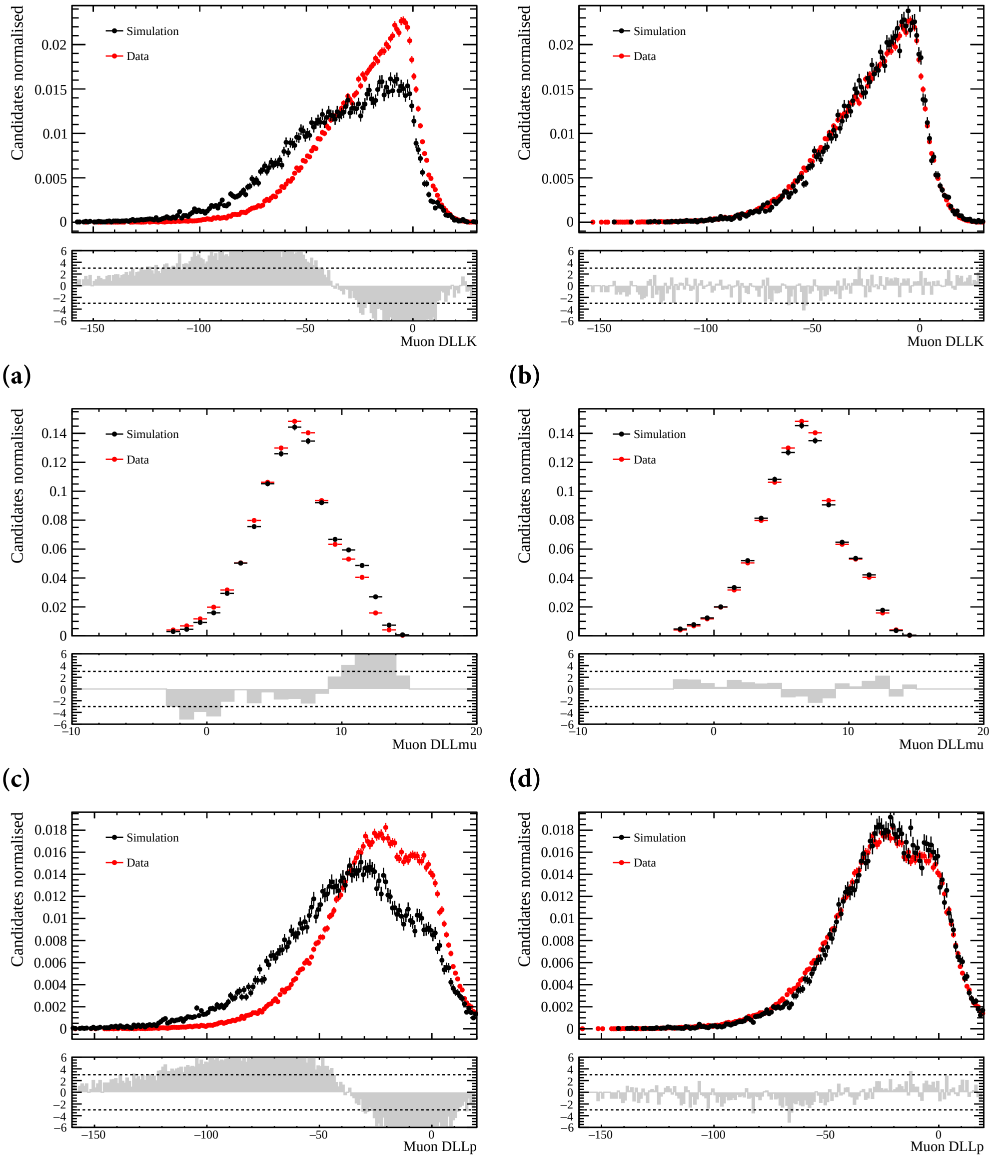

(a) (b) (c) (d) (e) (f)

Figure 5.14: Comparison of the DLL distribution for muons of the $B^0 \to J/\psi K^{*0}$ decay. The left (right) column shows the simulation without (with) resampling in comparison to data.

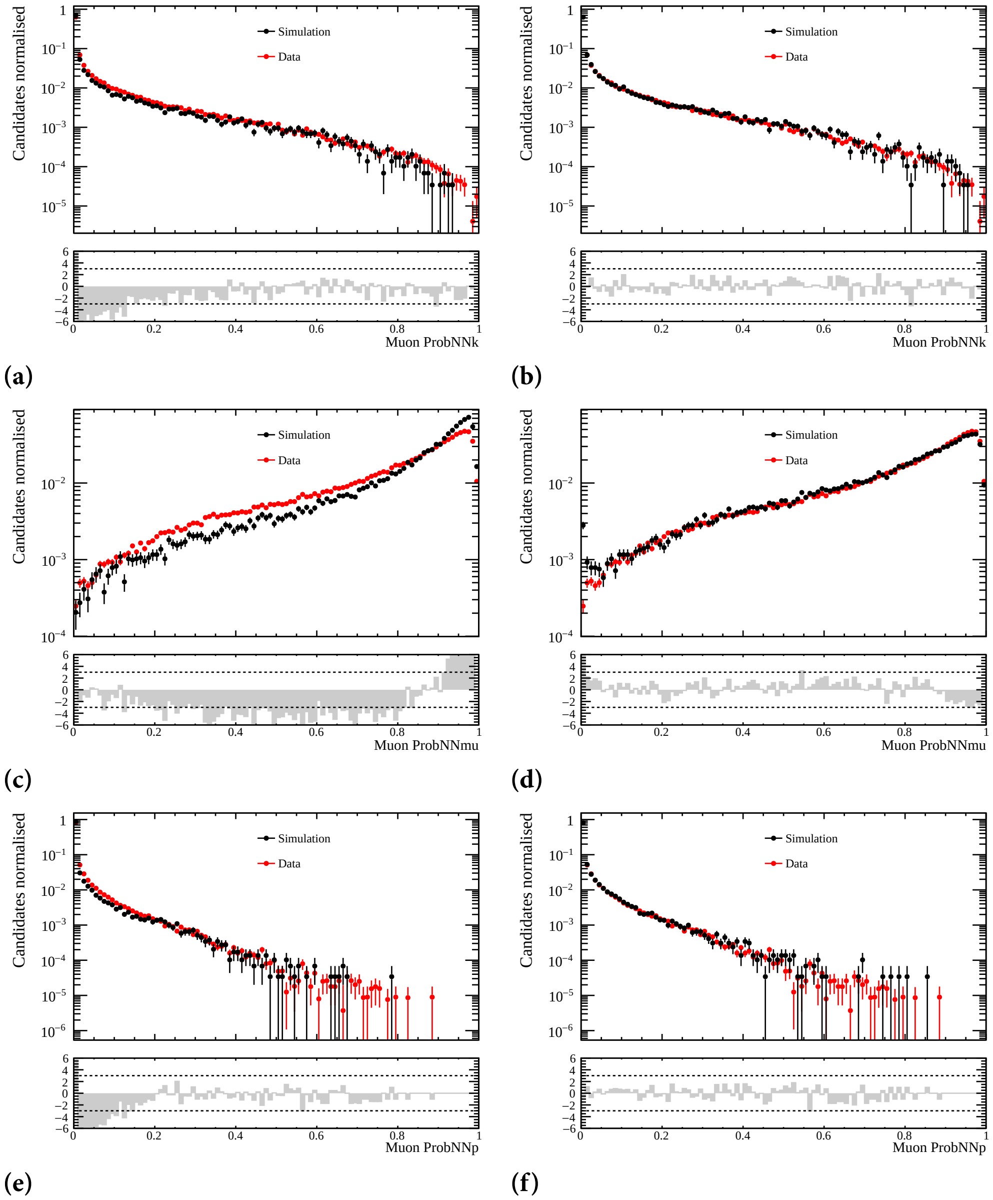

Figure 5.15: Comparison of the ProbNN distribution for muons of the $B^0 \to J/\psi K^{*0}$ decay. The left (right) column shows the simulation without (with) resampling in comparison to data.

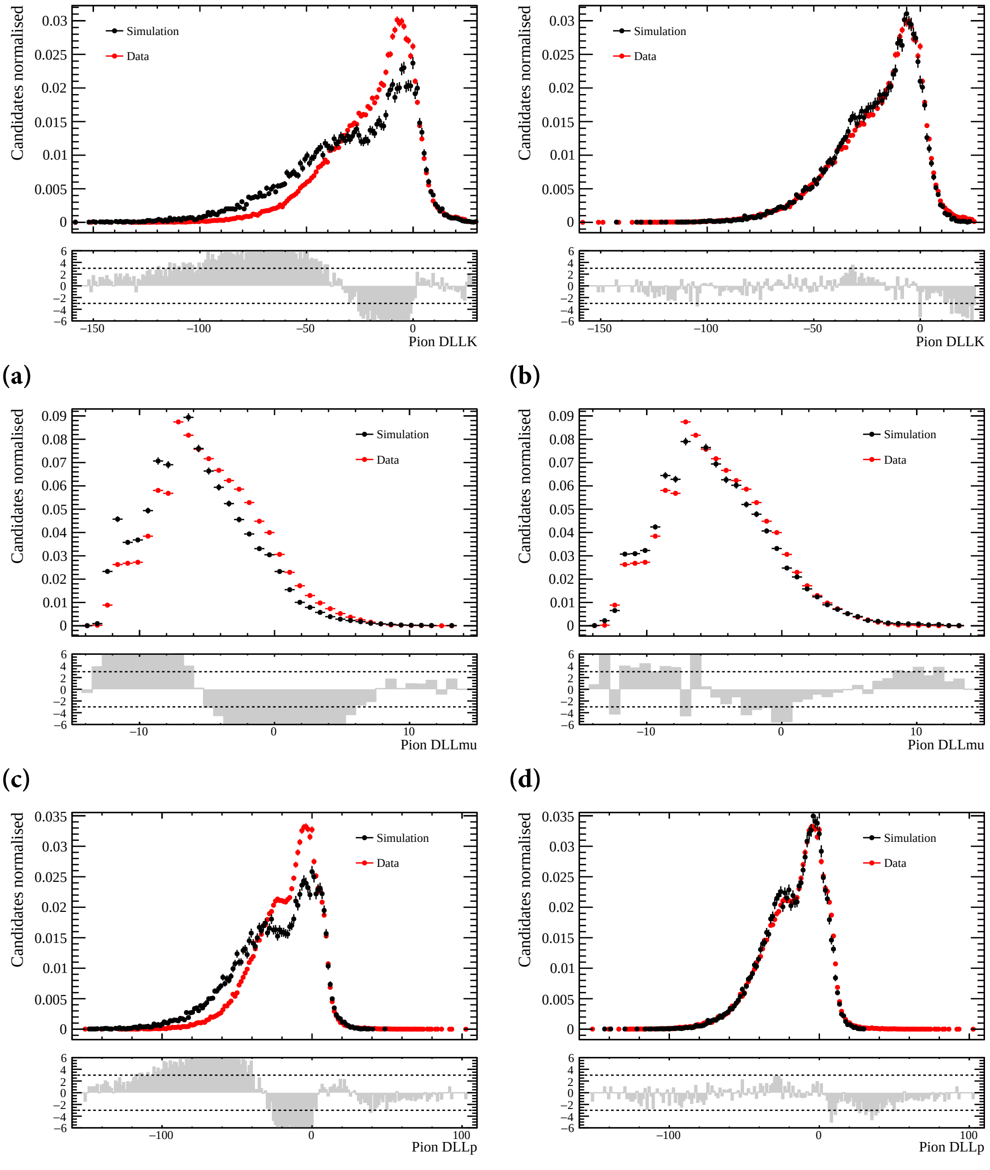

(a) (b) (c) (d) (e) (f)

Figure 5.16: Comparison of the DLL distribution for pions of the $B^0 \to J/\psi K^{*0}$ decay. The left (right) column shows the simulation without (with) resampling in comparison to data.

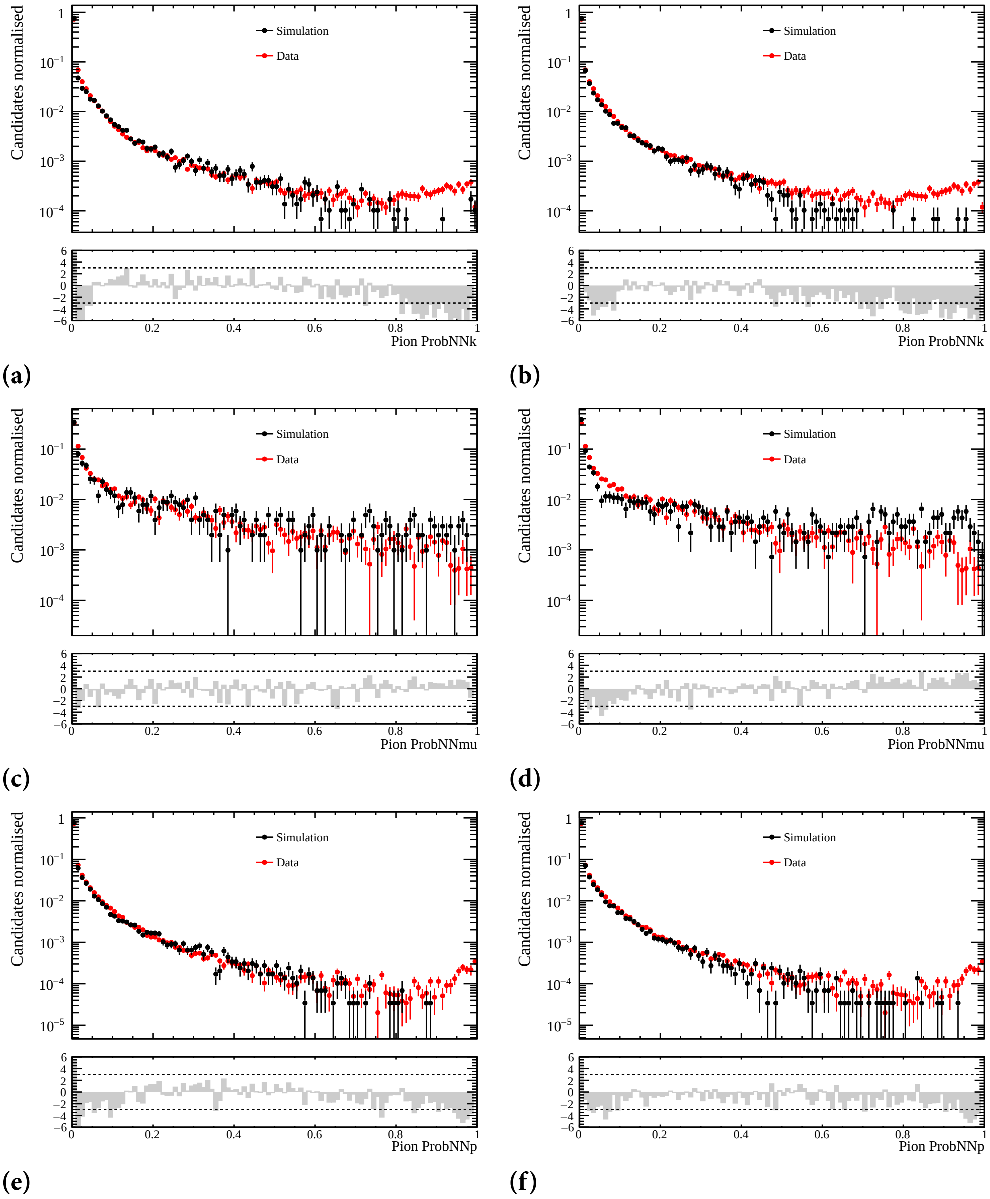

(a) **(b)**

(c) **(d)**

(e) **(f)**

Figure 5.17: Comparison of the ProbNN distribution for pions of the $B^0 \to J/\psi K^{*0}$ decay. The left (right) column shows the simulation without (with) resampling in comparison to data.

Science, my lad, is made up of mistakes, but they are mistakes which it is useful to make, because they lead little by little to the truth.

Jules Verne

6

Soft Particle Produced in Hard Event

Inelastic proton-proton (pp) interactions are usually described by phenomenological models of quantum chromodynamics (QCD), as processes cannot be completely determined via perturbative QCD due to divergences (see chapter 2). In this chapter, an overview of soft QCD phenomenas measured at the LHCb experiment is given. This is followed by a detailed description of the performed measurement of ZV_0, where V_0 are either K^0_S or $\mathit{\Lambda}/\overline{\mathit{\Lambda}}$. The measurement was done by myself.

6.1 EARLIER MEASUREMENTS

The final state of an inelastic pp collision at LHC can be described in QCD by contributions from hard and soft scattering processes between the constituents of the hadrons. Soft scattering processes include initial- and final-state radiation and the fragmentation of the initially coloured partonic final state into colour-neutral hadrons. The soft components are also called the underlying event (UE). The theoretical description of the soft component is based on phenomenological models, where the parameters need to be extracted from data. Hard scattering processes are well described in theory by perturbative QCD.

6.1.1 Energy Flow

One of the main sources of the UE are multi-parton interactions (MPI). These occur mainly in regions where the partons carry a very low parton momentum fraction, where the parton density is the largest. Hence the probability for more than one interaction to happen increases. The contribution of MPI to a collision event at LHC becomes increasingly important with higher LHC collision energies, because the interactions between very soft partons are energetic enough to contribute to the final state particle production. MPI phenomena can be tested for example by measuring the amount of energy produced in inelastic proton-proton interactions at large values of pseudo-rapidity, η. This is called energy flow, and it is expected to be directly sensitive to multi-parton interaction models [128].

The measurement of the energy flow in pp collisions was performed at $\sqrt{s}$ =7 TeV by determining the energy[1] of charged particles within $1.9 < \eta < 4.9$ recorded at the LHCb experiment. The events are classified as minimum-bias, hard scattering, diffractive enriched and non-diffractive enriched events in order to probe various aspects of multi-particle production in high-energy hadron-hadron collisions. Events with at least one track originating from the luminous region are called minimum-bias events. Events with two or more reconstructed primary vertices are rejected to suppress pile-up contamination. Minimum-bias events are further classified as: hard scattering events, where at least one track has $p_T > 3\,\text{GeV}/c$ and $1.9 < \eta < 4.9$; diffractive enriched events, where no track is reconstructed with $-3.5 < \eta < -1.5$; and non-diffractive enriched events, where at least one track is reconstructed with $-3.5 < \eta < -1.5$. The last two event classes are motivated by the fact that a sizeable rapidity gap is an experimental signature for diffractive processes [130]. The charged energy flow $EF(\eta) = 1/N_{int} dE/d\eta$ for the four different event classes is shown in fig. 6.1 superimposed with different Pythia versions and tunes: LHCb tune [131] of Pythia 6.4 [132], Perugia 0 and Perugia NOCR [133] tunes of Pythia 6.4, and Pythia 8.130 [33]. The LHCb tune uses the CTEQ6L parton density functions (PDFs) [134], while both Perugia tunes and Pythia 8.130 use the CTEQ5L PDFs [135]. In fig. 6.2, the four different event classes are shown superimposed with four cosmic-ray interaction models: EPOS 1.99 [136], QGSJET01, QGSJETII-03 [137] and SIBYLL 2.1 [138], which are used in extensive air shower simulations and are not tuned to LHC data.

The uncertainties are dominated by systematic effects like model dependence for correcting de-

---

[1] The energy is measured using the reconstructed momentum of long tracks. In average the momentum of long tracks in minimum-bias data is about 7 GeV/c and the masses of long-lived charged particles (with $\gamma\beta c\tau > 8$ m) are below 1 GeV/c^2, therefore one can safely assume that the momentum of these tracks is equivalent to the energy of the corresponding charged particles [129].

tector effects and uncertainties on track finding efficiency. Those effects are decreasing towards larger η, where differences between models are largest. None of the event generators used in the analysis is able to described the energy flow for all event classes. Especially in hard scattering events, no model is able to describe the data [129].

6.1.2 PARTICLE PRODUCTION RATIOS

Measurements of particle production ratios in pp-collisions yield information about the hadronisation process. By using the excellent particle identification capabilities of the LHCb detector, the measurement of the production ratios K^+/K^-, π^+/π^-, $p/\overline{p}$, $\frac{K^+ + K^-}{\pi^+ + \pi^-}$, $\frac{p+\overline{p}}{\pi^+ + \pi^-}$, $\overline{\Lambda}/\Lambda$ and $\overline{\Lambda}/K^0_S$ have been performed at centre-of-mass energies of $\sqrt{s}$ =0.9 TeV and $\sqrt{s}$ =7 TeV.

Figure 6.3 shows the results for the strangeness suppression and the baryon suppression in the fragmentation process as measured by $\frac{K^+ + K^-}{\pi^+ + \pi^-}$ and $\frac{p+\overline{p}}{\pi^+ + \pi^-}$ respectively. Both measured ratios are compared to PYTHIA 6 generator tunes: LHCb MC, Perugia 0 and Perugia NOCR as function of p_T and η at 0.9 TeV and 7 TeV (only the latter is shown in the figure). There is only a weak dependence on η, whereas the ratios rise significantly with p_T, as the mass differences are less important at larger momenta. There are two interesting facts: first, only the LHCb tune of PYTHIA reproduces the measurements of the baryon and strangeness suppression, the other tunes underestimate the ratio. The difference increases with increasing p_T. Second, the baryon and strangeness suppression are similar in size. The other results on K^+/K^-, π^+/π^- and $p/\overline{p}$ are presented in ref. [139].

Figure 6.4 shows the results of the baryon to meson ratio $\overline{\Lambda}/K^0_S$ and $\overline{\Lambda}/\Lambda$, which is sensitive to the transfer of baryon number from the beam particles to the final state, because the valence quarks of the Λ are also present in the colliding protons, but there is no overlap between the proton and the $\overline{\Lambda}$. Both measured ratios are compared to the same PYTHIA 6 generator tunes as the strangeness and baryon suppression measurements. None of the tunes are describing the data. Further details on the measurement are in ref. [140].

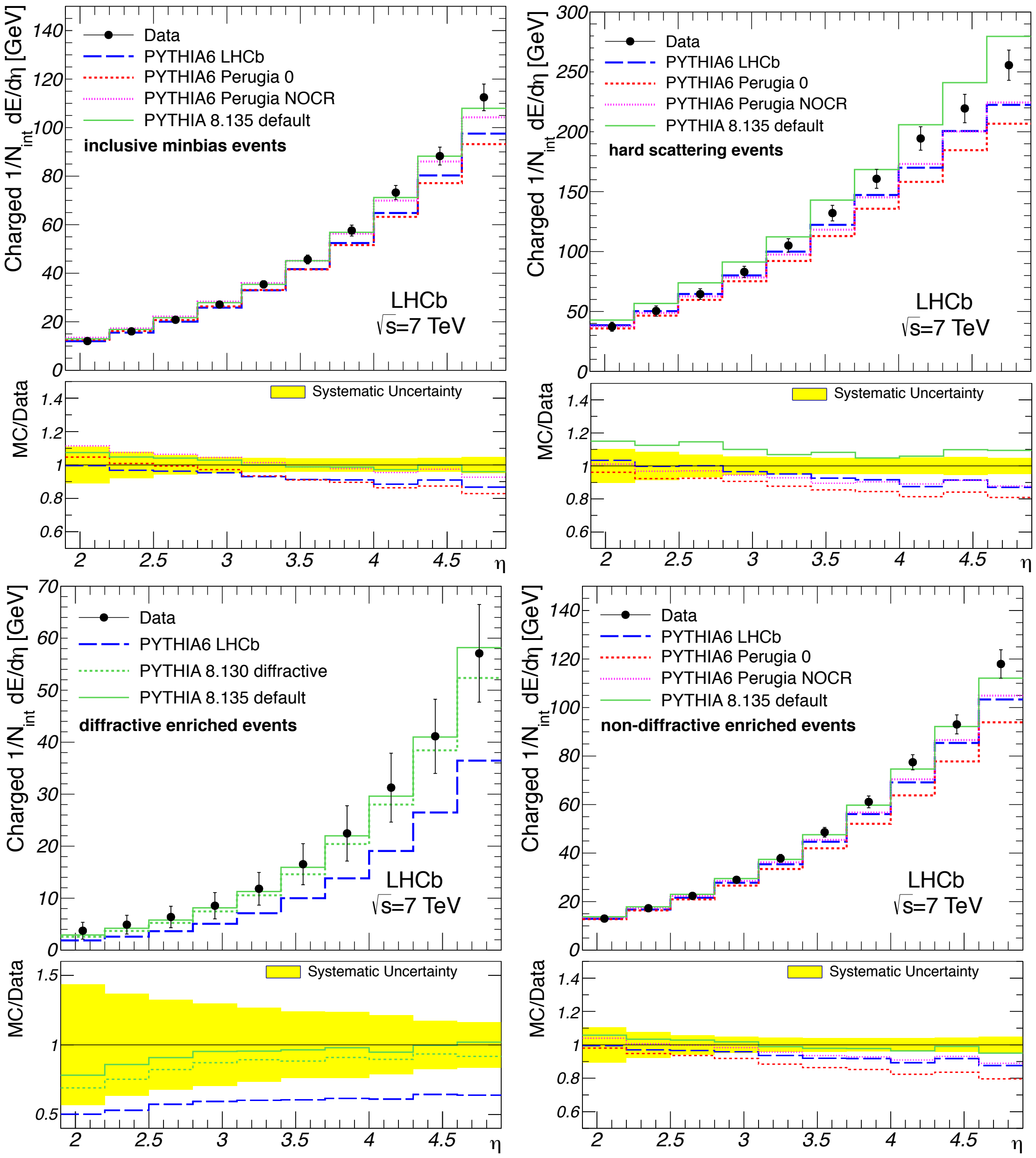

Figure 6.1: Charged energy flow as a function of η for all event classes as indicated in the figures. The corrected measurements are given by points with error bars, while the predictions by the Pythia tunes are shown as histograms. The error bars represent the systematic uncertainties, which are highly correlated between the bins. The statistical uncertainties are negligible. The ratios of the MC predictions to data are shown in addition [129].

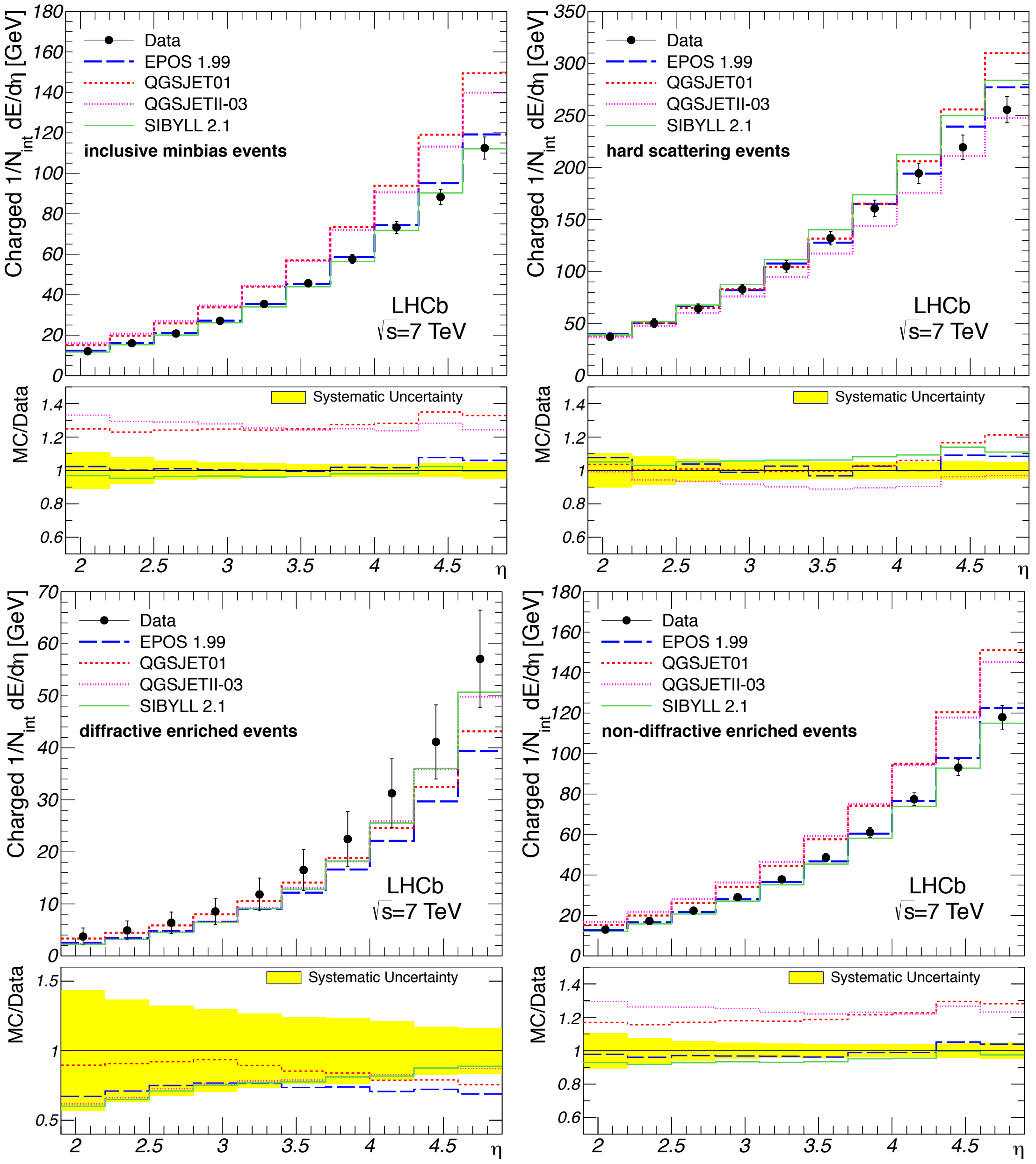

Figure 6.2: Charged energy flow as a function of η for all event classes as indicated in the figures. The corrected measurements are given by points with error bars, while the predictions by the cosmic-ray interaction models are shown as histograms. The error bars represent the systematic uncertainties, which are highly correlated between the bins. The statistical uncertainties are negligible. The ratios of the MC predictions to data are shown in addition [129].

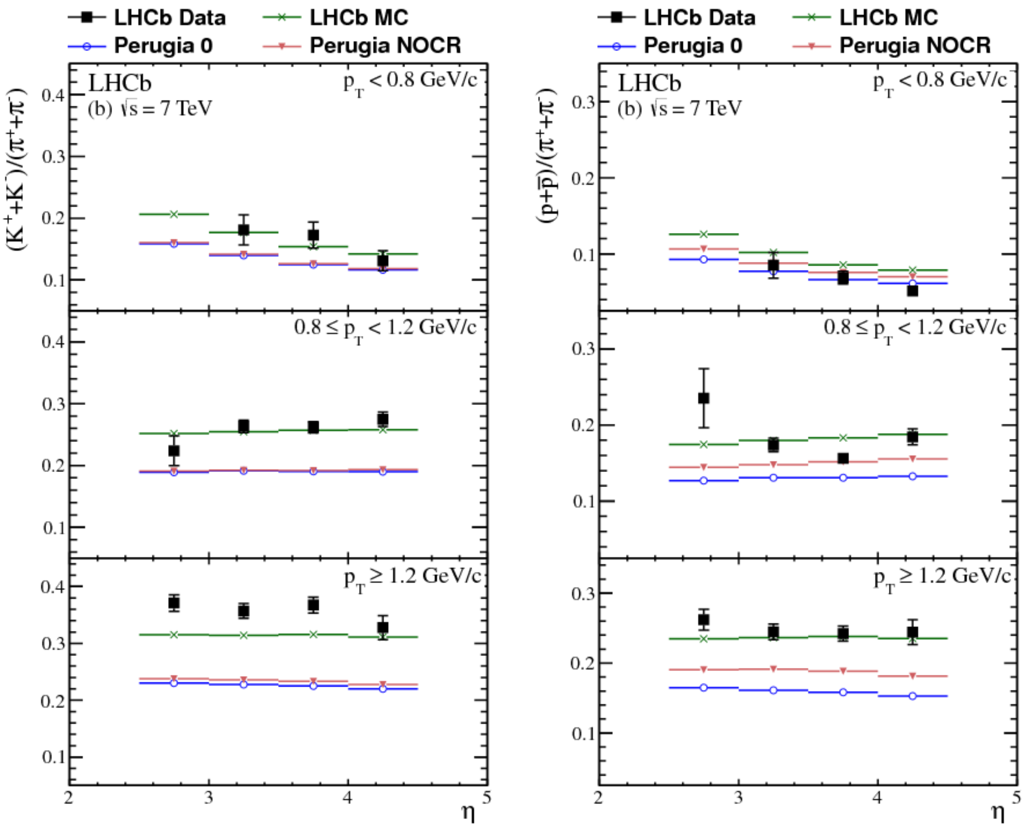

Figure 6.3: Results are shown for the $\frac{K^++K^-}{\pi^++\pi^-}$ on the left and $\frac{p+\bar{p}}{\pi^++\pi^-}$ on the right. Both are taken at $\sqrt{s}$ = 7 TeV and shown with the three PYTHIA event generator configuration overlaid [139].

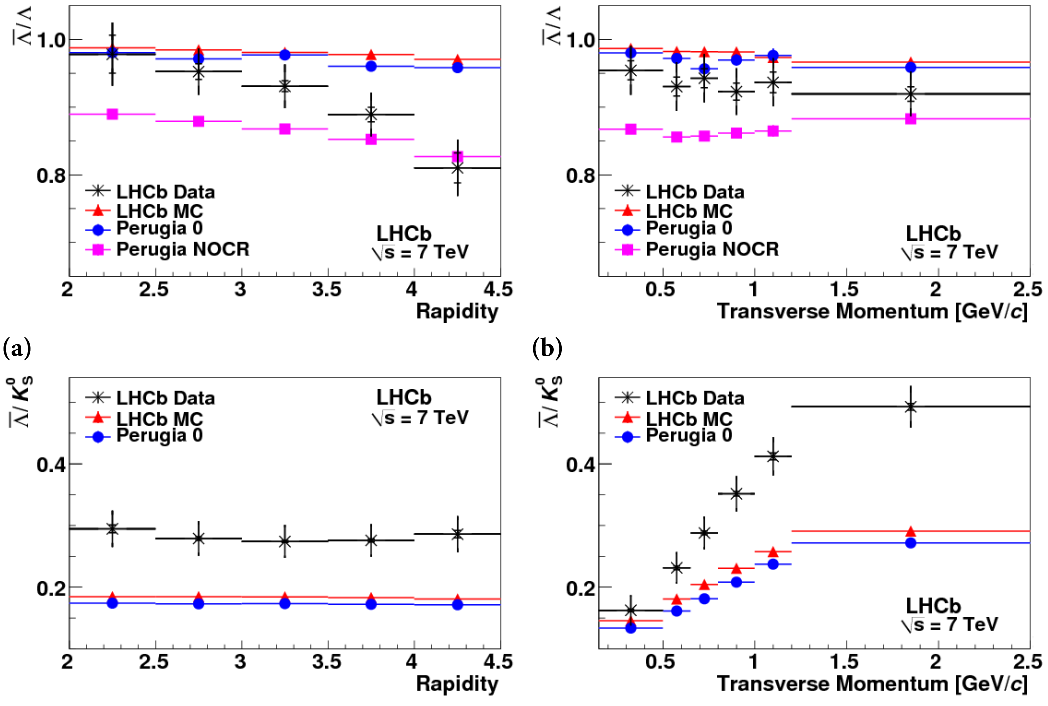

(a) (b)

(c) (d)

Figure 6.4: The ratios $\overline{\Lambda}/\Lambda$ and $\overline{\Lambda}/K^0_S$ at $\sqrt{s}$ =7 TeV are compared with the predictions of the LHCb MC, Perugia 0 and Perugia NOCR as a function of a & c rapidity and b & d transverse momentum. Vertical lines show the combined statistical and systematic uncertainties and the short horizontal bars (where visible) show the statistical component [140].

6.2 Conclusion from Earlier Measurements

The energy-flow and particle production ratio measurements show that the models cannot describe all aspects of the measurement and hence the model parameters are not properly tuned. Therefore, further measurements are helpful to allow proper tuning. If both conclusions from the energy-flow and particle production ratio measurements are combined, a possible interesting measurement would be the measurement of K^0_s, Λ and $\overline{\Lambda}$ particles in a hard scattering event. Especially interesting would be the ratio between the number of ZV_0 events and the total number of hard scattering events as a function of the transverse momentum of the V_0, as from the production ratio measurement results (see fig. 6.4d) follows that the V_0 production as function of p_T would have the largest difference in terms of the different model tunes. The ratio measurement as function of the opening angle between the V_0 and the hard scattering particle momenta holds additional information about the hadronisation in the UE.

6.3 ZV_0 Decay Topology

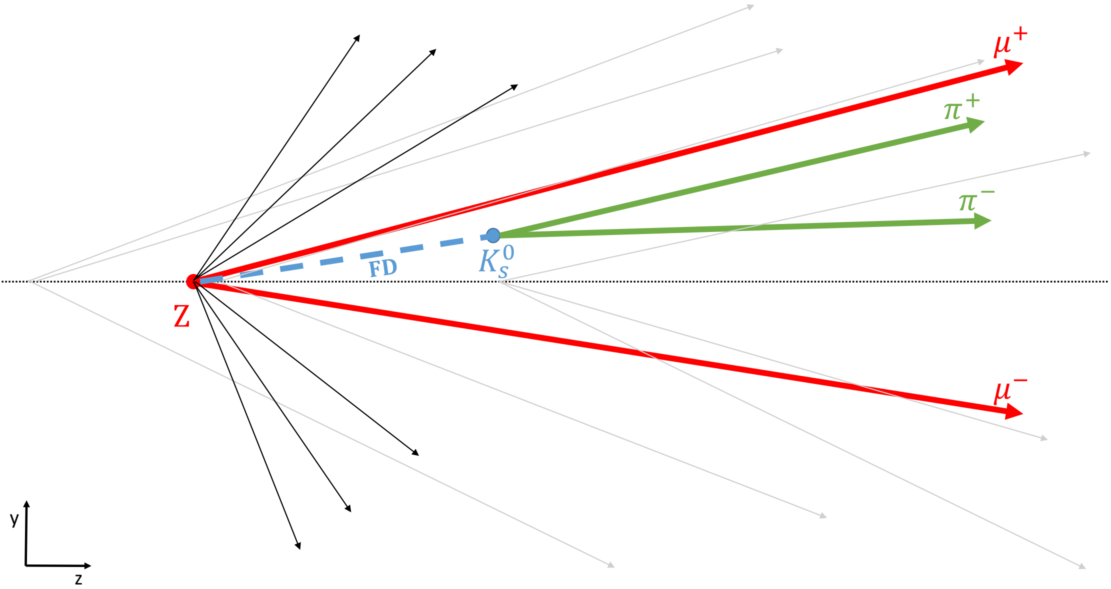

Figure 6.5: The figure shows a sketch of an interaction with a ZK^0_s event. The flight distance (FD) of the K^0_s is indicated. The grey tracks are particles produced in additional pp interactions, black tracks are particles produced in the same pp interaction.

In this analysis, the decay $Z \to \mu^+\mu^-$ is used as hard scattering process. Hence, the decay of interest consists of a Z boson decaying into two muons and a V_0 from the same interaction. The V_0 is either a K^0_S meson decaying into two pions or a Λ boson decaying into a proton and a pion, where no difference is made between Λ and $\overline{\Lambda}$. Figure 6.5 shows a sketch of the decay topology. The Z has a short lifetime and decays immediately at the primary interaction point. Therefore, it defines the primary vertex (PV). The long living particles K^0_S and Λ are flying a certain distance, called flight distance (FD), from the PV before they decay. In addition to the interaction at the PV, other pp interactions may happen at the same time and produce final state particles originating from other primary vertices. Those secondary pp interactions can also contain V_0s. If their flight path is close enough, they can fake a ZV_0 event. Furthermore, in one primary interaction, not only a Z is produced and not only in combination with a V_0. Many other intermediate particles are produced as well, which can fake a V_0 or Z through misidentification or by random combination of one or two final state particles.

The additional background processes can be separated into several categories:

- pile-up processes, where the V_0 is produced in another pp interaction and the flight path is close to the Z interaction vertex.
- peaking backgrounds, a resonant decay where one or more final state particles are misidentified and therefore imitates a V_0 or a Z decay.
- heavy flavour background, hadrons containing heavy quarks decaying semi-leptonically and faking a prompt Z decay.
- combinatorial background, where two final state particles are randomly combined to the mother particle in question.

Figure 6.6 shows a sketch of the angles used in this analysis. The angle φ is the azimuthal angle, whereas the angle θ is the polar angle. Both are defined as the angle between the x or z axis in the xy or yz plane, respectively. Instead of the polar angle, the pseudo-rapidity $\eta = -\ln(\tan(\theta/2))$ is used in the analysis, as it is easier to compare with other experiments. The opening angle R between the Z and the V_0 is defined as $R = \sqrt{\Delta\varphi^2 + \Delta\eta^2}$, where $\Delta\varphi = \varphi_Z - \varphi_{K^0_\mathrm{S}}$ and $\Delta\eta = \eta_Z - \eta_{K^0_\mathrm{S}}$.

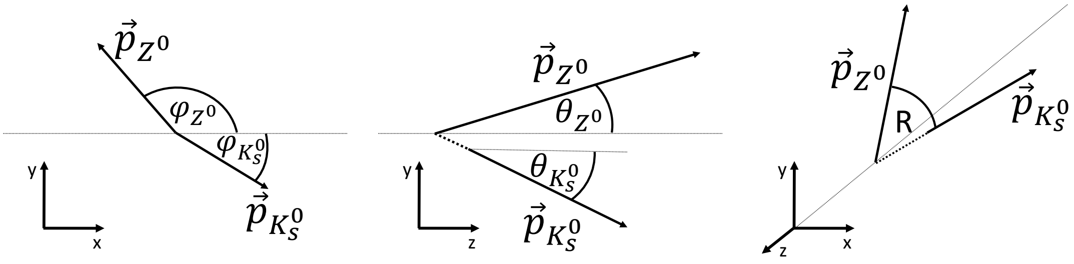

(a) **(b)** **(c)**

Figure 6.6: Figure a) shows the definition of the azimuthal angle φ, b) the definition of the polar angle θ and c) the definition of the opening angle R between Z and V_0.

6.4 Event Selection Strategy

A Z +V_0 event consists of two two-body decays. Measurements of such decays are generally performed in several steps. At first a pre-selection is applied individually to Z and V_0 final state particles to reject events with different decay signatures. Here, $Z \rightarrow \mu^+\mu^-$ candidates are selected according to ref. [141] and a loose selection is applied for V_0. Only long tracks are considered for the final state particle candidates of V_0, as the good vertex resolution of long tracks is needed for the pile-up separation. One of the muons from $Z \rightarrow \mu^+\mu^-$ is used to trigger the event. At the end of the pre-selection a vertex fit for the combination of both composite particle candidates is performed.

While the Z candidates are very pure, the pre-selected samples still contain background for the V_0 candidates. The combinatorial background from random combinations of two tracks is reduced to a manageable level by applying a gradient Boosted Decision Tree (gBDT). A sideband subtraction in the invariant mass of the V_0 removes then the remaining combinatorial background under the signal peak. The peaking backgrounds from real resonances are removed by rejection cuts. Signal candidates and the last remaining background, pile-up, are separated by a cut on the vertex fit quality the ZV_0 combination The details of the selection will be discussed in the next sections.

6.5 Data Samples

The data was collected in pp collisions at a centre of mass energy of 8 TeV in 2012 by the LHCb detector. The sample corresponds to a total integrated luminosity of 2 fb^{-1}. Collisions were recorded for both magnet polarities at equal fraction. For testing the event selection a Monte

Carlo (MC) simulation sample with one million generated $Z \rightarrow \mu^+\mu^-$ events at 8 TeV centre of mass energy with both magnet polarities was used. The simulated pp collisions are generated using Pythia 6 [132] with a specific LHCb configuration [131]. Decays of hadronic particles are described by EvtGen [142] in which final-state radiation is generated using photos [143]. The interaction of the generated particles with the detector, and its response, are implemented using the Geant4 toolkit [144, 145] as described in Ref. [146]. The same detector reconstruction software is applied as on the collision data set. For both simulated and measured data the same triggers as well the same centralised selection (stripping) were applied. The trigger configuration and the stripping selection are described in the following.

6.5.1 Trigger

An event candidate is triggered by requiring in a first step (LO), that at least one muon has a p_T higher than 1.5 GeV/c and that there are less than 600 hits in the scintillating pad detector (SPD). This latter cut, called global event cut (GEC), is applied to reject high particle multiplicity events, which would dominate the processing time in the further reconstruction. In a second step (HLT1), one reconstructed muon must have a p_T larger than 4.8 GeV/c and a momentum p larger than 8 GeV/c. Furthermore, the χ^2 of the track fit per degree of freedom has to be smaller than four. In the last step of the trigger (HLT2), it is required that at least one muon has a p_T large than 10 GeV/c. All three steps combined are called high-p_T single muon trigger line. Table 6.1 summarises the required cuts of the trigger line.

Table 6.1: Trigger requirements for the high-p_T single muon trigger line. They are split according to the trigger levels in LHCb.

Trigger level	**Condition**
L0	one muon $p > 1.5$ GeV/c SPD hits < 600
HLT1	one muon $p > 8$ GeV/c $p_T > 4.8$ GeV/c track χ^2/ndf < 4
HLT2	one muon $p_T > 10$ GeV/c

An additional trigger line, the dimuon trigger, is used for the efficiency study of the 600 SPD hit threshold of the high-p_T single muon trigger line. In the first step, an event with two muons needs to have less than 900 hits in the SPD and the product of the p_T of the two muon is required to satisfy a minimum ${p_T}^2 > (1.3\,\text{GeV}/c)^2$. In the second step, the events must contain two muons with p_{T} larger than 0.5 GeV/c, p larger than 6 GeV/c and χ^2 of the track fit per degree of freedom smaller than four. In addition, the event is required to have a dimuon invariant mass $M_{\mu\mu} > 2.7\,\mathrm{GeV}/c^2$. In the third step, the events need to have a χ^2 of the vertex fit of the two muons divided by the degree of freedom of less than 25 and a dimuon invariant mass $M_{\mu\mu} > 40\,\mathrm{GeV}/c^2$. Table 6.2 summarises the required cuts of the dimuon trigger line.

Table 6.2: Trigger requirements for the dimuon trigger line. They are split according to the trigger levels in LHCb.

Trigger level	**Condition**
L0	${p_{\mathrm{T}}}^2 > (1.3\,\mathrm{GeV}/c)^2$
	SPD hits < 900
HLT1	$p > 6\,\mathrm{GeV}/c$
	$p_{\mathrm{T}} > 0.5\ \mathrm{GeV}/c$
	track χ^2/ndf < 4
	$M_{\mu\mu} > 2.7\,\mathrm{GeV}/c^2$
HLT2	vertex χ^2/ndf < 25
	$M_{\mu\mu} > 40\,\mathrm{GeV}/c^2$

6.5.2 STRIPPING

The concept of stripping lines and particle containers is particular to LHCb. They are nothing else than generalised or most commonly used selection requirements (more information are given in 3.2.4). In this analysis the stripping line for the inclusive $Z \to \mu^+\mu^-$ analysis [141] is used (WMuLine). This line requires one muon with $p_{\mathrm{T}} > 15\,\mathrm{GeV}/c^2$ from the StdAllLooseMuons particle container. There exists no stripping line with the appropriate cuts for the V_0's, therefore the final state particle candidates are taken directly from the containers, StdAllNoPIDsPions and StdAllNoPIDsProtons.

The StdAllLooseMuons particle container requires a charged particle candidate with the particle identification (PID) consistent with the muon hypothesis. This hypothesis is used to calculate the particle properties. Both containers, StdAllNoPIDsPions and StdAllNoPIDsProtons have no requirement on the particle identification (PID). Particles in these containers have to be charged long tracks where the properties are calculated with the corresponding mass hypotheses.

6.6 *Z* Selection

The *Z* selection follows reference [141]. Event candidates consist of two oppositely charged tracks, which are well reconstructed and identified as muons. The combined dimuon mass, $M_{\mu\mu}$ has to be in the range of $60 < M_{\mu\mu} < 120\,\text{GeV}/c^2$. Furthermore each muon track must have a transverse momentum $p_{\text{T}} > 20\,\text{GeV}/c$ and lie in the pseudo-rapidity range $2 < \eta < 4.5$, which is motivated by the detector acceptance and the kinematic cut-off. The probability χ^2 of the track fit (Prob (χ^2_{trk} , ndf)) must be larger than 0.1% and the relative uncertainty on the momentum measurement has to be less than 10%. In addition, at least one muon has to satisfy the requirements of the high-p_{T} single muon trigger line. Table 6.3 summarises the selection cuts.

Table 6.3: Summary of the selection cuts of $Z \rightarrow \mu^+\mu^-$ taken from [141].

Variable	**Value**
Muons	
p_{T} [GeV/c]	> 20
η	[2.0,4.5]
Prob(χ^2_{trk}, ndf)	>0.001
σ_p/p	<0.1
***Z* candidate**	
$M_{\mu\mu}$ [GeV/c^2]	[60,120]
Trigger for one muon	
high-p_{T} single muon trigger line	

Figure 6.7 shows the invariant mass distribution of the selected *Z* candidates. From the studies in reference [141] it is known that the purity, defined as the ratio of signal to total candidate events, is almost 100%. Backgrounds from misidentified muons or from the decay of hadrons containing heavy quarks contribute less than 0.3%. Therefore, background contributions to the *Z* are neglected in the further analysis. The tail on the left of the *Z* peak consist of two contributions. One part is the radiative tail of *Z* events, due to photon radiation of the muons. The second part is coming from the Drell-Yan γ^* production and $\gamma^* Z$ interference. In the following, *Z* always includes γ^* and $\gamma^* Z$. In total 144293 $Z \rightarrow \mu^+\mu^-$ candidates are selected in data.

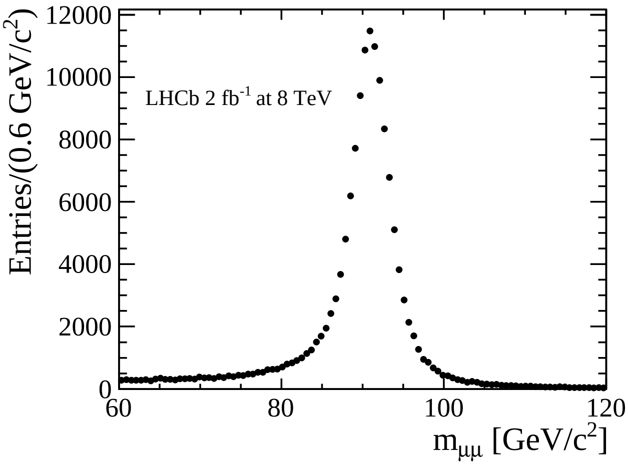

Figure 6.7: The invariant mass $m_{\mu\mu}$ is shown. The left tail consist of a radiative tail from the mass peak, due to photon radiation of the muons and contribution from the Drell-Yan γ^* and $\gamma^* Z$ interference.

6.7 ZV_0 SELECTION

6.7.1 LOOSE SELECTION OF ZV_0

Final state candidates of V_0 have, in contrast to the corresponding particle candidates in the Z selection, not passed through a stripping line. Accordingly a loose selection is applied to reduce the number of falsely identified V_0 candidates for the further analysis.

In general a V_0 particle decays in two daughter particles, the final state particles which are measured by the detector. At first, these final state particles have to lie in the geometrical acceptance of the experiment. This implies, in case of LHCb, the pseudo-rapidity has to satisfy $2.0 < \eta < 4.5$. Further, each final state particle needs to have a $p > 2\,\mathrm{GeV}/c$ and a track fit χ^2 divided by the number of degrees of freedom, $\chi^2/\mathrm{ndf} < 5$. The invariant mass of the combination of both final state particles has to satisfy the following conditions. In case of K^0_S the invariant mass of the two pions has to lie in a 100 MeV/c^2 range around the known mass of K^0_S [16]. For Λ the invariant mass of the combination of proton and pion has to lie in a 35 MeV/c^2 range to the known mass of Λ [16]. In addition, it is required that the two particles come from a common vertex. The vertex fit of both final state particles, representing the decay vertex of the mother particle V_0, has to fulfil the requirement, vertex fit $\chi^2/\mathrm{ndf} < 9$. Table 6.4 shows the properties of K^0_S and Λ and table 6.5 summarises the loose selection requirements. Figure 6.8 shows the invariant mass of the di-pion system for K^0_S in data with 4‘163‘852 candidates and the invariant mass of the proton, pion system for Λ in data with 988‘573 candidates after the loose selection. Both are dominated by combinatorial background.

Table 6.4: Properties of K^0_S and Λ taken from the PDF[16], where the decay width is calculated from the lifetime.

	K^0_S	Λ
mass	(497.614 ± 0.024) MeV/c^2	(1115.683 ± 0.006) MeV/c^2
lifetime τ	$(0.8954 \pm 0.0004) \cdot 10^{-10}$s	$(2.632 \pm 0.020) \cdot 10^{-10}$s
decay width	$\sim 7 \cdot 10^{-6}$ eV	$\sim 2.5 \cdot 10^{-6}$ eV
LHCb resolution σ	$\sim$3 MeV/c^2	$\sim$1 MeV/c^2

Table 6.5: Summary of the selection cuts of ZV_0.

Variable	**Value**
Final state particles	
p [GeV/c]	> 2
η	[2.0,4.5]
track fit χ^2/ndf	<5
V_0 **candidate**	
$\lvert M_{\pi\pi} - PDG_{K^0_S}\rvert$ [MeV/c^2]	<100
$\lvert M_{p\pi} - PDG_{\Lambda}\rvert$ [MeV/c^2]	<35
vertex fit χ^2/ndf	<9

Further, a vertex fit is run to combine Z and V_0. It is called DecayTreeFitter, a detailed description is given in [147]. Standard least-square vertex fits use an iterative approach, they start by fitting the vertices most downstream in the decay and build up the tree by propagating information upstream. The DecayTreeFitter algorithm instead parametrises the decay chain in terms of vertex positions, decay lengths and momentum parameters. Afterwards, the algorithm performs a simultaneously fit to these parameters, taking into account relevant constrains, such as the measured parameters of the final state tracks and 4-momentum conservation at each vertex. Furthermore, it is possible to constrain the mass of composite particles in the decay tree to their known particle mass, or constraining the head of the decay tree to the known interaction point. In case of neutral daughter particles the DecayTreeFitter leads to a more accurate fit than the standard least-square vertex fit.

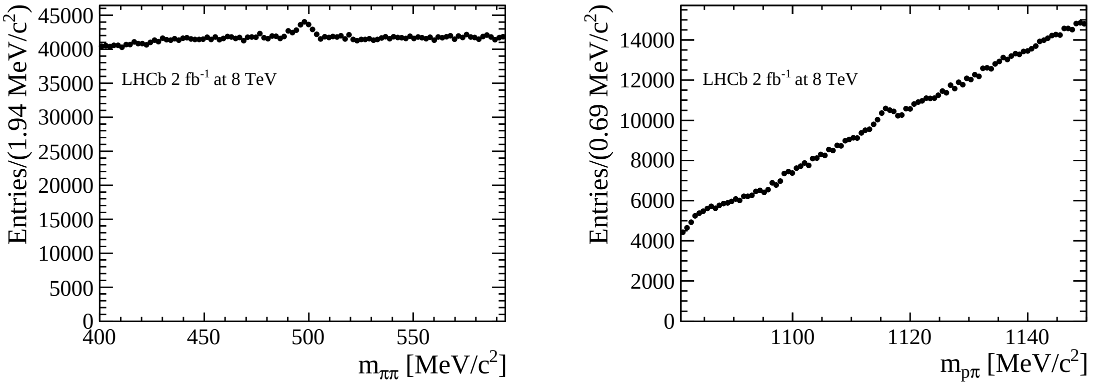

Figure 6.8: In the left (right) figure the invariant mass $m_{\pi\pi}$ ($m_{p\pi^-}$) of the K^0_S (Λ) candidates is shown after the loose selection.

6.7.2 Combinatorial Background

After the loose selection a large fraction of the remaining candidates are random combinations of two pions to a K^0_S or a proton and a pion to a Λ called combinatorial background. Instead of applying individual cuts for V_0 and the ZV_0 combination, the usage of the combined information from all observables results in a more powerful separation of signal candidates and combinatorial background. This type of analysis is called, Multi Variate Analysis (MVA). In general, MVAs are categorised in classification, regression and clustering algorithms. The separation of two samples, is an optimal job for classification algorithms (classifier). An introduction for the other two algorithms is given in ref. [148].

A simple type of a MVA classifier (a Fisher discriminant) was used in LHCb for the analysis of the prompt production of K^0_S in ref. [149]. This classifier is a linear combination of variables and is optimised to separate signal and background as far as possible from each other in the variables phase space. More information about the Fisher discriminant is given in ref. [150].

For this analysis a Boosted Decision Tree (BDT) is used. In the following, the terms decision tree and boosting are introduced.

6.7.2.1 Decision Tree

Decision trees are nowadays commonly used, most of the time the user does not even know he is using one. This trees are a graphical representation of a classification problem. One tree starts with a single decision on a certain condition and branches off into a number of solutions, like a real tree. The building of a decision tree is called training. For this step a sample of simulated events, containing background and signal, is split into a training and a testing data set. It is necessary to split the data sample, as a model optimised for a specific data can get a perfect separation on the same data and could fail completely to separate other data. Therefore a separate testing data set is needed for measuring the performance. The true category, signal or background, is known for each event in both data sets.

The first step in the training consist of finding the variable, which results in the best separation of the training data set in the signal and the background category. Then the first ”node” is built and the two data sets, separated by the variable with the best separation power, are called ”branches”. The branch with the best increase in the quality of separation is picked to split further into signal and background enhanced branches. The criterion for the decision which branch is of higher quality for the separation, is part of the algorithm used to build the decision tree. Despite some small differences between different algorithms, the quality criterion depends mostly on the purity of the branch. Final branches with no further splitting are called ”leaves”. The splitting stops, if either the quality of separation is not increasing or the maximum number of leafs is reached. In the end, if a leaf has a signal purity higher than 50%, it is called signal otherwise background leaf. Events are sorted as signal, if they are classified in a signal leaf and background, if they are classified in a background leaf. The resulting tree is called a decision tree.

Figure 6.9 shows a schematic of a decision tree. Three variables are used for the separation of signal and background: the event hit multiplicity and the energy and reconstructed radial position of a reconstructed object. Further information is given in ref. [151].

6.7.2.2 Boosting

Decision trees are extremely powerful but unstable as well. They are heavily depending on the training sample. Boosting algorithms were invented to create out of weak learners[2] a strong learner [152]. For the following discussion decision trees are taken as an example for a weak learners.

In general terms, a boosting algorithm starts with an unweighted event data set which is used to build a tree, as described in the last paragraph. The resulting classification is examined for misclassified events. Events are misclassified, if a signal event ends up in a background leaf or the other way around. Those events get a higher weight than the correct ones. This weighting procedure is called boosting, the calculation of the individual weights depends on the boosting

---

[2] learning algorithms which are performing just slightly better than random guessing [152].

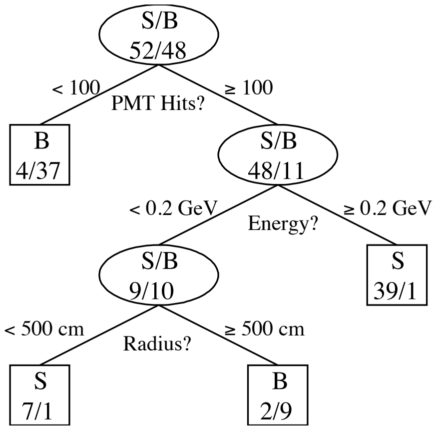

Figure 6.9: Diagram of a decision tree. S stands for signal and B for background. Black boxes are terminal nodes, called leaves. The category of the leave depends on what kind of event is dominant. The classification variables are the event multiplicity (PMT Hits) and the energy and the radial position of a reconstructed object [151].

algorithm. Afterwards a second tree is built with the newly weighted event data set. The procedure is repeated typically several hundred times, resulting in as many trees as repetitions.

As a final output a score is assigned to each event. Following each event through the trees in turn, if it ends up in a signal leaf a score of 1 is assigned and if it ends up in a background leaf a score of -1 is assigned. Generally, high scores are indicating that the event is most likely a signal event and low sores indicate that it is most likely a background event. This score is used to separate signal and background by choosing a cut value according to the desired signal significance of the classifier. The most commonly used metric to estimate the significance is

$$\mathrm{Sig} = \frac{S}{\sqrt{S+B}}, \tag{6.1}$$

where S and B are the number of signal and background events. Ref. [153] discusses additional metrics for estimating the signal significance.

6.7.2.3 MULTIVARIATE SELECTION

There are many Boosted Decision Tree (BDT) algorithms available. For this analysis the Gradient Boosted Decision Tree (gBDT) [154, 155] is used from the scikit-learn package [148]. As an advantage to other algorithms, it is not sensitive to the type of the input variables and allows different algorithm to calculate the weights.

The gBDT uses in total seven variables for each ZV_0 decay. Both, ZK_S^0 and $Z\Lambda$ use the same variables:

- The flight distance (FD) significance of the V_0, which is the ratio of the FD divided by its uncertainty;
- The χ^2 of the vertex fit of the V_0;
- The χ^2 of the vertex fit of the Z;
- The cosine of the angle between the sum of all momentum vectors of the daughter particles of the V_0 and the connection vector between the primary vertex and the decay vertex (DIRA), see fig. 6.10;
- The impact parameter (IP) χ^2 of the V_0 and of the two daughter particles (see fig. 6.11).[3]

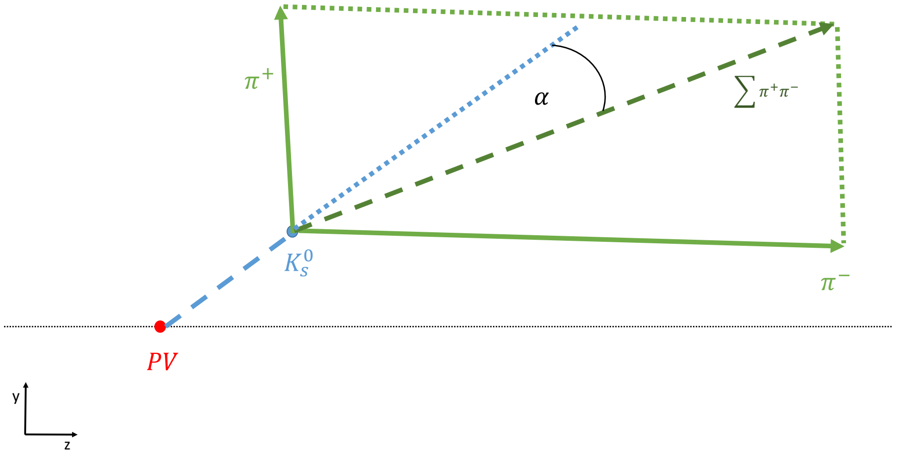

Figure 6.10: The angle α between the sum of all momentum vectors of the daughter particles of the K_S^0 in green and the connection vector between the primary vertex and the decay vertex in blue is shown.

The signal and combinatorial background sample are both taken from simulation. The signal candidates must be generated as Z and V_0 from the same production vertex. The combinatorial background sample consist of simulated event candidates from the invariant mass sideband of the V_0. The sideband definition is the same as for the signal extraction described in section 6.8.

---

[3] The impact parameter χ^2 gives a measure of the compatibility of the track with originating from the primary vertex.

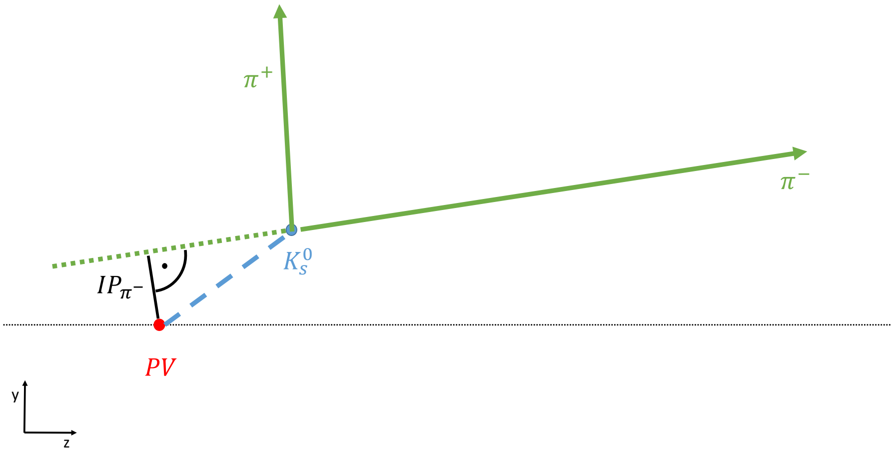

Figure 6.11: The impact parameter (IP) of the π^- is shown.

Figure 6.12 and 6.13 show the comparison of simulation and data in the gBDT variables after the pre-selection including signal and background. Overall, the simulation describes the data well enough to ensure that no bias is introduced by using only simulation for the training.

The comparison of the variables for signal and combinatorial background in simulation are shown in fig. 6.14 for ZK_S^0 and in fig. 6.15 for $Z\Lambda$. The behaviour is in both cases the same. As expected, there is a large difference in the decay length significance between signal and combinatorial background. In addition, the distribution in DIRA of the V_0 is quite different for signal and combinatorial background. The daughter particles in the signal are strongly boosted into the same direction as the mother particle. Also the IP χ^2 distributions of the daughter particles and the mother particle show large differences. The daughter particles tend to have larger and the mother particles smaller IP χ^2 values in the signal sample than in the combinatorial background sample. Both χ^2 values of the vertex fits of the Z and V_0 tend to have smaller values in signal than in combinatorial background, but the differences are small.

Figure 6.16 shows the relative importance of the various variables in the trained gBDT. The IP χ^2 of the proton is dominating the gBDT of the $Z\Lambda$, the other variables contribute between 5 to 15% to the classifier. No variable is clearly dominating in the gBDT of the ZK_S^0 sample, but the χ^2 of the vertex fits play a rather small role in the classifier.

A major issue of multivariate analyses is overtraining. This occurs, if the training of the classifier is done with too many variables for a too small data set or in case of a BDT, if the boosting is too exhausting. In fig. 6.17, the gBDT response of the training is compared to the response of

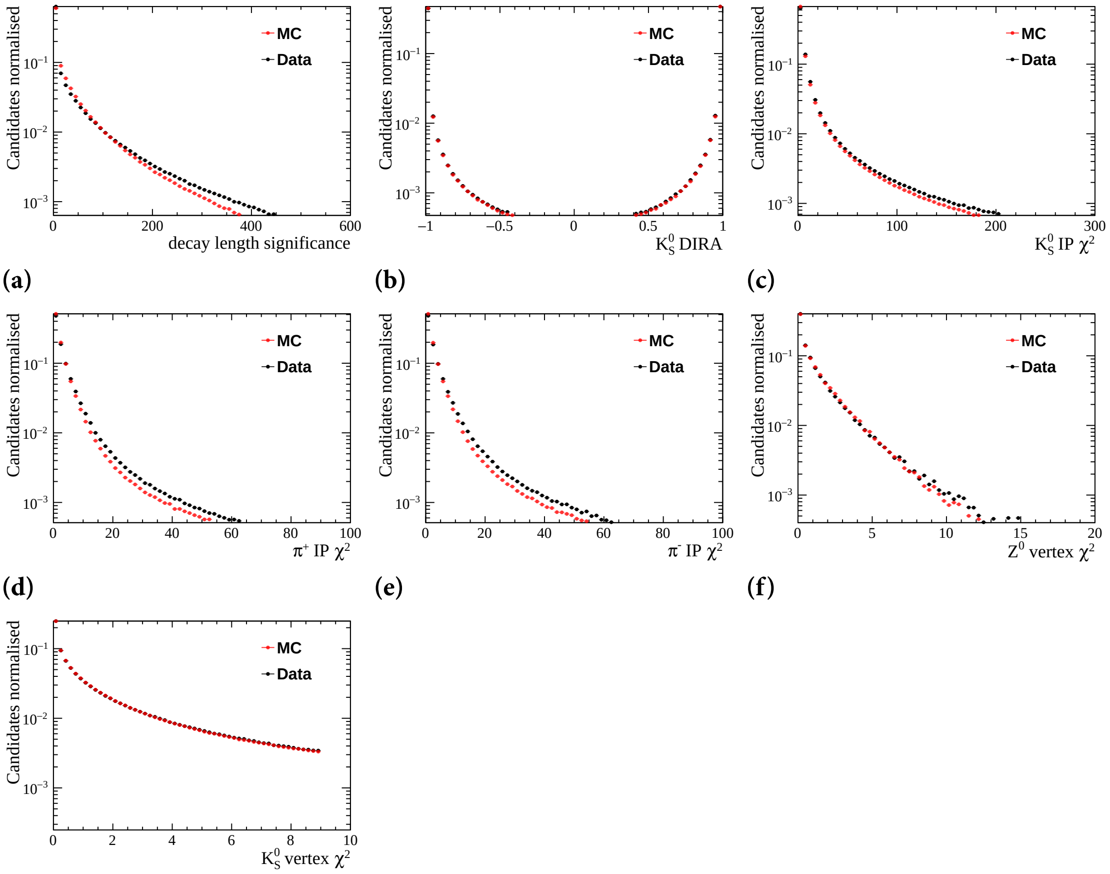

(a) **(b)** **(c)** **(d)** **(e)** **(f)** **(g)**

Figure 6.12: The BDT input variables are shown for the ZK_S^0 sample after preselection. Data is shown in black and simulation in red. The variables are a) the decay length significance of K_S^0, b) the cosine of the angle between the sum of all momentum vectors of the daughter particles of the K_S^0 and the connection vector between his primary vertex and decay vertex (DIRA), c)-e) the impact parameter (IP) χ^2 of the K_S^0 and of the two daughter particles and f)-g) the χ^2 of the vertex fit of Z and K_S^0 respectively.

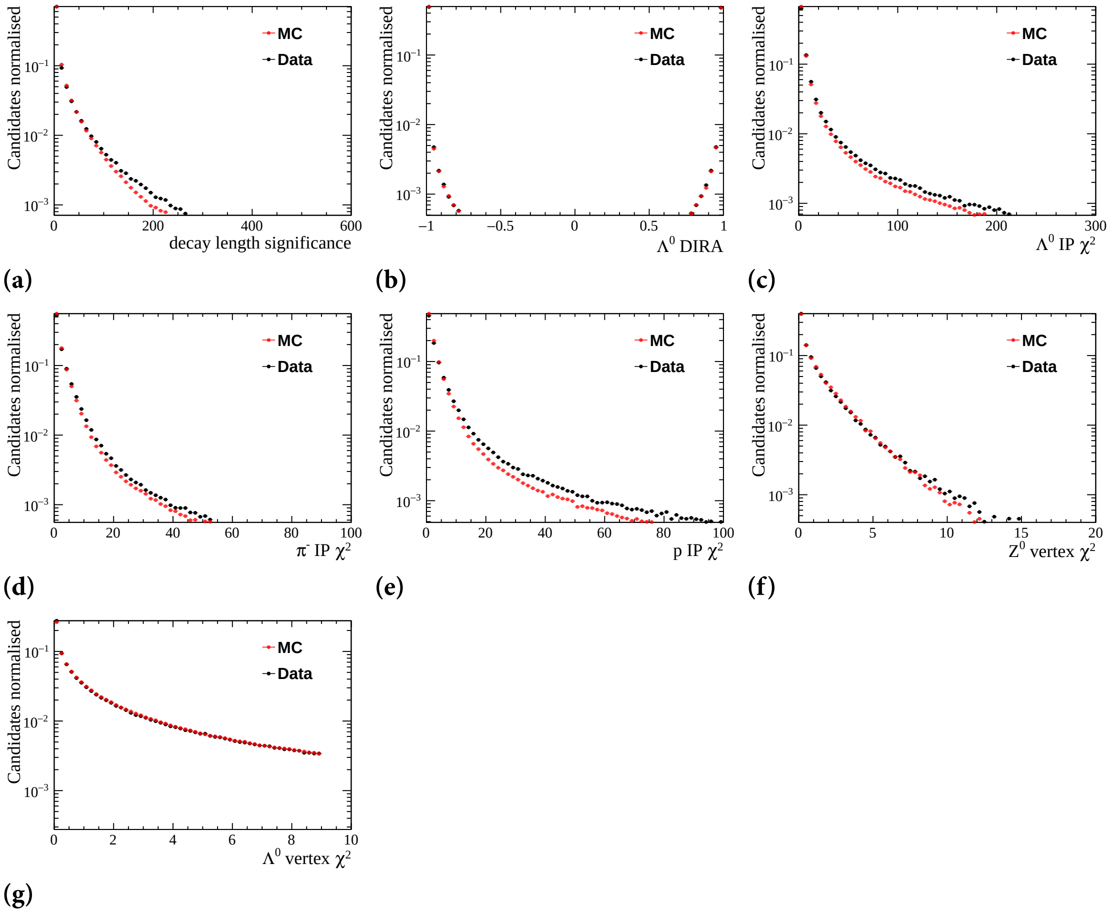

(a) **(b)** **(c)**

(d) **(e)** **(f)**

(g)

Figure 6.13: The BDT input variables are shown for the $Z\Lambda$ sample after preselection. Data is shown in black and simulation in red. The variables are a) the decay length significance of Λ, b) the cosine of the angle between the sum of all momentum vectors of the daughter particles of the Λ and the connection vector between his primary vertex and decay vertex (DIRA), c)-e) the impact parameter (IP) χ^2 of the Λ and of the two daughter particles and f)-g) the χ^2 of the vertex fit of Z and Λ respectively.

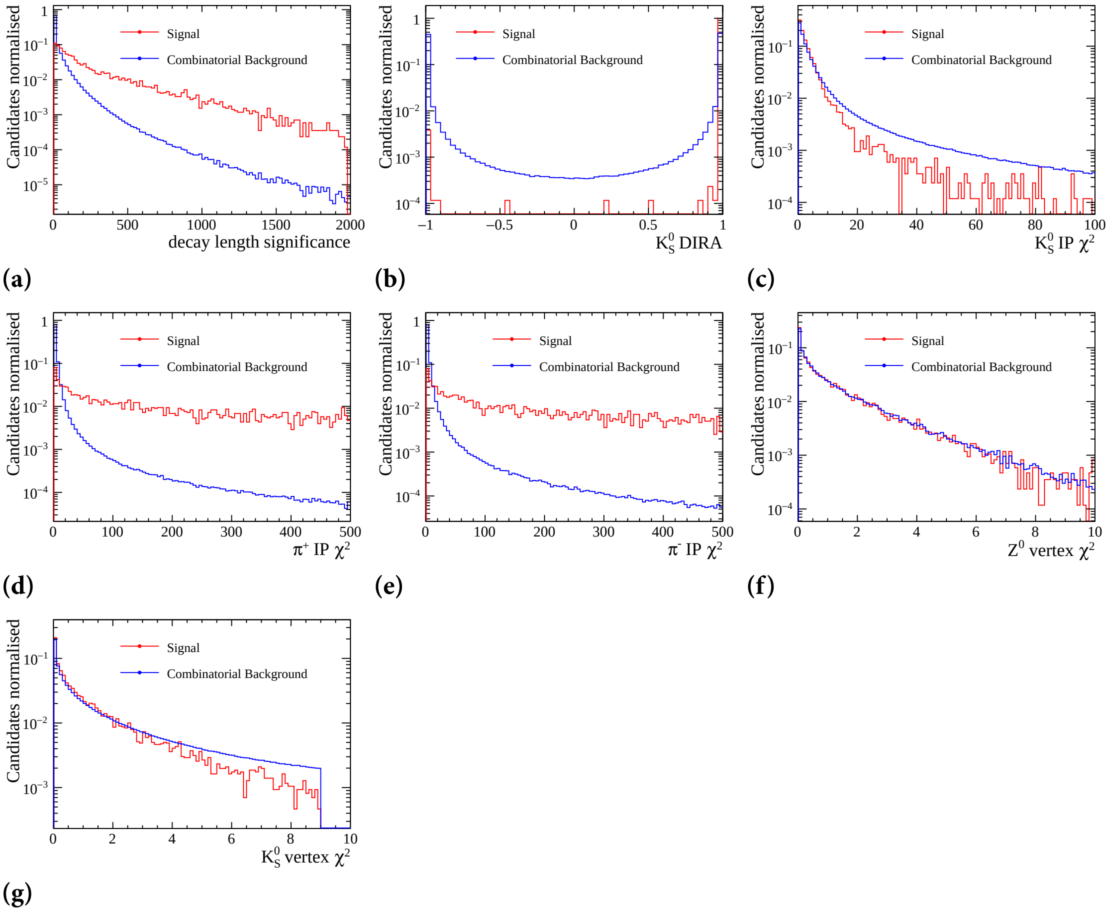

Figure 6.14: The BDT input variables in simulation are shown for the ZK^0_S sample after preselection. The signal sample is shown in red and the combinatorial background sample in blue. The variables are a) the decay length significance of K^0_S, b) the cosine of the angle between the sum of all momentum vectors of the daughter particles of the K^0_S and the connection vector between his primary vertex and decay vertex (DIRA), c)-e) the impact parameter (IP) χ^2 of the K^0_S and of the two daughter particles and f)-g) the χ^2 of the vertex fit of Z and K^0_S respectively.

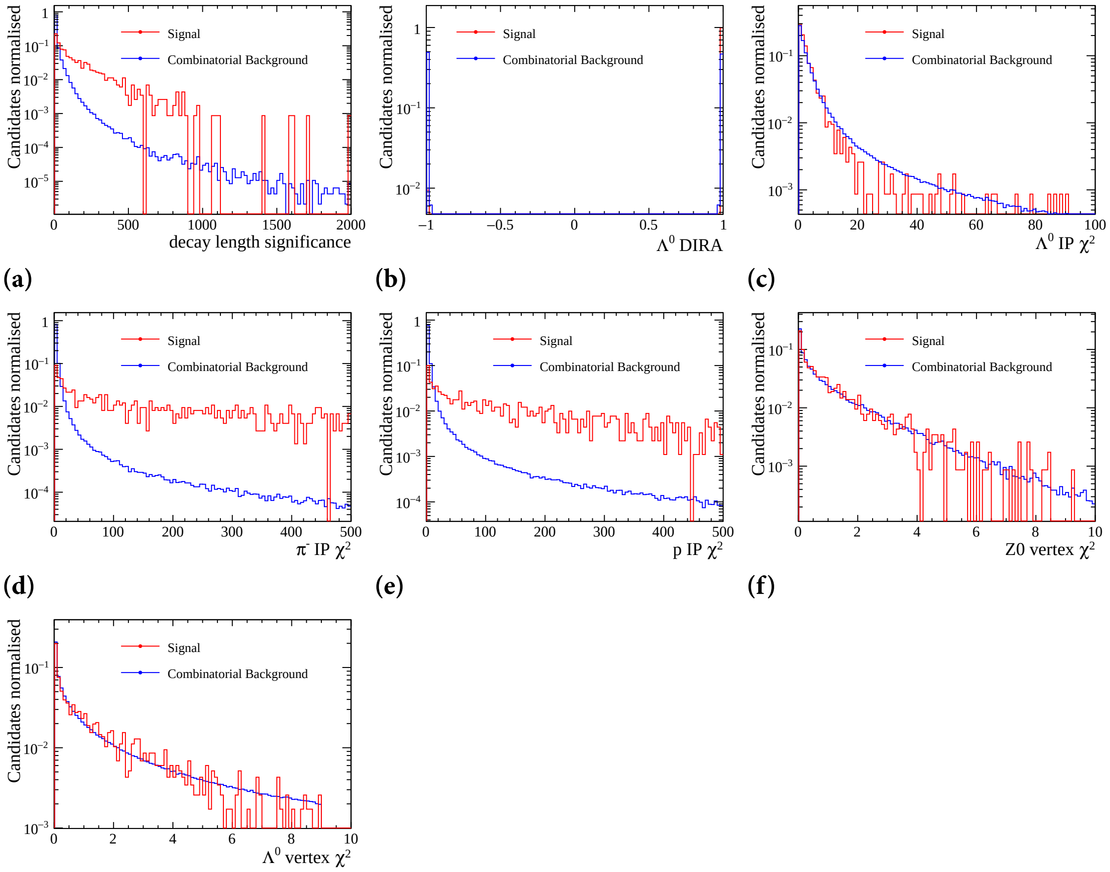

(a) **(b)** **(c)**

(d) **(e)** **(f)**

(g)

Figure 6.15: The BDT input variables in simulation are shown for the $Z\Lambda$ sample after preselection. The signal sample is shown in red and the combinatorial background sample in blue. The variables are a) the decay length significance of Λ, b) the cosine of the angle between the sum of all momentum vectors of the daughter particles of the Λ and the connection vector between his primary vertex and decay vertex (DIRA), c)-e) the impact parameter (IP) χ^2 of the Λ and of the two daughter particles and f)-g) the χ^2 of the vertex fit of Z and Λ respectively.

the testing data set. A difference between both would indicate an over-training of the classifier. In both cases a good separation of signal from combinatorial background is observed and no evidence for over-training is found.

For separating signal and background as good as possible, the best cut value on the gBDT response needs to be determined. Therefore the selection performance of the classifier is computed on simulation using the metric $\frac{S}{\sqrt{S+B}}$. The optimal selection cut on the gBDT response is found to be $gBDT > 4.8$ for ZK^0_S and $gBDT > 5.5$ for $Z\Lambda$. Figure 6.18 shows the metric as function of the gBDT response for ZK^0_S and $Z\Lambda$. The best cut values are indicated in red.

After the gBDT selection cut 10‘231 signal candidates for ZK^0_S and 1796 signal candidates for $Z\Lambda$ are left in data. The calculated purity in simulation is 0.65 for ZK^0_S and 0.56 for $Z\Lambda$. Both samples are still containing peaking backgrounds, pile-up and a small fraction of combinatorial background. The invariant mass distributions for ZK^0_S and $Z\Lambda$ are shown in fig. 6.19.

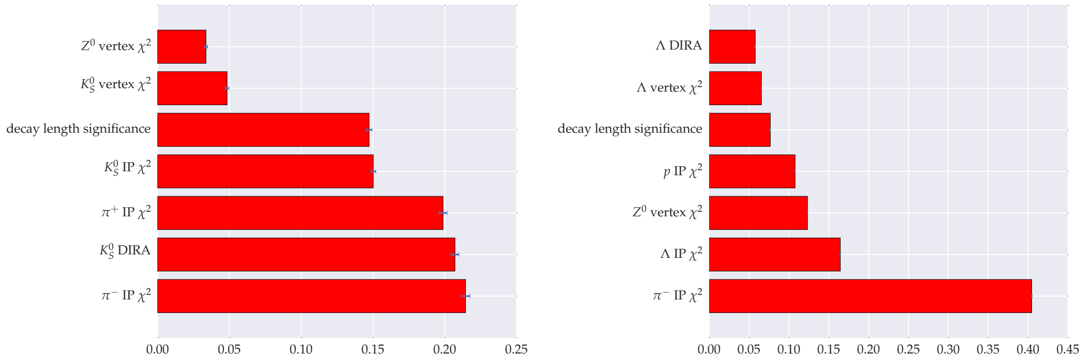

Figure 6.16: The variable importance is shown for ZK^0_S on the left and for $Z\Lambda$ on the right side. The importance is sorted from top to bottom starting with the least important one.

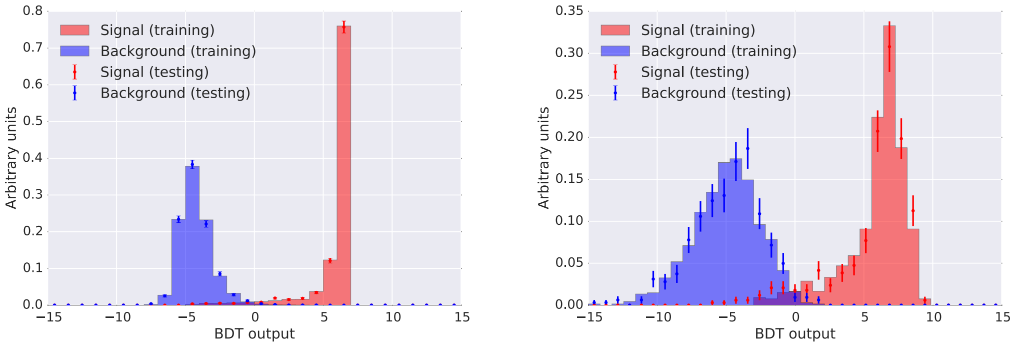

Figure 6.17: Gradient Boosted Decision Tree (gBDT) response for ZK^0_S is shown left, and for $Z\Lambda$ right. In the plots red is used for signal and blue for background. The filled area is the response resulting from the training data set, whereas the points are from the testing data set.

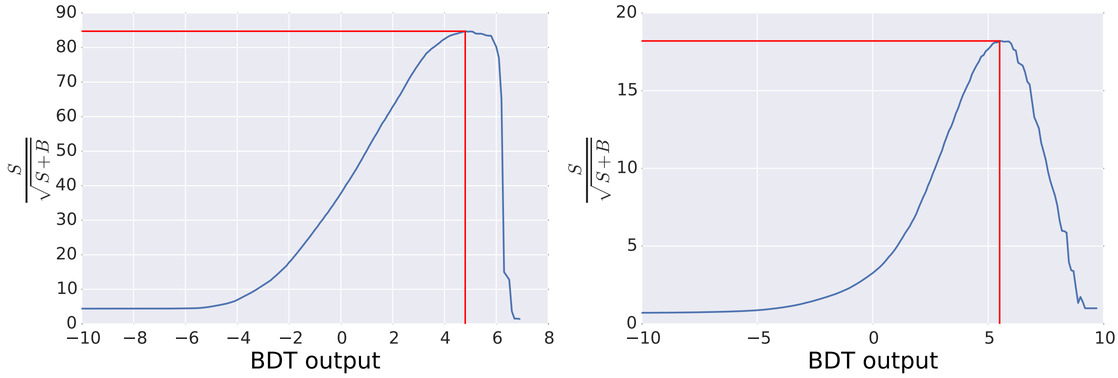

Figure 6.18: The signal significance is shown as a dependence of the gBDT classifier output cut for larger values. The maximum significance with the correspondent gBDT value is indicated in red. Figure left shows the distribution for ZK^0_S and figure right shows it for $Z\Lambda$.

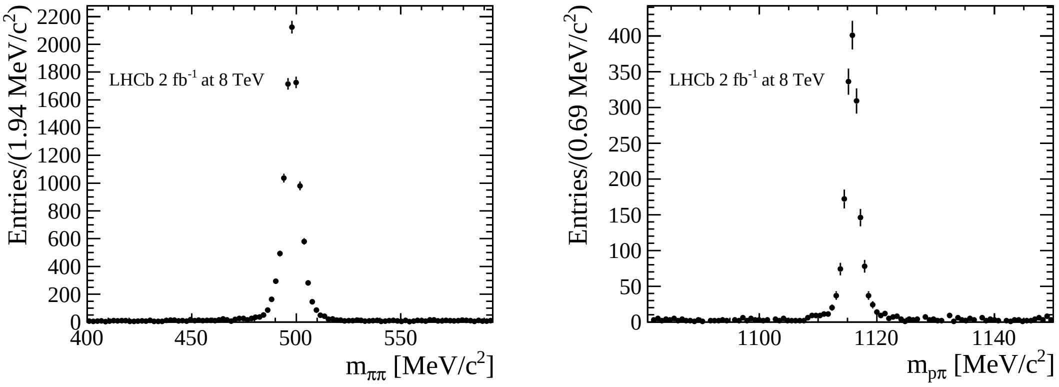

Figure 6.19: Figure left shows the invariant mass $m_{\pi\pi}$ from ZK^0_S after the gBDT selection. Figure right shows the invariant mass $m_{p\pi}$ from $Z\Lambda$ after the gBDT selection as well.

6.7.3 PEAKING BACKGROUNDS

The majority of peaking backgrounds are exclusive decays where one or more particles are misidentified. The strategy to remove peaking backgrounds is for all the same: Final state particles are reconstructed with a different mass hypotheses, corresponding to the mass hypothesis of the peaking background in question. If the newly reconstructed event peaks in the corresponding invariant mass region of the peaking background, it is rejected.

In case of the decay $Z + K^0_S$, where $K^0_S \to \pi^+\pi^-$, the decays $Z + (\Lambda \to p^+\pi^-)$ and $Z + (\overline{\Lambda} \to p^-\pi^+)$ is the most popular source of peaking background, if the proton is mis-reconstructed as a pion. The resulting invariant mass of the double pion system is reconstructed in the region of the K^0_S mass. To reject this background, the mass hypothesis of one of the pions is changed to a proton and the particle properties are recalculated with the new particle hypothesis. It is rejected, if the recalculated invariant mass lies in the range $1100 < M_{p\pi} < 1130\,\mathrm{MeV}/c^2$.

In case of the decay $Z + \mathit{\Lambda}$, where $\mathit{\Lambda} \rightarrow p\pi^-$, the decay $Z + (K^0_\mathrm{S} \rightarrow \pi^+\pi^-)$ is the most popular source of peaking backgrounds, if π^+ is mis-reconstructed as proton. Similar than before the resulting invariant mass of the proton pion system is reconstructed in the region of the $\mathit{\Lambda}$ mass. Now, the mass hypothesis of the proton is changed to a pion and the particle properties recalculated with the new particle hypothesis. The candidate is rejected if the invariant mass is in the range $475 < M_{\pi\pi} < 515\,\mathrm{MeV}/c^2$.

Other peaking background taken into account are $K^{*0}(892) \rightarrow K\pi$, $\Phi \rightarrow K^+K^-$, $D^0 \rightarrow K^-\pi^+$, $\rho \rightarrow \pi^+\pi^-$ and $\omega \rightarrow \pi^+\pi^-$. All of them are negligible in case of both decays, ZK^0_S and $Z\mathit{\Lambda}$.

Table 6.6 summarises the background level and signal loss estimate on simulation after the gBDT selection for various decay modes using the branching-fractions from the PDG [16].

Table 6.6: Summary of the background level and signal loss estimate for the ZK^0_S and $Z\mathit{\Lambda}$ on simulation using the branching-fractions from the PDG [16]. All decay modes except $\mathit{\Lambda} \rightarrow p\pi^-$ for ZK^0_S and $K^0_\mathrm{S} \rightarrow \pi^+\pi^-$ for $Z\mathit{\Lambda}$ are found to be negligible.

	ZK^0_S		$Z\mathit{\Lambda}$	
Decay mode	**Level [%]**	**Signal loss [%]**	**Level [%]**	**Signal loss [%]**
$K^0_\mathrm{S} \rightarrow \pi^+\pi^-$			32.4 ± 0.8	16.5 ± 1.2
$\mathit{\Lambda} \rightarrow p\pi^-$ [a]	7.1 ± 0.2	3.4 ± 0.2		
$K^{*0}(892) \rightarrow K\pi$	$0.000^{+0.010}_{-0.000}$		$0.00^{+0.05}_{-0.00}$	
$\Phi \rightarrow K^+K^-$	$0.006^{+0.013}_{-0.005}$		$0.00^{+0.05}_{-0.00}$	
$D^0 \rightarrow K^-\pi^+$	$0.067^{+0.025}_{-0.019}$		$0.03^{+0.07}_{-0.02}$	
$\rho \rightarrow \pi^+\pi^-$	$0.017^{+0.016}_{-0.009}$		$0.00^{+0.05}_{-0.00}$	
$\omega \rightarrow \pi^+\pi^-$	$0.056^{+0.023}_{-0.017}$		$0.00^{+0.05}_{-0.00}$	

---

[a] and charge conjugate

6.7.4 PODOLANSKI-ARMENTEROS

In 1953 J. Podolanski and R. Armenteros proposed a new way of analysing two-body decays in flight [156]. They introduced a set of variables built of measured quantities, which allows to separate decay types in a more convenient way. In detail, different decay types form distinct eclipse in the new variable set. The most famous set of variables are the transverse momentum with respect to the direction of flight of the decaying mother particle $\tilde{p}_\mathrm{T}$ and the combination of longitudinal momenta of the daughter particles again with respect to the flight direction of the mother particle,

$$\alpha = \frac{\tilde{p}_{\mathrm{L},1} - \tilde{p}_{\mathrm{L},2}}{\tilde{p}_{\mathrm{L},1} + \tilde{p}_{\mathrm{L},2}}. \tag{6.2}$$

Figure 6.20 shows the Podolanski-Armenteros plot for V_0 candidates acquired in the measurement of the inclusive V_0 production cross-section measurement at HERA-B [157]. The ellipse in the plot is symmetrical around $\alpha = 0$, if both daughter particles have equal or similar masses. If the daughter particles have non equal mass, the ellipse is asymmetrical. The K^0_S decays are distributed symmetrical and the Λ decays asymmetrical as expected. The ellipses from K^0_S, Λ and $\overline{\Lambda}$ overlap. This indicates that in certain kinematic regions the V_0 is ambivalent in terms of the Podolanski-Armenteros plot.

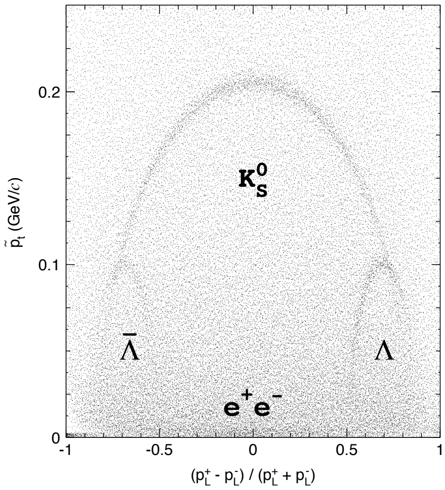

Figure 6.20: Podolanski-Armenteros plot for V_0 candidates from HERAb [157]. The y-axis shows the transverse momentum $\tilde{p}_\mathrm{T}$ of the oppositely charged decay products, the x-axis the α parameter from Podolanski and Armenteros. The different decay modes are indicated in the figure. Background from $\gamma \rightarrow e^+e^-$ conversions are slightly visible below $\tilde{p}_\mathrm{T}$ = 0.0015 GeV/c.

This new set of variables can be used to cross-check visually the peaking background rejection and the gBDT selection. Figure 6.21 shows the Podolanski-Armenteros plot directly after the loose selection for collision data. Since, in the analysis Λ and $\overline{\Lambda}$ are not separated, there is only one of the asymmetric eclipses. If the proton or the pion is particle one in eq. (6.2), either the left or the right eclipse is shown. In this analysis the pion is used as particle one in eq. (6.2). In red the signal simulation is overlaid over the collision data, outside of the red band the background is visible. The background candidates are not covering the whole (p_T,α) phase space, due to the kinematic of the decay and the loose selection cuts.

Figure 6.22 shows the data after the gBDT selection is applied, but no rejection of peaking backgrounds. Two small eclipses are visible with a maximum in $\tilde{p}_{\mathrm{T}}$ of 100 MeV/c for both at $\alpha = -0.75$ and at $\alpha = 0.75$ in fig. 6.22 left. These are the Λ peaking background components to the K^0_{S} signal candidates. For Λ in fig. 6.22 right, one part of the eclipse of the K^0_{S} peaking background is visible at the top of the Λ eclipse.

The Podolanski-Armenteros plots of the V_0s after the gBDT selection including the peaking background rejection are shown in fig. 6.23. The rejection cuts are visible in both cases, K^0_{S} and Λ. A comparison of fig. 6.23 and fig. 6.20 shows that the eclipses for K^0_{S} respectively for Λ are exactly at the same position in the ($\tilde{p}_{\mathrm{T}}$,α) phase space.

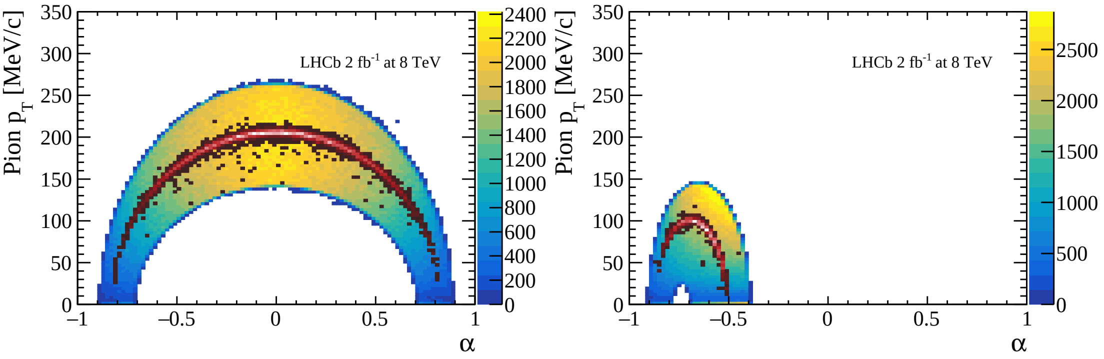

Figure 6.21: Figure left shows $\tilde{p}_{\mathrm{T}}$ of one pion vs the Podolanski-Armenteros parameter α for ZK^0_{S} candidates after the loose selection. The distribution is symmetrical around zero. Figure right shows the $\tilde{p}_{\mathrm{T}}$ of one of the pions vs α for $Z\Lambda$ with loose selection only. The distribution is asymmetrical and only with negative α, the explanation is given in the text. In both figures the eclipse for signal simulation is overlaid in red.

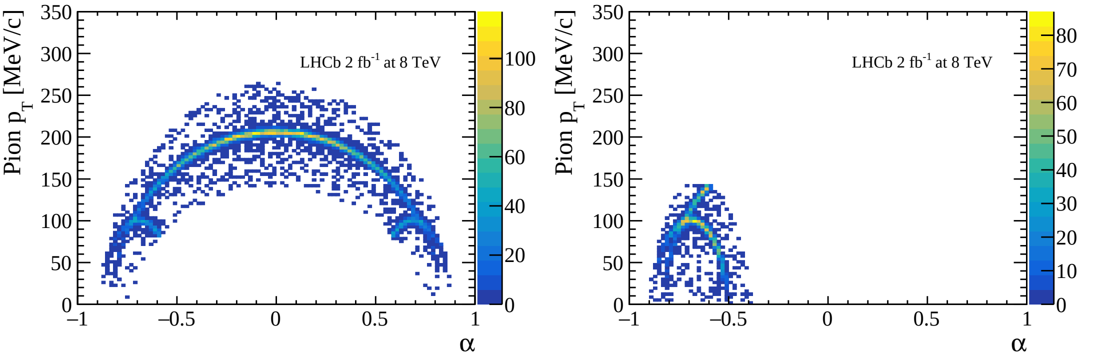

Figure 6.22: Figure left shows the $\tilde{p}_{\mathrm{T}}$ of one Pion the Podolanski-Armenteros parameter α for ZK^0_{S} candidate events after the loose selection and gBDT cuts. Two eclipses are visible at $\alpha = \pm 0.75$ induced by the peaking background from Λ and $\bar{\Lambda}$. Figure right shows the $\tilde{p}_{\mathrm{T}}$ of the pion vs α for $Z\Lambda$ candidate events after the loose selection and gBDT cuts. One part of the eclipse of the K^0_{S} peaking background visible.

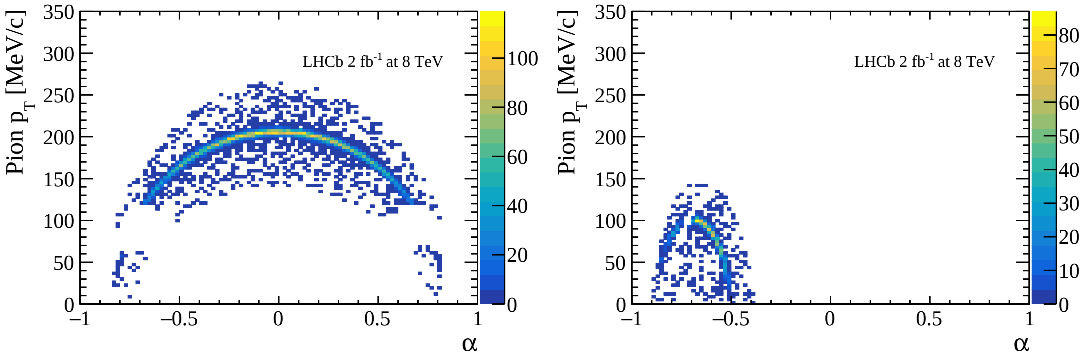

Figure 6.23: Figure left shows the $\tilde{p}_\mathrm{T}$ of one Pion vs the Podolanski-Armenteros parameter α for ZK^0_S candidate events with all selection cuts applied. At both sides the regions are visible where the peaking background veto is applied. Figure right shows the $\tilde{p}_\mathrm{T}$ of the pion vs α for $Z\Lambda$ candidate events with all selection cuts applied. A cut out region is as well visible, coming from the peaking background veto.

6.8 YIELD EXTRACTION

Four different event categories were discussed in section 6.3: signal candidates, combinatorial background, which is reduced to a minimum by the multivariate analysis described in section 6.7.2, peaking background which is fully rejected by applying appropriate cuts (see section 6.7.3) and pile-up events. The following sections explaine in detail, how the signal candidates are separated from the remaining background contributions.

6.8.1 METHOD

The combinatorial background and the pile-up contribution are separated from the signal candidates in two steps. First, a *sideband subtraction* is used to remove the combinatorial background from the signal candidates. The sidebands are defined as the area beside the signal region. The signal mass window for ZK^0_S is defined as $460 < m_{\pi\pi} < 540\,\mathrm{MeV}/c^2$. For $Z\Lambda$ the signal mass window is defined as $1100 < m_{p\pi} < 1130\,\mathrm{MeV}/c^2$. Figure 6.24 and 6.25 show the invariant mass distributions measured in simulation and data overlaid with the signal mass window indicated by the red dashed region. The combinatorial background contribution in the signal region is estimated from the sidebands by assuming a flat dependence on the invariant mass. The sidebands for ZK^0_S are defined as $400-460\,\mathrm{MeV}/c^2$ and $540-594\,\mathrm{MeV}/c^2$, and for $Z\Lambda$ as $1081-1100\,\mathrm{MeV}/c^2$ and $1130-1150\,\mathrm{MeV}/c^2$. A maximum likelihood fit is used to estimate the amount of combinatorial background in the signal mass window.

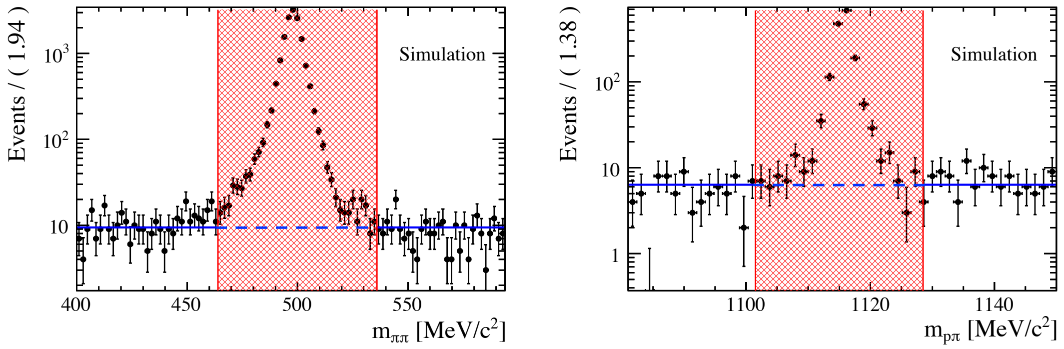

Figure 6.24: Sideband fit with a constant function on the invariant mass of $m_{\pi\pi}$ from ZK^0_S left and of $m_{p\pi}$ from $Z\Lambda$ right. Fit function overlaid in blue on the simulation.

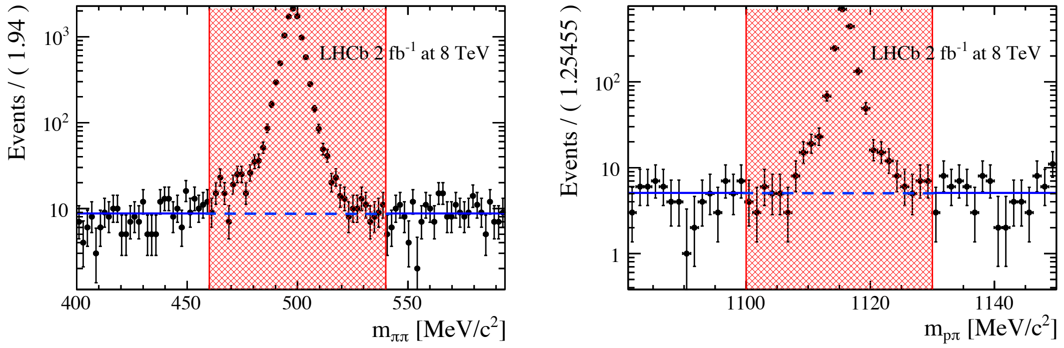

Figure 6.25: Sideband fit with a constant function on the invariant mass of $m_{\pi\pi}$ from ZK^0_S left and of $m_{p\pi}$ from $Z\Lambda$ right. Fit function overlaid in blue on data.

The pile-up contribution is separated from the signal candidates with a cut on the χ^2 of the vertex fit of Z and the V_0. Figure 6.26 shows the simulated candidates after the sideband subtraction as function of $\log(\chi^2/\text{ndf})$, where ndf is the number of degrees of freedom of the vertex fit. A clear peak at zero is visible, which are the signal candidates. The less prominent peak at higher values represents the pile-up contribution. Figure 6.27 shows the combinatorial background distribution in $\log(\chi^2/\text{ndf})$ inside and outside of the signal mass window in simulation. They are very similar, therefore it is assumed that the combinatorial background distribution in $\log(\chi^2/\text{ndf})$ is equal inside and outside the signal mass window. Figure 6.28 shows the same candidates as in Figure 6.26 as function of $\log(\chi^2/\text{ndf})$ but only for events with one reconstructed primary vertex (PV). Those events contain a negligible amount of pile-up contribution by construction. As a matter of fact, only the peak at zero is visible. Therefore, a cut of $\log(\chi^2/\text{ndf}) < 1$ is used to separate pile-up from signal candidates.

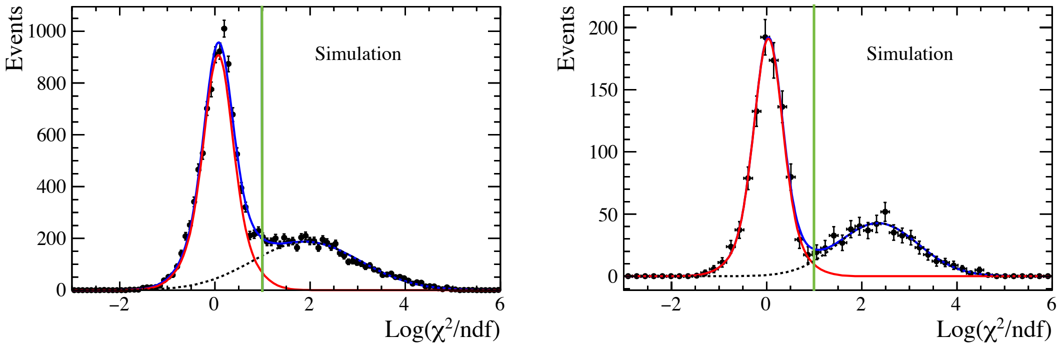

Figure 6.26: Sideband subtracted Log(χ^2/ndf) distribution in simulation with a fit separating signal and pile-up candidates. Signal is indicated with the red solid line, pile-up background is indicated in black dashed. The blue solid line shows the sum of signal and pile-up, while in green the Log(χ^2/ndf) < 1 cut is indicated by a vertical line. Figure left shows the distribution for ZK^0_S candidates and figure right the distribution for $Z\Lambda$.

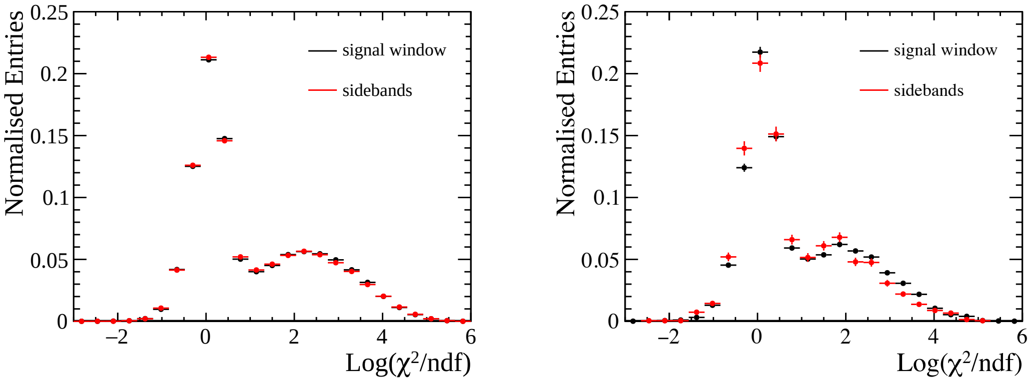

Figure 6.27: Comparison of the combinatorial background distribution in Log(χ^2/ndf) inside and outside of the signal window is shown for ZK^0_S candidates left and for $Z\Lambda$ right.

A binned maximum likelihood fit is used to estimate the purity ρ and signal loss $(1 - \varepsilon_{\chi^2})$ of the applied separation cut. The signal fit model is a double Gaussian with same mean and a single Gaussian for the pile-up distribution. In both figures 6.26 and 6.28, the signal model is indicated with a solid red line, the pile-up with a dashed black line and the total with a blue solid line. As the intention of the measurements is to keep the signal candidate extraction as far as possible independent of the simulation, the signal model was not chosen to be more complex. For example, in case of a Crystal Ball[120] function, the tail parameters would have been to be estimated from simulation, because the right side of the distribution has not enough information to fit a complex tail under the Gaussian distribution of the pile-up. In addition, the tails of the distribution for the one PV events are not necessary the same as for events with multiple interactions due to multiplicity effects. The systematic uncertainty induced by the choice of the fit model and the signal mass window definition is discussed in section 6.12.

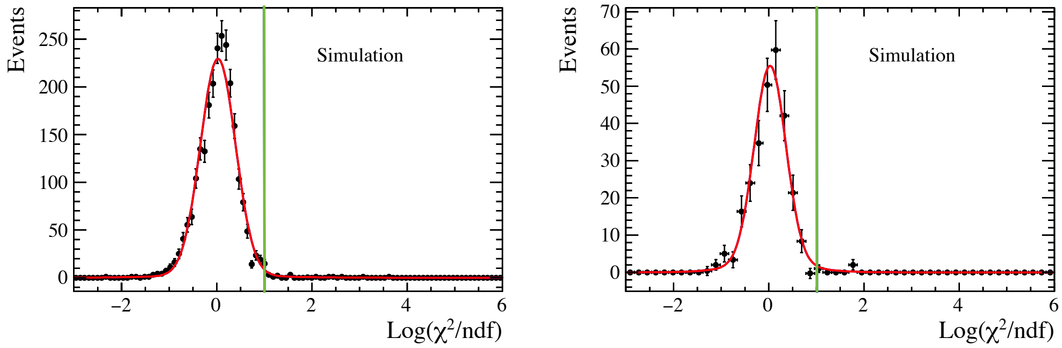

Figure 6.28: Sideband subtracted Log(χ^2/ndf) distribution in simulation for 1PV events only together with the fit result. Signal is indicated with the red solid line, pile-up is not existing as explained in the text. In green the Log(χ^2/ndf) < 1 cut is indicated by a vertical line. Figure left shows the distribution for ZK^0_S candidates and figure right the distribution for $Z\Lambda$.

6.8.2 CANDIDATE EXTRACTION

The measurement is performed in bins of p_T of the V_0 and R of Z and V_0. For the p_T of ZK^0_S a binning scheme is used, which is similar to earlier measurements [149] with an addition of one larger bin at high p_T to cover as much statistic as possible. The measurement of R of ZK^0_S is done in bin sizes of one unit, besides the last three bins from five to eight which are combined to one, due to limited statistics.

The binning schemes is chosen to be as similar as possible for the ZK^0_S and $Z\Lambda$. The first three bins in p_T up to 600 MeV/c are almost empty in $Z\Lambda$, since Λ with low p_T tend to have high η and decay products are more likely to be out of the acceptance. This, combined with the longer lifetime than K^0_S, results in almost empty bins up to 600 MeV/c. Due to lack of statistics the first two bins and the last two bins in R are combined in $Z\Lambda$. The resulting binning schemes for ZK^0_S and $Z\Lambda$ are summarised in table 6.7.

The extraction of the signal loss and purity is done separately for each bin. Since the statistics is significantly reduced all signal parameters of the fit model are Gaussian constrained to the values from the fit on the full data set, except for the yields. Figure 6.29 and 6.30 show the comparison of the signal distribution in simulation for 1 PV events for different bins in p_T and R. The signal distributions are very similar, therefore the width of the Gaussian constrain is taken as five sigma.

Table 6.7: Binning scheme for ZK_S^0 and $Z\Lambda$.

ZK_S^0		$Z\Lambda$	
p_T [MeV/c]	R	p_T [MeV/c]	R
$[0, 200)$	$[0, 1)$		$[0, 2)$
$[200, 400)$	$[1, 2)$		
$[400, 600)$	$[2, 3)$		$[2, 3)$
$[600, 800)$	$[3, 4)$	$[600, 800)$	$[3, 4)$
$[800, 1000)$	$[4, 5)$	$[800, 1000)$	$[4, 8)$
$[1000, 1200)$	$[5, 8)$	$[1000, 1200)$	
$[1200, 1400)$		$[1200, 1400)$	
$[1400, 1600)$		$[1400, 1600)$	
$[1600, 5000)$		$[1600, 5000)$	

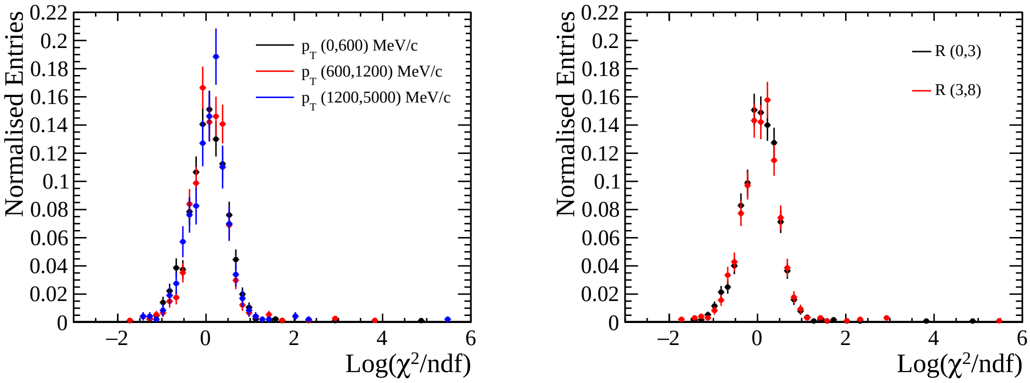

Figure 6.29: The comparison of ZK_S^0 1 PV events for three p_T and two R bins are shown left and right, respectively

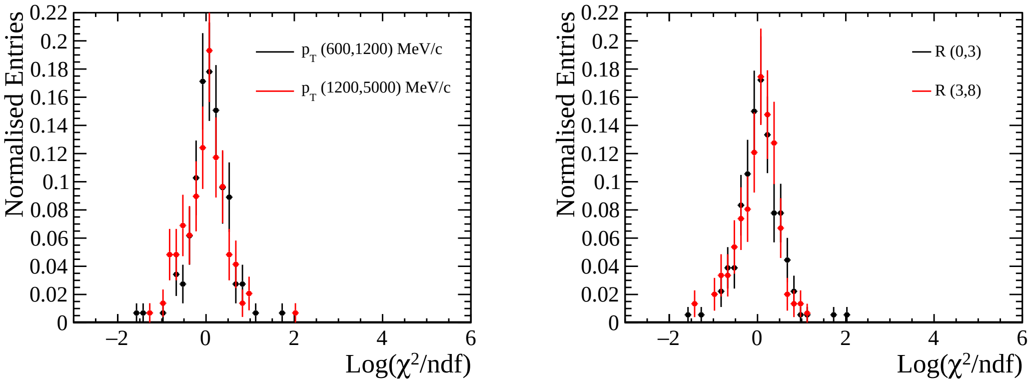

Figure 6.30: The comparison of $Z\Lambda$ 1 PV events for two p_T and R bins are shown left and right, respectively

Figure 6.31 and 6.32 shows the collider data together with the fit for events with one PV and without restriction on the number of PVs, respectively. In fig. 6.31 right a small undershoot at the tails is visible for the data. This is a statistical effect of the sideband subtraction for 1 PV events, as they have a small sideband sample. Table 6.8 and 6.9 show the fitted parameters for simulation and data. A significant shift in the mean of the pile-up distribution between data and simulation is visible. This can be understood from differences in the number of PVs between simulation and data. As the extraction method for data does not depend on input from the simulation, this discrepancy is not of concern for the analysis.

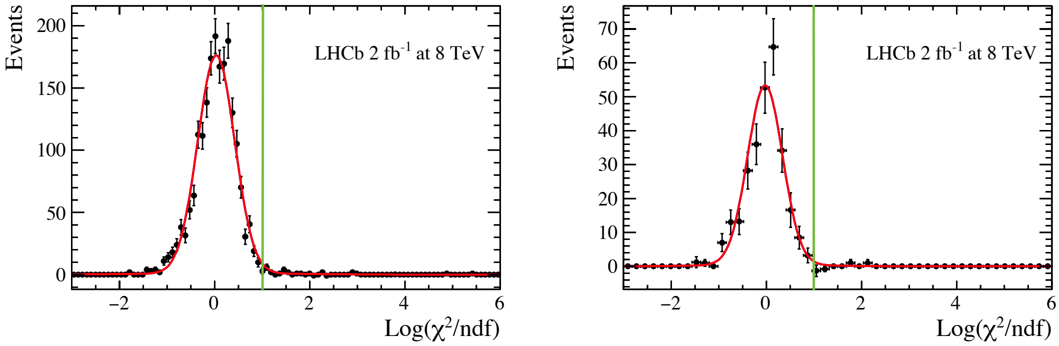

Figure 6.31: The sideband subtracted Log(χ^2/ndf) distribution for 1PV events of 2 fb^{-1} of data taken at 8 TeV together with the fit result. Signal is indicated with the red solid line and pile-up is not existing as explained in the text, while in green the Log(χ^2/ndf) < 1 cut is indicated by a vertical line. Figure left shows the distribution for ZK^0_S and figure right for $Z\Lambda$.

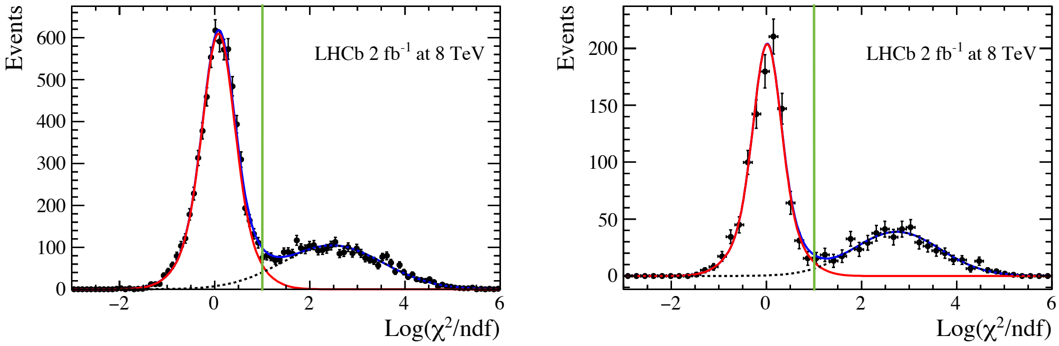

Figure 6.32: The sideband subtracted Log(χ^2/ndf) distribution for 2 fb^{-1} of data taken at 8 TeV with a fit separating signal and pile-up candidates. Signal is indicated with the red solid line, pile-up background is indicated in black dashed. The blue solid line shows the sum of signal and pile-up, while in green the Log(χ^2/ndf) < 1 cut is indicated by a vertical line. Figure left shows the distribution for ZK^0_S and figure right the distribution for $Z\Lambda$.

Table 6.8: Fit parameters measured in 2 fb^{-1} of data at 8 TeV for ZK^0_S and in simulation.

Parameter	Value Data	Value Simulation
Signal mean	$(8.3 \pm 0.6) \times 10^{-2}$	$(7.1 \pm 0.5) \times 10^{-2}$
Signal sigma	$(5.8 \pm 0.3) \times 10^{-1}$	$(5.3 \pm 0.2) \times 10^{-1}$
Signal sigma 2	$(3.14 \pm 0.16) \times 10^{-1}$	$(2.78 \pm 0.14) \times 10^{-1}$
Signal fraction Gaussians	0.44 ± 0.07	0.48 ± 0.06
Pile-up mean	2.47 ± 0.03	1.93 ± 0.04
Pile-up sigma	1.06 ± 0.02	1.13 ± 0.02
nSignal candidates	6673 ± 94	9075 ± 159
Background candidates	3101 ± 72	5819 ± 148

Table 6.9: Fit parameters measured in 2 fb^{-1} of data at 8 TeV for $Z\Lambda$ and in simulation.

Parameter	Value Data	Value Simulation
Signal mean	$(1.8 \pm 1.4) \times 10^{-2}$	$(3.2 \pm 1.3) \times 10^{-2}$
Signal sigma	$(5.5 \pm 0.5) \times 10^{-1}$	$(5.3 \pm 0.7) \times 10^{-1}$
Signal sigma 2	$(2.8 \pm 0.3) \times 10^{-1}$	$(2.8 \pm 0.3) \times 10^{-1}$
Signal fraction Gaussians	0.44 ± 0.11	0.35 ± 0.14
Pile-up mean	2.73 ± 0.05	2.36 ± 0.05
Pile-up sigma	0.92 ± 0.04	0.84 ± 0.04
nSignal candidates	1009 ± 33	892 ± 31
Background candidates	495 ± 24	489 ± 24

Figure 6.33 and 6.34 show the fit for each bin in p_{T}, respectively in R of ZK^0_S. The distance between pile-up distribution and signal distribution depends strongly on p_{T} of K^0_S and slightly on R. Figure 6.37 shows the mean of the pile-up distribution as function of p_{T} of K^0_S and R. Higher p_{T} for the mother particle implies that the p_{T} of the daughter particles is higher. As the track and vertex resolution in LHCb depend on p_{T}, a higher p_{T} results in a better vertex and higher track and IP resolution (see section 3.2). Because the DecayTreeFitter χ^2 depends on all three of them, the separation between signal and pile-up candidates gets better with higher p_{T}. Similarly, larger opening angles result in a more accurate vertex fit, which give a slightly better separation from pile-up and signal. Figure 6.35 and fig. 6.36 show the fit for each bin in p_{T}, respectively in R of $Z\Lambda$. Figure 6.38 shows the mean of the pile-up distribution as function of p_{T} of Λ and R. A similar dependence of the mean of the pile-up distribution on p_{T} of Λ is visible. The slight dependence on$R$ is not clearly visible due to the different binning scheme. In fig. 6.33f and 6.33h and in all bins of p_{T} and R of $Z\Lambda$ a small undershoot is visible. This can be explained by statistical effects from the sideband subtraction similar to the total 1PV sample of $Z\Lambda$.

Table 6.10 and table 6.11 show the fitted number of signal candidates, the purity and signal loss for each bin of ZK^0_S and $Z\Lambda$ with their statistical uncertainty from the fit. Figure 6.39 and 6.40 show the ratio of ZV_0 candidates per Z candidate in bins of R and p_T of the V_0 for data and simulation. The ratio is corrected for purity (ρ) and signal loss (ε_S) due to the pile-up separation cut in Log(χ^2/ndf):

$$\forall \text{ bin i} \quad \frac{N^i(ZV_0)\cdot\rho^i}{N(Z)\cdot\varepsilon_S^i}. \tag{6.3}$$

Table 6.10: Extracted number of signal candidates, purity ρ and signal loss $(1-\varepsilon_{\chi^2})$ for a cut $\log(\chi^2/\mathrm{ndf}) < 1$ in bins of p_T of V_0 for ZK^0_S and $Z\Lambda$ of 2 fb^{-1} data at 8 TeV.

	ZK^0_S			$Z\Lambda$		
p_T [MeV/c]	#Candidates	ρ [%]	$(1-\varepsilon_{\chi^2})$ [%]	#Candidates	ρ [%]	$(1-\varepsilon_{\chi^2})$ [%]
[0,200)	482 ± 67	77.88 ± 6.12	2.65 ± 0.89			
[200,400)	1004 ± 40	91.55 ± 1.72	2.37 ± 0.49			
[400,600)	1144 ± 38	96.31 ± 0.85	2.95 ± 0.48			
[600,800)	1015 ± 33	98.07 ± 0.50	2.11 ± 0.42	130 ± 13	97.22 ± 1.89	2.72 ± 1.15
[800,1000)	802 ± 29	99.44 ± 0.20	3.16 ± 0.49	159 ± 13	98.12 ± 1.01	1.92 ± 0.85
[1000,1200)	608 ± 25	99.35 ± 0.27	2.54 ± 0.51	139 ± 12	97.57 ± 1.35	1.26 ± 0.74
[1200,1400)	486 ± 22	99.45 ± 0.27	2.57 ± 0.58	129 ± 11	99.91 ± 0.09	1.16 ± 0.51
[1400,1600)	319 ± 18	99.82 ± 0.14	2.63 ± 0.68	98 ± 10	99.60 ± 0.38	1.09 ± 0.75
[1600,5000)	756 ± 28	99.79 ± 0.10	2.25 ± 0.43	246 ± 16	99.17 ± 0.51	1.75 ± 0.67

Table 6.11: Extracted number of signal candidates, purity ρ and $(1-\varepsilon_{\chi^2})$ for a cut $\log(\chi^2/\mathrm{ndf}) < 1$ in bins of R for ZK^0_S and $Z\Lambda$ of 2 fb^{-1} data at 8 TeV.

	ZK^0_S			$Z\Lambda$		
R	#Candidates	ρ [%]	$(1-\varepsilon_{\chi^2})$ [%]	#Candidates	ρ [%]	$(1-\varepsilon_{\chi^2})$ [%]
$[0,1)$	460 ± 27	91.57 ± 2.34	1.95 ± 0.64	242 ± 16	96.70 ± 1.30	1.80 ± 0.72
$[1,2)$	1312 ± 45	94.77 ± 1.30	3.42 ± 0.54			
$[2,3)$	1749 ± 48	95.85 ± 0.80	2.28 ± 0.34	294 ± 17	98.78 ± 0.62	1.79 ± 0.60
$[3,4)$	1631 ± 43	97.76 ± 0.51	3.16 ± 0.39	246 ± 16	99.35 ± 0.38	2.04 ± 0.69
$[4,5)$	1030 ± 36	95.55 ± 1.08	2.28 ± 0.44	225 ± 16	96.19 ± 1.85	2.03 ± 0.88
$[5,8)$	492 ± 24	98.19 ± 0.79	2.99 ± 0.73			

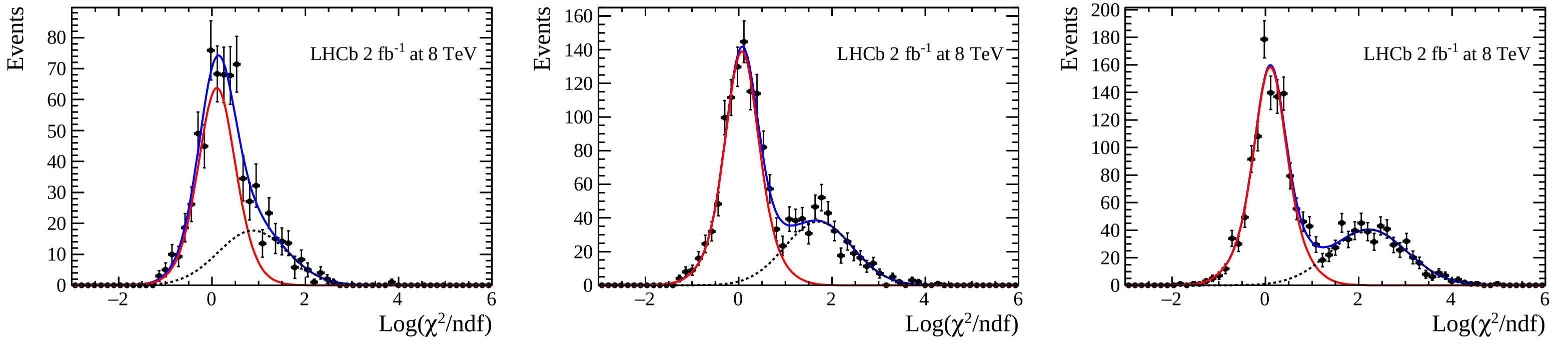

(a) $0 \le p_T < 200$ MeV/c **(b)** $200 \le p_T < 400$ MeV/c **(c)** $400 \le p_T < 600$ MeV/c

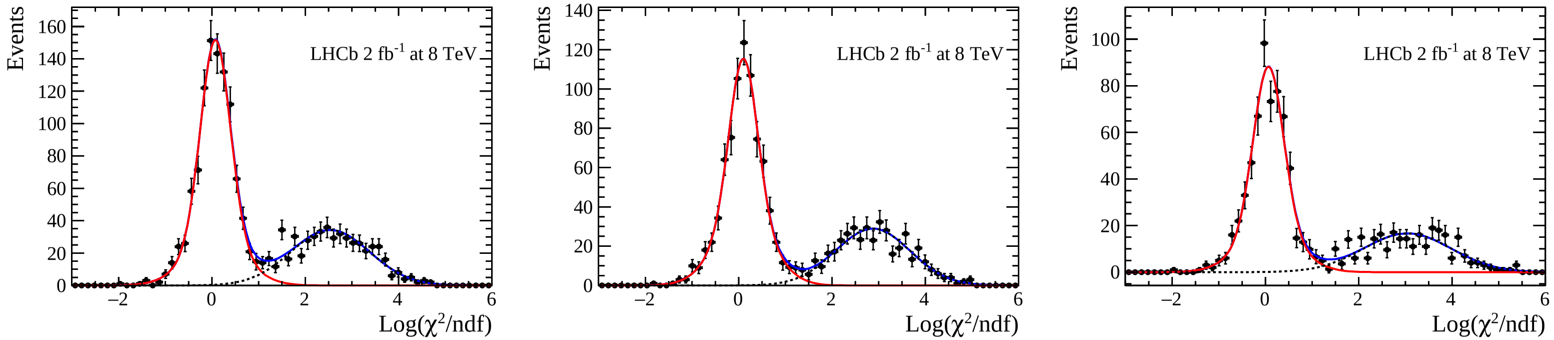

(d) $600 \le p_T < 800$ MeV/c **(e)** $800 \le p_T < 1000$ MeV/c **(f)** $1000 \le p_T < 1200$ MeV/c

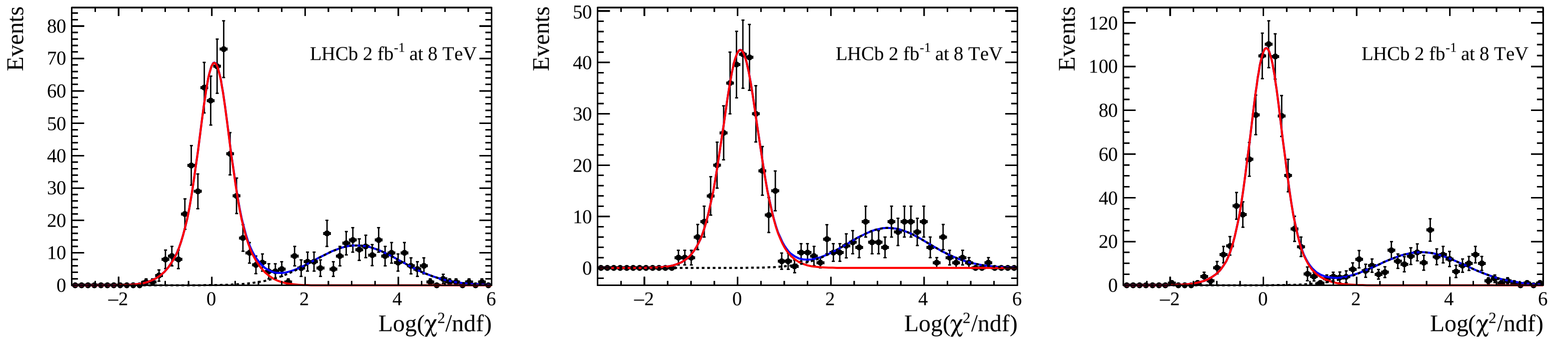

(g) $1200 \le p_T < 1400$ MeV/c **(h)** $1400 \le p_T < 1600$ MeV/c **(i)** $1600 \le p_T < 5000$ MeV/c

Figure 6.33: Figure 6.33a to fig. 6.33i show the Log(χ^2/ndf) distribution in bins of p_T of K^0_s for ZK^0_s of 2 fb^{-1} data at 8 TeV together with a fit separating signal and pile-up candidates. The colour definition is explained in fig. 6.32

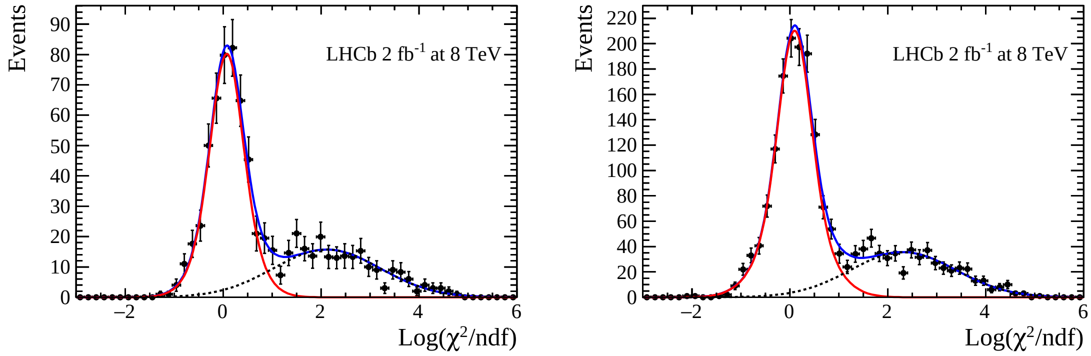

(a) $0 \leq R < 1$

(b) $1 \leq R < 2$

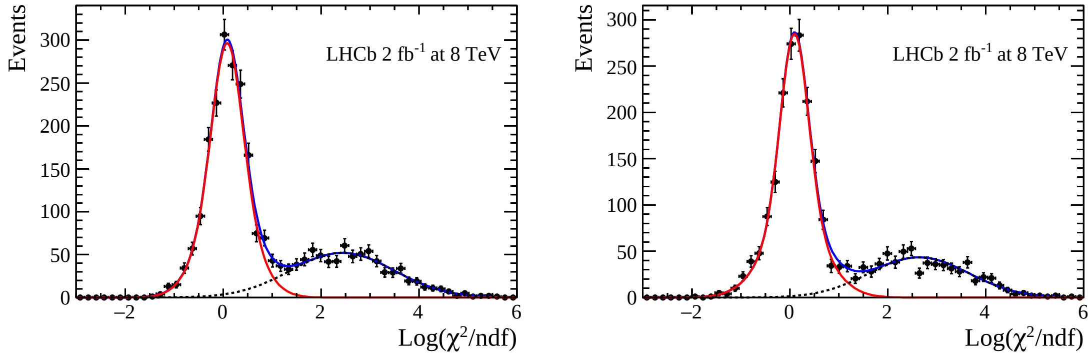

(c) $2 \leq R < 3$

(d) $3 \leq R < 4$

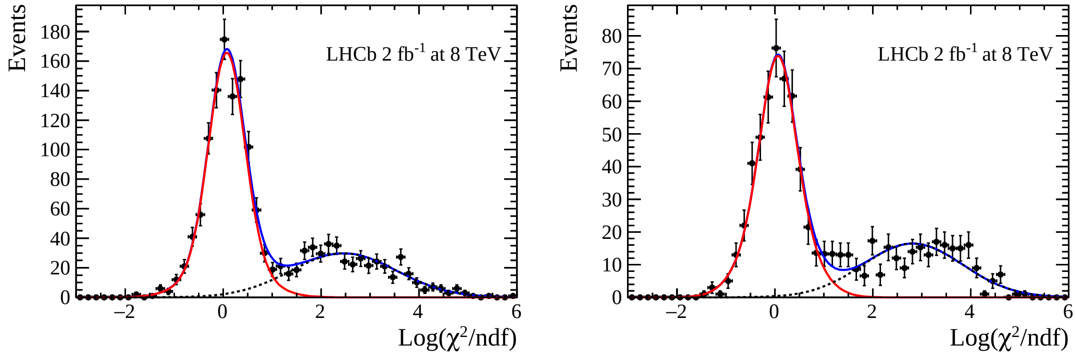

(e) $4 \leq R < 5$

(f) $5 \leq R < 8$

Figure 6.34: Figure 6.34a to fig. 6.34f show the Log(χ^2/ndf) distribution in bins of R for ZK^0_S of 2 fb^{-1} data at 8 TeV together with a fit separating signal and pile-up candidates. The colour definition is explained in fig. 6.32

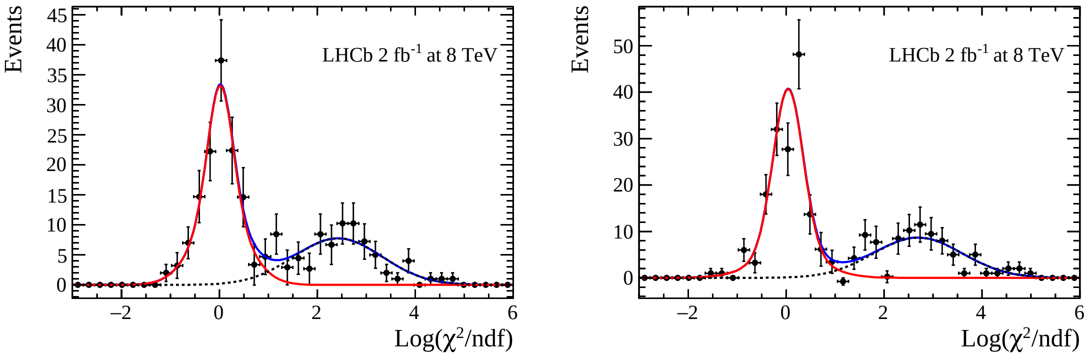

(a) $600 \leq p_{\mathrm{T}} < 800\,\mathrm{MeV}/c$ **(b)** $800 \leq p_{\mathrm{T}} < 1000\,\mathrm{MeV}/c$

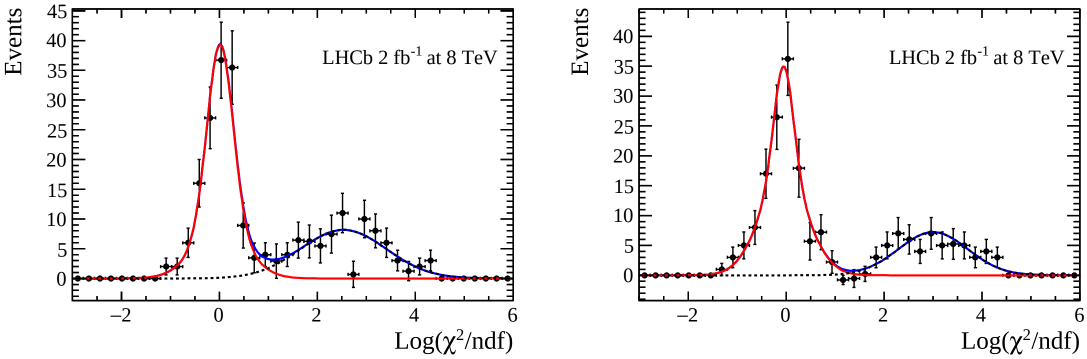

(c) $1000 \leq p_{\mathrm{T}} < 1200\,\mathrm{MeV}/c$ **(d)** $1200 \leq p_{\mathrm{T}} < 1400\,\mathrm{MeV}/c$

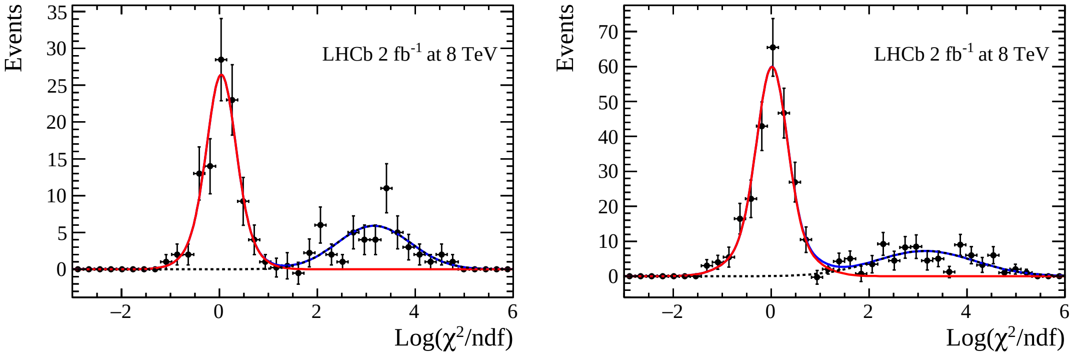

(e) $1400 \leq p_{\mathrm{T}} < 1600\,\mathrm{MeV}/c$ **(f)** $1600 \leq p_{\mathrm{T}} < 5000\,\mathrm{MeV}/c$

Figure 6.35: Figure 6.35a to fig. 6.35f show the Log(χ^2/ndf) distribution in bins of p_{T} of Λ for $Z\Lambda$ of 2 fb^{-1} data at 8 TeV together with a fit separating signal and pile-up candidates. The colour definition is explained in fig. 6.32

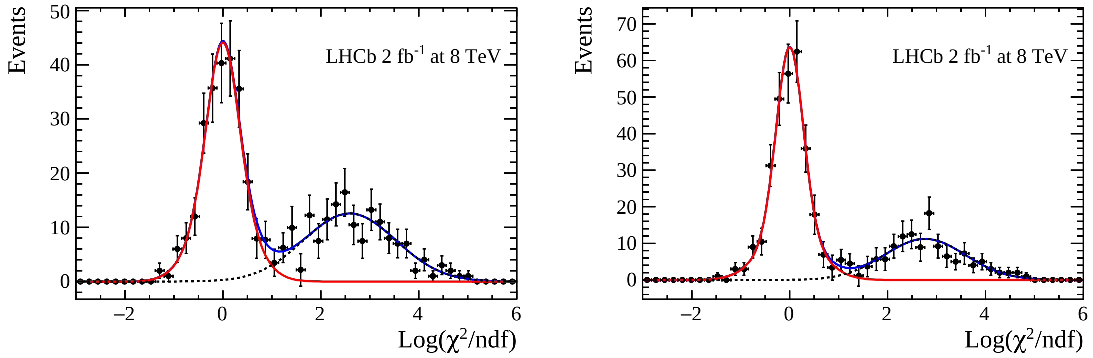

(a) $0 \leq R < 2$ **(b)** $2 \leq R < 3$

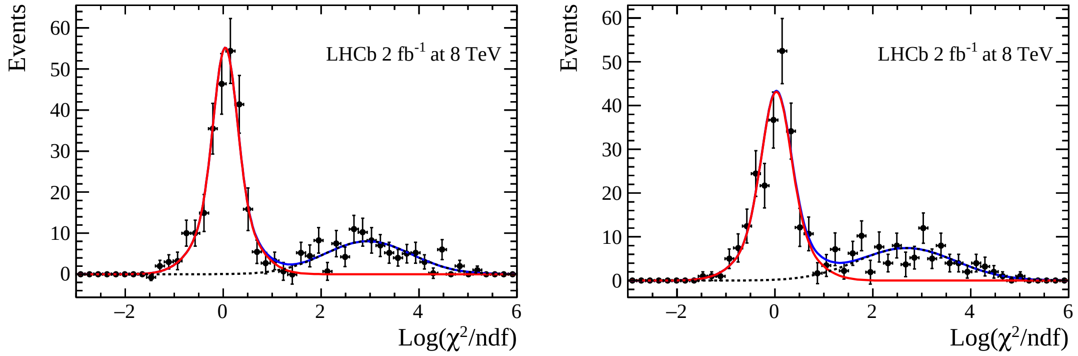

(c) $3 \leq R < 4$ **(d)** $4 \leq R < 8$

Figure 6.36: Figure 6.36a to fig. 6.36d show the Log(χ^2/ndf) distribution in bins of R for $Z\Lambda$ of 2 fb^{-1} data at 8 TeV together with a fit separating signal and pile-up candidates. The colour definition is explained in fig. 6.32

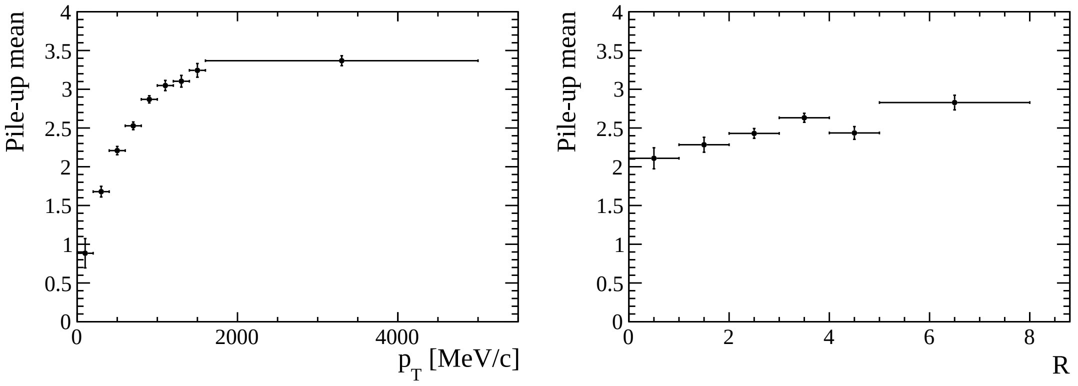

Figure 6.37: Mean of the pile-up distribution for ZK^0_S. The left figure shows the K^0_S p_T and the right figure the R dependency for collision data of 2 fb^{-1} at 8 TeV.

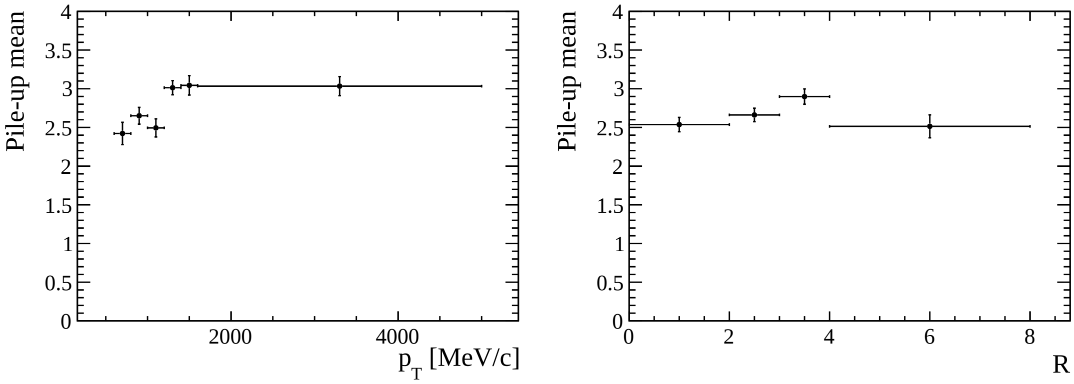

Figure 6.38: Mean of the pile-up distribution for $Z\Lambda$. The left figure shows the Λ p_{T} and the right figure the R dependency for collision data of 2 fb^{-1} at 8 TeV.

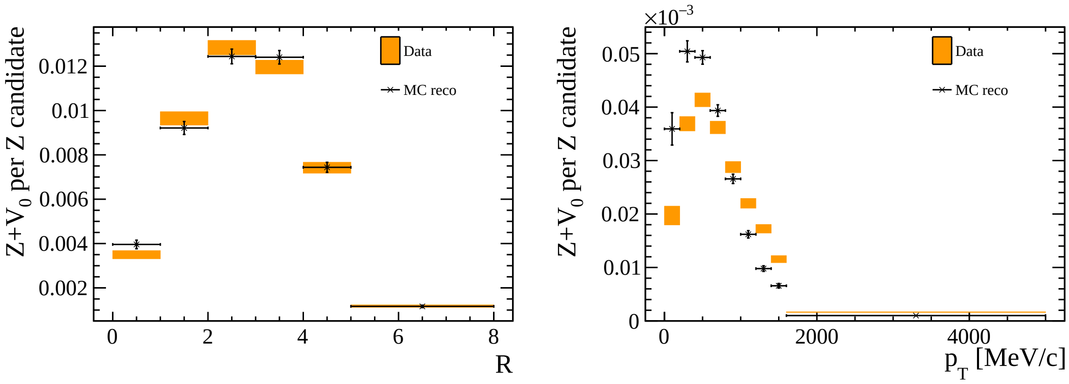

Figure 6.39: Ratio of ZK^0_{s} candidates per Z candidate in bins of R (left) and p_{T} (right) of the K^0_{s} for data and simulation. The number of ZK^0_{s} candidates are corrected for purity and signal loss due to the pile-up separation cut in $\mathrm{Log}(\chi^2/\mathrm{ndf})$. The numerical values are summarised in table B.9.

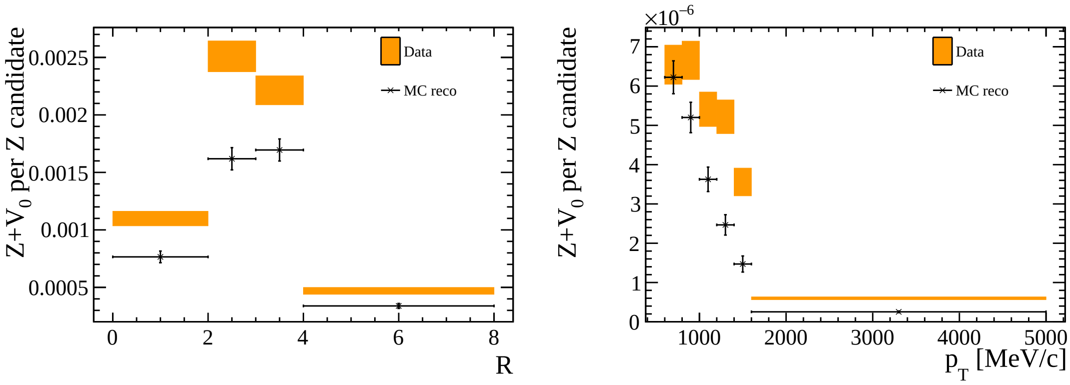

Figure 6.40: Ratio of $Z\Lambda$ candidates per Z candidate in bins of R (left) and p_{T} (right) of the Λ for data and simulation. The number of $Z\Lambda$ candidates are corrected for purity and signal loss due to the pile-up separation cut in $\mathrm{Log}(\chi^2/\mathrm{ndf})$. The numerical values are summarised in table B.10.

6.9 EFFICIENCY CALCULATIONS

The results obtained for ZK^0_S and $Z\Lambda$ suffer from inefficiencies associated with track reconstruction, particle identification, trigger requirements, global event cuts (GEC), as well as inefficiencies from the combination of the two particles. For this analysis the efficiencies can be separated into three categories: the Z reconstruction, the trigger and the ZV_0 selection efficiency. The vertex reconstruction efficiency of the Z is found to be negligible (see [141, 158]).

6.9.1 Z RECONSTRUCTION EFFICIENCY

The Z reconstruction efficiency yields two individual contributions: muon track reconstruction and muon identification. They are all evaluated using tag-and-probe methods on the $Z \to \mu^+\mu^-$ resonance [97, 141, 158]. Both tag and probe tracks have to satisfy the fiducial requirements. The tag must be identified as a muon which triggered the event. The definition of the probe is required to be unbiased regarding to the efficiency that is examined. The efficiency is studied as a function of several variables, which are related to the muon kinematics and detector occupancy. In this analysis the efficiency is evaluated as a function of the muon pseudo-rapidity η. In each bin of η, the efficiency is defined as the fraction of tag-and-probe candidate events where the probe satisfies the track reconstruction or muon identification. The probe track is defined as

- muon identification; the probe track is not allowed to have any PID requirement applied.
- muon track reconstruction; the probe track is reconstructed by combining hits from the muon stations and the TT.

Figure 6.41 shows the efficiency values as function η for high-p_T muons (p_T >20 GeV/c) in simulation and data at $\sqrt{s}$ =8 TeV. In both cases the efficiency is about a percent higher in simulation than in data but similar in shape. The uncertainties shown in the figures include the statistical and the systematic combinations added in quadrature. The muon identification efficiency has a systematic uncertainty due to background contamination in the evaluation sample. The muon track reconstruction efficiency has a systematic uncertainty due to a bias in the method and additional corrections. These have been studied in simulation [97].

The total Z reconstruction efficiency is the factorizable product of all individual efficiencies. It is determined on a event by event basis by

$$\varepsilon_Z(\mu^+,\mu^-) = \varepsilon_{trk}^{\mu^+} \cdot \varepsilon_{trk}^{\mu^-} \cdot \varepsilon_{id}^{\mu^+} \cdot \varepsilon_{id}^{\mu^-} \tag{6.4}$$

where ε_{trk} and ε_{id} stand for muon track reconstruction and muon identification efficiency.

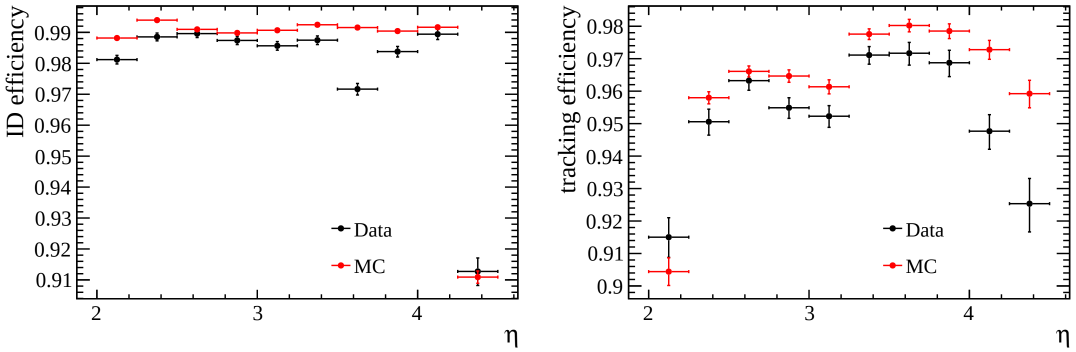

Figure 6.41: Figure left shows the muon identification (ID) efficiency and right the muon tracking efficiency as function of η for simulation and data at $\sqrt{s}$ =8 TeV using a tag-and-probe method on $Z \rightarrow \mu^+\mu^-$ events [97, 141, 158].

6.9.2 Trigger Efficiency

The trigger efficiency yields two individual contributions: the single muon trigger efficiency and the global event cut (GEC) efficiency. The single muon trigger efficiency is evaluated using a tag-and-probe method on the $Z \rightarrow \mu^+\mu^-$ resonance, as for the Z reconstruction efficiency. The tag muon has to be identified as a muon which triggered the event, while the probe muon has only to fulfil the fiducial requirements. Figure 6.42 shows the single muon trigger efficiency as function of η for high-p_{T} muons in simulation and data at $\sqrt{s}$ =8 TeV. The efficiency is defined as the fraction of tag-and-probe candidate events where the probe satisfies the trigger requirements. The efficiency in simulation is lower than in data by a few percent. The shape is similar in data and simulation, except for the last two bins. The single muon trigger efficiency has only statistical uncertainties [97, 141, 158]. The total muon trigger efficiency for the event is determined on an event by event basis by

$$\varepsilon_{trg}^{total}(\mu^+,\mu^-) = \left(\varepsilon_{trg}^{\mu^+} + \varepsilon_{trg}^{\mu^-} - \varepsilon_{trg}^{\mu^+} \cdot \varepsilon_{trg}^{\mu^-}\right) \tag{6.5}$$

where ε_{trg} stand for the single muon trigger efficiency.

Global event cuts are applied in the hardware trigger to reject high particle multiplicity events. Otherwise, these events would dominate the processing time. The main effect for this analysis origins in the cut applied on the number of SPD hits in the single muon trigger line.

The GEC efficiency was estimated with $Z \rightarrow \mu^+\mu^-$ events from collision data firing the dimuon

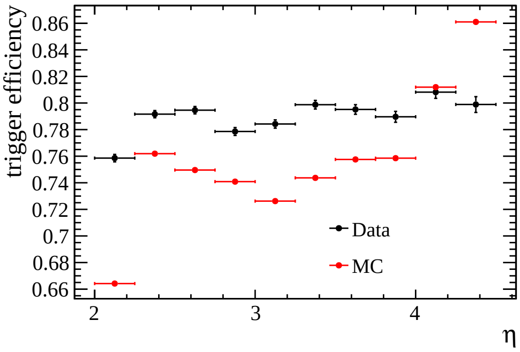

Figure 6.42: The muon trigger efficiency is shown as function of η for simulation and data at $\sqrt{s}$ =8 TeV using a tag-and-probe method on $Z \rightarrow \mu^+\mu^-$ events [97, 141, 158].

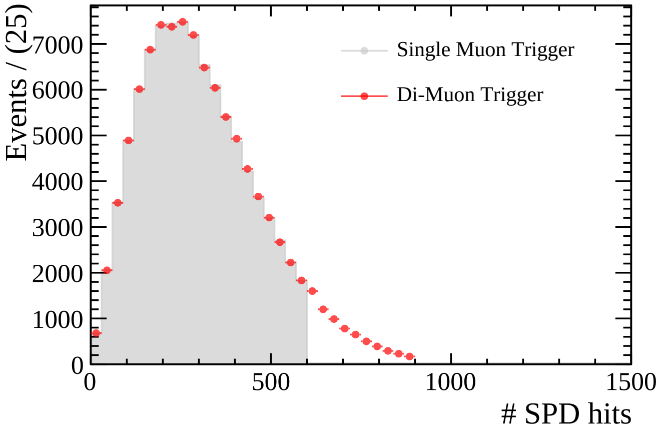

Figure 6.43: Comparison of the high-p_{T} single muon trigger and the dimuon trigger for events containing a Z.

trigger path described in section 6.5.1, which has a looser cut on the number of SPD hits. This choice relies on the fact that the SPD hit distribution is the same for events firing both trigger paths, the high-p_{T} single muon trigger and the dimuon trigger, as seen in fig. 6.43. They are the same except for the cut applied on the high-p_{T} single muon trigger which is lower than on the dimuon trigger, where the cut is set at 900.

A binned maximum likelihood fit of a gamma distribution to the distribution of the number of SPD hits of the dimuon trigger path is used to extract the integral for a certain range of SPD hits. The efficiency is defined as the ratio of the integral from 0-600 SPD hits to the integral from 0-2000 SPD hits. The contributions above 2000 SPD hits is negligible. Figure 6.44 left shows, that the efficiency calculation for events with only 1 PV results in (99.96±0.10)%, which is for the further analysis assumed to be 100%. Figure 6.44 right shows the fit to the data for events with more than 1 PV, which results in an efficiency of $(90.36 \pm 0.10)\%$. The uncertainty originates from the integration of the fit function and is purely statistical.

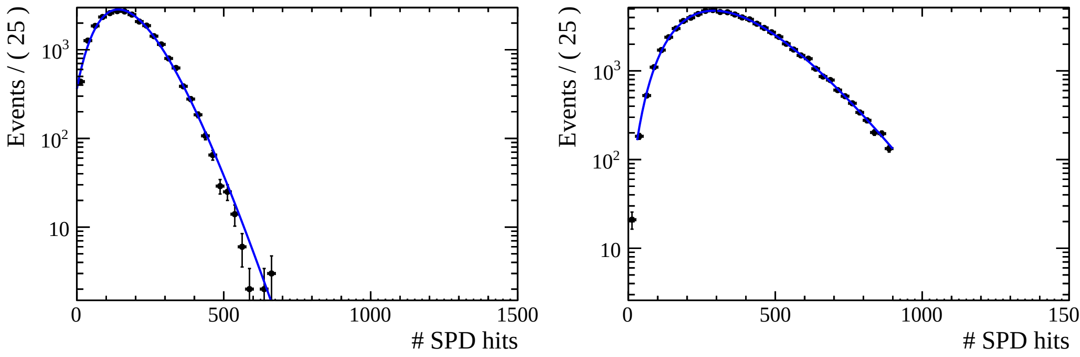

Figure 6.44: The figure shows the fit to the SPD hit multiplicity distribution for candidates firing the dimuon tigger. Figure left shows the fit for events with one PV only, whereas figure right shows the fit for events with more than one PV.

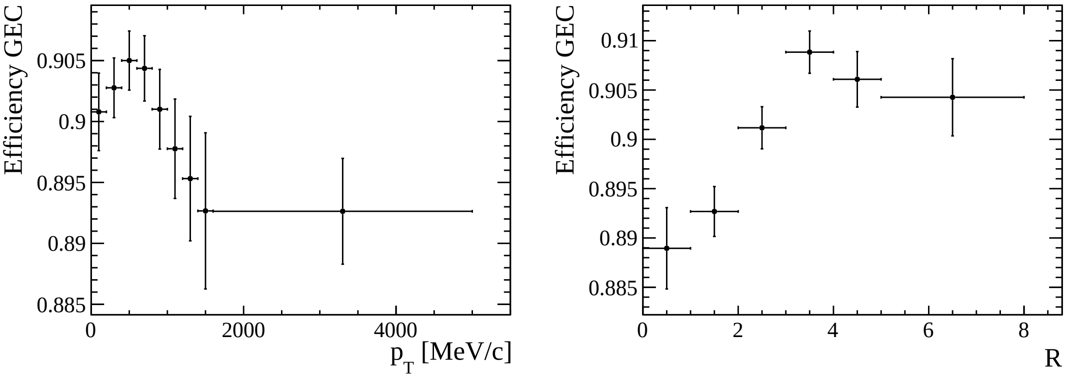

Figure 6.45: The GEC efficiency as function of K_S^0 p_T and R for data sample of ZK_S^0 with more than one PV.

The GEC efficiency as function of p_T of V_0 and R is measured on the corresponding data set. The dependences are shown in fig. 6.45 and fig. 6.46 for ZK_S^0 and for $Z\Lambda$ respectively for at least one K_S^0 or Λ candidate. For these fits the shape parameters were Gaussian constrained to the values of the total fit. The GEC efficiency varies weakly within one or two percentage over R and p_T. The efficiency gets smaller for larger p_T of the V_0 because the event activity rises with p_T. The dependence in R follows from the correlation between p_T and R. The GEC efficiency is used in the binned analysis as function of the corresponding binning variable in case of the ZV_0, whereas

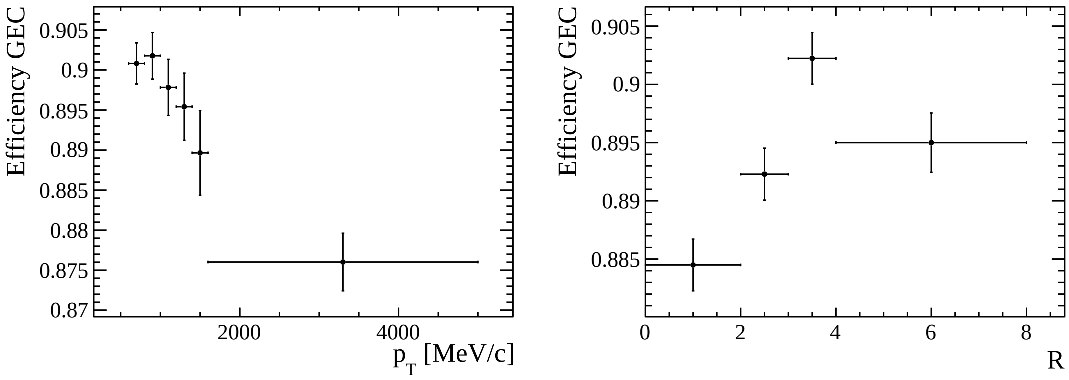

Figure 6.46: The GEC efficiency as function of Λ p_{T} and R for data sample of $Z\Lambda$ with more than one PV.

the total GEC efficiency is used for the normalisation channel $Z \rightarrow \mu^+\mu^-$. But in both cases, the GEC is set to 100% for events with only one reconstructed PV.

6.9.3 EFFICIENCY ZV_0

The ZV_0 event is triggered on the muons and no PID information of the V_0 and its daughter particles is used, which leaves to extract the selection and reconstruction efficiency of the ZV_0 candidate. The combined efficiency of selection and reconstruction is estimated on simulation as function of η and p_{T} of the V_0. The efficiency is defined as

$$\varepsilon_{ZV_0}(\eta, p_{\mathrm{T}}) = \frac{\mathrm{N}(ZV_0)_{\text{selected and reconstructed}}}{\mathrm{N}(pp \rightarrow ZV_0)_{\text{generated}}}. \tag{6.6}$$

The *generated* and *selected and reconstructed* sample have to satisfy the following conditions:

- The muons of the Z have to be reconstructed in the LHCb acceptance $2.0 < \eta < 4.5$ and have a p_{T} larger than 20 GeV/c.
- Both muons of the Z have to be reconstructed and identified, while only one has to be triggered.
- The generated daughter particles of the V_0 have to be generated within in the LHCb acceptance and have a p larger than 2 GeV/c.
- Both, V_0 and Z candidates must be generated as V_0 and Z, respectively.

- The generated primary vertices of Z and V_0 need to be close enough to be indistinguishable for the VELO. The separation in x and y has to be smaller than 115 µm and in z smaller than 630 µm. The values are calculated from ref. [159] [4].

In addition, the *selected and reconstructed* sample has to be reconstructed, pre-selected and satisfy the gBDT selection described in section 6.7.

The configuration in section 6.5 is used for the generation of the simulation sample. The binning scheme for the efficiency study is chosen to be the same scheme in p_T as for the extraction of the candidates shown in table 6.7. For η there is one bin from $2 - 2.5$ and the bins with $\eta > 2.5$ have all a bin size of 0.3.

Figure 6.47 and 6.48 show the efficiency either as function of η or p_T of the V_0. For both K^0_S and Λ the efficiencies drop at high p_T, as candidates with higher p_T are more likely to fly out of the VELO acceptance. The efficiency distribution as a function of η is rising with η and has two additional features: a plateau for $2.9 < \eta < 3.5$ and a falling part at large η. This is investigated in the following.

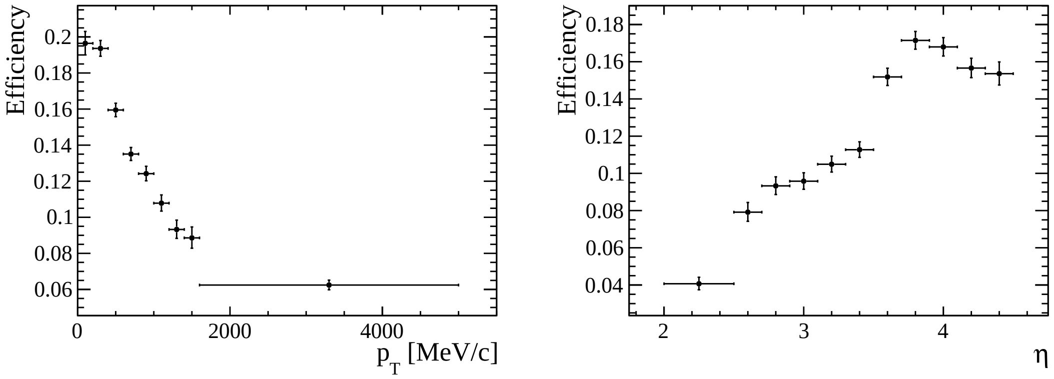

Figure 6.47: The selection and reconstruction efficiency of ZK^0_S as function of p_T of the K^0_S in figure left and as function of η of the K^0_S in figure right.

The size of the VELO detector and its reconstruction algorithm have an impact on the efficiency distribution in η. To visualise the first contribution, a rough estimate of the VELO acceptance was made and the resulting efficiency was studied. Figure 6.49 and 6.50 show the ratio of generated events, where the decay vertex of the V_0 is still inside the VELO, for events with both Z and V_0 generated from the same vertex and all final state particles inside the LHCb detector volume.

---

[4] The values correspond to five times the PV resolution, where the resolution is calculated for 25 tracks per PV and a maximum of 6 PVs per event

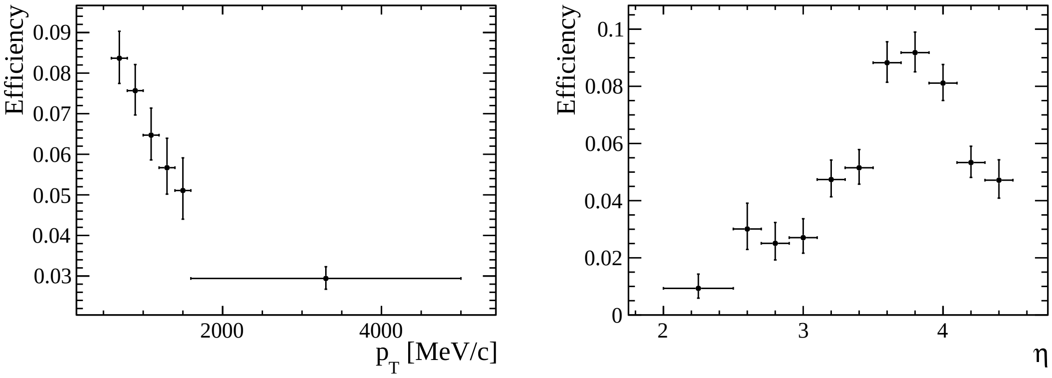

Figure 6.48: The selection and reconstruction efficiency of $Z\Lambda$ as function of p_T of the Λ in figure left and as function of η of the Λ in figure right.

The condition in z for the decay vertex is given by the requirement of the VELO reconstruction algorithm for at least three stations in the VELO with a hit [101]. Hence, the distance between primary vertex and decay vertex, Δz is required to be less than 400 mm. The radial distance $\Delta r = \sqrt{\Delta x^2 + \Delta y^2}$ of the decay vertex is constrained by the active area of the sensors in the VELO and is required to be less than 30 mm. The distribution in η for the radial restriction behaves as expected, with larger η more tracks are inside the radial distance and the ratio of events with the decay vertex with the VELO acceptance increases. The z restriction does introduce a falling distribution after $\eta = 2.5$, as the V_0 starts to decay outside the VELO. This has a larger impact on the Λ than the K^0_S due to the larger life time. The combination of the radial and longitudinal acceptance of the VELO shows a rising distribution up to $\eta = 3.2$, afterwards the distribution is falling again at higher η. This explains the falling part at large η in fig. 6.47 and 6.48.

The effect of the reconstruction algorithm is studied in the following. Figure 6.51 shows the efficiency projection in η for candidates satisfying the requirements to decay inside the VELO. Instead of a plateau, a dip is visible at $2.9 < \eta < 3.5$. As mentioned before the VELO reconstruction needs at least hits in three VELO stations. Figure 6.52 shows the cross-section of the VELO, with the plateau/dip edges indicated in red. At the lower border of the dip, $\eta = 2.9$ the first station of the last four stations in the VELO start to see hits from the candidate tracks. The last station is able to see hits for candidate tracks with η larger than $\eta = 3.5$. In between, the reconstruction algorithm needs hits in stations upstream of the large gap in the VELO. Because of the finite life time of V_0s, they can decay in this gap. This leads to the inefficiencies in the dip region, as not enough stations are able to see hits.

Due to lack of statistics the ZV_0 efficiency could not be fully extracted in two dimensions. The

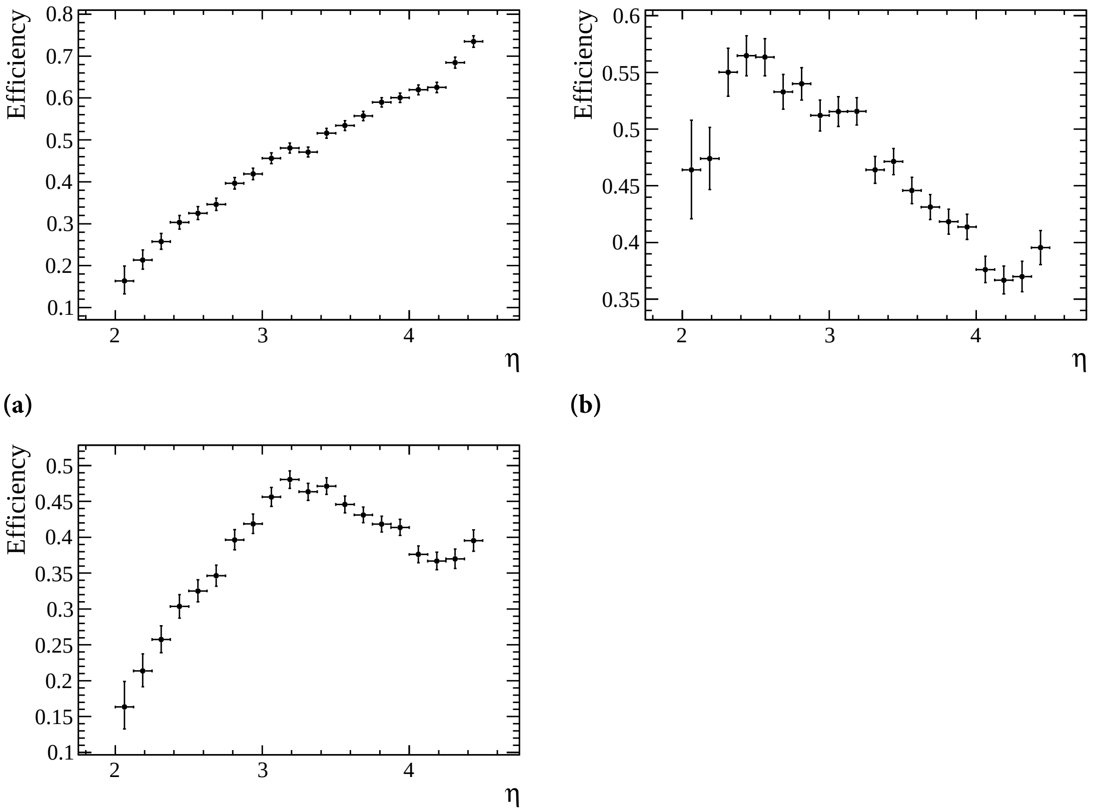

(a)

(b)

(c)

Figure 6.49: The ratio of generated events, where the decay vertex of the K^0_S is still inside the VELO. Here both Z and V_0 are required to come from the same vertex and all final state particles have to lie in the LHCb detector volume. Figure a) shows the ratio for a requirement of $\Delta r < 30$ mm. Figure b) shows the ratio for a requirement of $\Delta z < 400$ mm, and figure c) shows the ratio for both requirements.

final binning is different for ZK^0_S and $Z\Lambda$. A two dimensional approach in p_T and η is used in case of ZK^0_S. In p_T the same binning scheme as in fig. 6.47 left is used, and for the first four bins in p_T the same η binning scheme as in fig. 6.47 right, for the other p_T bins the bin size in η was increased to 0.4. The efficiency for $Z\Lambda$ is extracted only as function of p_T, due to the lower statistics. The binning scheme in p_T is the same as shown in fig. 6.48 left. The systematic uncertainty introduced by the chosen binning scheme is discussed in section 6.12. The efficiency plots of the individual p_T, η bins are shown in the appendix in section B.1.

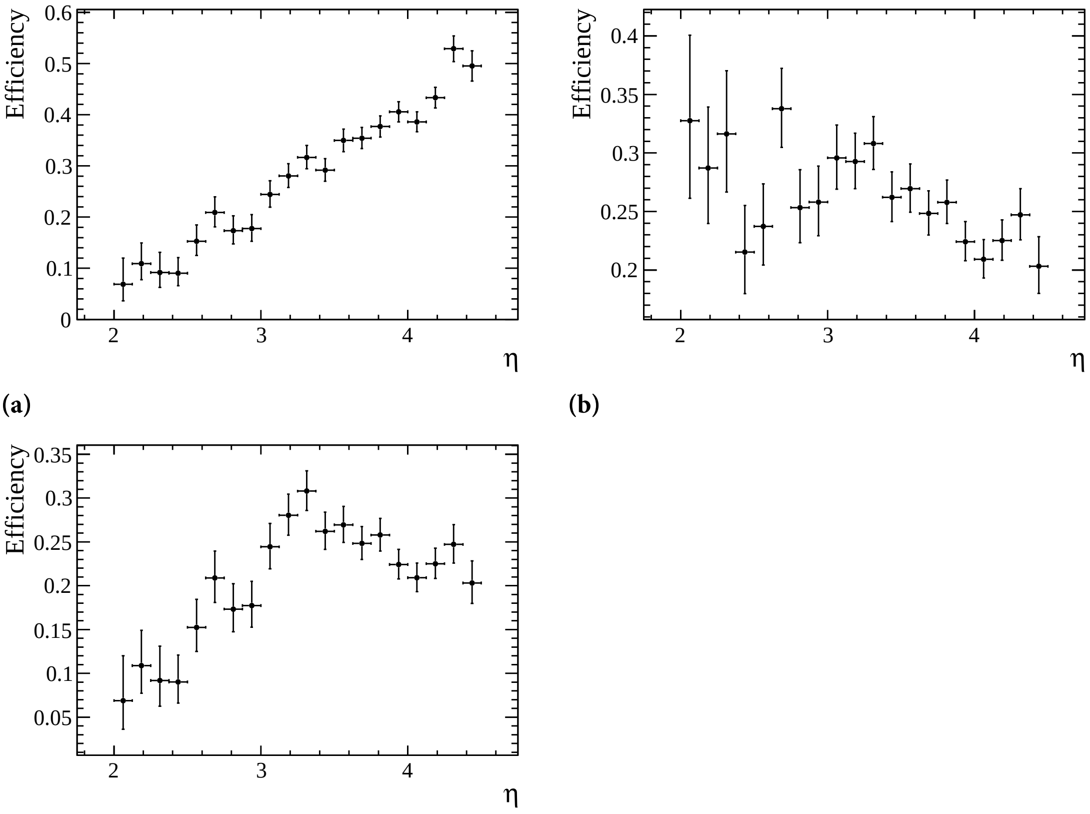

(a)

(b)

(c)

Figure 6.50: The ratio of generated events, where the decay vertex of the Λ is still inside the VELO. Here both Z and V_0 are required to come from the same vertex and all final state particles have to lie in the LHCb detector volume. Figure a) shows the ratio for a requirement of $\Delta r < 30$ mm. Figure b) shows the ratio for a requirement of $\Delta z < 400$ mm, and figure c) shows the ratio for both requirements.

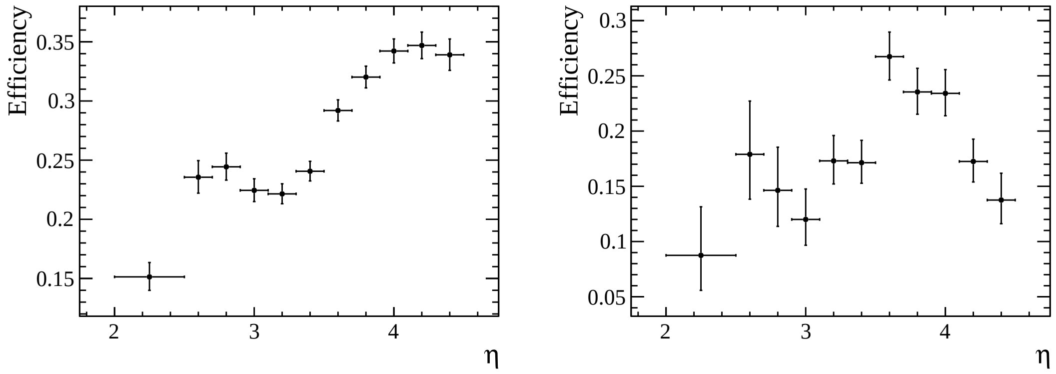

Figure 6.51: Figure left (right) shows the η projection of the selection and reconstruction efficiency of ZK_s^0 ($Z\Lambda$) with generated events inside the VELO acceptance, both Z and V_0 generated from the same vertex and all final state particles inside the LHCb detector volume.

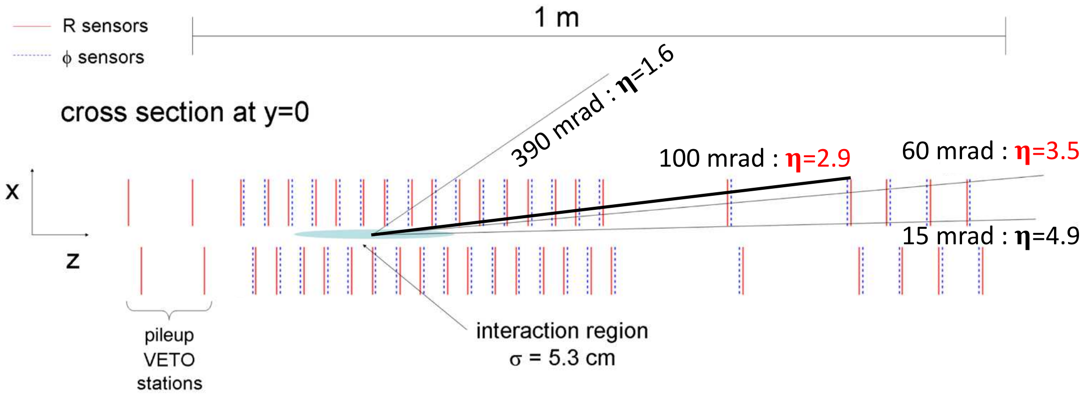

Figure 6.52: Cross-section in the (x,z) plane of the VELO silicon sensors, at $y = 0$, with the detector in the fully closed position. The figure is adapted from ref. [80].

6.10 Additional Corrections

The signal window definition in section 6.8.1 introduces an additional source of inefficiency. Th efficiency is determined from simulation as:

$$\varepsilon_{SW} = 99.52^{+0.08}_{-0.09} \quad \text{for } ZK^0_{\text{S}} \tag{6.7}$$

and

$$\varepsilon_{SW} = 99.53^{+0.23}_{-0.37} \quad \text{for } Z\mathit{\Lambda}. \tag{6.8}$$

It is applied globally.

For the comparison of generator level predictions to the measurements, two additional effects have to be considered, the combination of the vertices of Z and V_0, and bin migration. The combination of the vertices of Z and V_0 is ensured on generator level by the separation window of both decay vertices in x, y and z (defined in section 6.9.3 and herein after called combination cut). This requirement does not exist on reconstruction level, where the combination of the vertices is ensured by the cut on $\log(\chi^2/\text{ndf}) < 1$. Hence, an additional correction factor needs to be taken into account, if the measurements are compared to the MC predictions on generator level. Figure 6.53 shows the distribution of the distance between both decay vertices of Z and K^0_{S} in z of the simulated reconstructed signal candidates with $\log(\chi^2/\text{ndf}) < 1$ and pile-up candidates with $\log(\chi^2/\text{ndf}) \geq 1$. On one hand, on reconstruction level (14.37±0.13)% of the signal candidates of ZK^0_{S} are outside of the cut value on generator level. On the other hand (1.53±0.04)% of the pile-up candidates are inside of the cut value on generator level. This results in a net correction factor $corr_{vertex}$ of (86.94±0.14)%. For $Z\mathit{\Lambda}$, (11.64±0.22)% of the signal candidates are outside of the cut value on generator level, while (1.53±0.04)% of the pile-up candidates are inside of the cut value on generator level. This results in a net correction factor $corr_{vertex}$ of (90.49±0.21)%.

If the final result is compared to generator level predictions in p_{T} and R, it can be affected by bin migration which needs to be corrected. Figure 6.54 and 6.55 shows the comparison of generated and reconstructed p_{T} or R for candidates in simulation.

The bin migration can be different in data and simulation, as the p_{T} and R distributions are not equal (see fig. 6.39 and 6.40). Therefore, a correction factor is applied on simulation in order to match the p_{T} and R distributions from data. The factor is in the order of one percent in R and up to 50% for high p_{T} for both decays, ZK^0_{S} and $Z\mathit{\Lambda}$. The figures are in the appendix in fig. B.5 and B.6. The bin migration is locally smaller than 5%, hence no systematic uncertainty is assigned.

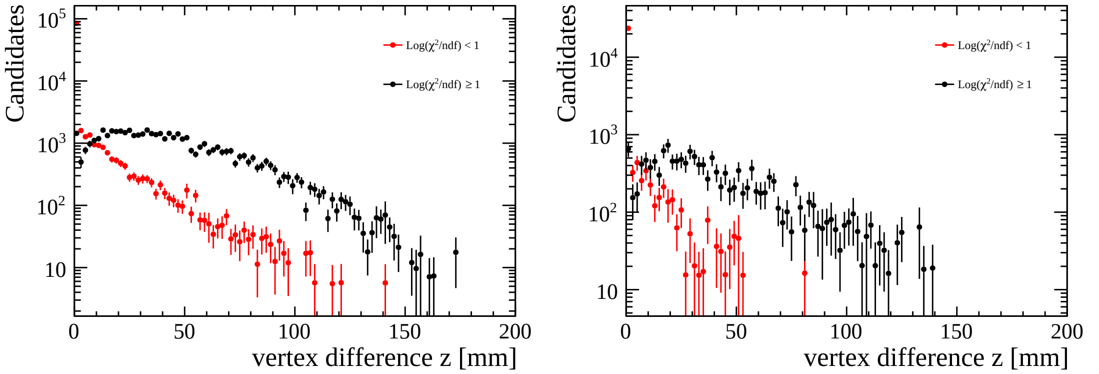

Figure 6.53: The distribution of the vertices difference in z for ZK_S^0 ($Z\Lambda$) candidates is shown in the left (right).

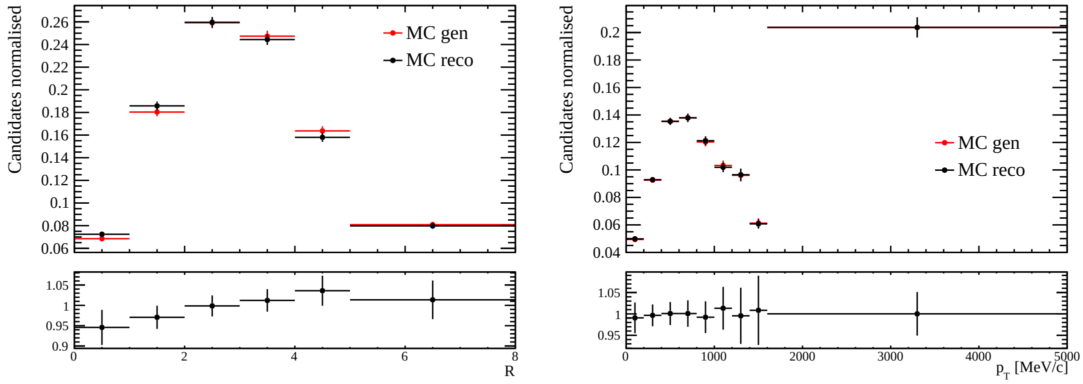

Figure 6.54: Comparison of the distributions of R and p_T on generator and reconstruction level for ZK_S^0, the lower part shows the ratio which is used as correction facto for the reconstructed quantities. The simulation distribution in p_T and R is corrected to match the distributions data.

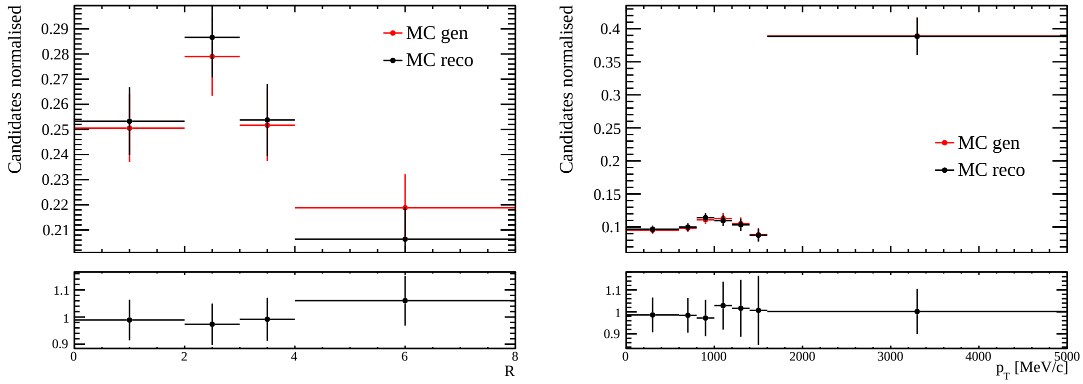

Figure 6.55: Comparison of the distributions of R and p_T on generator and reconstruction level for $Z\Lambda$, the lower part shows the ratio which is used as correction facto for the reconstructed quantities. The simulation distribution in p_T and R is corrected to match the distributions data.

6.11 Check Correction Procedure

The end result is the ratio of ZV_0 candidates per Z candidate in bin i:

$$\forall\, R^i_{rec} = \text{bin } i \qquad \frac{\rho^i \cdot \sum\limits_{l}^{Candidates} ZV_0 \dfrac{1}{\varepsilon_Z(\eta_{\mu^+},\eta_{\mu^-}) \cdot \varepsilon^{total}_{trg}(\eta_{\mu^+},\eta_{\mu^-}) \cdot \varepsilon_{ZV_0}(\eta^{V_0}, p_T^{V_0})}}{\varepsilon^i_{GEC}(ZV_0) \cdot \varepsilon^i_{\chi^2} \cdot \varepsilon_{SW} \cdot \sum\limits_{k}^{Events} Z \dfrac{1}{\varepsilon^k_{GEC}(Z) \cdot \varepsilon_Z(\eta_{\mu^+},\eta_{\mu^-}) \cdot \varepsilon^{total}_{trg}(\eta_{\mu^+},\eta_{\mu^-})}} \tag{6.9}$$

where ε_{GEC} stands for the GEC efficiency, $\varepsilon_Z(\eta_{\mu^+},\eta_{\mu^-})$ the Z reconstruction efficiency, $\varepsilon^{total}_{trg}(\eta_{\mu^+},\eta_{\mu^-})$ the total trigger efficiency, $\varepsilon_{ZV_0}(\eta^{V_0}, p_T^{V_0})$ the ZV_0 efficiency, ρ the purity, ε_{χ^2} the efficiency of the $\text{Log}(\chi^2/\text{ndf}) > 1$ cut and ε_{SW} the signal mass window cut correction. The denominator is summed over the events, while the nominator is summed over the number of candidates per bin. For a comparison to generator values, the bin migration has to be taken into account. Furthermore, the influence of the definition of Z and V_0 originating from the same vertex has to be considered. Therefore, the ratio for generator level is defined as:

$$R^i_{gen} = R^i_{rec} \cdot corr_{vertex} \cdot b, \tag{6.10}$$

where $corr_{vertex}$ stands for the correction factor of the vertex combination cut on generator level and b for the bin migration correction.

To check the applied inefficiency corrections, the ratio is compared in simulation on generator and reconstruction level. On generator level, the candidates have to fulfil the geometrical acceptance of LHCb, the momentum of the muons have to be larger than 20 GeV/c, the momentum of the pions and protons larger than 2 GeV/c and the separation between the primary vertices of the Z and the V_0 has to be smaller than 115 µm in x and y, and smaller than 630 µm in z. On reconstruction level, the same extraction and correction procedure as on data is applied. Figure 6.56 and 6.57 show the ratio in bins of R and p_{T} of the V_0 for generator level and reconstruction level in simulation. In addition to the statistical uncertainties, the systematic uncertainties are shown for the comparison. The systematic uncertainties are discussed in the next section 6.12. Generator and reconstruction level agree with each other within their uncertainties for both decays, ZK^0_S and $Z\Lambda$. In the latter, a small overestimation of the reconstruction level is present, but still within the uncertainties. Hence, the correction procedure is considered as confirmed.

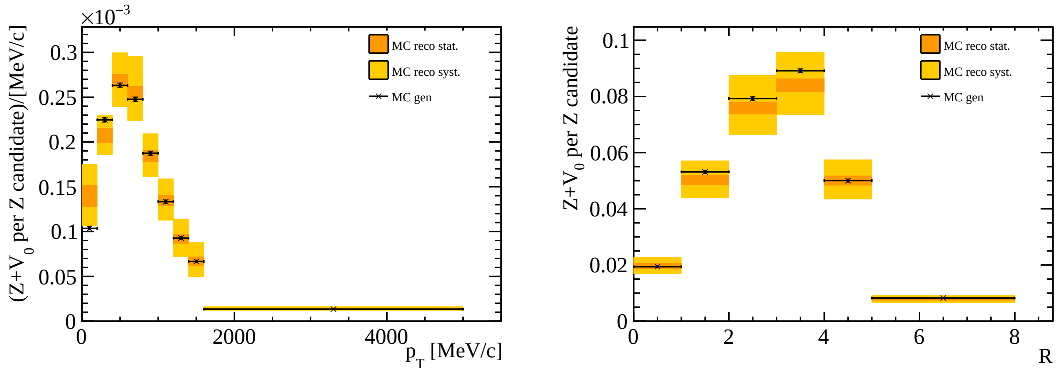

Figure 6.56: The number of ZK^0_s candidates per Z candidate as a function of p_T and R of K^0_s for generator level and reconstruction level in simulation. The numerical values are in table B.11.

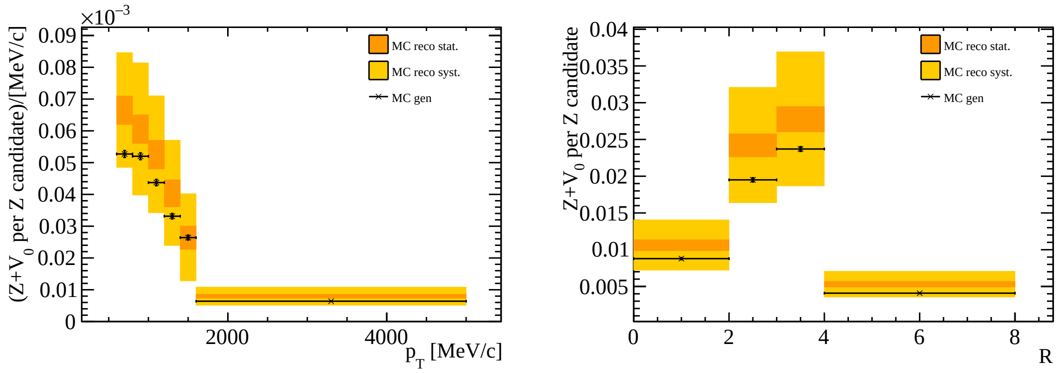

Figure 6.57: The number of $Z\Lambda$ candidates per Z candidate as a function of p_T and R of Λ for generator level and reconstruction level in simulation. The numerical values are in table B.12.

6.12 SYSTEMATIC UNCERTAINTIES

The systematic uncertainties can be grouped into three categories: the first involves the fit procedure to estimate the purity and signal loss due to the cut on $\mathrm{Log}(\chi^2/\mathrm{ndf}) > 1$, the second is related to the efficiency correction of the Z selection and the third refers to the efficiency correction of the ZV_0 selection. To estimate the systematic uncertainty on ε_{SW}, the difference in the mass resolution in data and simulation divided by the signal mass window size was taken. For both decays, ZK^0_s and $Z\Lambda$, the systematic uncertainty was found to be negligible. In order to estimate the systematic uncertainty from the correction factors, the vertex distance window on generator level was increased and decreased by 20% . All correction factors are compatible within the statistical uncertainty. Therefore, no additional systematic uncertainty is assigned for the correction.

The first category involves the following sources of systematic uncertainties:

- The effect of the chosen signal mass window size on the signal and combinatorial background candidate estimation is assessed by repeating the fit with a 10% larger signal mass window. A maximal effect is 0.9% for ZK_{S}^{0} and 0.4% for $Z\Lambda$.
- The effect of the sideband size on the combinatorial background subtraction is estimated by reducing the sidebands by 10%. A maximal effect of 0.2% for ZK_{S}^{0} and 0.3% for $Z\Lambda$ is observed.
- The impact of the parameter constrains from the total fit on the purity and signal loss estimation is evaluated by loosen the constrains to ten sigma and by tighten the constrains to one sigma. The fit model was not changed, as any more complex model would involve constrains from simulation due to limited statistics and the overlapping tails of the signal and pile-up distribution. A maximal effect of 5% for ZK_{S}^{0} and 0.5% for $Z\Lambda$ is observed. A maximal value in ZK_{S}^{0} is measured in the lowest p_{T} bin, where the signal and pile-up distributions are the closest.

The systematic uncertainties of the second category, concerning the Z reconstruction efficiency (muon tracking and identification) and the trigger efficiency (muon triggering and GEC) are determined by re-evaluating the amount of signal candidates with all values of the individual efficiencies increased or decreased by one standard deviation individually. A maximal effect comes from the muon tracking efficiency, where an effect of 0.7% is observed.

The third category involves the following sources of systematic uncertainties:

- The effect of the statistical uncertainty of the ZV_0 selection efficiency values on the final result is estimated by re-evaluating the amount of signal candidates by increasing or decreasing the efficiency values by one standard deviation. A maximal effect of 21% for ZK_{S}^{0} and 16% for $Z\Lambda$ is observed.
- The effect of the systematic uncertainty of the ZV_0 selection efficiency is estimated for the both, ZK_{S}^{0} and $Z\Lambda$, individually. For ZK_{S}^{0}, half of the difference between the values of two adjacent bins in η exceeding the statistical uncertainty is taken as systematic uncertainty of the two bins, respectively. A maximal effect of 10% is observed. In case of $Z\Lambda$, half of the variation of the efficiency values in η in one p_{T} bin is taken as systematic uncertainty of that p_{T} bin. The related plots are shown in the appendix in section B.1. A maximal effect of 35% is measured.

Furthermore, some crosschecks on the binning scheme in η of the ZK^0_S selection were performed to verify the systematic uncertainties of the third category:

- The boundaries of the bins in η for the ZK^0_S selection efficiency extraction are shifted by 20% in the positive and negative direction, respectively. A maximal effect of 9% is observed.
- The binning in η is enlarged by splitting the bins in half. A maximal effect of 10% is observed.

The crosschecks added in quadrature are of the same order as the systematic contributions from the statistical and systematical effect from the efficiency determination of the ZK^0_S selection. Hence the estimated systematic uncertainties from the third category are confirmed. No luminosity uncertainty is assigned, as the luminosity is canceling out in the ratio measurement.

Table 6.12: The systematic uncertainties ranges over the p_T or R bins for ZK^0_S are shown for the different systematic sources. In addition, the crosschecks are shown below.

	p_T [%]	R [%]
Signal mass window	$(0.0005 - 0.9)$	$(0.08 - 0.22)$
Sideband size	$(0.0005 - 0.2)$	$(0.01 - 0.08)$
Fit constrain 10 sigma	$(0.04 - 5)$	$(0.002 - 0.33)$
Fit constrain 1 sigma	$(0.03 - 4)$	$(0.002 - 0.34)$
GEC	$(0.1 - 0.6)$	$(0.1 - 0.3)$
Muon ID	$(0.0007 - 0.01)$	$(0.004 - 0.0025)$
Muon tracking	0.7	0.7
Muon trigger	$(8 \cdot 10^{-5} - 0.0021)$	$(7 \cdot 10^{-4} - 0.007)$
$Z\Lambda$ efficiency statistical	$(6 - 21)$	$(9 - 11)$
$Z\Lambda$ efficiency systematic	$(0.9 - 10)$	$(3 - 4.5)$
Total	$(6 - 23)$	$(10 - 18)$
Crosschecks		
Binning positive shift	$(0.6 - 9)$	$(0.1 - 2)$
Binning negative shift	$(0.1 - 8)$	$(0.8 - 4)$
Larger Binning	$(0.5 - 10)$	$(1.4 - 5)$
Crosschecks Total	$(0.8 - 16)$	$(1.6 - 7)$

The systematic uncertainties and crosschecks for ZK^0_S and $Z\Lambda$ are summarised in table 6.12 and 6.13. The complete tables are in the appendix section B.4. The total systematic uncertainties are evaluated by adding the individual sources in quadrature. In case of ZK^0_S, the systematic uncertainty is of the order of 6-23% in p_T and 10-18% in R, whereas the systematic uncertainty is of the order of 20-39% for p_T and 26-28% for R in case of $Z\Lambda$. The dominating systematic uncertainties are the statistical and systematical uncertainties from the efficiency determination of the ZV_0 selection.

Table 6.13: The systematic uncertainties ranges over the p_T or R bins for $Z\Lambda$ are shown for the different systematic sources.

	p_T [%]	R [%]
Signal mass window	$(0.01 - 0.4)$	$(0.07 - 0.3)$
Sideband size	$(0.01 - 0.2)$	$(0.005 - 0.3)$
Fit constrain 10 sigma	$(0.005 - 0.4)$	$(0.03 - 0.2)$
Fit constrain 1 sigma	$(0.01 - 0.5)$	$(0.04 - 0.2)$
GEC	$(0.1 - 0.5)$	$(0.11 - 0.3)$
Muon ID	$(0.004 - 0.02)$	$(8 \cdot 10^{-5} - 0.03)$
Muon tracking	0.7	0.7
Muon trigger	$(1 \cdot 10^{-4} - 0.004)$	$(1 \cdot 10^{-4} - 6 \cdot 10^{-3})$
$Z\Lambda$ efficiency statistical	$(7 - 16)$	$(9 - 11)$
$Z\Lambda$ efficiency systematic	$(19 - 35)$	$(25 - 26)$
Total	$(20 - 39)$	$(26 - 28)$

6.13 RESULTS

Figure 6.58 and 6.59 show the result for data and generator level, the latter is shown for PYTHIA 6 and PYTHIA 8[33]. Figure 6.60 and 6.61 show the result for data and reconstruction level. The systematic uncertainties of the reconstruction level and data are fully correlated, as the systematic uncertainty is dominated by the efficiency ε_{ZV_0}. Therefore, only the mean values have to be compared in case of data and reconstruction level. The PYTHIA 8 generator gives a more accurate description of diffractive pp interactions than PYTHIA 6, especially at high p_T, as it includes the contribution from hard diffractive processes, which is absent in PYTHIA 6 [160]. In addition, the default parameters of PYTHIA 8 lead to a higher event multiplicity. In terms of the energy flow in an event (see section 6.1.1), all PYTHIA 6 tunes underestimate the amount of energy flow at large pseudo-rapidities. PYTHIA 8 gives an accurate description of the energy flow, except for hard scattering events, where it overestimates the energy flow at large pseudo-rapidities.

The p_T distribution for ZK^0_S is harder than predicted by PYTHIA 6. The prediction by PYTHIA 8 is in agreement with data at high p_T. This is a reflection of the hard diffractive processes which are included in Pythia 8. At $p_{\mathrm{T}} < 500\,\mathrm{MeV}/c$ both predictions tend to overestimate the data. In R, the prediction by Pythia 8 overestimates the measurement in the highest bin, and is in agreement with data in the other bins, while the Pythia 6 prediction agrees in shape and is slightly below the data. The behaviour in R is strongly correlated to the p_{T} distribution, candidates with large and small R values tend to have a higher contribution from low p_{T} candidates.

A similar behaviour in terms of Pythia 6 is visible for $Z\Lambda$. In R, both generators agree in shape with the measurement, but underestimate the number of $Z\Lambda$ per Z candidate. In p_{T}, both predictions are underestimating the result, but the Pythia 8 prediction agrees in shape with the data. The overall underestimation of the amount of $Z\Lambda$ candidates is expected from the particle production ratio measurement, which is discussed in section 6.1.2. Here it was already found that the number of Λ candidates with respect to the number of K^0_{S} candidates in the event is larger in data than in simulation.

For a detailed discussion additional MC models would be helpful, for example Herwig++ and Sherpa generators, which use different hadronisation models. Unfortunately, those are not yet available for LHCb. Furthermore, the systematical uncertainty of the measurement is too large for firm conclusions. It could be reduced by significantly increasing the statistics of the simulated sample by roughly a factor 100. This limitation of the results was discovered only a few months before the end of this thesis, which was too late to produce larger simulation data sets. Nevertheless, the measurements show an indication of a discrepancy between simulation and measurement, which could be used in future tunes of the MC.

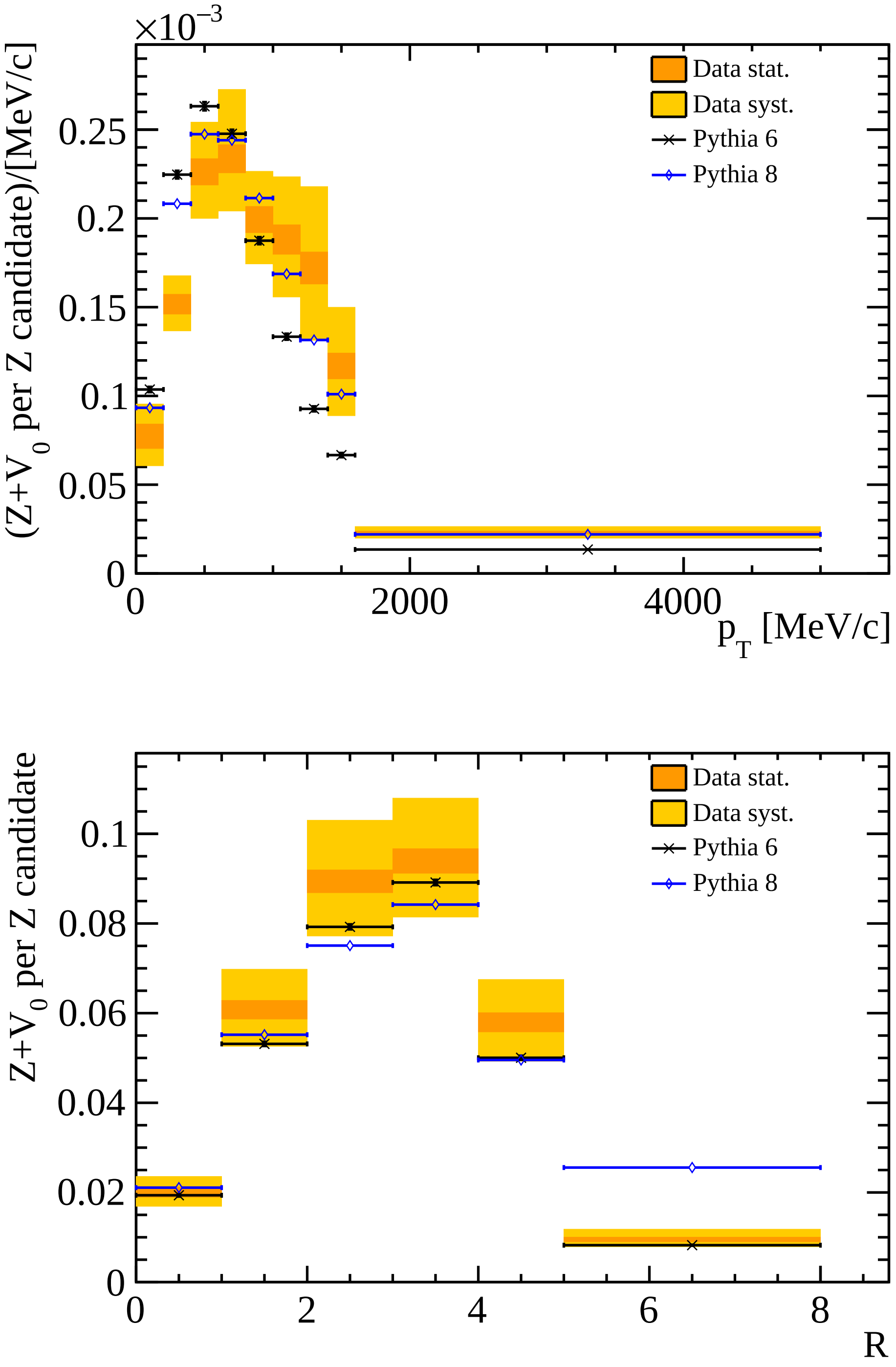

Figure 6.58: The number of ZK^0_s candidates per Z candidate as a function of p_T and R of K^0_s for data and generator level in simulation. The numerical values are summarised in section B.4.

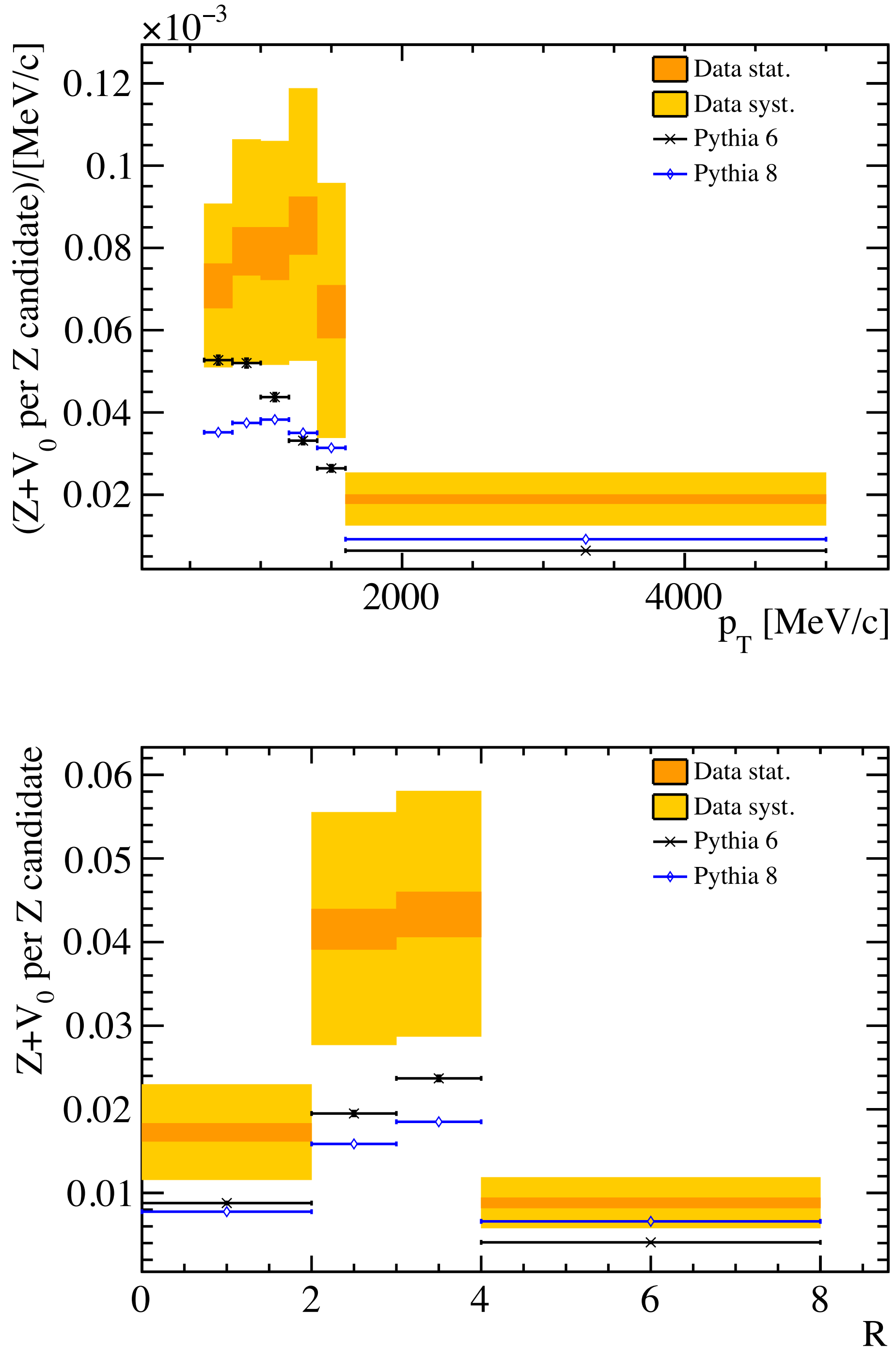

Figure 6.59: The number of $Z\Lambda$ candidates per Z candidate as a function of p_{T} and R of Λ for data and generator level in simulation. The numerical values are summarised in section B.4.

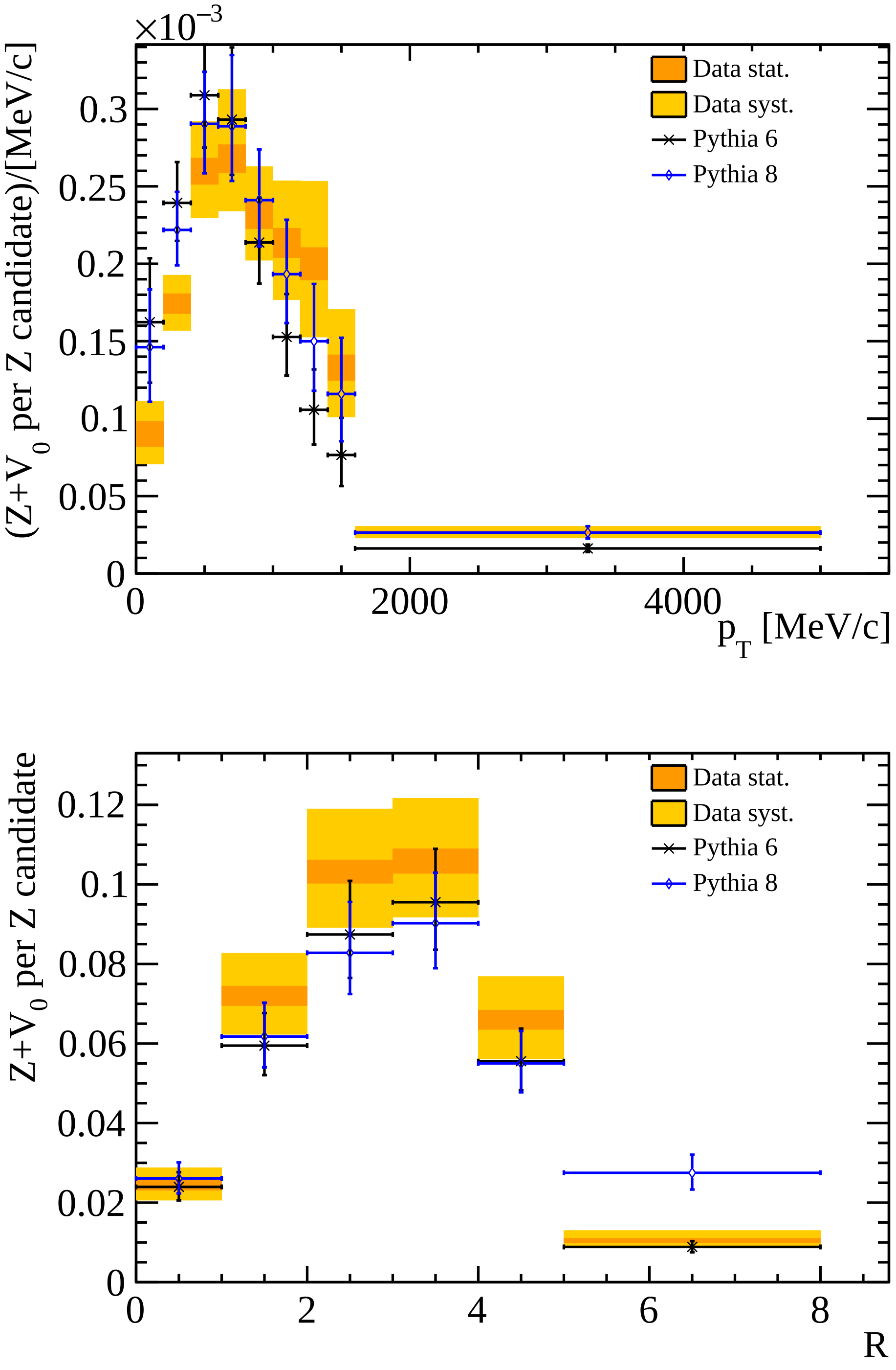

Figure 6.60: The number of ZK^0_S candidates per Z candidate as a function of p_T and R of K^0_S for data and reconstruction level in simulation. The numerical values are summarised in section B.4.

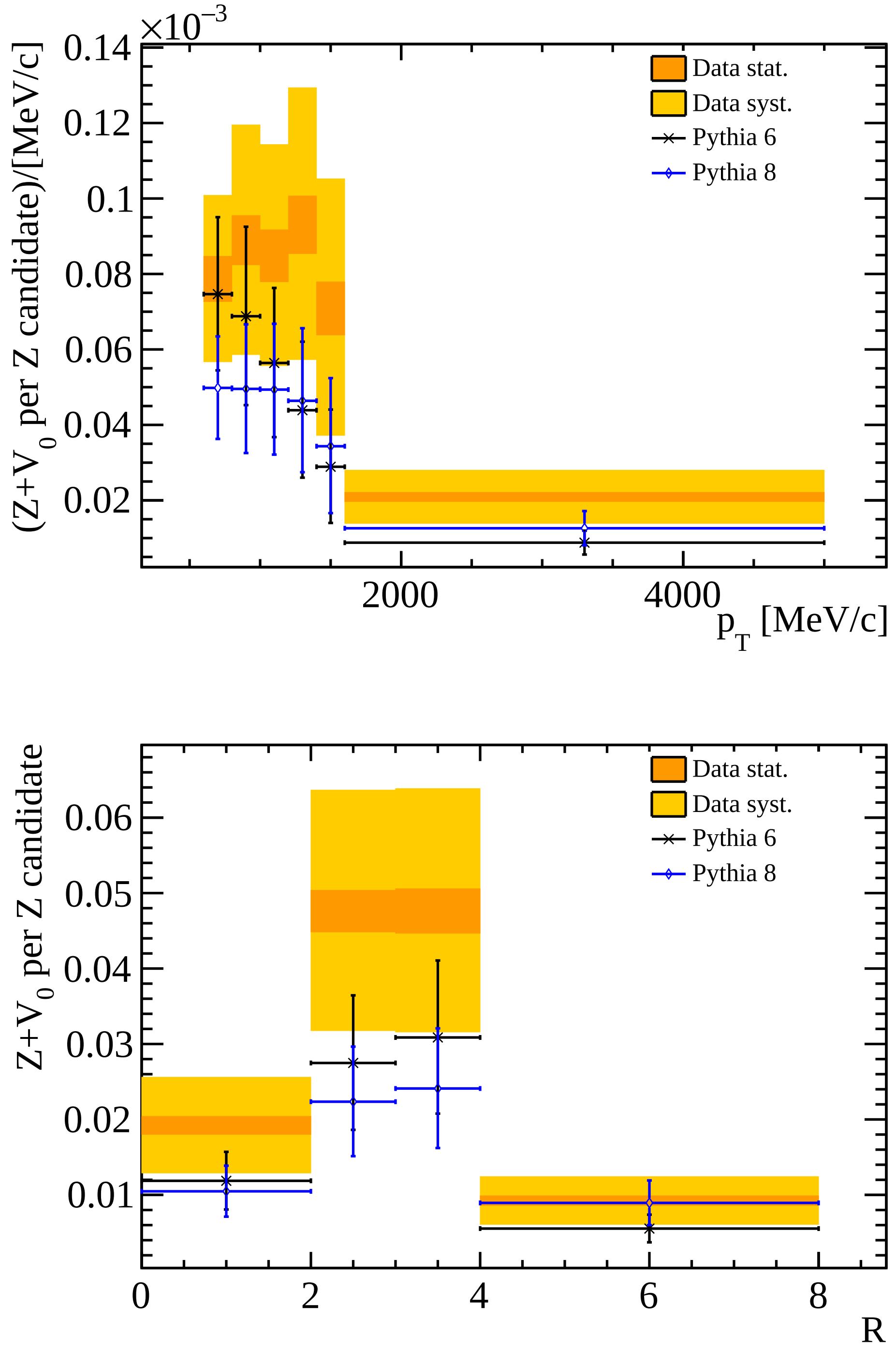

Figure 6.61: The number of $Z\Lambda$ candidates per Z candidate as a function of p_{T} and R of Λ for data and reconstruction level in simulation. The numerical values are summarised in section B.4.

The only source of knowledge is experience.

Albert Einstein

7

Conclusion

The first data acquisition period from spring 2010 until spring 2013 was a great success for the LHCb experiment. A total of 3.19 fb^{-1} of proton-proton collision data at centre of mass energies from 0.9 up to 8 TeV were collected. The detector showed an excellent performance and was able to take data at an instantaneous luminosity twice as high as the design value. This thesis discussed a new algorithm for the track reconstruction and its performance on data. This new algorithm has become a crucial part of the new trigger chain of the LHCb experiment in the second data taking period, which has started in spring 2015. The new track reconstruction has improved the execution time from 14 ms to 4 ms and has reduced the amount of tracks with no matching real particle from 46.8% to 17.13%, while leaving the efficiency almost untouched (from 93.15% down to 89.23%). The loss in efficiency can be retrieved in a later step of the trigger chain.

Particle identification has always been an essential ingredient for the majority of the LHCb analyses. The response of the detectors used in particle identification depends on environmental factors such as pressure or temperature, which are challenging to simulate. This leads to a poorly simulated particle identification response of the detector. In this thesis, the particle identification algorithms in LHCb were discussed and a software tool based on resampling of variables was introduced. This tool allowed an adaptation of the simulation to correctly describe the output of the particle identification algorithms. The agreement of the particle identification in the simulation with the measured data was then largely improved. Today, the tool has become part of the particle identification calibration software of LHCb.

The LHCb collaboration has published a large variety of measurements in different fields of high energy physics. Over the years, the experiment has extended its original physics focus on Flavour Physics to a variety of different measurements, for example production measurements of hard QCD processes like Z bosons or jets, exclusive processes or measurements describing event properties. The latter is very sensitive to so-called soft effects, including fragmentation or hadronisation. As the LHC is a hadron collider, the understanding of the soft part of QCD plays a crucial role also for measurements at ATLAS and CMS, such as searches for new particles or precision measurements of the Higgs boson. For a full picture the soft contribution should be measured in as many different processes as possible. In this thesis, a first measurement of the number of K^0_S or $\Lambda/\overline{\Lambda}$ in a $Z \to \mu^+\mu^-$ decay in the fiducial volume defined by the cuts $p_T(\mu) > 20\,\text{GeV}/c$, $p(\pi, p) > 2\,\text{GeV}$, $2.0 < \eta < 4.5$ and $60 < m_{p\pi^-} < 120\,\text{GeV}/c^2$ was performed as function of the opening angle between the Z boson and the strange composite particle or the p_T of the latter. These measurements probe the hadronisation model in the forward region. The results were compared to models on generator and reconstruction level. While the predictions by Pythia 6 underestimate the measurements in $Z\Lambda$ and the p_T distribution was not hard enough for ZK^0_S and $Z\Lambda$, the predictions by Pythia 8 seemed to better describe the data, *e.g.* for high p_T in ZK^0_S and the overall shape in η. The measurements however, suffered from large uncertainties mainly due to limited statistics in the simulation samples, which were needed for the efficiency correction. This issue is to be solved in order to benefit best form these measurements. The results could then be used in future tunings of generators. In addition to this, further comparisons to generators such as Herwig++ or Sherpa with different fragmentation models would be very helpful to better understand the differences between generator-based predictions and measurements.

A

Particle Identification

In the following a detailed list of the input variables used for the training of the multivariate particle identification variables, ProbNN, is given. Furthermore, a list of all input parameters for the PID distribution extraction script MakePIDdistribtuionsRunRange.py and the resampling script MakePIDCorrection.py is given and the comparison of the simulated and measured data samples with and without resampling for the PID variables of kaon, pion and muon of the $B^0 \to J/\psi K^{*0}$ decay is given without the correlation flag.

A.1 MULTIVARIATE APPROACH

Table A.1: IsMuonLoose definition [161].

Momentum range	**Muon stations**
$3\,\mathrm{GeV}/c < p < 6\,\mathrm{GeV}/c$	at least one hit in at least two stations among M2, M3 and M4
$p > 6\,\mathrm{GeV}/c$	at leas one hit in at least three stations among M2, M3, M4 and M5

Table A.2: Overview of the input variables of ProbNNs for long tracks, a detailed list per particle can be found in the configuration files of the tunes of charged proto particles in the LHCb reconstruction software.

Category	**Variable**
Tracking	track p
	track p_T
	track fit number of degrees of freedom (ndf)
	track fit χ^2/ndf
	track fit match χ^2
	track ghost probability
	track Kullback-Liebler distance [162] (CloneDist)
	track fit VELO ndf
	track fit VELO χ^2
	track fit T ndf
	track fit T χ^2
RICH	used aerogel
	used RICH1 gas
	used RICH2 gas
	above muon threshold
	above kaon threshold
	RICH_DLLe
	RICH_DLLmu
	RICH_DLLK
	RICH_DLLp
MUON	background likelihood
	muon likelihood
	isMuon
	in acceptance
	isMuonLoose (see table A.1)
	NShared [a]
CALO	ECAL DLLe
	ECAL DLLmu
	HCAL DLLe
	HCAL DLLmu
	PS DLLe
	bremsstrahlung in acceptance
	bremsstrahlung DLLe
VELO	charge of VELO track

---

[a] number of identified muon tracks sharing a hit with a given muon candidate

A.2 PID Distribution Extraction Extended

Table A.3 shows the input parameters for the extraction of the PID distributions. In the listing A.1 an example code-line is given. Figure A.1 shows the folder structure of the output ROOT file of the MakePIDdistribtuionsRunRange.py extraction script.

Listing A.1: Example running command

```
python MakePIDdistributionsRunRange.py --minRun=114205 --
    maxRun=116915 ”20” ”MagUp” ”[Pi,Mu,K,P]” ”[DLLp,DLLK]”
    --cuts=”[lab1:ALL,lab2:IsMuon==1]”
```

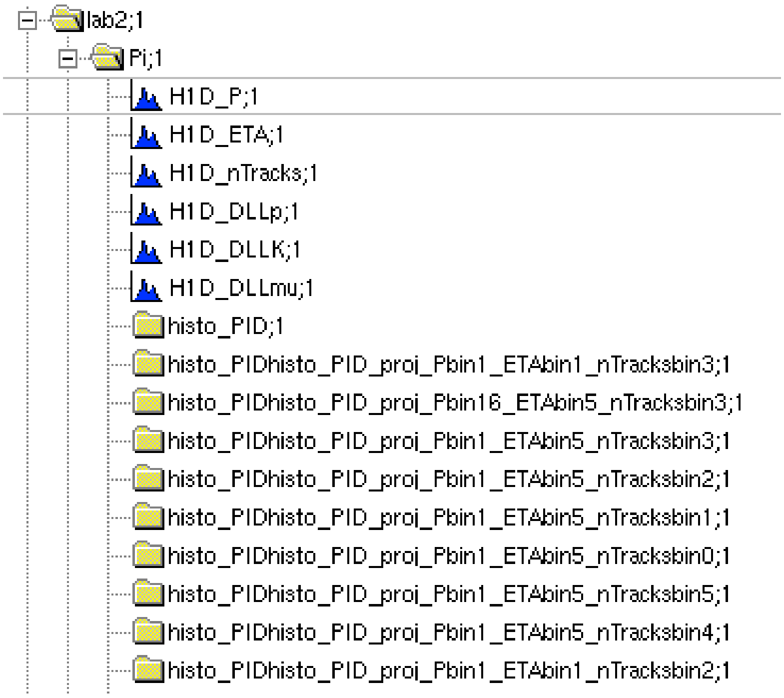

```
lab2;1
  Pi;1
    H1D_P;1
    H1D_ETA;1
    H1D_nTracks;1
    H1D_DLLp;1
    H1D_DLLK;1
    H1D_DLLmu;1
    histo_PID;1
    histo_PIDhisto_PID_proj_Pbin1_ETAbin1_nTracksbin3;1
    histo_PIDhisto_PID_proj_Pbin16_ETAbin5_nTracksbin3;1
    histo_PIDhisto_PID_proj_Pbin1_ETAbin5_nTracksbin3;1
    histo_PIDhisto_PID_proj_Pbin1_ETAbin5_nTracksbin2;1
    histo_PIDhisto_PID_proj_Pbin1_ETAbin5_nTracksbin1;1
    histo_PIDhisto_PID_proj_Pbin1_ETAbin5_nTracksbin0;1
    histo_PIDhisto_PID_proj_Pbin1_ETAbin5_nTracksbin5;1
    histo_PIDhisto_PID_proj_Pbin1_ETAbin5_nTracksbin4;1
    histo_PIDhisto_PID_proj_Pbin1_ETAbin1_nTracksbin2;1
```

Figure A.1: cutout from a sample output file of MakePIDdistribtuionsRunRange.py

Table A.3: required and optional input parameter of `MakePIDdistribtuionsRunRange.py`

required	
stripVersion ("20")	sets the stripping version
magPol ("MagUp")	sets the magnet polarity
partName ("[K,Pi]")	sets the particle type
pidVars ("[DLLp,DLLK]")	sets the PID variables to store
optional	
-h, –help	shows this help message and exit
-x NUM, –minRun NUM	sets the minimum run number to process (if applicable)
-y NUM, –maxRun NUM	sets the maximum run number to process (if applicable)
-c CUTS, –cuts CUTS	sets the list of cuts to apply to the calibration sample(s) prior to determine the PID efficiencies. It is up to the user to ensure that their reference sample has the same cuts applied.
-o DIR, –outputDir DIR	saves the performance histograms to directory DIR (default: current directory)
-q, –quiet	suppresses the printing of verbose information
-M, –allow-missing	allow missing calibration subsamples. This option should only be used if requested to do so by the PIDCalib authors
binning options	
-X NAME, –xVarName NAME	sets the NAME of the 1st (x) bin variable (default: P)
-Y NAME, –yVarName NAME	sets the NAME of the 2nd (y) bin variable (default: ETA). If 1D binning is required, then this option should be set to an empty string
-Z NAME, –zVarName NAME	sets the NAME of the 3rd (z) bin variable (default: nTracks). If 2D binning is required, then this option should be set to an empty string
-s NAME, –schemeName NAME	sets the NAME of the binning scheme, as defined in the module 'PIDPerfScripts.binning'. If this option is not set, the default binning scheme is used.
-b NAME, –binSchemeFile NAME	sets the NAME of the python file containing user-defined binning schema. Without this option, the script will only look for binning schema in the 'PIDPerfScripts.binning' module

A.3 RESAMPLING OF THE PID VARIABLES EXTENDED

Table A.4 gives an overview of all possible input parameters for the resampling script. In listing A.2 is given an example code-line, where lab1 and lab2 are the folder in the output of the PID distribution extraction which correspond to different cut conditions.

Table A.4: required and optional input parameter of MakePIDCorrection.py

required	
mcFile (”example.root”)	sets the MC file to correct
mcFilePathToTree (”tuple/DecayTree”)	sets the internal path to the TTree of the MC file
partName (”[K:lab1/K,Pi:lab2/Pi]”)	sets the particle type and lab folder from the table file of MakePIDdistributionRunRange.py
particles (”[K,Pi]”)	sets the particle to correct for (Naming scheme of the MC file)
pidVars (”[PIDp,PIDK]”)	sets the PID variables to correct
pidLibrary (”pidLibraryfile.root”)	sets the path to the library file with the PID distributions
binning options	
-X NAME, –xVarName NAME	sets the NAME of the 1st (x) bin variable (default: P)
-Y NAME, –yVarName NAME	sets the NAME of the 2nd (y) bin variable (default: ETA). If 1D binning is required, then this option should be set to an empty string
-Z NAME, –zVarName NAME	sets the NAME of the 3rd (z) bin variable (default: nTracks). If 2D binning is required, then this option should be set to an empty string
optional	
-fD DATAFILE	sets the data file to get reasonable multiplicity distribution (ntracks)
-fDP IPATHTTREE	sets the internal path to the TTree of the data file.
-id	uses the TRUE_ID information of the corrected particles
-uCorr	takes the correlation between the PID variables into account for resampling
-nE	number of Events to run over
-d	debug

Listing A.2: Example code

```
python −i MakePIDCorrection.py ”MC_file.root” ”tuple/
    DecayTree” ”[K:lab1/K,Pi:lab2/Pi]” ”[K,Pi]” ”[PIDK,
    PIDmu,PIDp]” output_MakePIDdistributionRunRange.root
```

A.4 COMPARISON WITHOUT CORRELATION FLAG

On the following pages, the comparison of the simulated and measured data samples with and without resampling for the PID variables of kaon, pion and muon of the $B^0 \to J/\psi K^{*0}$ decay is given without the correlation flag.

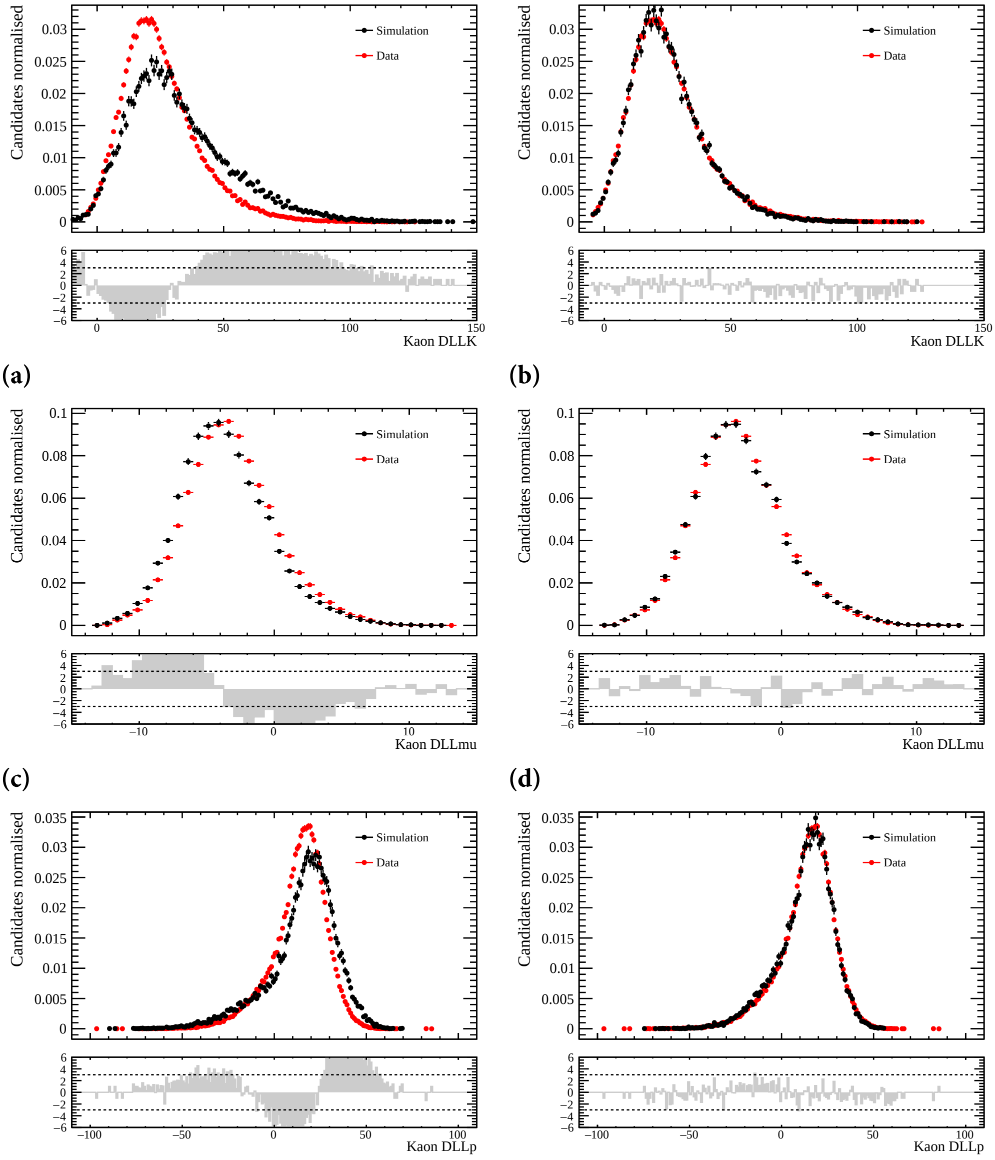

(a) (b)

(c) (d)

(e) (f)

Figure A.2: Comparison of the DLL distribution for kaons of the $B^0 \to J/\psi K^{*0}$ decay. The left (right) column shows the simulation without (with) resampling in comparison to data. The correlation flag was not enabled.

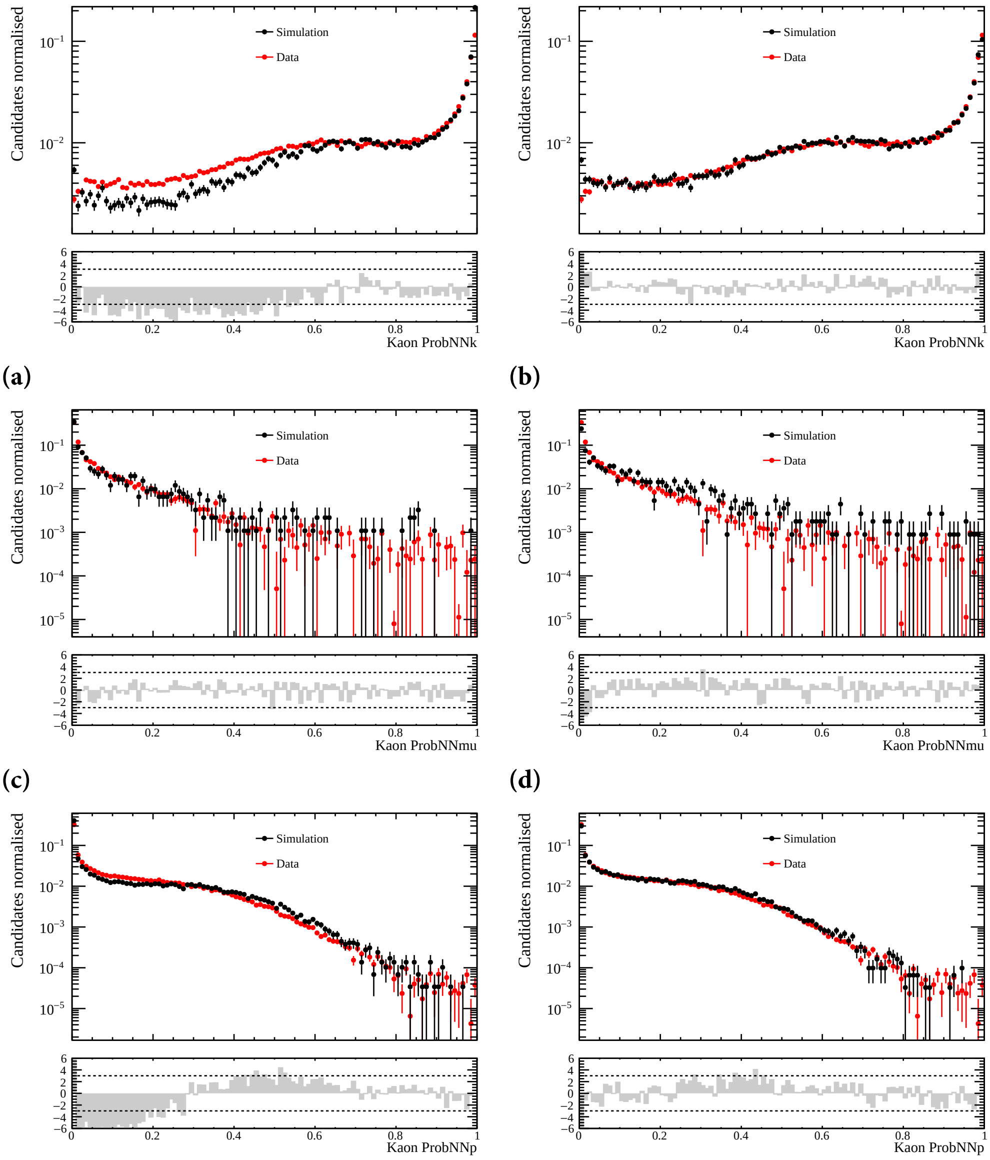

(a) **(b)**

(c) **(d)**

(e) **(f)**

Figure A.3: Comparison of the ProbNN distribution for kaons of the $B^0 \to J/\psi K^{*0}$ decay. The left (right) column shows the simulation without (with) resampling in comparison to data. The correlation flag was not enabled.

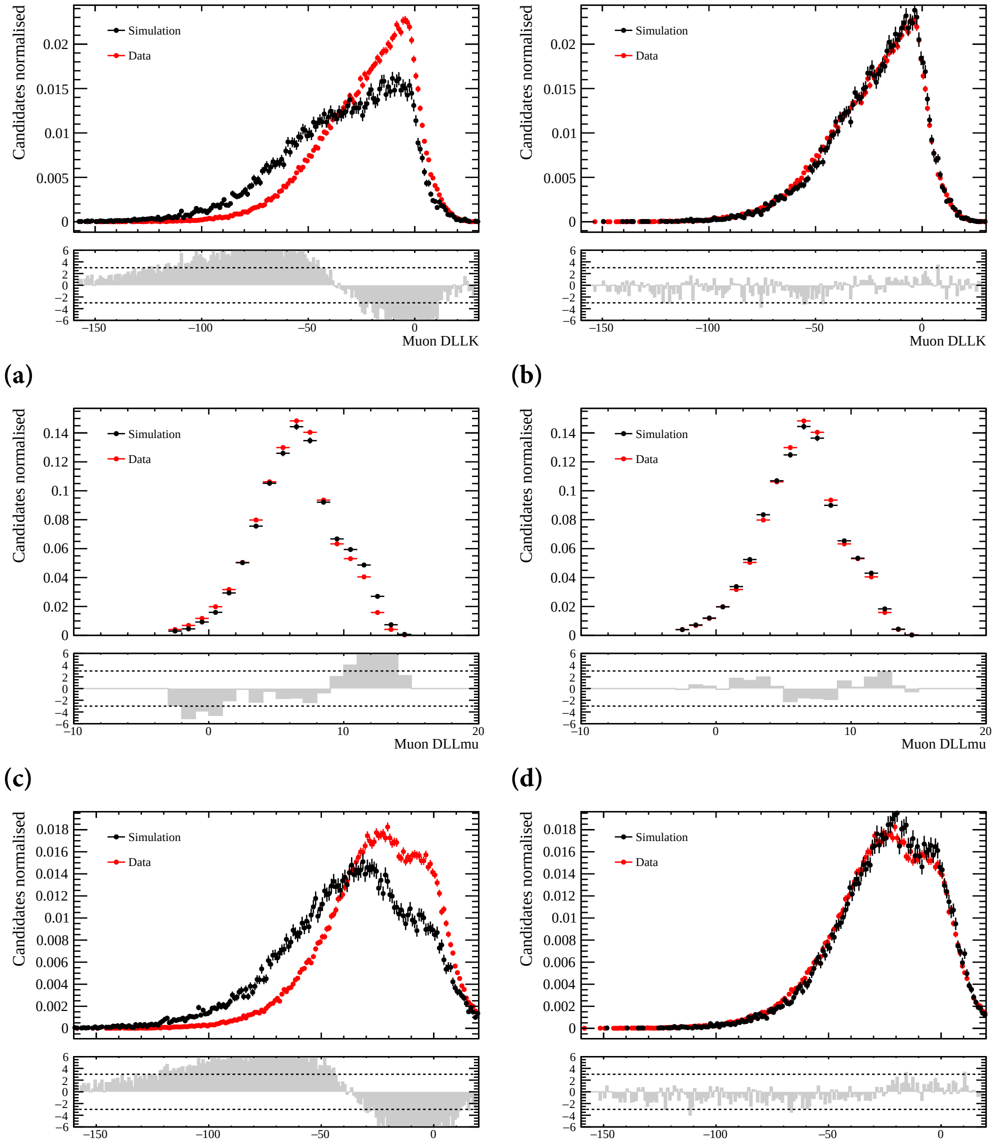

(a) **(b)**

(c) **(d)**

(e) **(f)**

Figure A.4: Comparison of the DLL distribution for muons of the $B^0 \to J/\psi K^{*0}$ decay. The left (right) column shows the simulation without (with) resampling in comparison to data. The correlation flag was not enabled.

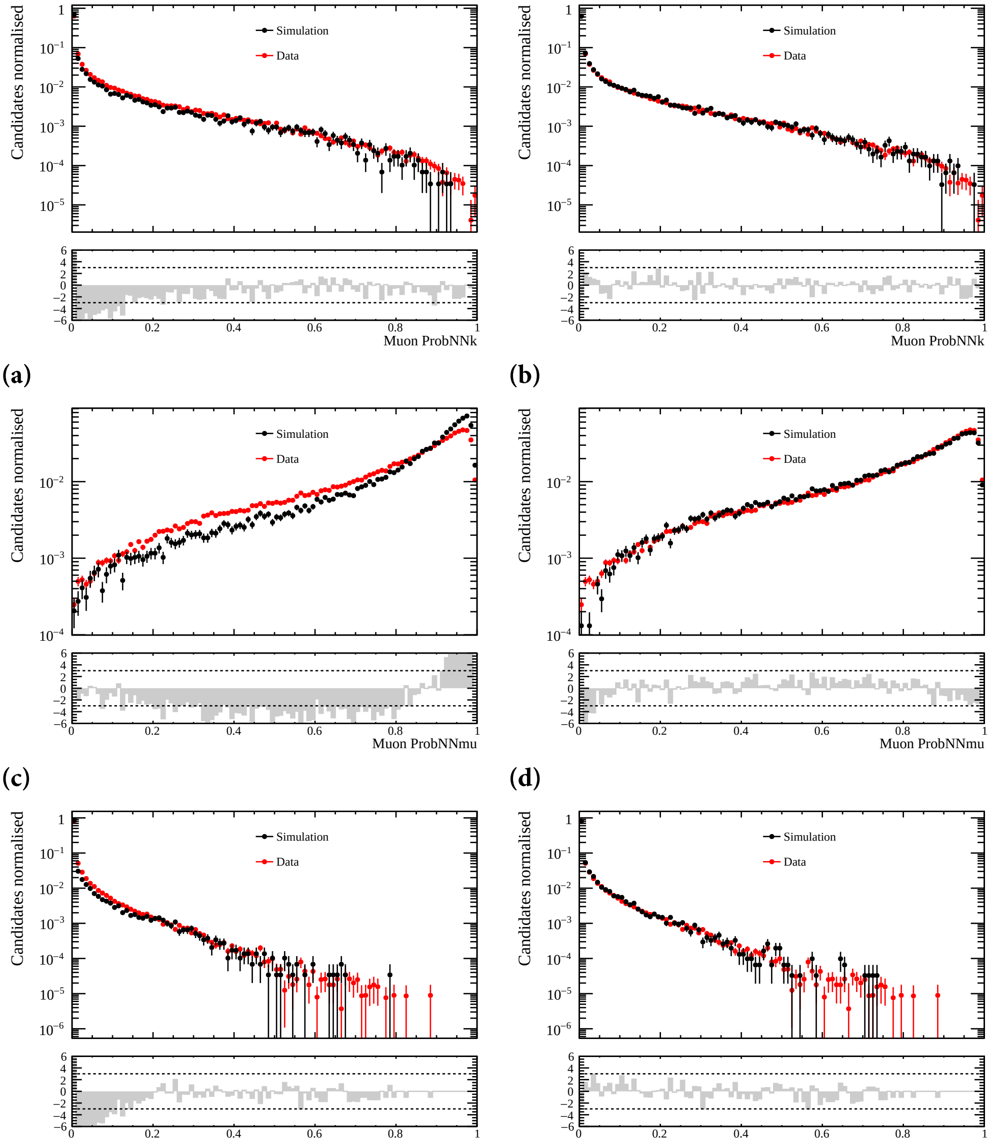

(a) **(b)**

(c) **(d)**

(e) **(f)**

Figure A.5: Comparison of the ProbNN distribution for muons of the $B^0 \to J/\psi K^{*0}$ decay. The left (right) column shows the simulation without (with) resampling in comparison to data. The correlation flag was not enabled.

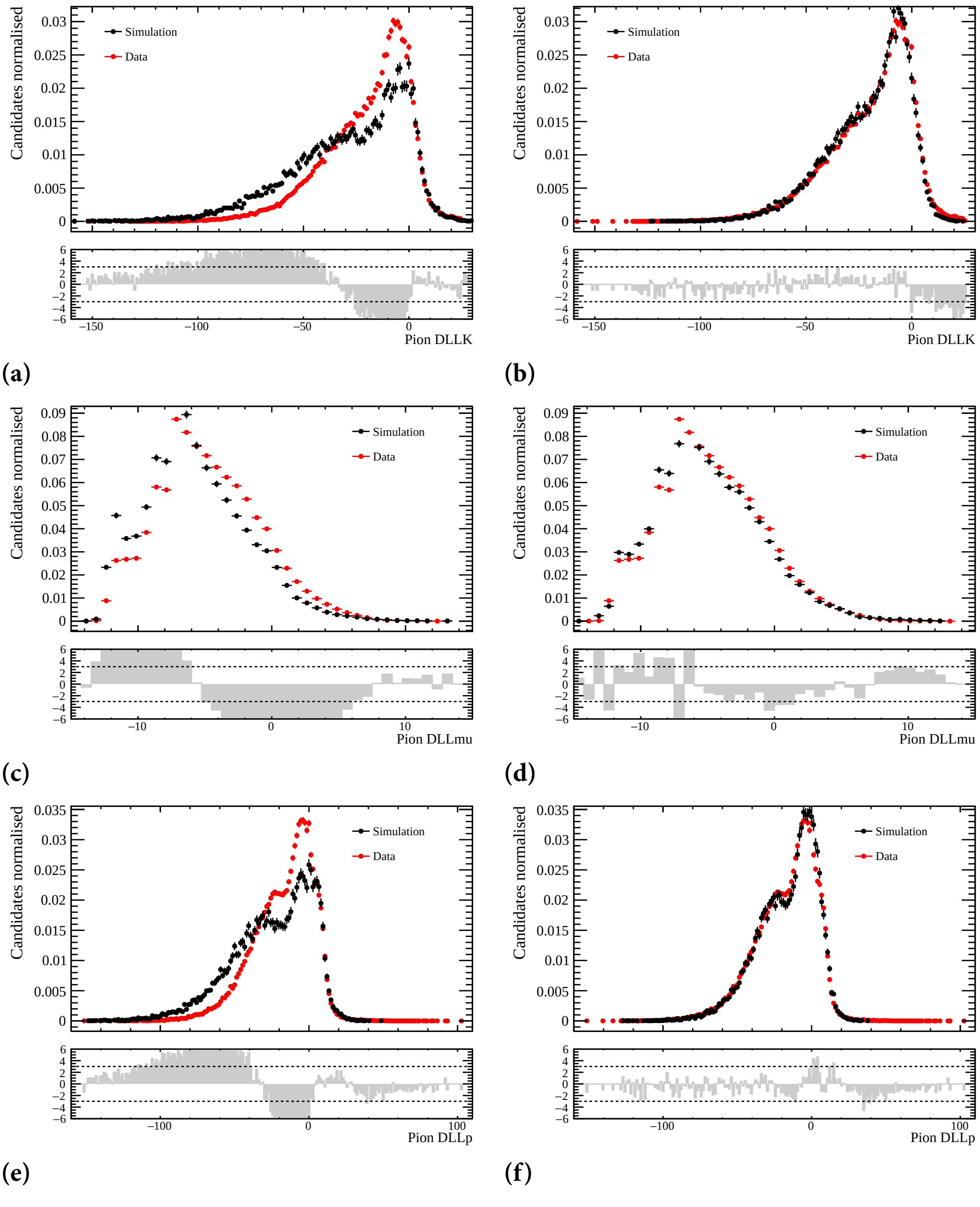

(a) (b) (c) (d) (e) (f)

Figure A.6: Comparison of the DLL distribution for pions of the $B^0 \to J/\psi K^{*0}$ decay. The left (right) column shows the simulation without (with) resampling in comparison to data. The correlation flag was not enabled.

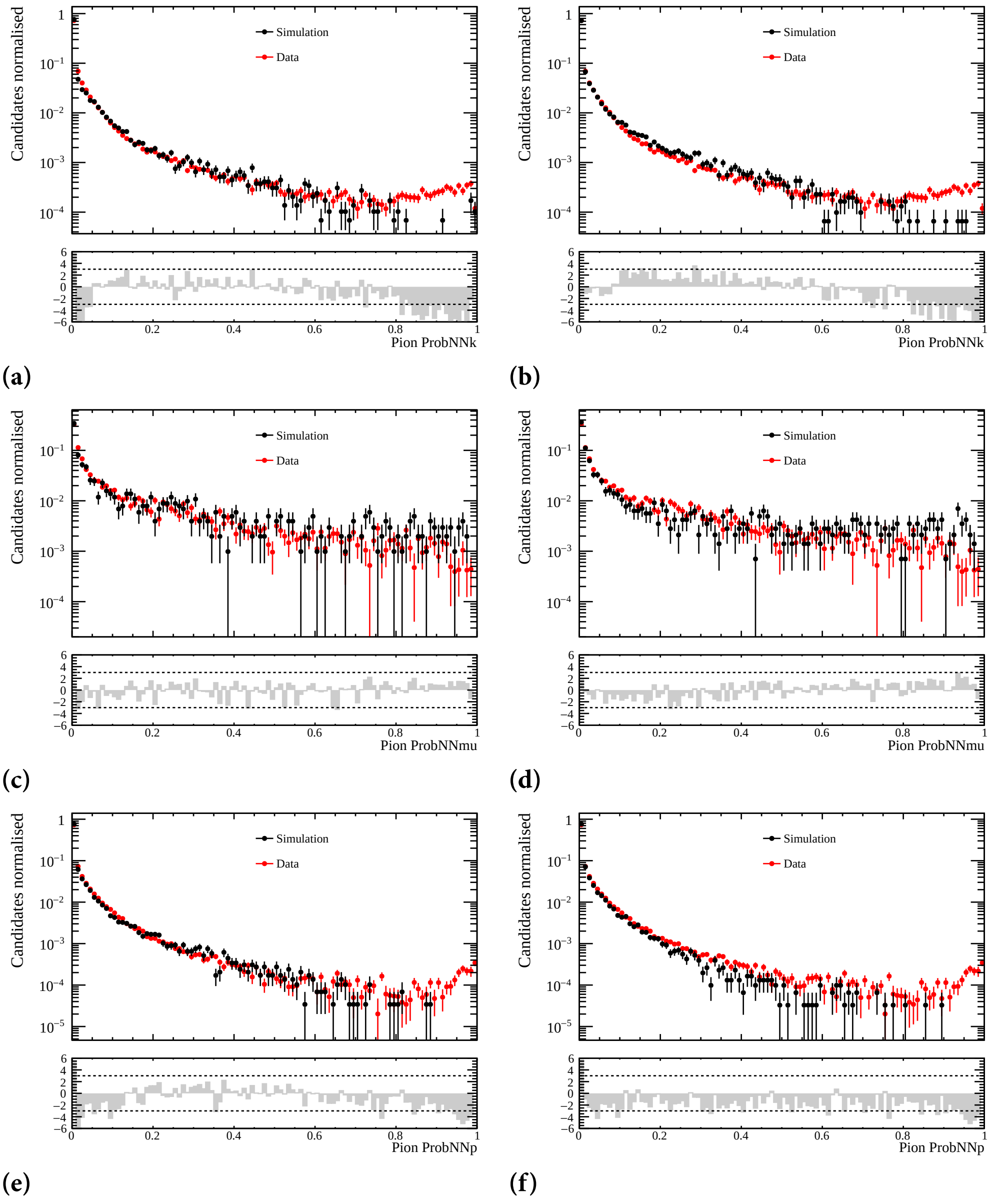

(a) **(b)**

(c) **(d)**

(e) **(f)**

Figure A.7: Comparison of the ProbNN distribution for pions of the $B^0 \to J/\psi K^{*0}$ decay. The left (right) column shows the simulation without (with) resampling in comparison to data. The correlation flag was not enabled.

B

Soft Particle Produced in Hard Event

B.1 ADDITIONAL EFFICIENCY PLOTS FOR SYSTEMATIC STUDIES

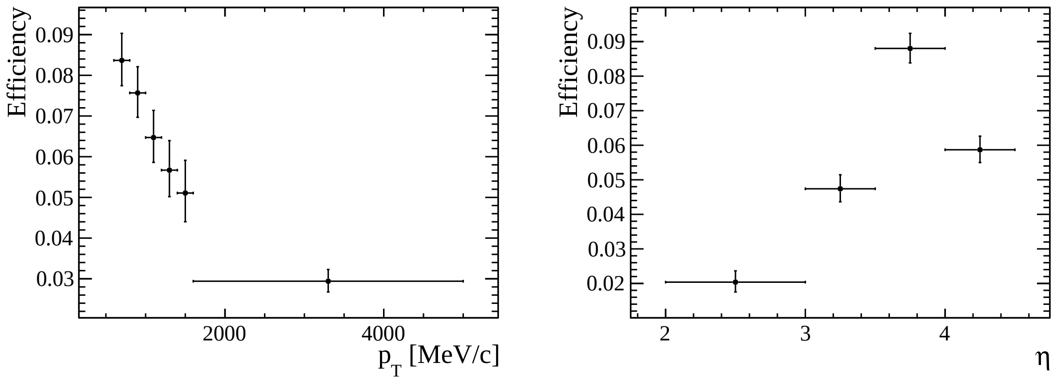

(a) **(b)**

Figure B.1: The selection and reconstruction efficiency of $Z+\Lambda$ as function of p_{T} of the Λ in figure a) and as function of η of the Λ in figure b).

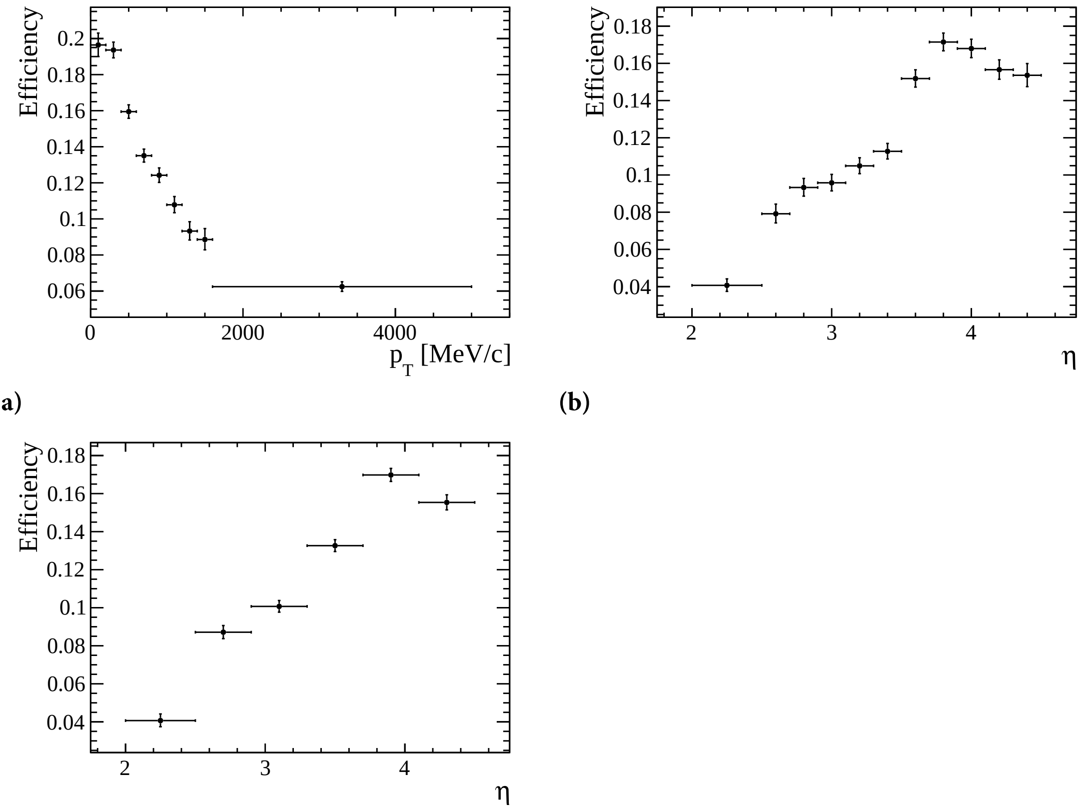

(a)

(b)

(c)

Figure B.2: The selection and reconstruction efficiency of $Z + K_{\mathrm{S}}^{0}$ as function of p_{T} of the K_{S}^{0} in figure a) and as function of η of the K_{S}^{0} with the binning scheme of the first four p_{T} bins in figure b) and with the binning scheme of the remaining p_{T} bins in figure c).

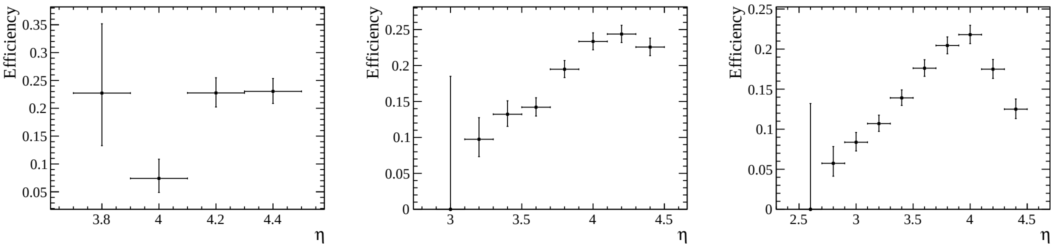

(a) 1. bin in p_T **(b)** 2. bin in p_T **(c)** 3. bin in p_T

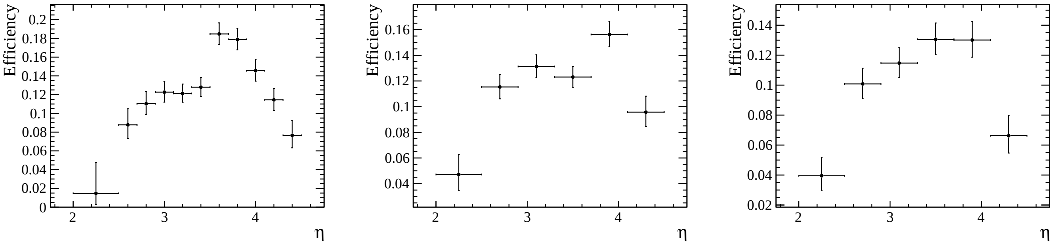

(d) 4. bin in p_T **(e)** 5. bin in p_T **(f)** 6. bin in p_T

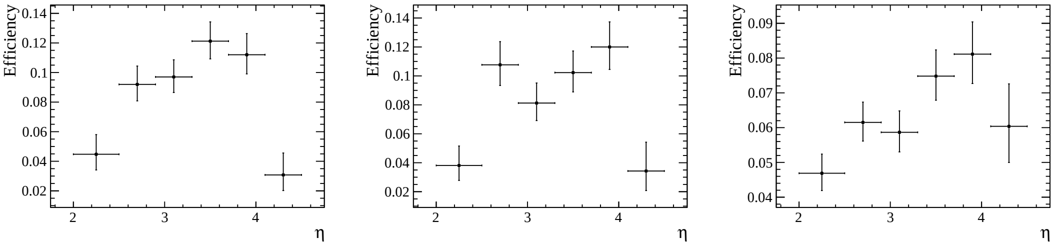

(g) 7. bin in p_T **(h)** 8. bin in p_T **(i)** 9. bin in p_T

Figure B.3: The figures show the η distribution within a certain p_T bin of $Z + K_s^0$

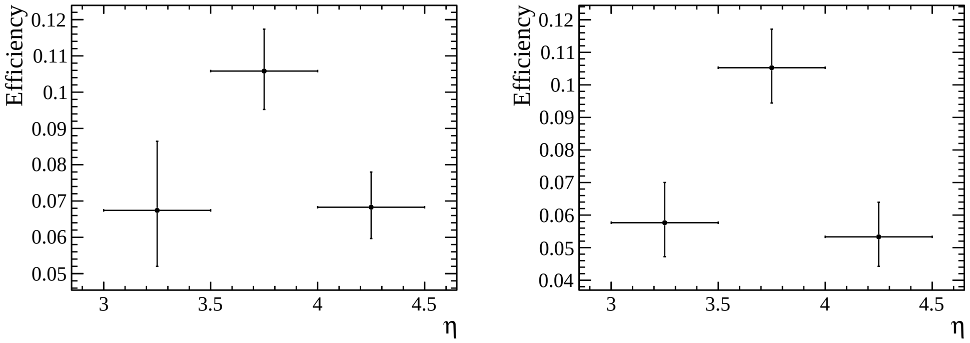

(a) 1. bin in p_T **(b)** 2. bin in p_T

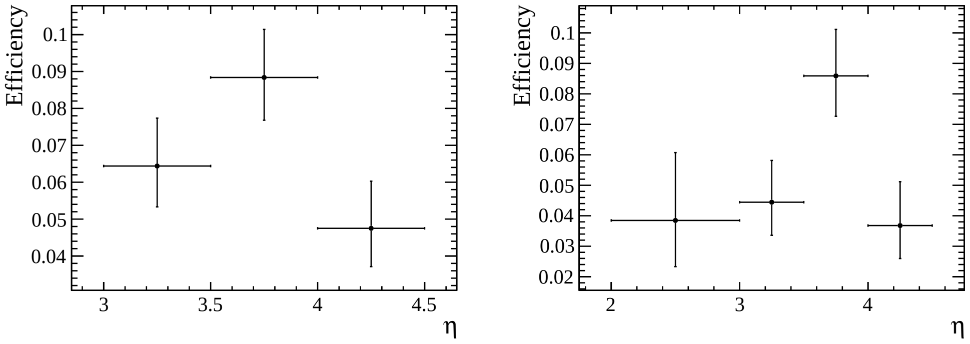

(c) 3. bin in p_T **(d)** 4. bin in p_T

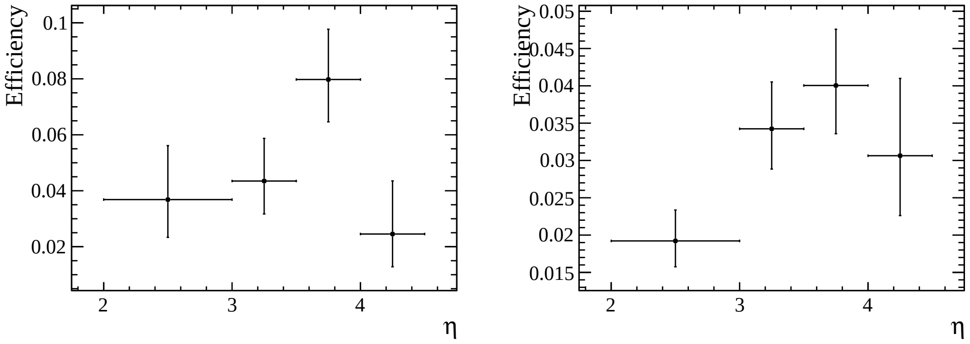

(e) 5. bin in p_T **(f)** 6. bin in p_T

Figure B.4: The figures show the η distribution within a certain p_T bin of $Z + \Lambda$

B.2 Systematic Tables

In the following, the relative systematic uncertainties are shown for $Z + K^0_S$ and $Z + \Lambda$ on 2 fb^{-1} of data collected at LHCb with a $\sqrt{s}$ =8 TeV. Furthermore the cross-checks for $Z + K^0_S$ are shown as well.

Table B.1: The lower relative systematic uncertainties on the final result of $Z + K_S^0$ in bins of K_S^0 p_T for data and cross-checks.

Bin	1	2	3	4	5	6	7	8	9
Signal mass window	8.67e-03	1.61e-03	6.71e-05	8.07e-04	2.21e-04	3.49e-04	8.05e-05	5.45e-06	1.82e-04
Sideband size	1.78e-03	2.42e-04	1.53e-04	1.49e-04	1.66e-04	1.09e-04	5.49e-06	8.91e-06	6.91e-05
Fit constrain 10 sigma	5.28e-02	4.13e-03	1.89e-03	9.21e-04	8.34e-04	3.72e-04	1.83e-03	1.76e-03	8.93e-04
Fit constrain 3 sigma	3.63e-02	4.93e-03	2.89e-03	1.17e-03	1.35e-03	3.48e-04	1.84e-03	1.47e-03	1.14e-03
GEC	3.72e-03	2.85e-03	2.67e-03	2.98e-03	3.37e-03	4.16e-03	5.06e-03	6.31e-03	4.33e-03
Muon ID	5.57e-05	7.38e-06	6.50e-05	4.00e-05	5.57e-05	2.17e-05	8.16e-06	4.15e-05	5.04e-05
Muon tracking	7.03e-03	7.03e-03	7.03e-03	7.03e-03	7.02e-03	7.04e-03	7.04e-03	7.04e-03	7.03e-03
Muon trigger	6.50e-06	1.45e-06	4.10e-06	6.10e-06	1.56e-05	8.29e-07	1.72e-06	4.58e-06	4.75e-06
$Z + K_S^0$ efficiency statistical	1.30e-01	6.63e-02	8.52e-02	1.32e-01	8.73e-02	1.33e-01	2.07e-01	2.14e-01	1.11e-01
$Z + K_S^0$ efficiency systematic	9.29e-03	1.53e-02	3.04e-02	1.96e-02	4.67e-02	5.36e-02	5.46e-02	5.41e-02	1.00e-02
Total	1.46e-01	6.88e-02	9.09e-02	1.33e-01	9.93e-02	1.44e-01	2.14e-01	2.21e-01	1.12e-01
Crosschecks									
Binning positive shift	8.66e-02	2.08e-02	2.05e-02	5.98e-03	1.06e-02	2.80e-02	5.10e-02	1.61e-02	1.12e-02
Binning negative shift	1.37e-02	2.22e-02	8.67e-03	1.50e-02	4.18e-02	1.32e-02	1.03e-01	3.93e-02	4.61e-03
Larger Binning	8.06e-02	1.33e-02	7.42e-03	1.39e-03	1.46e-03	6.15e-02	4.13e-02	7.70e-02	5.15e-02
Total	1.19e-01	3.32e-02	2.35e-02	1.62e-02	4.31e-02	6.88e-02	1.22e-01	8.79e-02	5.28e-02

Table B.2: The upper systematic uncertainties on the final result of $Z + K^0_\mathrm{S}$ in bins of K^0_S p_T for data and cross-checks.

Bin	1	2	3	4	5	6	7	8	9
Signal mass window	8.67e-03	1.61e-03	6.71e-05	8.07e-04	2.21e-04	3.49e-04	8.05e-05	5.45e-06	1.82e-04
Sideband size	1.78e-03	2.42e-04	1.53e-04	1.49e-04	1.66e-04	1.09e-04	5.49e-06	8.91e-06	6.91e-05
Fit constrain 10 sigma	5.28e-02	4.13e-03	1.89e-03	9.21e-04	8.34e-04	3.72e-04	1.83e-03	1.76e-03	8.93e-04
Fit constrain 3 sigma	3.63e-02	4.93e-03	2.89e-03	1.17e-03	1.35e-03	3.48e-04	1.84e-03	1.47e-03	1.14e-03
GEC	2.01e-03	1.20e-03	1.06e-03	1.34e-03	1.76e-03	2.52e-03	3.41e-03	4.64e-03	2.70e-03
Muon ID	5.25e-05	9.84e-05	4.15e-05	6.76e-05	5.34e-05	8.33e-05	9.81e-05	6.31e-05	5.62e-05
Muon tracking	7.05e-03	7.05e-03	7.05e-03	7.05e-03	7.04e-03	7.05e-03	7.05e-03	7.06e-03	7.05e-03
Muon trigger	9.88e-06	1.46e-05	1.21e-05	1.02e-05	8.45e-07	1.68e-05	1.78e-05	2.06e-05	1.14e-05
$Z + K^0_\mathrm{S}$ efficiency statistical	1.06e-01	6.01e-02	7.50e-02	8.84e-02	7.74e-02	1.11e-01	1.55e-01	1.63e-01	9.84e-02
$Z + K^0_\mathrm{S}$ efficiency systematic	2.13e-02	1.33e-02	3.50e-02	2.48e-02	4.16e-02	6.21e-02	9.88e-02	6.97e-02	1.21e-02
Total	1.26e-01	6.23e-02	8.31e-02	9.21e-02	8.82e-02	1.28e-01	1.84e-01	1.78e-01	9.95e-02
Crosschecks									
Binning positive shift	8.66e-02	2.08e-02	2.05e-02	5.98e-03	1.06e-02	2.80e-02	5.10e-02	1.61e-02	1.12e-02
Binning negative shift	1.37e-02	2.22e-02	8.67e-03	1.50e-02	4.18e-02	1.32e-02	1.03e-01	3.93e-02	4.61e-03
Larger Binning	8.06e-02	1.33e-02	7.42e-03	1.39e-03	1.46e-03	6.15e-02	4.13e-02	7.70e-02	5.15e-02
Total	1.19e-01	3.32e-02	2.35e-02	1.62e-02	4.31e-02	6.88e-02	1.22e-01	8.79e-02	5.28e-02

Table B.3: The lower systematic uncertainties on the final result of $Z + K_S^0$ in bins of K_S^0 R for data and cross-checks.

Bin	0	1	2	3	4	5
Signal mass window	1.17e-03	8.90e-04	2.15e-03	7.74e-04	1.37e-03	1.58e-03
Sideband size	8.34e-04	5.70e-04	2.05e-04	1.21e-04	5.25e-04	3.24e-04
Fit constrain 10 sigma	2.73e-03	1.98e-03	1.89e-05	6.81e-04	1.75e-03	3.30e-03
Fit constrain 3 sigma	3.44e-03	3.20e-03	2.36e-05	1.12e-03	2.44e-03	2.93e-03
GEC	4.32e-03	2.87e-03	2.53e-03	2.54e-03	3.10e-03	4.09e-03
Muon ID	1.57e-04	7.37e-05	1.77e-05	4.12e-05	1.53e-04	2.89e-04
Muon tracking	7.09e-03	7.07e-03	7.03e-03	7.03e-03	7.00e-03	6.98e-03
Muon trigger	5.50e-05	2.97e-05	1.35e-06	9.70e-06	3.14e-05	5.80e-05
$Z + K_S^0$ efficiency statistical	1.14e-01	1.10e-01	1.20e-01	1.16e-01	1.24e-01	1.85e-01
$Z + K_S^0$ efficiency systematic	2.72e-02	3.00e-02	3.07e-02	2.89e-02	3.00e-02	3.19e-02
Total	1.18e-01	1.15e-01	1.24e-01	1.20e-01	1.28e-01	1.88e-01
Binning positive shift	4.67e-02	3.25e-02	2.66e-02	1.35e-02	1.99e-02	1.64e-02
Binning negative shift	8.58e-03	8.09e-03	2.10e-02	2.63e-02	4.20e-02	4.02e-02
Larger Binning	1.22e-03	9.93e-03	1.30e-02	1.34e-02	1.91e-02	1.67e-02
Total	4.75e-02	3.50e-02	3.63e-02	3.24e-02	5.02e-02	4.65e-02

Table B.4: The upper systematic uncertainties on the final result of $Z + K_S^0$ in bins of K_S^0 R for data and cross-checks.

Bin	0	1	2	3	4	5
Signal mass window	1.17e-03	8.90e-04	2.15e-03	7.74e-04	1.37e-03	1.58e-03
Sideband size	8.34e-04	5.70e-04	2.05e-04	1.21e-04	5.25e-04	3.24e-04
Fit constrain 10 sigma	2.73e-03	1.98e-03	1.89e-05	6.81e-04	1.75e-03	3.30e-03
Fit constrain 3 sigma	3.44e-03	3.20e-03	2.36e-05	1.12e-03	2.44e-03	2.93e-03
GEC	2.66e-03	1.23e-03	8.99e-04	8.99e-04	1.46e-03	2.43e-03
Muon ID	2.46e-04	1.71e-04	8.84e-05	6.74e-05	3.94e-05	1.66e-04
Muon tracking	7.10e-03	7.08e-03	7.05e-03	7.04e-03	7.02e-03	7.00e-03
Muon trigger	6.90e-05	4.47e-05	1.48e-05	6.69e-06	1.43e-05	3.98e-05
$Z + K_S^0$ efficiency statistical	9.49e-02	9.38e-02	9.96e-02	9.87e-02	1.04e-01	1.09e-01
$Z + K_S^0$ efficiency systematic	3.45e-02	3.46e-02	4.07e-02	3.21e-02	4.34e-02	4.30e-02
Total	1.01e-01	1.00e-01	1.08e-01	1.04e-01	1.13e-01	1.18e-01
Binning positive shift	4.67e-02	3.25e-02	2.66e-02	1.35e-02	1.99e-02	1.64e-02
Binning negative shift	8.58e-03	8.09e-03	2.10e-02	2.63e-02	4.20e-02	4.02e-02
Larger Binning	1.22e-03	9.93e-03	1.30e-02	1.34e-02	1.91e-02	1.67e-02
Total	4.75e-02	3.50e-02	3.63e-02	3.24e-02	5.02e-02	4.65e-02

Table B.5: The lower systematic uncertainties on the final result of $Z + \Lambda$ in bins of $\Lambda\ p_{\mathrm{T}}$ for data.

Bin	0	1	2	3	4	5
Signal mass window	3.88e-03	2.53e-03	1.90e-03	6.68e-04	1.29e-04	1.11e-04
Sideband size	2.98e-04	6.63e-04	1.60e-03	2.28e-04	2.73e-04	1.07e-04
Fit constrain 10 sigma	3.90e-03	1.76e-03	5.20e-05	1.26e-03	3.53e-04	3.28e-04
Fit constrain 3 sigma	5.05e-03	1.86e-03	3.22e-04	2.17e-03	1.15e-04	9.21e-04
GEC	3.03e-03	3.26e-03	3.65e-03	4.44e-03	5.31e-03	3.95e-03
Muon ID	7.22e-05	5.13e-05	1.55e-04	4.05e-05	6.61e-05	7.46e-05
Muon tracking	7.04e-03	7.03e-03	7.02e-03	7.05e-03	7.04e-03	7.06e-03
Muon trigger	7.97e-06	7.35e-06	1.51e-05	9.67e-06	8.63e-06	2.05e-05
$Z + K^0_{\mathrm{S}}$ efficiency statistical	8.02e-02	8.60e-02	1.04e-01	1.30e-01	1.60e-01	9.90e-02
$Z + K^0_{\mathrm{S}}$ efficiency systematic	1.89e-01	2.56e-01	2.45e-01	2.80e-01	3.50e-01	2.63e-01
Total	2.06e-01	2.70e-01	2.66e-01	3.08e-01	3.85e-01	2.81e-01

Table B.6: The upper systematic uncertainties on the final result of $Z + \Lambda$ in bins of $\Lambda\ p_{\mathrm{T}}$ for data.

Bin	0	1	2	3	4	5
Signal mass window	3.88e-03	2.53e-03	1.90e-03	6.68e-04	1.29e-04	1.11e-04
Sideband size	2.98e-04	6.63e-04	1.60e-03	2.28e-04	2.73e-04	1.07e-04
Fit constrain 10 sigma	3.90e-03	1.76e-03	5.20e-05	1.26e-03	3.53e-04	3.28e-04
Fit constrain 3 sigma	5.05e-03	1.86e-03	3.22e-04	2.17e-03	1.15e-04	9.21e-04
GEC	1.36e-03	1.60e-03	2.02e-03	2.77e-03	3.66e-03	2.29e-03
Muon ID	1.75e-04	5.54e-05	4.72e-05	1.43e-04	1.69e-04	1.74e-04
Muon tracking	7.06e-03	7.04e-03	7.04e-03	7.06e-03	7.06e-03	7.07e-03
Muon trigger	2.37e-05	8.81e-06	1.27e-06	2.53e-05	2.43e-05	3.57e-05
$Z + K^0_{\mathrm{S}}$ efficiency statistical	7.36e-02	7.84e-02	9.34e-02	1.13e-01	1.36e-01	8.95e-02
$Z + K^0_{\mathrm{S}}$ efficiency systematic	1.89e-01	2.56e-01	2.45e-01	2.80e-01	3.50e-01	2.63e-01
Total	2.03e-01	2.68e-01	2.62e-01	3.02e-01	3.76e-01	2.78e-01

Table B.7: The lower systematic uncertainties on the final result of $Z + \Lambda$ in bins of Λ R for data.

Bin	0	1	2	3
Signal mass window	2.80e-03	7.13e-04	1.22e-03	8.18e-04
Sideband size	1.66e-03	8.99e-04	5.62e-05	3.10e-03
Fit constrain 10 sigma	2.75e-04	3.22e-04	9.26e-04	2.15e-03
Fit constrain 3 sigma	6.81e-04	3.76e-04	1.31e-03	1.72e-03
GEC	2.73e-03	2.73e-03	2.71e-03	3.05e-03
Muon ID	1.36e-04	1.64e-05	8.18e-07	4.49e-05
Muon tracking	7.08e-03	7.05e-03	7.04e-03	7.02e-03
Muon trigger	4.06e-05	1.04e-05	5.31e-06	1.53e-05
$Z + K_S^0$ efficiency statistical	1.02e-01	1.05e-01	1.03e-01	1.03e-01
$Z + K_S^0$ efficiency systematic	2.50e-01	2.58e-01	2.59e-01	2.56e-01
Total	2.70e-01	2.79e-01	2.78e-01	2.76e-01

Table B.8: The upper systematic uncertainties on the final result of $Z + \Lambda$ in bins of Λ R for data.

Bin	0	1	2	3
Signal mass window	2.80e-03	7.13e-04	1.22e-03	8.18e-04
Sideband size	1.66e-03	8.99e-04	5.62e-05	3.10e-03
Fit constrain 10 sigma	2.75e-04	3.22e-04	9.26e-04	2.15e-03
Fit constrain 3 sigma	6.81e-04	3.76e-04	1.31e-03	1.72e-03
GEC	1.07e-03	1.07e-03	1.05e-03	1.37e-03
Muon ID	2.29e-04	1.20e-04	1.05e-04	6.39e-05
Muon tracking	7.09e-03	7.06e-03	7.06e-03	7.04e-03
Muon trigger	5.50e-05	2.61e-05	2.12e-05	1.06e-06
$Z + K_S^0$ efficiency statistical	9.10e-02	9.36e-02	9.22e-02	9.18e-02
$Z + K_S^0$ efficiency systematic	2.50e-01	2.58e-01	2.59e-01	2.56e-01
Toal	2.66e-01	2.75e-01	2.75e-01	2.72e-01

B.3 BIN MIGRATION

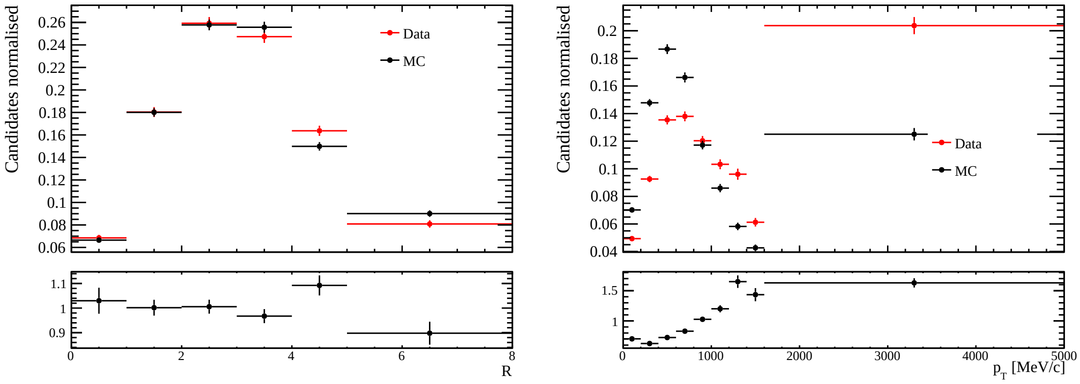

Figure B.5: The figures show the comparison of the distributions of R and p_{T} on data and reconstruction level for $Z + K^0_{\mathrm{S}}$, whereas in the lower part the correction factor for reconstruction level is shown.

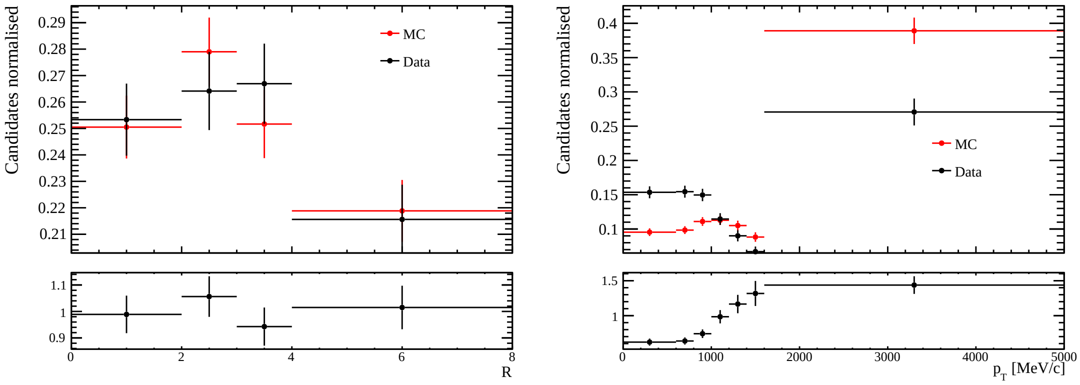

Figure B.6: The figures show the comparison of the distributions of R and p_{T} on data and reconstruction level for $Z + \Lambda$, whereas in the lower part the correction factor for reconstruction level is shown.

B.4 Result as Tables

Table B.9: The number of $Z + K^0_\mathrm{S}$ candidates per Z candidate as dependence of R and p_T of K^0_S for reconstructed simulation and data, before efficiency correction. The figure is shown in fig. 6.39.

	Data			MC reconstructed		
p_T [MeV/c]	centre value	statistical up	statistical low	centre value	statistical up	statistical low
$[0, 200)$	1.97e-05	1.75e-06	1.75e-06	3.59e-05	3.02e-06	3.02e-06
$[200, 400)$	3.69e-05	1.34e-06	1.34e-06	5.04e-05	1.97e-06	1.97e-06
$[400, 600)$	4.14e-05	1.29e-06	1.29e-06	4.93e-05	1.26e-06	1.26e-06
$[600, 800)$	3.62e-05	1.17e-06	1.17e-06	3.94e-05	1.08e-06	1.08e-06
$[800, 1000)$	2.88e-05	1.04e-06	1.04e-06	2.66e-05	8.68e-07	8.68e-07
$[1000, 1200)$	2.20e-05	9.06e-07	9.06e-07	1.62e-05	6.82e-07	6.82e-07
$[1200, 1400)$	1.72e-05	8.00e-07	8.00e-07	9.79e-06	5.26e-07	5.26e-07
$[1400, 1600)$	1.16e-05	6.56e-07	6.56e-07	6.58e-06	4.31e-07	4.31e-07
$[1600, 5000)$	1.65e-06	6.06e-08	6.06e-08	1.00e-06	4.07e-08	4.07e-08

	Data			MC reconstructed		
R	centre value	statistical up	statistical low	centre value	statistical up	statistical low
$[0, 1)$	3.50e-03	1.83e-04	1.83e-04	3.96e-03	1.93e-04	1.93e-04
$[1, 2)$	9.64e-03	3.01e-04	3.01e-04	9.21e-03	2.92e-04	2.92e-04
$[2, 3)$	1.28e-02	3.26e-04	3.26e-04	1.24e-02	3.31e-04	3.31e-04
$[3, 4)$	1.20e-02	3.09e-04	3.09e-04	1.24e-02	3.04e-04	3.04e-04
$[4, 5)$	7.42e-03	2.47e-04	2.47e-04	7.44e-03	2.25e-04	2.25e-04
$[5, 8)$	1.18e-03	5.49e-05	5.49e-05	1.17e-03	5.41e-05	5.41e-05

Table B.10: The number of $Z + \Lambda$ candidates per Z candidate as dependence of R and p_T of Λ for reconstructed simulation and data, before efficiency correction. The figure is shown in fig. 6.40.

	Data			reconstructed		
p_T [MeV/c]	centre value	statistical up	statistical low	centre value	statistical up	statistical low
$[600, 800)$	6.54e-06	4.99e-07	4.99e-07	6.22e-06	4.18e-07	4.18e-07
$[800, 1000)$	6.66e-06	4.89e-07	4.89e-07	5.20e-06	3.87e-07	3.87e-07
$[1000, 1200)$	5.41e-06	4.39e-07	4.39e-07	3.63e-06	3.11e-07	3.11e-07
$[1200, 1400)$	5.22e-06	4.29e-07	4.29e-07	2.47e-06	2.59e-07	2.59e-07
$[1400, 1600)$	3.56e-06	3.54e-07	3.54e-07	1.47e-06	2.05e-07	2.05e-07
$[1600, 5000)$	5.99e-07	3.55e-08	3.55e-08	2.53e-07	2.03e-08	2.03e-08

	Data			MC reconstructed		
R	centre value	statistical up	statistical low	centre value	statistical up	statistical low
$[0, 2)$	1.10e-03	6.35e-05	6.35e-05	7.65e-04	5.06e-05	5.06e-05
$[2, 3)$	2.51e-03	1.34e-04	1.34e-04	1.62e-03	9.66e-05	9.66e-05
$[3, 4)$	2.21e-03	1.26e-04	1.26e-04	1.69e-03	9.59e-05	9.59e-05
$[4, 8)$	4.70e-04	3.00e-05	3.00e-05	3.39e-04	2.16e-05	2.16e-05

Table B.11: The number of $Z + K^0_\mathrm{S}$ candidates per Z candidate as dependence of R and p_T of K^0_S for generator level and reconstruction level in simulation for Pythia 6.

	MC reconstruction level					MC generator level		
p_T [MeV/c]	centre value	statistical up	statistical low	systematic up	systematic low	centre value	statistical up	statistical low
[0, 200)	1.40e-04	1.18e-05	1.18e-05	2.19e-05	2.38e-05	1.04e-04	1.49e-06	1.49e-06
[200, 400)	2.07e-04	8.17e-06	8.17e-06	1.31e-05	1.47e-05	2.25e-04	2.16e-06	2.16e-06
[400, 600)	2.69e-04	7.17e-06	7.17e-06	2.23e-05	2.38e-05	2.63e-04	2.33e-06	2.33e-06
[600, 800)	2.55e-04	7.36e-06	7.36e-06	2.37e-05	3.32e-05	2.48e-04	2.26e-06	2.26e-06
[800, 1000)	1.84e-04	6.20e-06	6.20e-06	1.67e-05	1.88e-05	1.87e-04	1.98e-06	1.98e-06
[1000, 1200)	1.35e-04	5.98e-06	5.98e-06	1.60e-05	1.84e-05	1.33e-04	1.68e-06	1.68e-06
[1200, 1400)	9.15e-05	5.42e-06	5.42e-06	1.41e-05	1.71e-05	9.27e-05	1.41e-06	1.41e-06
[1400, 1600)	6.70e-05	4.82e-06	4.82e-06	1.28e-05	1.61e-05	6.67e-05	1.20e-06	1.20e-06
[1600, 5000)	1.41e-05	5.81e-07	5.81e-07	1.42e-06	1.61e-06	1.35e-05	1.28e-07	1.28e-07

	MC reconstruction level					MC generator level		
R	centre value	statistical up	statistical low	systematic up	systematic low	centre value	statistical up	statistical low
[0, 1)	1.97e-02	1.00e-03	1.00e-03	1.80e-03	2.04e-03	1.94e-02	2.88e-04	2.88e-04
[1, 2)	5.02e-02	1.67e-03	1.67e-03	4.60e-03	5.24e-03	5.31e-02	4.68e-04	4.68e-04
[2, 3)	7.59e-02	2.17e-03	2.17e-03	7.31e-03	9.54e-03	7.92e-02	5.63e-04	5.63e-04
[3, 4)	8.40e-02	2.26e-03	2.26e-03	8.26e-03	9.54e-03	8.91e-02	5.94e-04	5.94e-04
[4, 5)	5.01e-02	1.67e-03	1.67e-03	4.94e-03	5.72e-03	5.00e-02	4.55e-04	4.55e-04
[5, 8)	7.81e-03	3.96e-04	3.96e-04	7.92e-04	8.98e-04	8.24e-03	1.08e-04	1.08e-04

Table B.12: The number of $Z + \Lambda$ candidates per Z candidate as dependence of R and p_T of Λ for generator level and reconstruction level in simulation for Pythia 6

	MC reconstruction level					MC generator level		
p_T [MeV/c]	centre value	statistical up	statistical low	systematic up	systematic low	centre value	statistical up	statistical low
[600, 800)	6.65e-05	4.48e-06	4.48e-06	1.35e-05	1.37e-05	5.27e-05	1.07e-06	1.07e-06
[800, 1000)	6.05e-05	4.51e-06	4.51e-06	1.62e-05	1.64e-05	5.20e-05	1.06e-06	1.06e-06
[1000, 1200)	5.25e-05	4.51e-06	4.51e-06	1.38e-05	1.40e-05	4.37e-05	9.78e-07	9.78e-07
[1200, 1400)	4.04e-05	4.25e-06	4.25e-06	1.22e-05	1.24e-05	3.31e-05	8.53e-07	8.53e-07
[1400, 1600)	2.64e-05	3.68e-06	3.68e-06	9.91e-06	1.02e-05	2.64e-05	7.64e-07	7.64e-07
[1600, 5000)	7.97e-06	6.40e-07	6.40e-07	2.22e-06	2.24e-06	6.40e-06	8.97e-08	8.97e-08

	MC reconstruction level					MC generator level		
R	centre value	statistical up	statistical low	systematic up	systematic low	centre value	statistical up	statistical low
[0, 2)	1.06e-02	7.48e-04	7.48e-04	2.65e-03	2.69e-03	8.79e-03	1.38e-04	1.38e-04
[2, 3)	2.42e-02	1.57e-03	1.57e-03	6.23e-03	6.32e-03	1.95e-02	2.89e-04	2.89e-04
[3, 4)	2.78e-02	1.73e-03	1.73e-03	7.35e-03	7.44e-03	2.37e-02	3.18e-04	3.18e-04
[4, 8)	5.31e-03	3.68e-04	3.68e-04	1.38e-03	1.40e-03	4.09e-03	6.64e-05	6.64e-05

Table B.13: The number of $Z + K^0_\mathrm{S}$ candidates per Z candidate as dependence of R and p_T of K^0_S for generator level and reconstruction level in simulation for Pythia 8.

	MC reconstruction level					MC generator level		
p_T [MeV/c]	centre value	statistical up	statistical low	systematic up	systematic low	centre value	statistical up	statistical low
[0, 200)	1.46e-04	1.25e-05	1.25e-05	3.52e-05	3.73e-05	9.33e-05	4.38e-07	4.38e-07
[200, 400)	2.22e-04	9.02e-06	9.02e-06	2.29e-05	2.45e-05	2.08e-04	6.45e-07	6.45e-07
[400, 600)	2.90e-04	8.19e-06	8.19e-06	3.19e-05	3.36e-05	2.47e-04	7.01e-07	7.01e-07
[600, 800)	2.89e-04	8.77e-06	8.77e-06	3.53e-05	4.60e-05	2.44e-04	6.96e-07	6.96e-07
[800, 1000)	2.41e-04	8.53e-06	8.53e-06	3.00e-05	3.27e-05	2.11e-04	6.50e-07	6.50e-07
[1000, 1200)	1.93e-04	8.96e-06	8.96e-06	3.16e-05	3.51e-05	1.69e-04	5.84e-07	5.84e-07
[1200, 1400)	1.50e-04	9.18e-06	9.18e-06	3.20e-05	3.70e-05	1.32e-04	5.17e-07	5.17e-07
[1400, 1600)	1.16e-04	8.60e-06	8.60e-06	3.05e-05	3.63e-05	1.01e-04	4.55e-07	4.55e-07
[1600, 5000)	2.64e-05	1.12e-06	1.12e-06	3.77e-06	4.11e-06	2.20e-05	5.00e-08	5.00e-08

	MC reconstruction level					MC generator level		
R	centre value	statistical up	statistical low	systematic up	systematic low	centre value	statistical up	statistical low
[0, 1)	2.61e-02	1.39e-03	1.39e-03	3.74e-03	4.05e-03	2.11e-02	9.29e-05	9.29e-05
[1, 2)	6.18e-02	2.13e-03	2.13e-03	7.73e-03	8.52e-03	5.52e-02	1.48e-04	1.48e-04
[2, 3)	8.28e-02	2.45e-03	2.45e-03	1.04e-02	1.28e-02	7.51e-02	1.70e-04	1.70e-04
[3, 4)	9.03e-02	2.50e-03	2.50e-03	1.13e-02	1.27e-02	8.42e-02	1.79e-04	1.79e-04
[4, 5)	5.50e-02	1.91e-03	1.91e-03	7.28e-03	8.14e-03	4.95e-02	1.40e-04	1.40e-04
[5, 8)	2.75e-02	1.44e-03	1.44e-03	4.20e-03	4.57e-03	2.56e-02	5.73e-05	5.73e-05

Table B.14: The number of $Z + \Lambda$ candidates per Z candidate as dependence of R and p_T of Λ for generator level and reconstruction level in simulation for Pythia 8.

	MC reconstruction level					MC generator level		
p_T [MeV/c]	centre value	statistical up	statistical low	systematic up	systematic low	centre value	statistical up	statistical low
[600, 800)	4.98e-05	3.53e-06	3.53e-06	1.35e-05	1.36e-05	3.52e-05	2.71e-07	2.71e-07
[800, 1000)	4.95e-05	3.84e-06	3.84e-06	1.70e-05	1.71e-05	3.75e-05	2.79e-07	2.79e-07
[1000, 1200)	4.94e-05	4.40e-06	4.40e-06	1.72e-05	1.74e-05	3.83e-05	2.82e-07	2.82e-07
[1200, 1400)	4.64e-05	5.04e-06	5.04e-06	1.89e-05	1.92e-05	3.50e-05	2.70e-07	2.70e-07
[1400, 1600)	3.43e-05	4.90e-06	4.90e-06	1.77e-05	1.81e-05	3.14e-05	2.56e-07	2.56e-07
[1600, 5000)	1.26e-05	1.03e-06	1.03e-06	4.52e-06	4.56e-06	9.18e-06	3.30e-08	3.30e-08

	MC reconstruction level					MC generator level		
R	centre value	statistical up	statistical low	systematic up	systematic low	centre value	statistical up	statistical low
[0, 2)	1.05e-02	7.57e-04	7.57e-04	3.36e-03	3.39e-03	7.76e-03	4.00e-05	4.00e-05
[2, 3)	2.24e-02	1.50e-03	1.50e-03	7.22e-03	7.30e-03	1.59e-02	8.08e-05	8.08e-05
[3, 4)	2.41e-02	1.54e-03	1.54e-03	7.89e-03	7.97e-03	1.85e-02	8.72e-05	8.72e-05
[4, 8)	8.94e-03	6.38e-04	6.38e-04	2.94e-03	2.98e-03	6.60e-03	2.59e-05	2.59e-05

Table B.15: The number of $Z + K_S^0$ candidates per Z candidate as dependence of R and p_T of K_S^0 for data.

p_T [MeV/c]	Data centre value	statistical up	statistical low	systematic up	systematic low
[0, 200)	7.73e-05	6.91e-06	6.91e-06	9.72e-06	1.12e-05
[200, 400)	1.52e-04	5.61e-06	5.61e-06	9.45e-06	1.04e-05
[400, 600)	2.26e-04	7.43e-06	7.43e-06	1.88e-05	2.06e-05
[600, 800)	2.34e-04	7.92e-06	7.92e-06	2.15e-05	3.11e-05
[800, 1000)	1.99e-04	7.41e-06	7.41e-06	1.76e-05	1.98e-05
[1000, 1200)	1.88e-04	8.34e-06	8.34e-06	2.40e-05	2.71e-05
[1200, 1400)	1.72e-04	9.04e-06	9.04e-06	3.17e-05	3.69e-05
[1400, 1600)	1.17e-04	7.27e-06	7.27e-06	2.08e-05	2.58e-05
[1600, 5000)	2.30e-05	8.61e-07	8.61e-07	2.29e-06	2.57e-06

R	Data centre value	statistical up	statistical low	systematic up	systematic low
[0, 1)	2.01e-02	1.14e-03	1.14e-03	2.03e-03	2.36e-03
[1, 2)	6.08e-02	2.08e-03	2.08e-03	6.09e-03	6.96e-03
[2, 3)	8.94e-02	2.55e-03	2.55e-03	9.64e-03	1.11e-02
[3, 4)	9.39e-02	2.74e-03	2.74e-03	9.78e-03	1.13e-02
[4, 5)	5.80e-02	2.14e-03	2.14e-03	6.54e-03	7.42e-03
[5, 8)	9.51e-03	5.11e-04	5.11e-04	1.12e-03	1.79e-03

Table B.16: The number of $Z + \Lambda$ candidates per Z candidate as dependence of R and p_T of Λ for data.

p_T [MeV/c]	Data centre value	statistical up	statistical low	systematic up	systematic low
[600, 800)	7.08e-05	5.41e-06	5.41e-06	1.44e-05	1.46e-05
[800, 1000)	7.92e-05	5.83e-06	5.83e-06	2.12e-05	2.14e-05
[1000, 1200)	7.86e-05	6.40e-06	6.40e-06	2.06e-05	2.09e-05
[1200, 1400)	8.54e-05	7.03e-06	7.03e-06	2.58e-05	2.63e-05
[1400, 1600)	6.45e-05	6.42e-06	6.42e-06	2.42e-05	2.48e-05
[1600, 5000)	1.89e-05	1.13e-06	1.13e-06	5.26e-06	5.32e-06

R	Data centre value	statistical up	statistical low	systematic up	systematic low
[0, 2)	1.72e-02	1.08e-03	1.08e-03	4.59e-03	4.66e-03
[2, 3)	4.15e-02	2.42e-03	2.42e-03	1.14e-02	1.16e-02
[3, 4)	4.33e-02	2.70e-03	2.70e-03	1.19e-02	1.21e-02
[4, 8)	8.81e-03	6.15e-04	6.15e-04	2.40e-03	2.43e-03

Bibliography

[1] S. L. Glashow, "Partial Symmetries of Weak Interactions," *Nucl. Phys.*, vol. 22, pp. 579–588, 1961.

[2] S. Weinberg, "A model of leptons," *Phys. Rev. Lett.*, vol. 19, pp. 1264–1266, Nov 1967.

[3] A. Salam, "Weak and Electromagnetic Interactions," *Conf. Proc.*, vol. C680519, pp. 367–377, 1968.

[4] P. Skands, "Introduction to QCD," in *Proceedings, Theoretical Advanced Study Institute in Elementary Particle Physics: Searching for New Physics at Small and Large Scales (TASI 2012): Boulder, Colorado, June 4-29, 2012*, pp. 341–420, 2013.

[5] G. Sterman *et al.*, "Handbook of perturbative qcd," *Rev. Mod. Phys.*, vol. 67, pp. 157–248, Jan 1995.

[6] R. K. Ellis, W. J. Stirling, and B. R. Webber, "QCD and collider physics," *Camb. Monogr. Part. Phys. Nucl. Phys. Cosmol.*, vol. 8, pp. 1–435, 1996.

[7] G. Dissertori, I. G. Knowles, and M. Schmelling, *Quantum chromodynamics: high energy experiments and theory*. International series of monographs on physics, Oxford: Oxford Univ. Press, 2002.

[8] F. Halzen and A. Martin, *Quarks and leptons: an introductory course in modern particle physics*. Wiley, 1984.

[9] G. Altarelli, "The Standard model of particle physics," 2005.

[10] T. Binoth, C. Buttar, P. Clark, and E. Glover, *LHC Physics*. Scottish Graduate Series, CRC Press, 2012.

[11] P. A. M. Dirac, "On the theory of quantum mechanics," *Proceedings of the Royal Society of London A: Mathematical, Physical and Engineering Sciences*, vol. 112, no. 762, pp. 661–677, 1926.

[12] E. Fermi, "Zur Quantelung des idealen einatomigen Gases," *Zeitschrift für Physik*, vol. 36, no. 11, pp. 902–912, 1926.

[13] Bose, "Plancks Gesetz und Lichtquantenhypothese," *Zeitschrift für Physik*, vol. 26, no. 1, pp. 178–181, 1924.

[14] K. Nishijima, "Charge independence theory of V particles," *Progress of Theoretical Physics*, vol. 13, no. 3, pp. 285–304, 1955.

[15] M. Gell-Mann, "The interpretation of the new particles as displaced charge multiplets," *Il Nuovo Cimento (1955-1965)*, vol. 4, no. 2, pp. 848–866, 1956.

[16] K. A. Olive *et al.*, "Review of Particle Physics," *Chin. Phys.*, vol. C38, p. 090001, 2014.

[17] S. Weinberg, "New approach to the renormalization group," *Phys. Rev. D*, vol. 8, pp. 3497–3509, Nov 1973.

[18] C. Elsasser, U. Straumann, K. Müller, O. Steinkamp, and L. Baudis, *The Rare Decays $B^0_{(s)} \to \mu^+\mu^-$ and Z Boson Production at LHCb and Radiation Damage in its Silicon Tracker*. PhD thesis, Zurich U., Feb 2015. Presented 02 Oct 2014.

[19] E. Noether, "Invarianten beliebiger Differentialausdrücke," *Nachrichten von der Gesellschaft der Wissenschaften zu Göttingen, Mathematisch-Physikalische Klasse*, vol. 1918, pp. 37–44, 1918.

[20] M. Kobayashi and T. Maskawa, "CP Violation in the Renormalizable Theory of Weak Interaction," *Prog. Theor. Phys.*, vol. 49, pp. 652–657, 1973.

[21] V. Khachatryan *et al.*, "First Measurement of the Underlying Event Activity at the LHC with $\sqrt{s} = 0.9$ TeV," *Eur. Phys. J.*, vol. C70, pp. 555–572, 2010.

[22] T. Aaltonen *et al.*, "Studying the Underlying Event in Drell-Yan and High Transverse Momentum Jet Production at the Tevatron," *Phys. Rev.*, vol. D82, p. 034001, 2010.

[23] S. D. Drell and T.-M. Yan, "Partons and their Applications at High-Energies," *Annals Phys.*, vol. 66, p. 578, 1971. [Annals Phys.281,450(2000)].

[24] L. N. Lipatov, "The parton model and perturbation theory," *Sov. J. Nucl. Phys.*, vol. 20, pp. 94–102, 1975. [Yad. Fiz.20,181(1974)].

[25] V. N. Gribov and L. N. Lipatov, "Deep inelastic e p scattering in perturbation theory," *Sov. J. Nucl. Phys.*, vol. 15, pp. 438–450, 1972. [Yad. Fiz.15,781(1972)].

[26] G. Altarelli and G. Parisi, "Asymptotic Freedom in Parton Language," *Nucl. Phys.*, vol. B126, pp. 298–318, 1977.

[27] Y. L. Dokshitzer, "Calculation of the Structure Functions for Deep Inelastic Scattering and e+ e- Annihilation by Perturbation Theory in Quantum Chromodynamics.," *Sov. Phys. JETP*, vol. 46, pp. 641–653, 1977. [Zh. Eksp. Teor. Fiz.73,1216(1977)].

[28] H. Abramowicz *et al.*, "Combination of measurements of inclusive deep inelastic $e^{\pm}p$ scattering cross sections and QCD analysis of HERA data," *Eur. Phys. J.*, vol. C75, no. 12, p. 580, 2015.

[29] "CTEQ collaboration." http://cteq.org, February 2016.

[30] "MSTW collaboration." http://mstwpdf.hepforge.org, November 2016.

[31] "HERAFitter collaboration." https://www.herafitter.org/HERAFitter/, November 2016.

[32] J. S. Anderson, *Testing the electroweak sector and determining the absolute luminosity at LHCb using dimuon final states*. PhD thesis, University Coll., Dublin, 2008.

[33] T. Sjostrand, S. Mrenna, and P. Z. Skands, "A Brief Introduction to PYTHIA 8.1," *Comput. Phys. Commun.*, vol. 178, pp. 852–867, 2008.

[34] M. Bahr *et al.*, "Herwig++ Physics and Manual," *Eur. Phys. J.*, vol. C58, pp. 639–707, 2008.

[35] J. Bellm *et al.*, "Herwig 7.0/Herwig++ 3.0 release note," *Eur. Phys. J.*, vol. C76, no. 4, p. 196, 2016.

[36] T. Gleisberg, S. Hoeche, F. Krauss, M. Schonherr, S. Schumann, F. Siegert, and J. Winter, "Event generation with SHERPA 1.1," *JHEP*, vol. 02, p. 007, 2009.

[37] R. Astalos *et al.*, "Proceedings of the Sixth International Workshop on Multiple Partonic Interactions at the Large Hadron Collider," 2015.

[38] A. Buckley, H. Hoeth, H. Schulz, and J. E. von Seggern, "Monte Carlo event generator validation and tuning for the LHC," *PoS*, vol. ACAT08, p. 112, 2008.

[39] R. Aaij *et al.*, "Observation of associated production of a Z boson with a D meson in the forward region," *JHEP*, vol. 04, p. 091, 2014.

[40] R. Placakyte, "Impact of lhc on the parton distribution functions," in *Precision theory for precise measurements at LHC and future colliders, Quy-Nhon, Vietnam*, Sept.-Oct. 2016.

[41] J. M. Campbell, J. W. Huston, and W. J. Stirling, "Hard interactions of quarks and gluons: a primer for lhc physics," *Reports on Progress in Physics*, vol. 70, no. 1, p. 89, 2007.

[42] S. Farry and N. Chiapolini, "A measurement of high-pT muon reconstruction efficiencies in 2011 and 2012 data," Tech. Rep. LHCb-INT-2014-030. CERN-LHCb-INT-2014-030, CERN, Geneva, Jul 2014.

[43] E. Norrbin and T. Sjöstrand, "Production and hadronization of heavy quarks," *The European Physical Journal C - Particles and Fields*, vol. 17, no. 1, pp. 137–161, 2000.

[44] "LHCb homepage." http://lhcb.cern.ch, May 2016.

[45] B. Russell, *History of Western Philosophy*. Routledge classics, Routledge, 1946.

[46] J. J. T. M. F.R.S., "Xl. cathode rays," *Philosophical Magazine Series 5*, vol. 44, no. 269, pp. 293–316, 1897.

[47] E. Rutherford, "The scattering of alpha and beta particles by matter and the structure of the atom," *Phil. Mag.*, vol. 21, pp. 669–688, 1911.

[48] CERN, *CAS - CERN Accelerator School : 50 Years of Synchrotrons*, (Geneva), CERN, 1997. Early synchrotrons in Britain. Early work for CERN/J Lawson ; The CERN synchrotrons/G Brianti. - short version of RAL-97-011.

[49] C. Llewellyn Smith, "The Large Hadron Collider: Lessons learned and summary," *Phil. Trans. Roy. Soc. Lond.*, vol. A370, pp. 995–1004, 2012.

[50] R. Heuer and H. Schopper, *LEP - The Lord of the Collider Rings at CERN 1980-2000: The Making, Operation and Legacy of the World's Largest Scientific Instrument*. Springer Berlin Heidelberg, 2009.

[51] J. D. Jackson, *Classical electrodynamics*. New York, NY: Wiley, 3rd ed. ed., 1999.

[52] J. Schwinger, "On the classical radiation of accelerated electrons," *Phys. Rev.*, vol. 75, pp. 1912–1925, Jun 1949.

[53] A. Chao, "Accelerators for high-energy physics research," in *Looking to the 21st century. Proceedings, 1st International Conference on Frontiers of Physics, Joint Meeting of the Chinese Physical Societies, Shantou, P.R. China, August 5-9, 1995*, 1995.

[54] C. Rubbia, "A few considerations of strategy on the future of CERN: opening talk," 1990.

[55] B. Barish and J. E. Brau, "The International Linear Collider," *Int. J. Mod. Phys.*, vol. A28, no. 27, p. 1330039, 2013.

[56] R. Billinge and M. C. Crowley-Milling, "The cern proton-antiproton colliding beam facilities," *IEEE Transactions on Nuclear Science*, vol. 26, pp. 2974–2977, June 1979.

[57] L. Evans and P. Bryant, "LHC Machine," *JINST*, vol. 3, p. S08001, 2008.

[58] J. P. Blewett, "200-GeV intersecting storage accelerators," 1971.

[59] T. Schoerner-Sadenius, ed., *The Large Hadron Collider : Harvest of Run 1*. Cham: Springer International Publishing, 2015.

[60] *ATLAS: letter of intent for a general-purpose pp experiment at the large hadron collider at CERN*. Letter of Intent, Geneva: CERN, 1992.

[61] M. Markytan *et al.*, "Letter of intent: by the CMS Collaboration for a general purpose detector at LHC," Tech. Rep. CERN-LHCC-92-003. CERN-LHCC-92-3. LHCC-I-1, CERN, Geneva, 1992.

[62] "Letter of Intent for A Large Ion Collider Experiment [ALICE]," Tech. Rep. CERN-LHCC-93-016. LHCC-I-4, CERN, Geneva, 1993.

[63] "LHCb: letter of intent," Tech. Rep. CERN-LHCC-95-5. LHCC-I-8. CERN-LHCC-1995-005, CERN, Geneva, 1995.

[64] W. Kienzle *et al.*, *Total cross section: elastic scattering and diffraction dissociation at the LHC*. Letter of Intent, Geneva: CERN, 1997.

[65] O. Adriani, "LHCf Letter of Intent for a p-Pb run. A precise study of forward physics in $\sqrt{s_N N}$= 4.4 TeV proton-Lead ion collisions with LHCf at the LHC," Tech. Rep. CERN-LHCC-2011-015. LHCC-I-021, CERN, Geneva, Dec 2011.

[66] G. Giacomelli, A. A. Faust, and J. L. Pinfold, "A search for highly ionizing particles and slow exotic decays at the LHC using the MOEDAL detectors: letter of intent," Tech. Rep. CERN-LHCC-98-005. LHCC-19. LHCC-I-19, CERN, Geneva, Feb 1998.

[67] O. S. Bruning *et al.*, "LHC Design Report Vol.1: The LHC Main Ring," 2004.

[68] F. Marcastel, "CERN's Accelerator Complex. La chaîne des accélérateurs du CERN," Oct 2013. General Photo.

[69] G. Aad *et al.*, "Observation of a new particle in the search for the Standard Model Higgs boson with the ATLAS detector at the LHC," *Phys. Lett.*, vol. B716, pp. 1–29, 2012.

[70] S. Chatrchyan *et al.*, "Observation of a new boson at a mass of 125 GeV with the CMS experiment at the LHC," *Phys. Lett.*, vol. B716, pp. 30–61, 2012.

[71] "Lhc long term schedule," September 2016.

[72] R. Alemany-Fernandez *et al.*, "Operation and Configuration of the LHC in Run 1," Nov 2013.

[73] M. Lamont, "Status of the lhc," *Journal of Physics: Conference Series*, vol. 455, no. 1, p. 012001, 2013.

[74] R. Aaij *et al.*, "Measurement of $\sigma(pp \to b\bar{b}X)$ at $\sqrt{s} = 7$ TeV in the forward region," *Phys. Lett.*, vol. B694, pp. 209–216, 2010.

[75] R. Aaij *et al.*, "Prompt charm production in pp collisions at sqrt(s)=7 TeV," *Nucl. Phys.*, vol. B871, pp. 1–20, 2013.

[76] *LHCb : Technical Proposal*. Tech. Proposal, Geneva: CERN, 1998.

[77] R. Antunes-Nobrega *et al.*, *LHCb reoptimized detector design and performance: Technical Design Report*. Technical Design Report LHCb, Geneva: CERN, 2003.

[78] R. Aaij *et al.*, "LHCb Detector Performance," *Int. J. Mod. Phys.*, vol. A30, no. 07, p. 1530022, 2015.

[79] "LHCb VELO TDR: Vertex locator. Technical design report," 2001.

[80] A. A. Alves, Jr. *et al.*, "The LHCb Detector at the LHC," *JINST*, vol. 3, p. S08005, 2008.

[81] P. R. Barbosa-Marinho *et al.*, *LHCb inner tracker: Technical Design Report*. Technical Design Report LHCb, Geneva: CERN, 2002. revised version number 1 submitted on 2002-11-13 14:14:34.

[82] "Silicon Tracker Webpage." http://lhcb.physik.uzh.ch/SiliconTracker/, May 2016.

[83] "LHCb magnet: Technical design report," 2000.

[84] J. A. N. van Tilburg, *Track Simulation and Reconstruction in LHCb*. PhD thesis, Vrije U., Amsterdam, 2005.

[85] P. R. Barbosa-Marinho *et al.*, *LHCb outer tracker: Technical Design Report*. Technical Design Report LHCb, Geneva: CERN, 2001.

[86] P. A. Cherenkov, "Visible emission of clean liquids by action of γ radiation," *Doklady Akademii Nauk SSSR 2: 451*, 1934.

[87] S. Amato *et al.*, *LHCb RICH: Technical Design Report*. Technical Design Report LHCb, Geneva: CERN, 2000.

[88] M. Adinolfi *et al.*, "Performance of the LHCb RICH detector at the LHC," *Eur. Phys. J.*, vol. C73, p. 2431, 2013.

[89] S. Amato *et al.*, *LHCb calorimeters: Technical Design Report*. Technical Design Report LHCb, Geneva: CERN, 2000.

[90] P. R. Barbosa-Marinho *et al.*, *LHCb muon system: Technical Design Report*. Technical Design Report LHCb, Geneva: CERN, 2001.

[91] R. Antunes-Nobrega *et al.*, *LHCb trigger system: Technical Design Report*. Technical Design Report LHCb, Geneva: CERN, 2003. revised version number 1 submitted on 2003-09-24 12:12:22.

[92] C. Møller, "Zur Theorie des Durchgangs schneller Elektronen durch Materie," *Annalen der Physik*, vol. 406, pp. 531–585, 1932.

[93] H. J. Bhabha, "The scattering of positrons by electrons with exchange on dirac's theory of the positron," *Proceedings of the Royal Society of London A: Mathematical, Physical and Engineering Sciences*, vol. 154, no. 881, pp. 195–206, 1936.

[94] M. E. Peskin and D. V. Schroeder, *An Introduction to quantum field theory*. 1995.

[95] S. Tavernier, *Experimental Techniques in Nuclear and Particle Physics*. Springer Berlin Heidelberg, 2010.

[96] R. Mankel, "Pattern recognition and event reconstruction in particle physics experiments," *Reports on Progress in Physics*, vol. 67, no. 4, p. 553, 2004.

[97] M. De Cian, U. Straumann, O. Steinkamp, and N. Serra, *Track Reconstruction Efficiency and Analysis of* $B^0 \to K^{*0}\mu^+\mu^-$ *at the LHCb Experiment*. PhD thesis, Zurich U., Sep 2013. Presented 14 Mar 2013.

[98] E. Bos and E. Rodrigues, "The LHCb Track Extrapolator Tools," Tech. Rep. LHCb-2007-140. CERN-LHCb-2007-140, CERN, Geneva, Nov 2007.

[99] S. Stevenson and G. Wilkinson, *A Study of Central Exclusive Production at LHCb*. PhD thesis, Oxford U., Sep 2015. Presented 20 Nov 2015.

[100] D. Hutchcroft, "VELO pattern recognition," 2007.

[101] O. Callot, "FastVelo, a fast and efficient pattern recognition package for the Velo," 2011.

[102] M. T. Schiller, *Track reconstruction and prompt* K_S^0 *production at the LHCb experiment*. PhD thesis, Heidelberg U., 2011.

[103] O. Callot and M. Schiller, "PatSeeding: A standalone track reconstruction algorithm," 2008.

[104] M. Benayoun and O. Callot, "The forward tracking, an optical model method," Tech. Rep. LHCb-2002-008, CERN, Geneva, Feb 2002. revised version number 1 submitted on 2002-02-22 17:19:02.

[105] O. Callot and S. Hansmann-Menzemer, "The Forward Tracking: Algorithm and Performance Studies," Tech. Rep. LHCb-2007-015. CERN-LHCb-2007-015, CERN, Geneva, May 2007.

[106] M. Needham and J. Van Tilburg, "Performance of the track matching," 2007.

[107] M. Needham, "Performance of the track matching," 2007.

[108] O. Callot, "Downstream pattern recognition," 2007.

[109] O. Callot, M. Kucharczyk, and M. Witek, "VELO-TT track reconstruction," Tech. Rep. LHCb-2007-010. CERN-LHCb-2007-010, CERN, Geneva, Apr 2007.

[110] E. Rodrigues, "Dealing with clones in the tracking," Tech. Rep. LHCb-2006-057. CERN-LHCb-2006-057, CERN, Geneva, Nov 2006.

[111] R. E. Kalman, "A new approach to linear filtering and prediction problems," *ASME Journal of Basic Engineering*, 1960.

[112] "LHCb Trigger and Online Upgrade Technical Design Report," Tech. Rep. CERN-LHCC-2014-016. LHCB-TDR-016, CERN, Geneva, May 2014.

[113] "Letter of Intent for the LHCb Upgrade," Tech. Rep. CERN-LHCC-2011-001. LHCC-I-018, CERN, Geneva, Mar 2011.

[114] J. Albrecht, V. V. Gligorov, and G. Raven, "Review Document: Full Software Trigger," Tech. Rep. LHCb-PUB-2014-036. CERN-LHCb-PUB-2014-036, CERN, Geneva, May 2014. On behalf of the the HLT software group.

[115] L. Collaboration, "LHCb Tracker Upgrade Technical Design Report," Tech. Rep. CERN-LHCC-2014-001. LHCB-TDR-015, CERN, Geneva, Feb 2014.

[116] E. Bowen and B. Storaci, "VeloUT tracking for the LHCb Upgrade," Tech. Rep. LHCb-PUB-2013-023. CERN-LHCb-PUB-2013-023. LHCb-INT-2013-056, CERN, Geneva, Apr 2014.

[117] E. E. Bowen, B. Storaci, and M. Tresch, "VeloTT tracking for LHCb Run II," Tech. Rep. LHCb-PUB-2015-024. CERN-LHCb-PUB-2015-024. LHCb-INT-2014-040, CERN, Geneva, Apr 2016.

[118] R. Aaij *et al.*, "Performance of the lhcb full real-time reconstruction and high-level trigger with 13 tev data," *CERN-LHCb-DP-2016-002*.

[119] R. Aaij *et al.*, "Measurement of the track reconstruction efficiency at LHCb," *JINST*, vol. 10, no. 02, p. P02007, 2015.

[120] T. Skwarnicki, "A study of the radiative cascade transitions between the upsilone-prime and upsilon resonances," DESY-F31-86-02.

[121] O. Deschamps, F. P. Machefert, M. H. Schune, G. Pakhlova, and I. Belyaev, "Photon and neutral pion reconstruction," Tech. Rep. LHCb-2003-091, CERN, Geneva, Sep 2003.

[122] F. Archilli *et al.*, "Performance of the muon identification at lhcb," *Journal of Instrumentation*, vol. 8, no. 10, p. P10020, 2013.

[123] A. Hocker *et al.*, "TMVA - Toolkit for Multivariate Data Analysis," *PoS*, vol. ACAT, p. 040, 2007.

[124] L. Anderlini *et al.*, "The PIDCalib package," Tech. Rep. LHCb-PUB-2016-021. CERN-LHCb-PUB-2016-021, CERN, Geneva, Jul 2016.

[125] O. Lupton, L. Anderlini, B. Sciascia, and V. Gligorov, "Calibration samples for particle identification at LHCb in Run 2," Tech. Rep. LHCb-PUB-2016-005. CERN-LHCb-PUB-2016-005, CERN, Geneva, Mar 2016.

[126] M. Pivk and F. R. Le Diberder, "SPlot: A Statistical tool to unfold data distributions," *Nucl. Instrum. Meth.*, vol. A555, pp. 356–369, 2005.

[127] R. Aaij *et al.*, "Differential branching fraction and angular analysis of the decay $B^0 \to K^{*0}\mu^+\mu^-$," *JHEP*, vol. 08, p. 131, 2013.

[128] T. Sjostrand and M. van Zijl, "A Multiple Interaction Model for the Event Structure in Hadron Collisions," *Phys. Rev.*, vol. D36, p. 2019, 1987.

[129] R. Aaij *et al.*, "Measurement of the forward energy flow in pp collisions at $\sqrt{s} = 7$ TeV," *Eur. Phys. J.*, vol. C73, p. 2421, 2013.

[130] E. Nurse and S. Sen, "Methods to Select Soft Diffraction Dissociation at the LHC," 2011.

[131] I. Belyaev *et al.*, "Handling of the generation of primary events in Gauss, the LHCb simulation framework," *J. Phys. Conf. Ser.*, vol. 331, p. 032047, 2011.

[132] T. Sjostrand, S. Mrenna, and P. Z. Skands, "PYTHIA 6.4 Physics and Manual," *JHEP*, vol. 05, p. 026, 2006.

[133] P. Z. Skands, "Tuning Monte Carlo Generators: The Perugia Tunes," *Phys. Rev.*, vol. D82, p. 074018, 2010.

[134] J. Pumplin *et al.*, "New generation of parton distributions with uncertainties from global QCD analysis," *JHEP*, vol. 07, p. 012, 2002.

[135] H. L. Lai *et al.*, "Global QCD analysis of parton structure of the nucleon: CTEQ5 parton distributions," *Eur. Phys. J.*, vol. C12, pp. 375–392, 2000.

[136] T. Pierog and K. Werner, "EPOS Model and Ultra High Energy Cosmic Rays," *Nucl. Phys. Proc. Suppl.*, vol. 196, pp. 102–105, 2009.

[137] S. Ostapchenko, "Status of QGSJET," *AIP Conf. Proc.*, vol. 928, pp. 118–125, 2007.

[138] E.-J. Ahn, R. Engel, T. K. Gaisser, P. Lipari, and T. Stanev, "Cosmic ray interaction event generator SIBYLL 2.1," *Phys. Rev.*, vol. D80, p. 094003, 2009.

[139] R. Aaij *et al.*, "Measurement of prompt hadron production ratios in pp collisions at $\sqrt{s} =$ 0.9 and 7 TeV," *Eur. Phys. J.*, vol. C72, p. 2168, 2012.

[140] R. Aaij *et al.*, "Measurement of V^0 production ratios in pp collisions at $\sqrt{s} = 0.9$ and 7 TeV," *JHEP*, vol. 08, p. 034, 2011.

[141] R. Aaij *et al.*, "Measurement of forward W and Z boson production in pp collisions at $\sqrt{s} = 8$ TeV," *JHEP*, vol. 01, p. 155, 2016.

[142] D. J. Lange, "The EvtGen particle decay simulation package," *Nucl. Instrum. Meth.*, vol. A462, pp. 152–155, 2001.

[143] P. Golonka and Z. Was, "PHOTOS Monte Carlo: A Precision tool for QED corrections in Z and W decays," *Eur. Phys. J.*, vol. C45, pp. 97–107, 2006.

[144] J. Allison *et al.*, "Geant4 developments and applications," *IEEE Trans. Nucl. Sci.*, vol. 53, p. 270, 2006.

[145] S. Agostinelli *et al.*, "GEANT4: A Simulation toolkit," *Nucl. Instrum. Meth.*, vol. A506, pp. 250–303, 2003.

[146] M. Clemencic *et al.*, “The LHCb simulation application, Gauss: Design, evolution and experience,” *J. Phys. Conf. Ser.*, vol. 331, p. 032023, 2011.

[147] W. D. Hulsbergen, “Decay chain fitting with a Kalman filter,” *Nucl. Instrum. Meth.*, vol. A552, pp. 566–575, 2005.

[148] F. Pedregosa *et al.*, “Scikit-learn: Machine learning in Python,” *Journal of Machine Learning Research*, vol. 12, pp. 2825–2830, 2011.

[149] R. Aaij *et al.*, “Prompt K^0_s production in pp collisions at $\sqrt{s} = 0.9$ TeV,” *Phys. Lett.*, vol. B693, pp. 69–80, 2010.

[150] R. A. Fisher, “The use of multiple measurements in taxonomic problems,” *Annals of Eugenics*, vol. 7, no. 2, pp. 179–188, 1936.

[151] B. P. Roe, H.-J. Yang, J. Zhu, Y. Liu, I. Stancu, and G. McGregor, “Boosted decision trees, an alternative to artificial neural networks,” *Nucl. Instrum. Meth.*, vol. A543, no. 2-3, pp. 577–584, 2005.

[152] Y. Freund and R. E. Schapire, “A decision-theoretic generalization of on-line learning and an application to boosting,” *Journal of Computer and System Sciences*, vol. 55, no. 1, pp. 119 – 139, 1997.

[153] G. Punzi, “Sensitivity of searches for new signals and its optimization,” *eConf*, vol. C030908, p. MODT002, 2003. [,79(2003)].

[154] J. H. Friedman, “Greedy function approximation: A gradient boosting machine.,” *Ann. Statist.*, vol. 29, pp. 1189–1232, 10 2001.

[155] J. H. Friedman, “Stochastic gradient boosting,” *Computational Statistics & Data Analysis*, vol. 38, no. 4, pp. 367 – 378, 2002. Nonlinear Methods and Data Mining.

[156] J. Podolanski and R. Armenteros, “III. Analysis of V-events,” *The London, Edinburgh, and Dublin Philosophical Magazine and Journal of Science*, vol. 45, no. 360, pp. 13–30, 1954.

[157] I. Abt *et al.*, “Inclusive V0 production cross-sections from 920-GeV fixed target proton nucleus collisions,” *Eur. Phys. J.*, vol. C29, pp. 181–190, 2003.

[158] R. Aaij *et al.*, “Measurement of the forward Z boson production cross-section in pp collisions at $\sqrt{s} = 7$ TeV,” *JHEP*, vol. 08, p. 039, 2015.

[159] R. Aaij *et al.*, “Performance of the LHCb Vertex Locator,” *JINST*, vol. 9, p. 09007, 2014.

[160] S. Navin, “Diffraction in Pythia,” 2010.

[161] G. Lanfranchi, X. Cid Vidal, S. Furcas, M. Gandelman, J. A. Hernando, J. H. Lopez, E. Polycarpo, and A. Sarti, “The Muon Identification Procedure of the LHCb Experiment for the First Data,” Tech. Rep. LHCb-PUB-2009-013. CERN-LHCb-PUB-2009-013, CERN, Geneva, Aug 2009.

[162] M. Needham, “Clone Track Identification using the Kullback-Liebler Distance,” Tech. Rep. LHCb-2008-002. CERN-LHCb-2008-002. LPHE-2008-002, CERN, Geneva, Jan 2008.

[163] S. Farry, “Forward EW Physics at the LHC,” in *3rd Large Hadron Collider Physics Conference (LHCP 2015) St. Petersburg, Russia, August 31-September 5, 2015*, 2016.

[164] S. Schael *et al.*, “Precision electroweak measurements on the Z resonance,” *Phys. Rept.*, vol. 427, pp. 257–454, 2006.

[165] M. De Cian, S. Hansmann-Menzemer, A. Jaeger, P. Seyfert, J. van Tilburg, and S. Wandernoth, “Measurement of the track finding efficiency,” Tech. Rep. LHCb-PUB-2011-025. CERN-LHCb-PUB-2011-025, CERN, Geneva, Apr 2012.

[166] *LHCb muon system: addendum to the Technical Design Report*. Technical Design Report LHCb, Geneva: CERN, 2003.

[167] *LHCb muon system: second addendum to the Technical Design Report*. Technical Design Report LHCb, Geneva: CERN, 2005. Submitted on 9 Apr 2005.

[168] R. Fruhwirth, “Application of Kalman filtering to track and vertex fitting,” *Nucl. Instrum. Meth.*, vol. A262, pp. 444–450, 1987.

[169] P. Billoir, “Track fitting with multiple scattering: A new method,” *Nuclear Instruments and Methods in Physics Research*, vol. 225, no. 2, pp. 352 – 366, 1984.

[170] R. Barlow, *Statistics: A Guide to the Use of Statistical Methods in the Physical Sciences*. Manchester Physics Series, Wiley, 1989.

[171] “The Large Hadron Collider Project (Resolution Annex 1+2). Le projet du grand collisionneur de hadrons. 100th Session of Council,” Jun 1994.

[172] C. H. Llewellyn Smith, “Chapter I: The Physics Case: Physics with a multi TeV hadron collider,” 1984.

[173] R. J. Wallace and R. McNulty, *A precise measurement of the Z boson cross-section and a test of the Standard Model using the LHCb detector*. PhD thesis, University Coll., Dublin, Nov 2015. Presented 16 Oct 2015.

Curriculum Vitae

Personal Information

Name: Tresch, Marco

Date of birth: 18. Juli 1987

Hometown: Silenen UR

Education

2012 – 2017	Dissertation in Physics, University of Zurich “Tracking and particle identification at LHCb and strange hadron production in events with Z boson” Supervisor: Prof. Dr. Ulrich Straumann, Dr. Katharina Müller
2012	Master of Science in Physics UZH “Measurement of Asymmetries in the Decay $B^0 \to K^0\mu^+\mu^-$ at the LHCb Experiment” Supervisor: Prof. Dr. Ulrich Straumann, Prof. Dr. Nicola Serra
2010 – 2012	Master Program Particle Physics UZH
2010	Bachelor of Science in Physics UZH “Extended Measurements of Charge Sharing at the TT Test Stand” Supervisor: Prof. Dr. Ulrich Straumann, Dr. Olaf Steinkamp
2007 – 2010	Bachelor Program Physics UZH
2006	Maturität mit Schwerpunktfach Physik und Anwendungen der Mathematik, Kantonale Mittelschule Uri